Kinetic and Spectroscopic Studies of Singlet Molecular Oxygen at High Temperatures

by

Razmik B. Boodaghians, B.Sc.

This thesis is submitted to the University of Keele in partial fulfilment of the requirements for the degree of Doctor of Philosophy.

Department of Chemistry
University of Keele

September 1983

To My Parents

The work reported in this thesis was carried out by the author under the supervision of Dr. Peter Borrell. Experimental results in Chapter Eight were obtained in collaboration with Dr. Patricia Borrell, who performed and analysed shocks with run numbers beginning with P; all other shocks (beginning with R) were performed and analysed by the author.

Acknowledgements

In presenting this thesis I would like to thank the following people:

Dr. Peter Borrell for his supervision and advice during the course of this work.

My co-workers, Dr. Patricia Borrell and Mr. Don Richards and also Dr. Melanie Thorne for many helpful discussions.

Professor I.T. Millar for the facilities in the Department of Chemistry.

Dr. P. Collis in the Computer Centre.

The technical staff of the Department particularly Chris Cork, Ralph Pattison, Peter Holbrook, Richard Goodwin and David Olivant.

Mrs. Margaret Furnival for her excellent typing of the text, Mrs. Christine Owen who patiently typed the tables and Mr. Terry Bolam for graphic and photographic work.

Mr. Edward Melikof for his unceasing encouragement.

The University of Keele for a departmental studentship.

Olga and Ohan Mesropian for their help throughout my career.

Last but not least my wife for her patience, help and encouragement.

ABSTRACT

This thesis describes the kinetic and spectroscopic studies of singlet molecular oxygen by observing their emissions in a discharge flow shock tube apparatus.

The rate constants k_d^M and k_q^M for the quenching of $O_2(a^1\Delta_g)$ and $O_2(b^1\Sigma_g^+)$ by M, M = NH_3, NO, HCl and SO_2, have been measured at 295 K and between 600 and 1100 K by studying the emissions at 634 and 762 nm.

At 295 K the rate constants are:

M	$k_d^M/dm^3\ mol^{-1}\ s^{-1}$	$k_q^M/dm^3\ mol^{-1}\ s^{-1}$
NH_3	$(5.37\pm0.14) \times 10^3$	$(7.05\pm0.10) \times 10^7$
NO	$(2.10\pm0.28) \times 10^4$	$(1.70\pm0.13) \times 10^7$
HCl	$(8.00\pm0.34) \times 10^4$	$(1.60\pm0.20) \times 10^7$
SO_2	3×10^3	$(2.50\pm0.50) \times 10^5$

The values for k_d^{HCl} and $k_d^{SO_2}$, determined from extrapolation of high temperature data, are new. The rest are similar to the values determined previously.

The rate constants for quenching of $O_2(a^1\Delta_g)$ by NO, HCl and SO_2 increase with temperature and can be fitted between 295 and 1100 K to the simple Arrhenius equations:

$$k_d^{NO}/dm^3\ mol^{-1}\ s^{-1} = (1.90\pm0.20) \times 10^7 \exp[-(2030\pm50)/T]$$

$$k_d^{HCl}/dm^3\ mol^{-1}\ s^{-1} = (2.34\pm1.00) \times 10^7 \exp[-(1660\pm180)/T]$$

$$k_d^{SO_2}/dm^3\ mol^{-1}\ s^{-1} = (8.90\pm3.45) \times 10^6 \exp[-(2370\pm90)/T].$$

No appreciable temperature dependence was seen for the quenching of $O_2(a^1\Delta_g)$ by NH_3.

For the quenching of $O_2(b^1\Sigma_g^+)$ by HCl and NO the rate constants are nearly independent of temperature but fall slightly above 1000 K. A negative temperature dependence was observed for the quenching of $O_2(b^1\Sigma_g^+)$ by NH_3. The quenching by SO_2 proved too slow to be measured by this technique.

The present results for the quenching of $O_2(b^1\Sigma_g^+)$ together with previous studies show a simple correlation of the type of temperature dependence and the room temperature quenching efficiency, with the most efficient quenchers having a decreasing probability and the least an increasing probability with temperature.

The different temperature dependences observed are interpreted on the basis of long and short range interactions.

The temperature dependences of the three dimol emissions of $O_2(a^1\Delta_g)$ at 579, 634 and 703 nm has been studied between 295 and 1500 K. The intensity increases with temperature and concentration as expected for these bimolecular processes, but there is a further increase which is attributed to the appearance of overlapping hot-band emissions from vibrationally excited molecules of $O_2(a^1\Delta_g)$. For 703 nm emission there is an additional contribution from hot bands of $O_2(b^1\Sigma_g^+)$.

The relative emissivities of the bands and the rate constants for the collisional emission reactions have been determined and are presented in table 8.3. It appears that the intensities are governed by an electronic transition probability which changes rapidly with intermolecular distance.

CONTENTS

CHAPTER ONE

1 Introduction

1.1 Scope of the Thesis

In the past few years there has been a great deal of interest in the reactivity of electronically excited singlet molecular oxygen, $O_2(a^1\Delta_g)$ and $O_2(b^1\Sigma_g^+)$. For example, reactions of these metastable states are not only thought to be involved in biological processes[1] upper atmosphere[2] and air pollution[3] chemistry but also in lasers of the energy transfer type, the O_2-iodine laser[4]. Hence, on the practical side, it is important to know the rates of collisional quenching and the mechanism by which the electronic energy is dissipated. From the point of view of basic science, the high stability of singlet molecular oxygen[5] permits the study of fundamental physical processes such as energy transfer, quenching, and relaxation. To understand these processes several pieces of information are desirable such as the functional dependence of the reaction rate constant on temperature which can provide information about the intermolecular potentials involved.

The theoretical aspects of these reactions have not yet been fully understood and generally there is a lack of convincing correlation between the experimental and theoretical approaches despite the major developments in both areas.

Kinetic measurements of reaction and physical deactivation of singlet molecular oxygen have been obtained by several techniques[5]. Most of these techniques have the drawback that only a small temperature range may be obtained 200 - 406 K.

The technique used in this study of reactions of singlet molecular oxygen is a combined discharge flow shock tube which has the advantage of producing much higher temperatures up to 1600 K. Therefore, the temperature dependence of the reaction rate constants can be studied over a wider temperature range than hitherto have been possible.

This first chapter serves to introduce the area of study; the properties of singlet molecular oxygen, the technique and concludes with an indication of the objectives that it was hoped to achieve.

1.2 Temperature Dependence of the Reaction Rates

Studying the temperature dependence of the rate of a chemical reaction can provide useful information about its nature.

For the majority of chemical reactions, the rate increases with temperature and the experimental Arrhenius equation:

$$k(T) = A \exp(- E_a/RT) \qquad (1.1)$$

provides a convenient way of displaying the temperature dependence of reaction rate constant, k, as a function of temperature T; where E_a is the experimental activation energy and A the pre-exponential factor.

The units of k will depend upon the overall order of a reaction; for zero order, mol dm^{-3} s^{-1}; for first order, s^{-1}; and for second order, dm^3 mol^{-1} s^{-1}.

The Arrhenius equation in its simplest form equation (1.1), can only be an approximation since both parameters A and E_a show at least some temperature dependence on the basis of any theoretical approach. However, experimentally it is very difficult to detect any temperature variation for these parameters.

The two main theoretical approaches that are currently used for understanding, and discussing the temperature dependence of reaction rates are; Simple Collision Theory [6], SCT, and Activated Complex Theory [6], ACT.

The SCT assumes molecules are simple hard spheres which can exchange kinetic energy along the line of centres on collision. The rate constant for a bimolecular reaction based on the SCT is given by:

$$k(T) = \sigma_{AB}(8KT/\pi\mu)^{\frac{1}{2}} \exp(- E_{min}/RT) \qquad (1.2)$$

where σ_{AB} is the collisional cross-section, μ is the reduced mass, K is the Boltzmann constant and E_{min} is the minimum energy required for collisions to result in reaction.

The SCT result for the rate constant has the same form as the experimental Arrhenius equation but it has introduced a slight temperature dependence of $T^{\frac{1}{2}}$ in addition to that implied in the Arrhenius equation.

If E_{min} is very small or zero then the reaction rate will depend on the collision frequency and the rate constant will have a temperature dependence of the form:

$$k(T) = CT^{\frac{1}{2}}. \qquad (1.3)$$

The dimol emission at 634 nm is a good example of such collision controlled reaction (chapter 8).

The defects of the SCT are that there is no definite way to allow for steric effects, that it ignores energy contributions from rotational and vibrational degrees of freedom, and that the minimum energy cannot be determined independently.

The ACT focuses attention on the activated complex, the complex which has only a transient existence is formed at the top of the potential energy barrier between reactants and products. The assumption is that it behaves like a normal molecule which has lost one of its vibrational degrees of freedom by becoming a motion along the reaction coordinate. The theory also assumes a state of equilibrium between the reactants and the activated complex which allows the use of a thermodynamic treatment. This is an important aspect of the ACT since a time dependent problem is changed into an equilibrium problem.

The rate constant for a bimolecular reaction based on ACT is given by:

$$k(T) = (KT/h)(Q^{\ddagger}/Q_A Q_B)\exp(-E^{\ddagger}/RT) \qquad (1.4)$$

where $Q^{\ddagger}$ is the molecular partition function per unit volume for the activated complex and $E^{\ddagger}$ is the energy barrier to the reaction.

Substitution of the appropriate partition function expressions[7] into equation (1.4) for the simplest diatomic-activated complex would give:

$$k(T) = \sigma_{AB}(8KT/\pi\mu)^{\frac{1}{2}} \exp(-E^{\ddagger}/RT). \qquad (1.5)$$

This result is similar to that obtained from SCT where $E^{\ddagger}$ may be identified with the molar equivalent of the minimum energy, E_{min}. Therefore, both theories can lead to similar numerical results and also similar molecular features. Neither model is entirely satisfactory for a complete theoretical prediction of rate constants especially when internal excitation modes are involved where the understanding of energy transfer is necessary for a reasonably complete description of the influence of temperature.

Another form of temperature dependence is based on the classical Landau-Teller theory[8] which appears in vibrational relaxation. This model is based on a collinear collision between two diatomic molecules where one is vibrationally excited. It assumes that only the short range repulsive interactions influence the process of energy transfer and predicts that the probability of vibrational energy transfer, P_{10}, from v = 1 to v = 0 at temperature, T, is given by:

$$P_{10} = C \exp(-\text{const.}/T)^{1/3}. \qquad (1.6)$$

Experimental measurements usually give a relaxation time, τ; the time for establishment of equilibrium between translational motion and the intramolecular vibration, which P_{10} is then calculated from:

$$1/P_{10} = Z\tau\{1 - [\exp(- h\nu/KT)]\} \qquad (1.7)$$

where Z is the collision rate.

The Landau-Teller theory does not account for the attractive part of the intermolecular potential which becomes important for all molecules at low temperatures, and for strongly polar molecules at all temperatures [8].

Many non-polar molecules have shown a linear Landau-Teller plot of Log P_{10} against $T^{1/3}$ over a wide temperature range [8].

Therefore, for reactions with an appreciable activation energy the SCT and ACT predict an exponential dependence of the rate constant on temperature while for energy transfer processes where there is no obvious energy barrier they predict that the rate constant will vary with the square root of the temperature. For a vibrational relaxation process the Landau-Teller theory predicts a $T^{1/3}$ dependence. Clearly, based on these theories it is difficult to predict the form of the temperature dependence for an electronic energy transfer process. Borrell et al.[9,10] having studied the quenching of $O_2(b^1\Sigma_g^+)$ by O_2, N_2, CO_2 and N_2O over a wide temperature range were able to show that none had a simple temperature behaviour. In contrast to these the present results for the quenching of $O_2(a^1\Delta_g)$ by NO, HCl and SO_2 have shown a linear Arrhenius temperature dependence (Chapter 6).

These various results indicate the importance of understanding of k(T) vs. T behaviour and the need for reliable high temperature data since the predictive ability of theory has yet to be improved.

1.3 Singlet Molecular Oxygen

Over the past several years there has been much interest in singlet molecular oxygen and its reactions. Singlet molecular oxygen is now believed to be involved in many processes[11] such as; chemiluminescence, photocarcinogenicity and decomposition of oxygen rich compounds.

This section describes structure, spectroscopy and reactions of singlet molecular oxygen, the features which make it particularly suitable to be studied by the discharge flow shock tube technique.

1.3.1 Electronic Structure

The ground state electron configuration of molecular oxygen may be written as:

$$(K)(K)(\sigma_g 2s)^2(\sigma_u 2s)^2(\sigma_g 2p)^2(\pi_u 2p)^4(\pi_g 2p)^2,\ {}^3\Sigma_g^-.$$

Figure 1.1 shows the corresponding molecular orbital energy level diagram.

The formulation suggests that there should be three states for molecular oxygen; ${}^3\Sigma_g^-$, ${}^1\Delta_g$, and ${}^1\Sigma_g^+$ since the two degenerate pi antibonding molecular orbitals hold only two electrons which may be arranged in several ways, figure 1.2.

The state, ${}^3\Sigma_g^-$, arises when the two electrons are unpaired and have parallel spins. If the two electrons are paired in the same orbital with opposed spins their angular momentum is in the same direction, $\Lambda = 2$, giving rise to the first excited state ${}^1\Delta_g$. This state is doubly degenerate since $M_L = \pm 2$. The second excited state, ${}^1\Sigma_g^+$, arises when the two electrons are in different orbitals with their spins opposed and their angular momentum in opposite direction, $\Lambda = 0$.

Figure 1.1 A molecular orbital diagram for oxygen

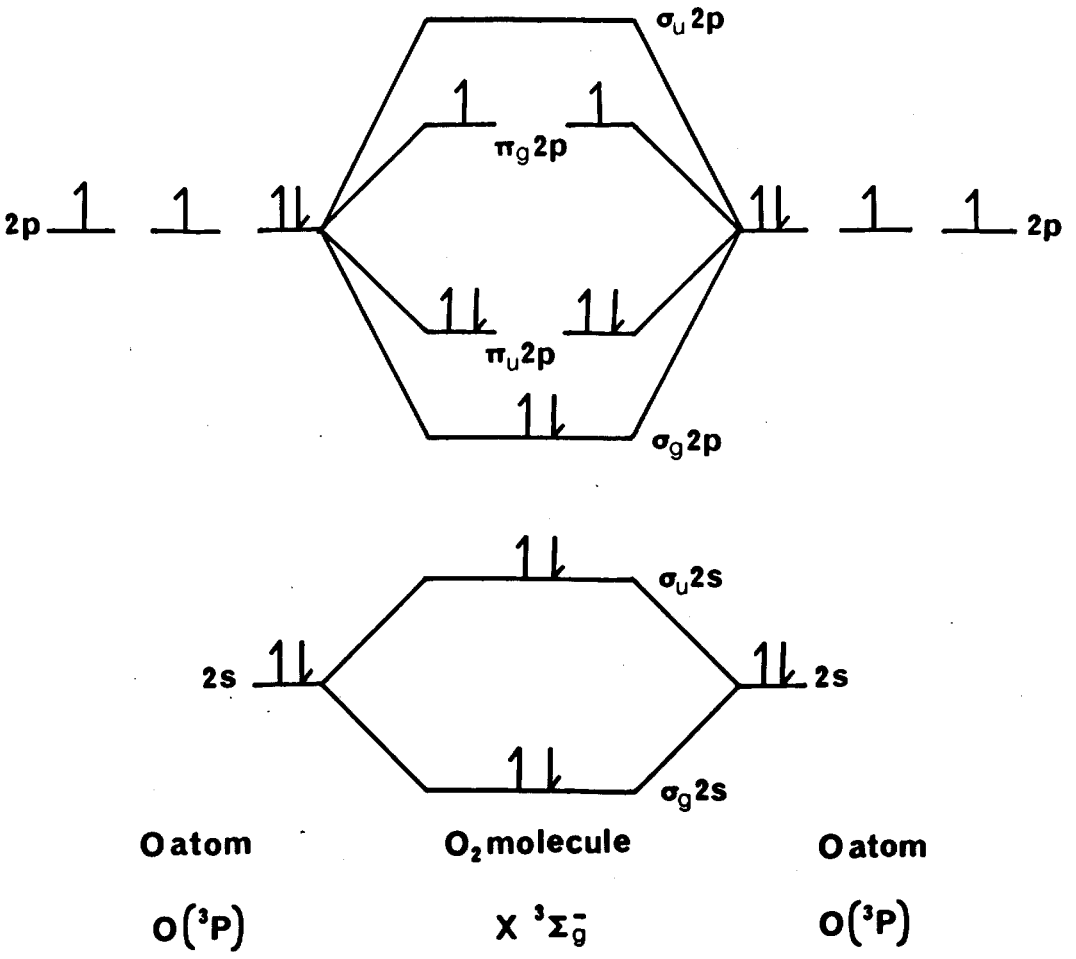

Figure 1.2 Electronic states of molecular oxygen

State	Symbol	Energy above ground state KJ	Orbital occupancy
2nd. excited	$b^1\Sigma_g^+$	157	1 ↓
1 st. excited	$a^1\Delta_g$	94	1↓ —
ground	$X^3\Sigma_g^-$	0	1 1

According to Hund's rule the term state with maximum multiplicity lies lowest in energy and for states of equal multiplicity that with the greatest Λ lies lowest. Therefore, in order of increasing energy the molecular states for oxygen are; $^3\Sigma_g^-$, $^1\Delta_g$, $^1\Sigma_g^+$, and there are three degenerate $^3\Sigma_g^-$ states, two equal energy $^1\Delta_g$ states, and a unique $^1\Sigma_g^+$ state.

Figure 1.3 shows an energy level diagram for some of the lower states of molecular oxygen[12]. The two lowest excited states; $^1\Delta_g$ and $^1\Sigma_g^+$, are often collectively referred to as singlet molecular oxygen.

The detailed forms corresponding to the state symbols are well described in several texts e.g. Herzberg (1939). Here a brief summary of the main points are given.

The state symbols are similar to the molecular orbital (MO) symbols except that capital letters are used, which represent the total orbital angular momentum $\Lambda h/2\pi$ around the symmetry axis: Σ, π, Δ, Φ, etc. However, there are two kinds of Σ states, Σ^+ and Σ^-, depending on whether the wave function does (Σ^-) or does not (Σ^+) change sign on reflection in a plane (any plane) passing through the nuclei.

For linear molecules with center of inversion, $D_{\infty h}$, each symbol also contains a subscript which indicates the symmetry (g for even, u for odd) with respect to the operation of inversion of the wave function at the center of the molecule.

The state symbols are also prefixed by a multiplicity superscript which indicates the quantum number of the resultant spin S (1,2,3, ... for S = o, $\frac{1}{2}$, 1,... respectively).

Figure 1.3 A potential energy level diagram for oxygen

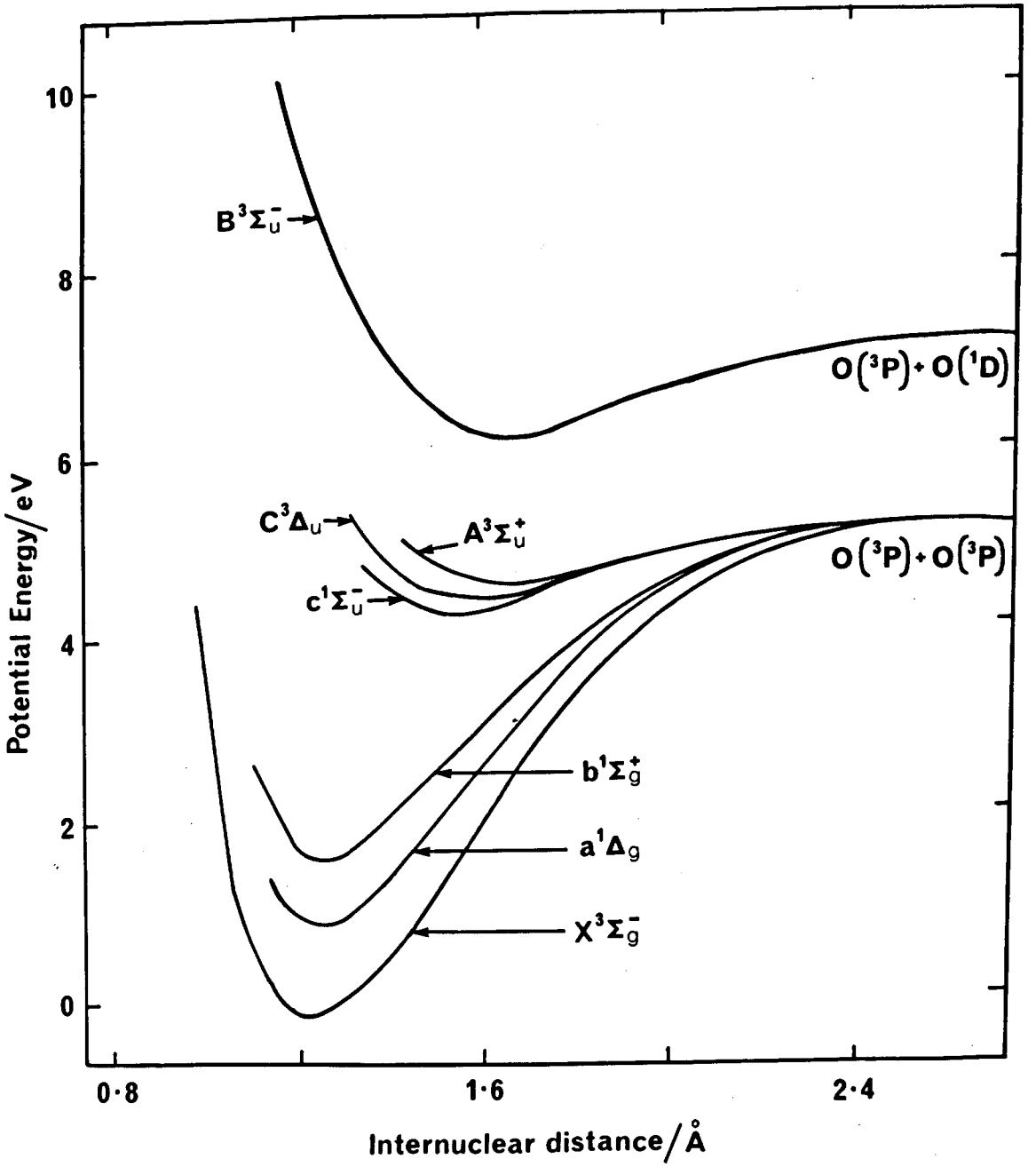

1.3.2 Electronic Transitions and Spectroscopy

The states $^1\Delta_g$ and $^1\Sigma_g^+$ are 0.98 eV and 1.63 eV above the ground state, $^3\Sigma_g^-$, respectively.

The optical transitions:

$$O_2(b^1\Sigma_g^+) \longrightarrow O_2(\chi^3\Sigma_g^-) + h\nu \ (\lambda = 762 \text{ nm}) \quad (1.8)[4.22]$$

$$O_2(a^1\Delta_g) \longrightarrow O_2(\chi^3\Sigma_g^-) + h\nu \ (\lambda = 1270 \text{ nm}) \quad (1.9)[4.4]$$

are strictly electric dipole forbidden.

The numbers in square bracket are the number of these equations as they appear in Chapter 4. A sequence of numbers has been used in Chapter 4 for ease of reference there.

The transition at 762 nm represents a spin-forbidden, symmetry-forbidden magnetic dipole transition [5]. The 1270 nm transition is a spin-forbidden, symmetry-forbidden, and orbitally-forbidden magnetic dipole transition [5]. These transitions which involve magnetic dipole interactions are relatively weak but their presence as atmospheric emission bands have been known [5] for some time. Since transitions to the ground state are forbidden in an unperturbed system, both the $^1\Delta_g$ and $^1\Sigma_g^+$ states are long lived species. Radiative life times of 45 minutes for $^1\Delta_g$, and 7 to 12 seconds for $^1\Sigma_g^+$ have been reported [5].

Simultaneous transitions can also occur under conditions where oxygen-oxygen collisions are more probable. For the simultaneous transition the spin-forbidden single molecule transition becomes spin-allowed. During this process the electronic energies of the two colliding molecules appear as a single photon:

$$2O_2(a^1\Delta_g)_{v=o} \rightarrow 2O_2(\chi^3\Sigma_g^-)_{v=o} + h\nu \ (\lambda = 634 \text{ nm}) \quad (1.10)[4.3]$$

$$2O_2(a^1\Delta_g)_{v=o} \rightarrow O_2(\chi^3\Sigma_g^-)_{v=1} + O_2(\chi^3\Sigma_g^-)_{v=o} + h\nu. \quad (\lambda = 703 \text{ nm}) \quad (1.11)$$

It is now accepted[12] that the dimol emission at 634 nm is the cause for the red glow observed when $O_2(^1\Delta_g)$ is generated chemically in an alkaline. H_2O_2 - Cl_2 system or by a microwave discharge.

A further dimol emission seen at 579 nm arises when one of the $O_2(a^1\Delta_g)$ molecules is also vibrationally excited[14]:

$$O_2(a^1\Delta_g)_{v=1} + O_2(a^1\Delta_g)_{v=o} \rightarrow 2O_2(\chi^3\Sigma_g^-)_{v=o} + h\nu \ (\lambda = 579 \text{ nm}). \quad (1.12)$$

Figure 1.4 is an illustration of the emissions studied in this laboratory, and it has been shown[15] that the emission at 634 nm is a simple collisional process.

In this work the temperature dependence of these three dimol emissions has been studied and the anomalous rise in their emission intensities are assigned to hot bands. Also reported are the rate constants determined for the hot band emissions; Chapter 8.

Simultaneous transitions which lead to "pooling" of the excitation energy into a single photon has been also observed for various combinations[16] of $^1\Sigma_g^+$, $^1\Delta_g$, $^3\Sigma_g^-$ states leading to photons of wavelengths as short as 380 nm. For example Khan and Kasha[17] have reported the emission from a mixed cooperative band at 478 nm:

$$O_2(a^1\Delta_g)_{v=o} + O_2(b^1\Sigma_g^+)_{v=o} \rightarrow 2O_2(\chi^3\Sigma_g^-)_{v=o} + h\nu \ (\lambda = 478 \text{ nm}). \quad (1.13)$$

1.3.3 Generation of Singlet Molecular Oxygen

Singlet molecular oxygen can be produced by a variety of physical and chemical methods.

(a) Physical Methods

1 - Electrical Discharge

Electrical discharges have been used as a convenient gas phase

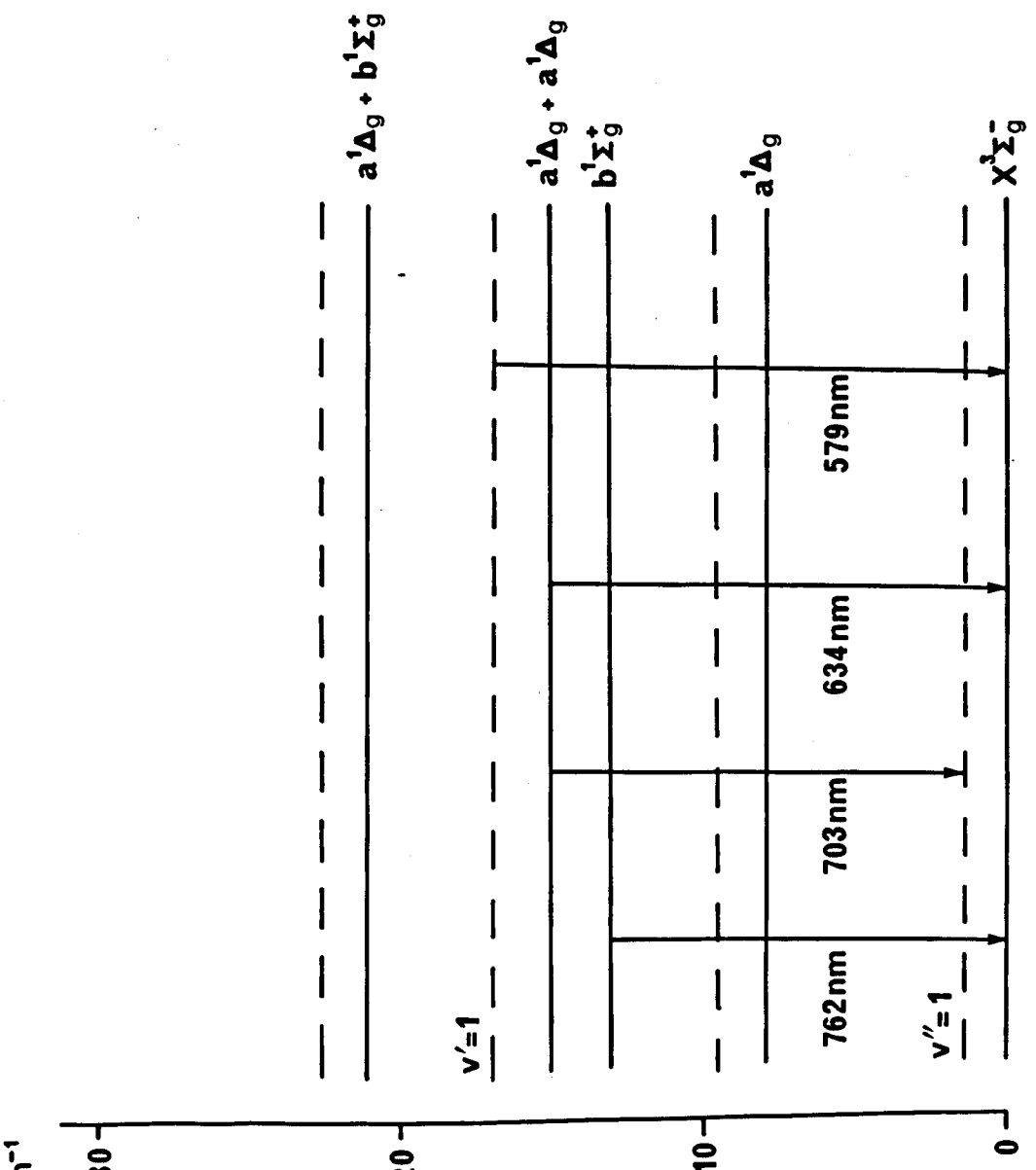

Figure 1.4 Singlet molecular oxygen emissions studied

method of generating singlet molecular oxygen. The most commonly used generators are microwave where the power is localized and directed via waveguides.

The purified oxygen at 1 to 10 torr pressure is passed through the discharge, after which the gas stream can contain[5] up to 10% of $^1\Delta_g$ and about 0.001% of $^1\Sigma_g^+$. Oxygen atoms are also formed in the discharge but these can be removed from the discharge products[18] by passing the gas over a mercury surface prior to its entry into the discharge. This causes a film of mercuric oxide to be deposited after the discharge. The effectiveness of the mercury can be tested by addition of nitric oxide to the discharged gas. The absence of atomic oxygen is signalled when no white glow is observed in the flow tube[18].

The mechanism by which excited molecular oxygen, $O_2(a^1\Delta_g)$, is formed in the discharge is not clear but it is thought that it may involve atom recombination[5]. However, $O_2(b^1\Sigma_g^+)$ is mainly formed outside the discharge from $O_2(a^1\Delta_g)$ by the energy-pooling reaction[19].

$$2O_2(a^1\Delta_g) \rightarrow O_2(b^1\Sigma_g^+) + O_2(\chi^3\Sigma_g^-). \qquad (1.14)[4.5]$$

In our apparatus, which is described in detail in Chapter 2, this is the technique employed for generating singlet molecular oxygen.

2 - Photolysis of Ozone

One of the mechanisms suggested for the presence of singlet molecular oxygen in upper and lower atmosphere is the photolysis of ozone[20].

It has been shown that the irradiation of ozone[21] in the region

310 - 330 nm results in the formation of singlet molecule oxygen:

$$O_3 + h\nu(\lambda = 310 - 330\ nm) \rightarrow O_2(a^1\Delta_g \text{ or } b^1\Sigma_g^+) + O(^3P). \quad (1.15)$$

This reaction could be an important process in the lower atmosphere where shorter wave lengths do not penetrate[22].

Irradiation of ozone[23] with λ in the region of 210 to 310 nm appears to generate $O_2(a^1\Delta_g)$ and oxygen atom in an excited state ^1D:

$$O_3 + h\nu(\lambda = 210 - 310\ nm) \rightarrow O_2(a^1\Delta_g) + O(^1D). \quad (1.16)$$

3 - Photosensitization

The sensitizer used in this technique may be any one of a variety of organic compounds, a dye or an aromatic hydrocarbon, that can absorb radiation at suitable wavelengths then act as donors in an energy transfer mechanism. Experiments for production of singlet molecular oxygen in solution[24] are well documented but gas phase experiments have not yet been fully tried. Steer, Sprung and Pitts[25] have studied gas-phase photosensitized oxygenations involving benzene oxygen systems. Also in the gas phase SO_2 has been used[26,27] as a sensitizer to produce singlet molecular oxygen. Reactions of this type have been thought to be responsible for the presence of singlet molecular oxygen in polluted urban atmospheres.

4 - Laser Excitation

This technique is particularly useful for selective production of the excited states. Furthermore, the narrow bandwidth of laser sources enable particular vibrational levels to be populated. Tunable dye lasers have been used[28,29] to produce $O_2(b^1\Sigma_g^+)$ and $O_2(b^1\Sigma_g^+)_{v=1}$. Kohse-Hoinghaus and Stuhl[30] have recently used a H_2-VUV laser to generate $O_2(^1\Sigma_g^+)$ molecules in the photolysis of O_2. A Nd-glass

laser[31] has been used to produce $O_2(a^1\Delta_g)_{v=1}$ from ground state molecular oxygen.

(b) Chemical Methods

Singlet molecular oxygen is generated from mixed hydrogen peroxide/sodium hypochlorite solutions:

$$OCl^- + H_2O_2 \rightarrow Cl^- + H_2O + O_2.$$

Spectroscopic evidence has shown[32] that both $a^1\Delta_g$ and $b^1\Sigma_g^+$ are generated according to the above equation and in methanolic solutions the efficiency of a $^1\Delta_g$ production approaches ca. 80%.

This reaction is the original system from which the red luminescence, now attributed to the dimol emission[12], was first observed[33]. Since then various peroxides[34] have been used as a means of producing singlet molecular oxygen.

It has been shown[35] that organic phosphites on interaction with ozone yield adducts that on warming decompose to give phosphate and singlet molecular oxygen:

$$(C_6H_5O)_3P + O_3 \xrightarrow[CH_2Cl_2]{-\ 70°C} (C_6H_5O)_3P\begin{smallmatrix}O\\ \diagup\ \diagdown\\ O\quad\ O\\ \diagdown\ \diagup\\ O\end{smallmatrix}$$

$$(C_6H_5O)_3P\begin{smallmatrix}O\\ \diagup\ \diagdown\\ O\quad\ O\\ \diagdown\ \diagup\\ O\end{smallmatrix} \xrightarrow{>\ -35°C} (C_6H_5O)_3P{=}O + O_2(a^1\Delta_g).$$

There are some other chemical methods for generating singlet molecular oxygen for example the decomposition of superoxide ion O_2^- or that of the peroxyacetynitrate in the presence of a base[36,37].

1.3.4 Methods for Detection of Singlet Molecular Oxygen

Methods for detecting singlet molecular oxygen can also be classified into physical and chemical methods.

(a) Physical Methods

Physical techniques are usually applied for the gas-phase detection of singlet molecular oxygen. There are several reviews[5] which discuss the various techniques used to detect singlet oxygen in the gas-phase. Here, only the methods used are mentioned.

Electron paramagnetic resonance spectroscopy (epr) is used for detection of molecular oxygen in the $a^1\Delta_g$ state[38].

$O_2(a^1\Delta_g)$ is also detected by photoionization technique[39]. This detection method has had only limited application in singlet oxygen studies because it requires a relatively large $a^1\Delta_g/\chi^3\Sigma_g^-$ ratio, and it is difficult to introduce the stream of excited molecular oxygen into the spectrometer without collisionally deactivating them.

Emission spectroscopy is used for detection of both $O_2(a^1\Delta_g)$ and $O_2(b^1\Sigma_g^+)$ states. Single molecule emission bands occur at 762 nm and 1270 nm, reactions (1.8) and (1.9) respectively. For high concentrations of $O_2(a^1\Delta_g)$, as in discharges, the cooperative emission bands at 634 nm and 703 nm, reactions (1.10) and (1.11) respectively, can also be detected. This technique overcomes the limitations of epr and photoionization methods which only permit the detection of $O_2(a^1\Delta_g)$.

Calorimetric methods[40] have also been used to detect singlet oxygen in the gas-phase. In this technique a thermal probe is introduced into the gas flow, and the detection is followed by monitoring the amount of heat released when the excited states are deactivated. The disadvantage of this method is that it is not

selective to any particular state or species that are present in the flow.

(b) Chemical Methods

In comparison with the physical methods the chemical methods used for the detection of singlet molecular oxygen in the condensed phase are limited since they have to be fast, specific to singlet molecular oxygen, free from side reactions and easily analysed for products. Of all the reactions investigated the system which is found most satisfactory is 1,4 cyclo addition of singlet molecular oxygen to conjugated dienes[41,42]. For example:

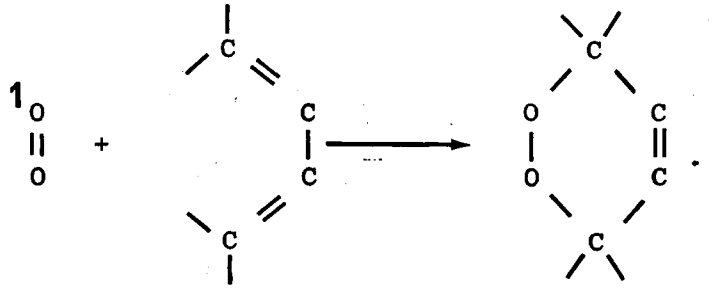

In this laboratory singlet molecule oxygen, which has been produced by a microwave discharge, is detected by optical emission using photomultipliers, this is fully discussed in Chapter 2. Absolute concentrations have not been measured since the studies carried out have only required comparative measurements.

1.3.5 Reactions of Singlet Molecular Oxygen

Singlet molecular oxygen can lose its energy by the emission of radiation and by several non-radiative pathways. The non-radiative processes can involve chemical reactions, energy transfer and physical quenching.

(a) Chemical Reactions

The gas phase chemical reactions reported for singlet molecular oxygen are the ones with ozone[5] and with olefinic[5] substances. For example the reaction of tetramethylethylene (TME) with $O_2(a^1\Delta_g)$

to form the hydroperoxide:

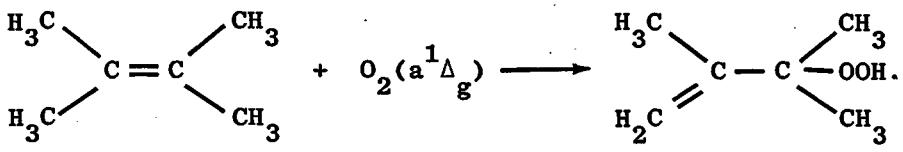

Reactions of singlet molecular oxygen with a wide variety of organic compounds have been studied and the reactions reported in the literature[32,43] are largely concerned with reactions of $O_2(a^1\Delta_g)$ in solution. These reactions will not be considered here.

(b) Energy-Transfer

During this process a second species becomes electronically excited. An example of such a process is the reaction known as "the energy-pooling" where $O_2(a^1\Delta_g)$ acts as an excited donor molecule:

$$2O_2(a^1\Delta_g) \longrightarrow O_2(b^1\Sigma_g^+) + O_2(\chi^3\Sigma_g^-). \qquad (1.14)[4.5]$$

This reaction was first postulated by Young and Black[19] to account for the concentration proportionality observed between the two singlet states $[O_2(a^1\Delta_g)]^2 \propto [O_2(b^1\Sigma_g^+)]$, in discharged oxygen system.

Schurath[44] has studied the energy distribution in the pooling reaction at room temperature by observing the emission from several vibrational levels of $O_2(b^1\Sigma_g^+)$ and found that (2,0) transition to be much stronger than that expected from Boltzmann distribution. This suggests that in the energy pooling reaction $O_2(b^1\Sigma_g)$ is preferentially formed in the v=2 level which is also the most nearly resonant reaction channel. However, Thomas and Thrush[45] in comparing the energy pooling reaction with a variety of quenching reactions, suggested that energy pooling may take place by two parrallel mechanisms; one which

involves long-range interactions and is nearly resonant, and another involving short-range interactions and giving a more statistical vibrational distribution.

As will be shown later this is one of the areas in which the discharge flow shock tube technique is used to study the nature of the energy pooling reaction by measuring its rate constant as a function of temperature.

Another example for an energy transfer process is the reaction of $O_2(a^1\Delta_g)$ with ground state iodine atom[46]:

$$O_2(a^1\Delta_g) + I(^2P_{3/2}) \longrightarrow O_2(\chi^3\Sigma_g^-) + I(^2P_{1/2}). \qquad (1.17)$$

In this process $O_2(a^1\Delta_g)$ transfers energy rapidly to I atom to form the excited state $I(^2P_{1/2})$.

Recent studies[47] have shown this is an important energy transfer process in $O_2(a^1\Delta_g)$ - I atom transfer laser.

(c) Physical Quenching

In this process the electronic excitation energy is lost by non-reactive collisions in the gas-phase or by deactivating collisions with surfaces. For a quenching gas M:

$$O_2(b^1\Sigma_g^+) + M \longrightarrow O_2(a^1\Delta_g) + M \qquad (1.18)[4.20]$$

and

$$O_2(a^1\Delta_g) + M \longrightarrow O_2(\chi^3\Sigma_g) + M. \qquad (1.19)[4.1]$$

In the last few years several laboratories have studied the room temperature quenching reactions of singlet molecular oxygen, reactions (1.18) and (1.19), and have reported quenching rate constants for these species. However, the theories presented to account for the large variations seen in quenching efficiencies have not been consistent.

For example, Davidson and Ogryzlo[48] studied the variation of the quenching rate constant of $O_2(a^1\Delta_g)$ and $O_2(b^1\Sigma_g^+)$ with the fundamental vibrational frequency of the quencher and found that the quenching efficiency increased with increasing value of the fundamental vibrational frequency. On the other hand Thomas and Thrush[45] having studied the quenching of both $O_2(a^1\Delta_g)$ and $O_2(b^1\Sigma_g^+)$ with a variety of quenchers were able to show a common surprisal plot for both species. This lead them to suggest, that although energy goes into vibration of the products, resonant quenching paths are not important so the quenching had to occur on the repulsive part of the intermolecular potential.

The theoretical approaches to the quenching in these systems are mainly developed for the quenching of $O_2(b^1\Sigma_g^+)$ and can be characterized in terms of long and short range interactions. These are mentioned briefly here, but are discussed further in Chapter 7 in relation to the results obtained in this work.

Kear and Abrahamson[49] developed a theory based on short-range mechanism which envisages an energy transfer when the molecules are very close together, on the repulsive part of the intermolecular potential energy curve. The other theory presented by Braithwaite, Davidson, and Ogryzlo[50] considers quenching as a long-range interaction process, taking place between the transition dipole of the excited molecule and the transition dipoles or quadrapoles of the quencher. Both theories assume that the electronic energy lost by the excited state is the vibrational energy acquired by the quencher. For a near-resonance quenching process the temperature dependences predicted by these two theories are markedly different; the one based on short range interactions predicts a positive temperature dependence whereas,

long range interactions predict a negative temperature dependence. Hence, a study of the temperature dependence could be useful for these quenching systems.

In comparison with the room temperature studies the high temperature studies have been limited both in the number of gases examined and the temperature range used. Ogryzlo and co-workers[51,52] have studied the temperature dependence of the quenching of $O_2(a^1\Sigma_g^+)$ by H_2 and HBr, between 173 and 393 K, and found that the sum of the two theoretical values of the rate constants best fitted the experimental result. Kohse-Hoinghaus and Stuhl[30] have studied the temperature dependence of the quenching rate constant of $O_2(b^1\Sigma_g^+)$ for H_2, HCl, NH_3, CH_4 and their deuterated analogs, between 200 and 350 K and found that the rates increased with temperature and that they could be fitted to the Arrhenius equation. Meanwhile Borrell and co-workers[9,10] having studied the quenching of $O_2(a^1\Sigma_g^+)$ by O_2, N_2, CO_2 and N_2O over a much wider temperature range were able to show that the quenching rate constant for O_2 and N_2 increased with temperature in contrast to those for CO_2 and N_2O which declined with temperature. This is interesting because O_2 and N_2 are poor quenchers of $O_2(b^1\Sigma_g^+)$ at room temperature whereas CO_2 and N_2O are efficient quenchers at room temperature.

These various considerations suggest that more work is required both theorctical and experimental to understand the temperature dependences of the quenching processes in these systems and any studies of the temperature dependence must be made over a large temperature range. At present time the discharge-flow shock tube technique seems to offer the best way of obtaining such results.

1.4 The Discharge Flow Shock Tube

This thesis is concerned with the study of singlet molecular oxygen in a discharge flow shock tube. In this section a brief history of the development of the technique and its adoption to study singlet molecular oxygen is given.

A combined discharge flow shock tube was first constructed by Hartunian, Thompson and Hewitt[53] in 1966. They used an RF discharge to dissociate nitrogen, and studied the temperature dependence of the afterglow recombination reaction. Gross and Cohen[54] have used the same system with a microwave discharge to study further chemiluminescent reactions. Breen, Quy and Glass[55] then used an RF discharge to study the vibrational relaxation of oxygen and hydrogen. Later on they also studied the reaction of hydrogen atoms with nitrous oxide.

The discharge flow shock tube system in this laboratory was constructed in 1969 to study active nitrogen. Since then it has been developed and modified further for studying the quenching and reactions of singlet molecular oxygen.

Our system differs from those used previously in the direction of the flow; the gas flows along the shock tube in the opposite direction to the shock, the facilities for pre-shock analysis of the concentration gradient along the tube and the use of the whole post-shock regime for the analysis.

The method has certain limitations for the study of the quenching reaction rates of $O_2(a^1\Delta_g)$ and $O_2(b^1\Sigma_g^+)$.

The reactions removing $O_2(a^1\Delta_g)$, generated in the microwave discharge, at room temperature must be slow enough so that an appreciable concentration of $O_2(a^1\Delta_g)$ is present along the tube; then at the high temperature, the reaction must be fast enough to

produce a measurable change in the concentration of $O_2(a^1\Delta_g)$ within the hot flow time of the experiment. As it will be shown later (Chapters 5 and 6) for the quenchers NO, HCl, NH_3 and SO_2 studied in this work NH_3 did not meet the second condition.

For $O_2(b^1\Sigma_g^+)$ generated in the flow, the condition to be satisfied is that the two or more reactions which form and remove $O_2(b^1\Sigma_g^+)$, establishing a steady state concentration, must have different temperature dependences. From the quenchers examined in this work SO_2 did not satisfy the conditions (Chapter 6).

The apparatus and experimental techniques used are described in detail in Chapter 2.

1.5 The Aim of the Present Work

The present project was undertaken to study further the temperature dependence of the reactions of singlet molecular oxygen in view of previously[9,10] observed differences in behaviour.

The discharge flow shock tube system was used to make measurements of the rate of deactivation of $O_2(a^1\Delta_g)$ and $O_2(b^1\Sigma_g^+)$ both at room temperature and at high temperatures by SO_2, NO, NH_3 and HCl. These quenchers were chosen because of their different quenching efficiencies at room temperature in order to find out whether the form of temperature dependency will be consistent with the previously observed temperature behaviour where the quenching rate constant increased with temperature for the least efficient quencher at room temperature, while it decreased with an increase in temperature for the more efficient quencher at room temperature. Furthermore the study of temperature dependence of the quenching rate constant over a wide temperature range were clearly needed to help to distinguish between the roles of long and short range interactions in the quenching process.

Also further studies were carried out on the temperature dependence of the emission intensity of the three dimol emissions of $O_2(a^1\Delta_g)$ at 579, 634 and 703 nm. Since in an earlier study[56,57] an anomalous rise in the intensity of the dimol emission was noticed for temperatures above 1000 K.

CHAPTER TWO

2 Experimental

2.1 Introduction

This chapter describes the discharge flow shock tube apparatus used in these experiments to study singlet molecular oxygen.

In the discharge flow shock tube, the test section of the shock tube is also the flow tube of the discharge flow system, and the apparatus can be used for discharge flow experiments at room temperature.

In this chapter the discharge flow and the shock tube sections are described separately. Also outlined are the tests carried out on the measuring devices, to make sure that the readings taken are accurate, and that meaningful kinetic data can be obtained from such a system. The chapter concludes with a standard procedure for operating the apparatus.

A general view of apparatus can be seen in plates 1 and 2 and a schematic diagram is shown in figure 2.1.

2.2 Discharge Flow System

Figure 2.2 shows the discharge flow section of the apparatus, it consists of the microwave cavity, the flow-tube, system of flow-meters and pressure regulators, a mercury reservoir prior to the discharge, a nitric oxide supply tube after the discharge and a wood's horn light trap.

The discharge is produced in an air-cooled quartz discharge tube of 10 mm i.d., powered by a 2450 MHz microwave generator (E.M.S. Microtron 200) operated at 100 W power. The cavity (E.M.S. 214L)

Plate 1

The discharge flow/shock tube, looking towards the driver section. The flow tube, covered with black cloth, can be seen behind the low pressure gas handling system. The transient recorders, timers and the oscilloscope can also be seen. At the far left the high pressure gas handling system is visible.

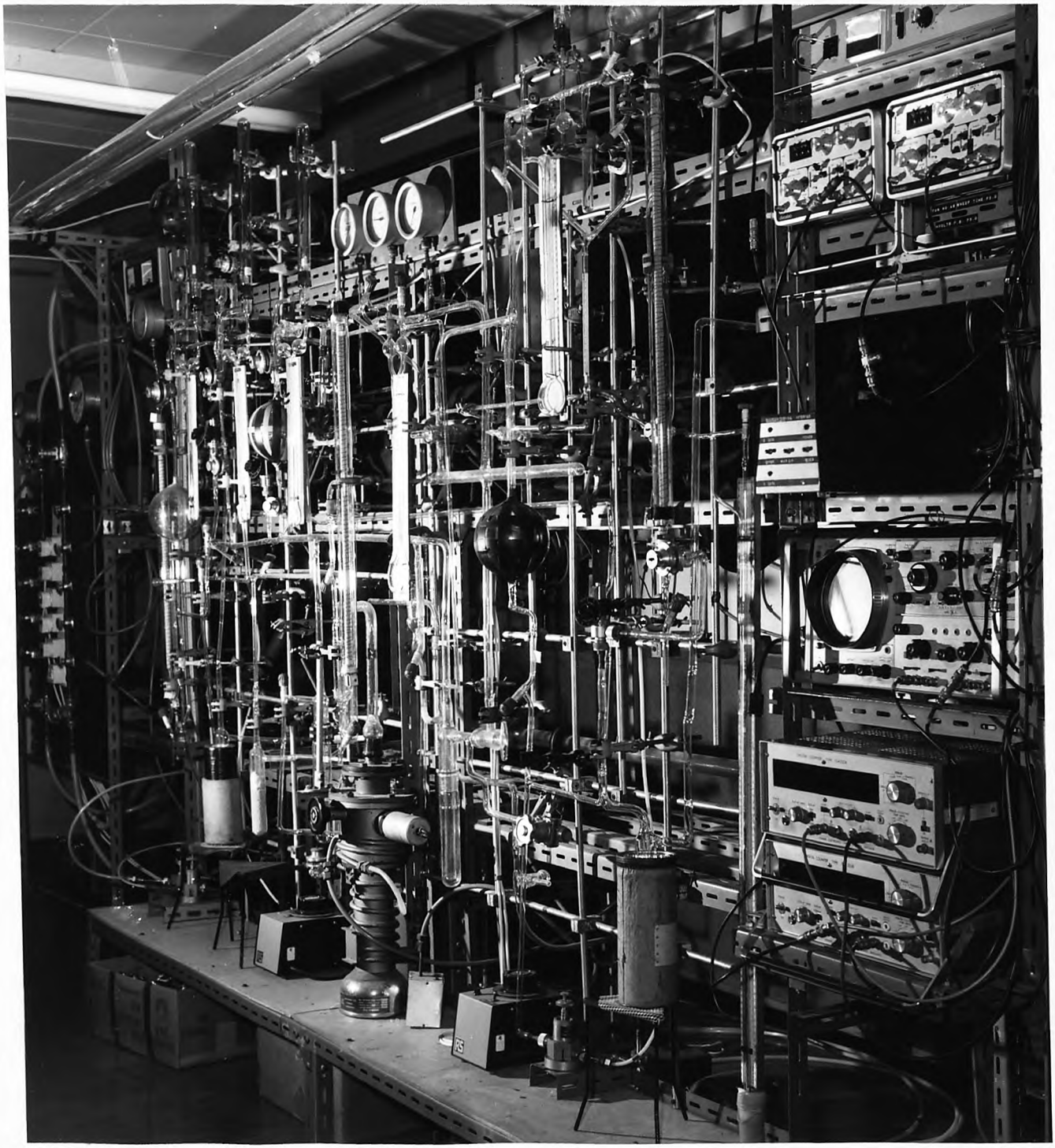

Plate 2

The discharge flow/shock tube, looking towards the discharge. The console on the right houses the light screen detectors.

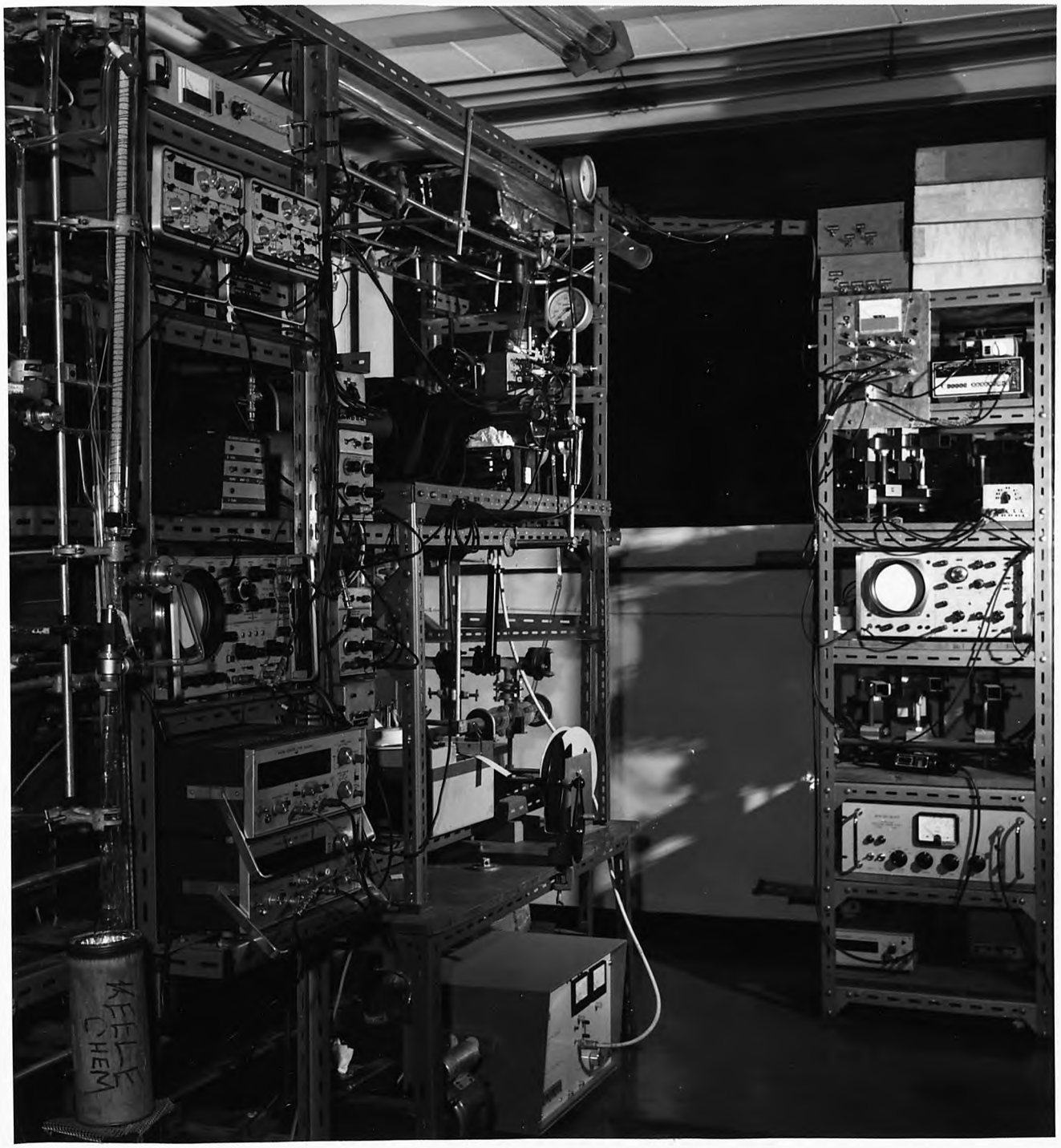

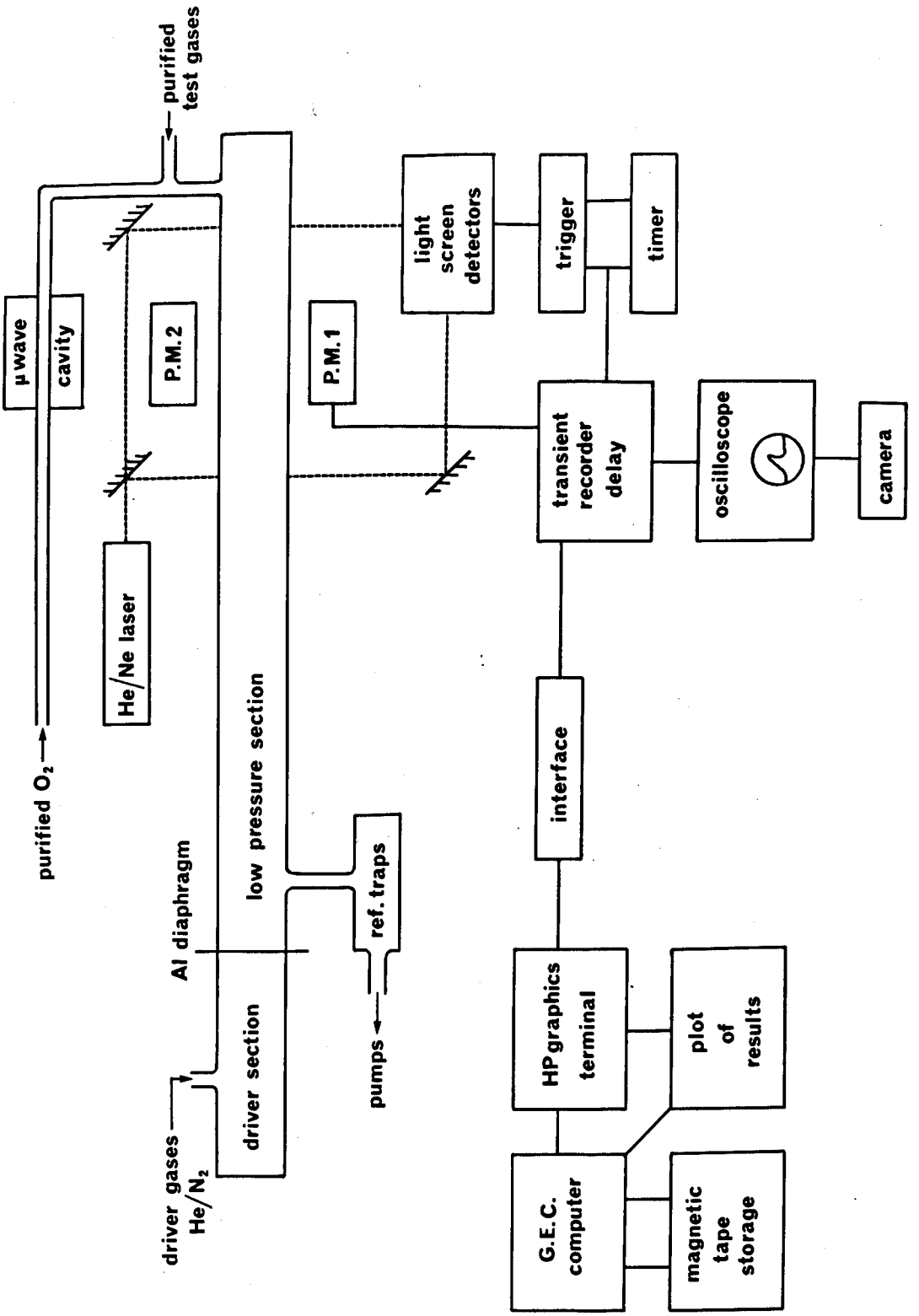

Figure 2.1 A schematic diagram of the apparatus

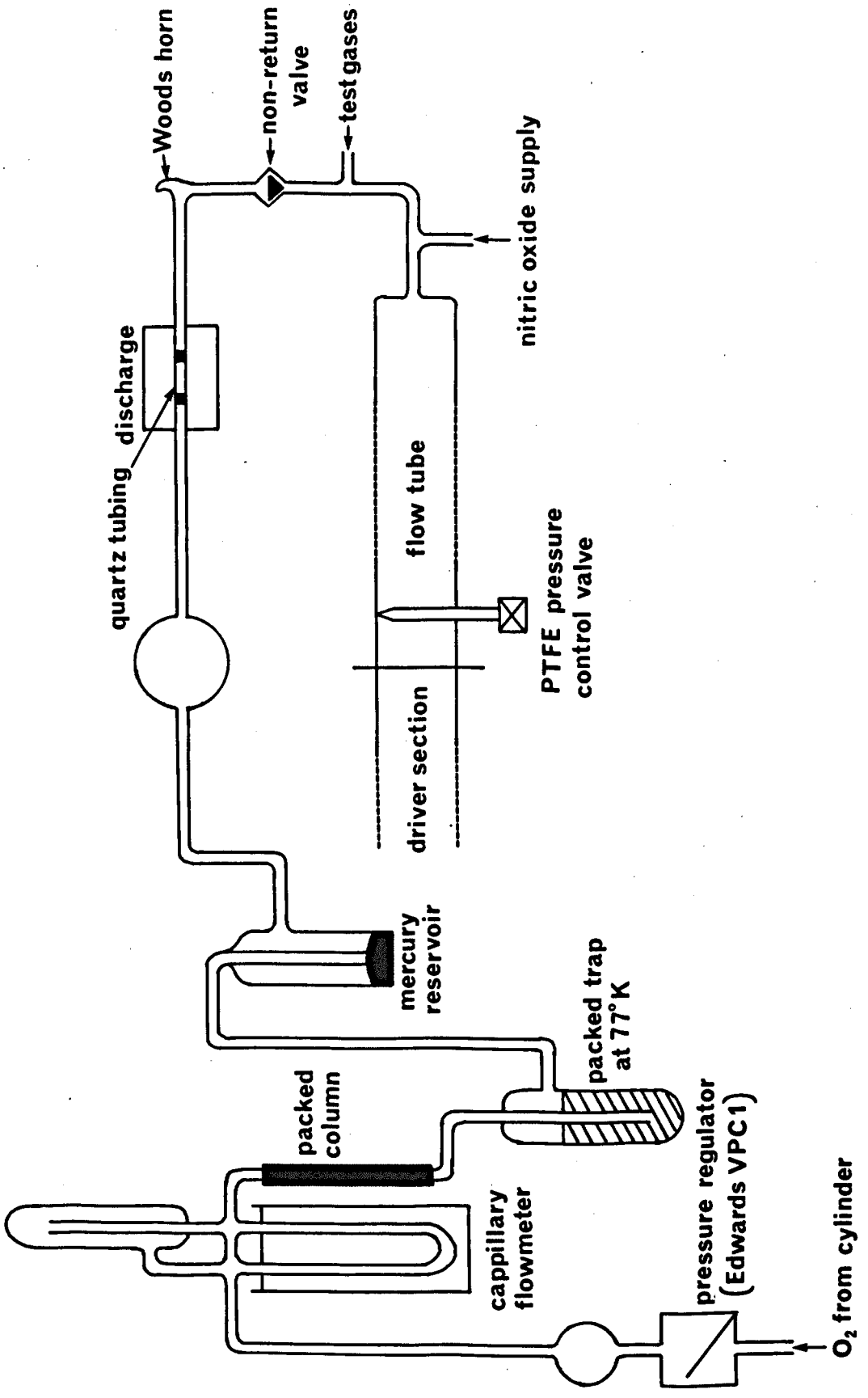

Figure 2.2 A diagram of the discharge section and gas entry

is a $^1/_4$ wave radial type, tuned for a minimum reflected power reading of the microwave unit. The microwave cavity and the discharge tube are situated in a Faraday cage about 1.6 m upstream of the observation station. The flow tube is 5 m long pyrex tubing with i.d. of 5 cm (Corning Ltd.). The discharge section is protected from the shock wave by a cutoff valve which shuts as the shock wave lifts the movable cap. This prevents the mercury being blown back into the system and also stops pieces of diaphragm material reaching the cavity.

The purified oxygen is passed over a clean mercury surface before entering the discharge to remove atomic oxygen from the products. A film of mercuric oxide is deposited after the discharge. The mercury reservoir is frequently cleaned and refilled with fresh mercury. The absence of atomic oxygen in the flow is tested by addition of nitric oxide to the flow immediately after the discharge. No detectable air afterglow was observed indicating that the flowing discharged gas was free of atomic oxygen.

The pressure in the flow tube is measured using a pumped diethyl phthalate manometer; the density of the diethyl phthalate was measured as 1.1136×10^3 Kg m^{-3}.

2.2.1 Gas Handling System

Figure 2.3 shows a schematic diagram for regulating and purifying the gases. The non-corrosive test gases are delivered from the cylinder to pressure regulators (Edward VPC1) using 6 mm and 10 mm nylon tubing. The pressure regulators are set to maintain the pressure in the glassware system below atmospheric at ca. 720 mm Hg (96 KPa). Rotaflow type (Corning Quickfit) taps are used to switch on and off the flowing gas. The amount of gas flowing into the discharge and the flow tube

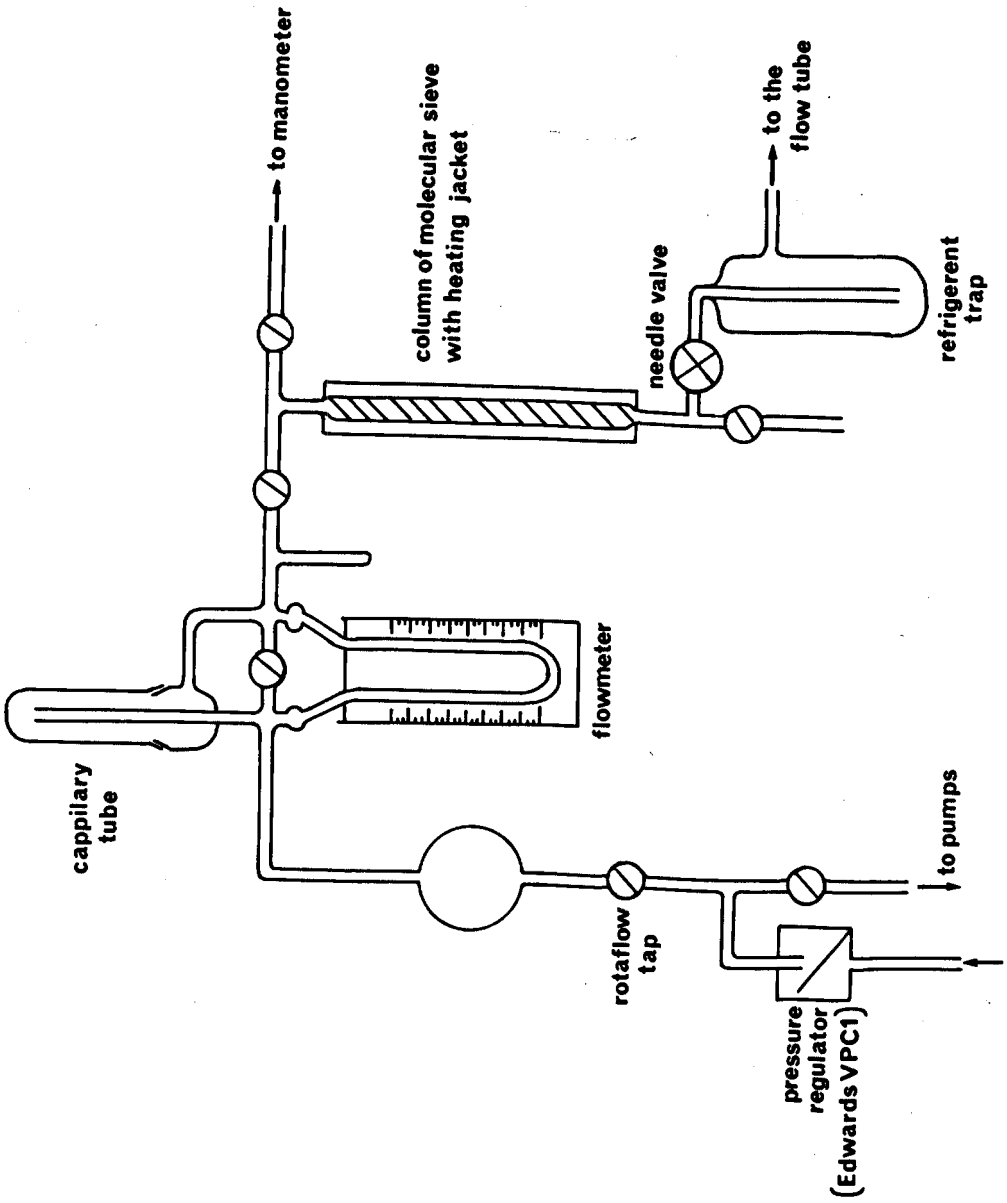

Figure 2.3 A flow system for purifying and regulating test gases

is controlled by stainless steel needle valves (Edwards). After leaving the pressure regulators, the gas passes through a calibrated capillary flowmeter. Then the gas is dried and purified by passing through a molecular sieve, type 4A, column (60 cm x 1.0 cm i.d.) and the appropriate refrigerant traps. The flow in the tube is maintained by a water cooled pump (Edwards ISC 3000). A PTFE regulating valve (Corning Quickfit) is used to isolate the main tube from the pump. This valve is used to adjust the pressure in the flow tube. The total flow into the tube is usually kept constant at 28 $ml s^{-1}$ at S.T.P. giving linear flow velocity in the range of 1.0 to 1.6 ms^{-1} depending upon the total pressure of the flow tube.

For the corrosive gases the system had to be modified since the pressure regulators were found to be unsuitable for the handling of corrosive gases. Figure 2.4 shows a schematic diagram of the system, constructed to replace the pressure regulators, which was situated in a fume cupboard. It consisted of a 4 dm^3 inert PTFE sampling bag protected from outside by another PVC bag. The corrosive test gas was delivered from the cylinder to the PTFE bag using PTFE tubing. An oil pump was used to evacuate the bag arrangement before introducing the test gas. The bag was usually kept half inflated to make sure of a steady flow into the main system. This arrangement was found satisfactory and no fluctuations were observed in the flow rate measured by the capillary flowmeters as before.

The molecular sieves are regularly regenerated and dried by electrically heating the columns to 473 K. At the same time gas is passed through the columns to sweep out the moisture.

Figure 2.4 A schematic diagram of the system used to regulate the pressure of corrosive gases

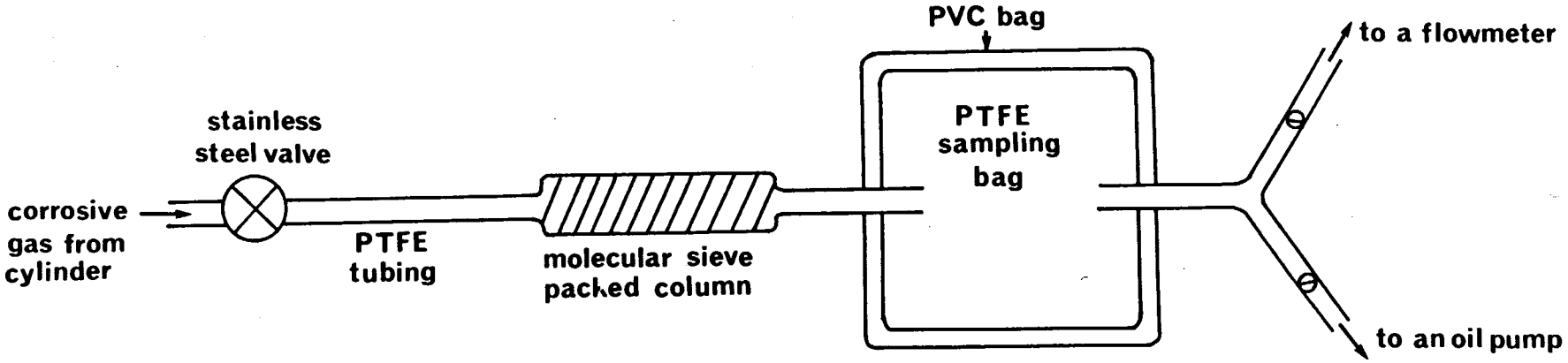

2.2.2 The Capillary Flowmeters and the Calibration

All gas flows are measured with calibrated capillary flowmeters fitted with diethyl phthalate and controlled with stainless steel needle valves.

All the capillary flowmeters are calibrated first with oxygen. To calibrate a flowmeter the system is set running with oxygen then the pressure rise for the closed system is measured for a given time at various flowmeter readings. The time is chosen such that the increase in pressure for the closed system did not effect the flow rate.

The timing (timed with a stop watch) was started when the main pump was cut off from the system and stopped when the oxygen flow was switched off. Then the closed system was allowed to come to equilibrium by fully opening the needle valve which controlled the flow of oxygen, and the final pressure reading was taken using a mercury manometer. The values measured were corrected for zero pressure which was obtained by simultaneously shutting off the oxygen flow and the valve to the main pump.

The volume of the evacuated closed system was measured by expanding a known volume of air at S.T.P. into the system and noting the pressure. The volume determined this way was 15.2 dm^3. Hence, from these measurements the rate of flow of oxygen at S.T.P. was determined for a given height of the flowmeter. A calibration graph was plotted for each flowmeter.

The capillary flowmeters calibrated this way are then related to the rate of flow of the test gas M using Poiseulle's Law[58]:

$$\phi_M = \phi_{O_2} \eta_{O_2} / \eta_M \qquad (2.1)$$

where ϕ_{O_2} and η_{O_2} are the flow rate and the viscosity of oxygen respectively and ϕ_M and η_M for the test gas M. Table 2.1 gives the viscosities of the various gases at 295 K obtained by plotting the literature values of viscosity against temperature.

2.3 The Shock Tube

The shock tube used in these experiments (see figure 2.1) has a 1.3 m stainless steel high pressure driver section separated from the low pressure test section, the 5 m long pyrex flow tube, by an aluminium diaphragm. The tube is of cylindrical cross section with internal diameter of 5 cm.

The shock is produced by rupturing the diaphragm using helium and nitrogen as the driver gases. When the diaphragm is burst, a compression wave, which rapidly develops into a shock wave, moves into the low pressure gas. The shock strength produced in the tube increases with the pressure ratio across the diaphragm and with the sound speed in the driver gas.

A wide range of shock speeds, 0.8 Kms^{-1} to 1.6 Kms^{-1}, were obtained by varying the thickness of the aluminium diaphragms, 0.002" to 0.004", and by adjustment of driver gas composition. Depending on these conditions a bursting pressure range of 2.6 - 6.4 atmospheres (2.7×10^2 to 6.4×10^2 KPa) was obtained corresponding to an overall temperature range of 600 - 1500 K. The pressure in the driver section of the shock tube was measured by a Budenberg dial gauge; a pointer recorded the bursting pressure.

The observation station, at which the photomultipliers are positioned, is 4.4 m from the diaphragm along the low pressure test section (see figure 2.1) and the test gases enter at the end of the

Table 2.1. Viscosities of Gases at 295 K

Gas, M	Viscosity, $\eta/Kgs^{-1}m^{-1}10^{-5}$
O_2	2.04
CO_2	1.51
NH_3	0.99
NO	1.88
HCl	1.43
SO_2	1.26

Table 2.2. Quantums Efficiency of E.M.I. 9658B Photomultiplier

Wavelength, λ/nm	Quantum Efficiency %
579	14.6
634	11.2
703	7.8
762	5.0

test section so that the direction of flow is in the opposite direction to the shock wave.

The high pressure driver section and the low pressure test section are left under vacuum when not in use.

2.4 Measurement Techniques and Associated Instruments

The emissions studied in this work were measured with two photomultipliers (E.M.I. 9658B) fitted with interference filters (Balzer). The absorption characteristics of each filter were measured with a Pye-Unicam spectrometer; the details of these are discussed in chapter 8.

The two photomultipliers are positioned opposite each other at the observation station 4.4 m from the diaphragm. One of the photomultipliers could also be moved along the tube as it rested on a slide running in parallel to the tube. The track is 2.5 m long and is marked out at 10 cm intervals. This photomultiplier is used for measuring the concentration gradient along the tube whereas the other is kept stationary at the observation station to act as a reference. The photomultipliers are situated in a housing which had filter holders (8 cm from the cathode) with variable slit sizes to control the emission intensities. Figures 2.5 and 2.6 show the arrangement and the alignment of the photomultipliers.

The same type of photomultipliers were used to monitor all the emissions. Each photomultiplier was operated at the voltage recommended by the supplier, using Brandenburg 472 E.H.T. supply. The relative quantum efficiency with wavelength was taken from the manufacturer's data given in table 2.2.

Figure 2.5 Photomultiplier and housing

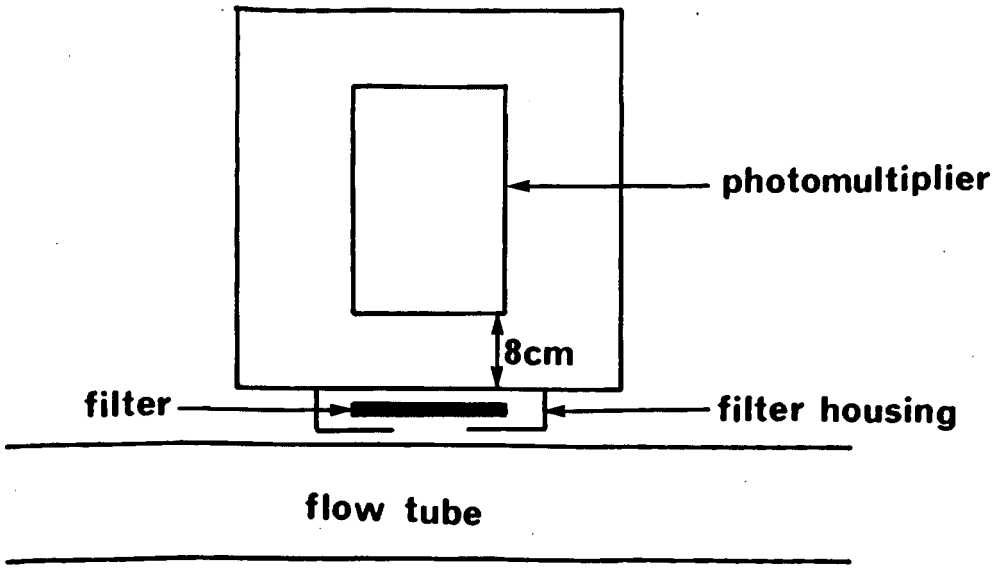

Figure 2.6 The alignment of the photomultipliers

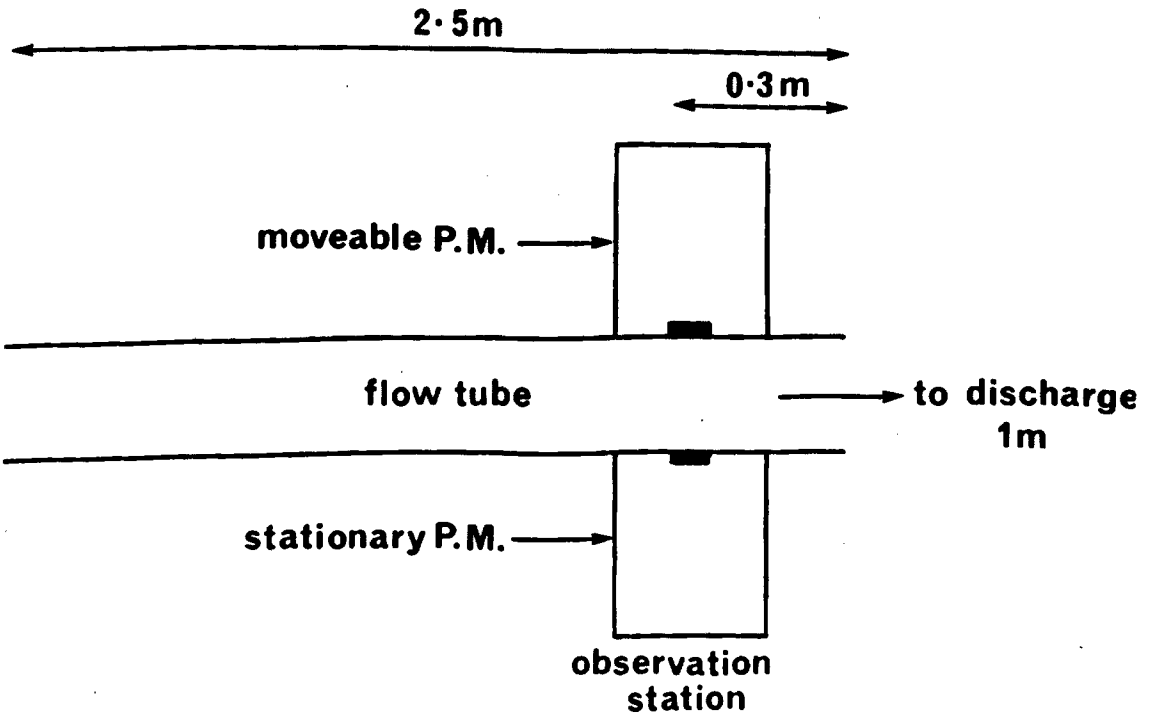

The output from each photomultiplier is fed via a voltage follower to either a digital voltmeter (Solartron 7040) to meassure the pre-shock value or to a transient recorder (Datalab 905) for the post-shock measurement. A block diagram of the recording circuits is shown in figure 2.7.

The transient recorders are triggered by the arrival of the shock front, they in turn trigger two oscilloscopes (Hewlett Packard series 140) allowing the shock trace to be displayed and then photographed. After each shock the digitalized data are transferred from the transient recorders to a graphics computer terminal (Hewlett Packard F2647) for storage on magnetic tape and subsequent computer analysis. The 2647 can also be run in conjunction with the University's main computer, G.E.C. 4082.

The shock speed is measured by means of laser light screens and is determined from the time taken for the shock front to travel a known distance along the tube.

Two He/Ne lasers (Ferranti GP2, 1 mW; Rofin 7906, 1.5 mW) are used. The beam from one of the lasers is split into two by a half silvered mirror. The three beams are passed via a system of mirrors through the tube across the laboratory onto three light screen detectors. The optical path is 5 m long and the beam hits the tube on an angle of about 87°. The system of mirrors, the lasers, and the photomultipliers are mounted independently from the shock tube frame so that any possible vibration should not interfere with their stability.

The change in density at the shock front deflects the laser beams causing a sharp rise in output from the photomultipliers. The pulse is used to trigger a trigger unit (Hewlett Packard) to start and stop the time interval meters (Vernner TSA 5536).

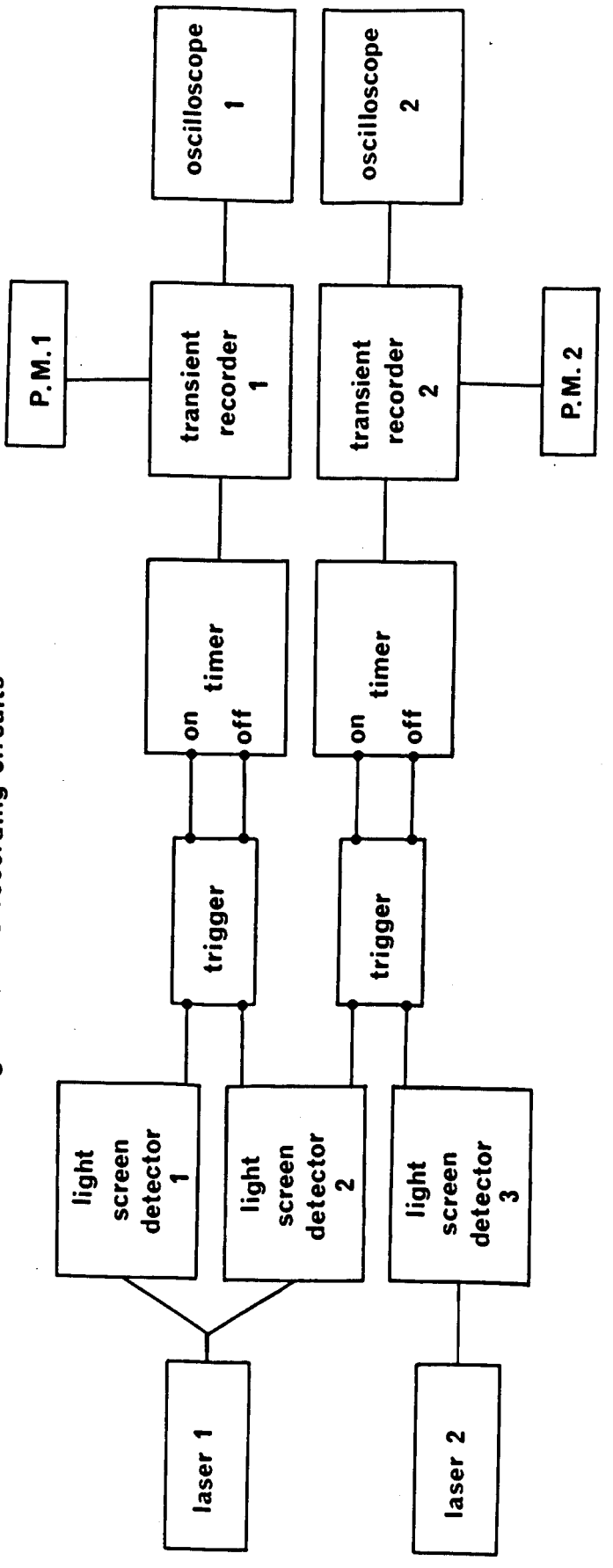

Figure 2.7 A block diagram of the recording circuits

Before each shock the adjustment of each light screen is checked by monitoring the output on an oscilloscope.

It has been shown[59] that both the reflected and the refracted beams from the back of the shock front reinforce one another.

In these experiments the fundamental measurements are; voltage, time, pressure and speed so the quality of the results obtained will depend on the accuracy of these measurements. Hence, periodically checks are carried out to make sure that the readings obtained are correct.

The output voltage from the crystal controlled transient recorders, oscilloscopes and the digital voltmeters was checked against the output of a signal generator (Marconi TF2010) to make sure that all three instruments gave identical readings for the same voltage input. The time scale for the oscilloscope and the transient recorder was similarly checked using the crystal oscillator in the timer.

The pressure along the flow tube was checked by means of two dial gauges one at each end. No pressure gradient was observed along the tube within the experimental pressure range of 2-12 torr.

The attenuation of the shock front was checked using an extra light screen, 1 m from the diaphragm, and it was found that the deceleration is less than 1% per metre.

The rise time of the detector was checked using a square wave generator coupled with a light emitting diode, L.E.D.. The rise times of less than 5 microseconds were found for anode load resistor of 51 Kohms. The rise time of the anode circuit depends on the resistor load such as; high resistor load gives large voltage output but long rise time whereas, a low load gives shorter rise time but poorer voltage output. For shock experiments the rise time was determined by the slit width.

2.5 Hazards

Hazards which may be encountered in operating the system are;

(a) Microwave leakage, this was reduced with surrounding the discharge by a Faraday cage.

(b) The high pressure section was operated up to 6.5×10^2 KPa pressure to prevent any structural damage. The glassware used on the low pressure side was wrapped with sellotape to reduce the risk of flying glass in case of an accident. Manometers were provided with an overflow volume to prevent any spillage if the system is accidently overpressurised. The gas cylinders were checked for any leak especially the driver section to prevent the tube from firing itself.

(c) Hydrogen was not used as a driver gas since there is some danger of explosion when driving into oxygen, especially in the presence of an electrical discharge. Corrosive gases were trapped by appropriate refrigerants before reaching the pumps and disposed of later by means of a water-pump.

(d) High voltage, low impedence sources such as photo-multiplier supplies were earthed for safety and also to reduce mains pick up and stray interference.

(e) Staring into the laser beam or viewing it directly with optical instruments was avoided.

2.6 Standard Experimental Procedure

The following procedure is carried out for a typical experiment; any modifications to this routine are described in the appropriate chapter.

An aluminium diaphragm of the desired thickness is positioned between the driver and the test section and both sections evacuated

thoroughly. Oxygen flow is switched on and adjusted to the required flow rate. A dewar of liquid nitrogen is placed around the trap on the oxygen line. The downstream pressure is set to about 6 torr which is measured using the diethyl phthalate manometer. The discharge is started with a tesla coil, the power is adjusted to 100 W and the cooling air is switched on. Then the overhead lights are switched off before turning on the E.H.T. photomultiplier power supply. The system is left to stabilize for at least half an hour.

The fall in emission of $O_2(a^1\Delta_g)$ or $O_2(b^1\Sigma_g^+)$ is measured, using the digital voltmeters, along the tube by means of the travelling photomultiplier. Then the quenching gas is switched on, entering the flow tube just after the discharge. The flow rate of the quenching gas is adjusted to the required value relative to the flow rate of the oxygen. Again the system is left to equilibrate and the emission fall is measured along the tube.

For the shock measurements the two photomultipliers are placed opposite one another at the observation station and the emissions measured simultaneously. These recorded values are known as pre-shock glows. The lasers are switched on and the light screen detectors are adjusted for optimum sensitivity. Now the photomultiplier outputs are disconnected from the digital voltmeters and are plugged into the transient recorders where the sweep speed, voltage sensitivity, and the delay time are set for the expected shock speed. The transient recorders, time interval meters and the trigger units are armed. Finally the flow rates and the total pressure are checked and the tap to the manometer is closed.

The vacuum pump connected to the driver section is isolated and the driver gas or gases are let in at a steady, fairly slow rate.

When sufficient pressure has been built up the diaphragm bursts and the shock is then propagated into the flowing gas. The driver gas inlet is immediately closed after the shock is fired. After the shock the discharge is switched onto the standby position and the photomultiplier voltage zero corrections are checked.

Before the overhead lights are turned back on the gases, high voltage suppliers and the lasers are switched off. The times are recorded for the determination of the shock speed and the emission traces are photographed. The recorded shock trace data is then transferred from the transient recorders to the graphics computer terminal for storage on a magnetic tape and later analysis.

The diaphragm is replaced by opening the high and low pressure sections to the atmosphere via the driver section and for the next experiment the entire procedure is repeated from the beginning.

Both sections of the shock tube are regularly cleaned using cotton wool soaked in ether, followed by thorough pumping.

CHAPTER THREE

3. Shock wave theory and production of High-Temperatures

In this chapter the nature of shock waves and the associated phenomena in gases are briefly discussed. The basic equations for a shock wave in an ideal gas; having heat capacity independent of temperature, are derived by consideration of physical laws governing the flow. The equations obtained are modified for a real gas and the shock front conditions are determined from the knowledge of the shock velocity and the initial state of the gas.

3.1 Formation of a Shock Wave

A shock wave is a moving pressure disturbance in which the pressure amplitude is very much larger than that in a sound wave, and whose velocity is much greater than that of a sound wave.

The formation of the shock wave is best explained by considering the expanding driver gas as a piston accelerating from rest to a constant velocity, u, by small increments, du, in a short but finite time, where u is greater than that of the sound speed, a, in the cool gas.

For the first increment du, a weak compression wave is propagated moving into the low pressure region with velocity a. With the piston acquiring the second velocity increment another wave is developed which is travelling with a faster velocity a + da; since it is going through a slightly heated gas. After many such successive events the piston gains its final velocity u and the compression waves coalesce to form a shock wave moving with velocity, v_s, ahead of the interface between the driver and low pressure gas. Between the shock front

and the driving piston is a column of gas of continually increasing length, flowing with the velocity u of the piston.

The collision processes cause the change in the gas flow velocity across the shock front. The change of this directed kinetic energy into random kinetic or thermal energy is accompanied by an increase in entropy, $\Delta S>0$ and the irreversible process raises the state of the shocked gas above that in an ordinary isentropic compression, $\Delta S=0$. However a knowledge of these irreversible collision processes is not necessary for the determination of the conditions of the shocked gas since for a gas the entropy is only a function of its thermodynamic state.

3.2 The Wave Pattern in a Shock Tube

A schematic pressure driven shock tube and the accompanying wave diagram is shown in figure 3.1. This time-distance plot shows the flow pattern which occurs after the rupture of the diaphragm. The incident shock wave moves at constant velocity into the low pressure gas until it is reflected from the end plate, while a rarefaction wave spreads out into the high pressure section at the sound speed of that gas. The rarefaction head is also reflected from the end plate of the driver section, accelerating as it passes through the fan, but now travelling into a gas which is going down the tube with a final velocity greater than that of the incident shock wave.

Also propagated simultaneously from the diaphragm is the contact surface, the leading edge of the expanding driver gas, moving with a velocity slower than that of the incident shock wave. The gas particles behind the shock front travel with velocity of the

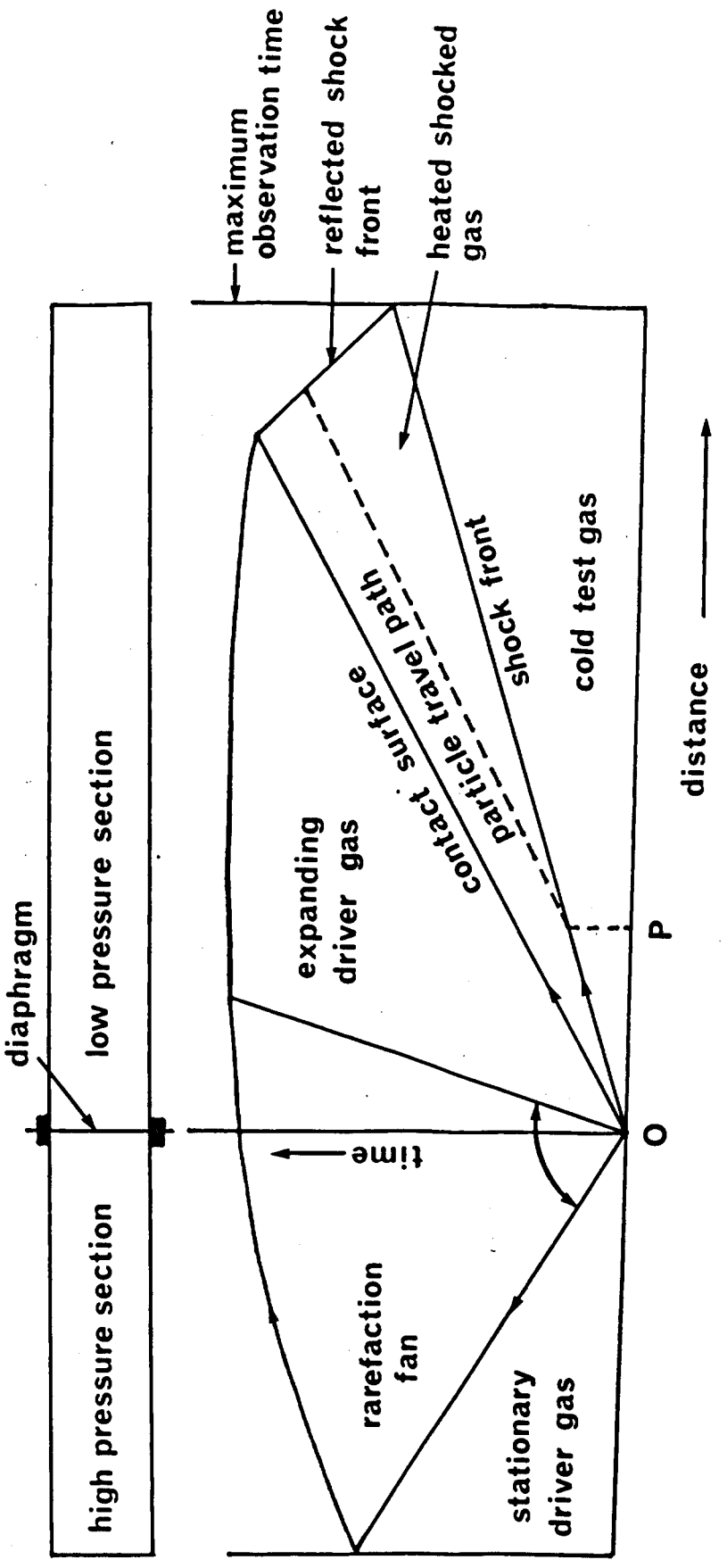

Figure 3.1 Distance vs. time diagram for a pressure driven shock tube

contact surface, their travel paths can be shown by lines parallel to that of the contact surface.

The observation of the heated test gas is done during the hot flow time, the time between the arrival of the shock front and the contact surface, which depends upon the lengths of the two sections and the properties of the gases used.

The duration and shape of the shock wave produced in a shock tube is determined by wall effects and by the length of the high pressure section. The latter parameter enters into the problem because the reflection of the rarefaction from the end of the tube produces a stronger rarefaction which eventually overtakes and attenuates the shock itself. The effect of the wall[60] on shock velocity becomes reasonably small if the diameter of the tube is greater than about 5 cm.

3.3 Derivation of Shock Front Conditions

The basic equations of steady gas dynamics are derived on the assumption that the flow is steady. Hence, the amount of matter, momentum and energy flowing per unit time into the control volume (see figure 3.2) at, A, must be equal to the amount leaving the control volume at, B. The control volume also includes a shock wave shown by the dashed line.

For the purpose of having a shock wave normal to the flow the control planes A and B are set arbitrarily close to either side of the shock wave. Assuming that the material immediately behind the shock front is in a state of thermodynamic equilibrium, the transition is described by the equations of conservation of matter, momentrum and energy.

Figure 3.2 Control volume for derivation of steady-flow equations

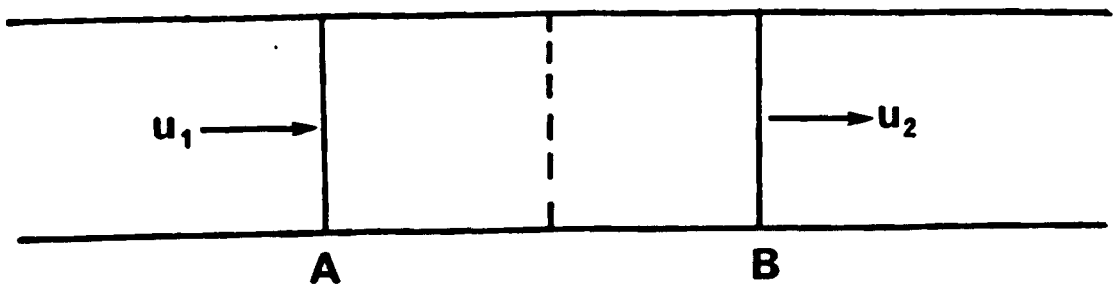

Figure 3.3 Flow through a uniform shock wave

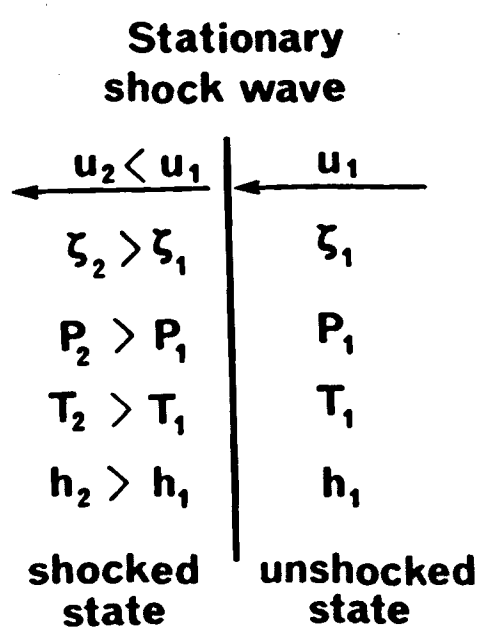

The amount of matter transported across unit area per unit time is the product of flow velocity u and density ρ, and for conservation of mass;

$$\rho_1 u_1 = \rho_2 u_2. \qquad [\text{Kg m}^{-2}\text{ sec}^{-1}] \qquad (3.1)$$

The momentum transported across each plane per unit time is the sum of the pressure P and the flow momentum ρu^2. Balancing the forces:

$$\rho_1 u_1^2 + P_1 = \rho_2 u_2^2 + P_2 \quad [\text{Pa} = \text{Nm}^{-2} = \text{Jm}^{-3}]. \qquad (3.2)$$

The energy is transported as flow, $\rho u^2/2$ and as thermal energy, h. Hence, for unit mass across a control plane the conservation of energy requires;

$$h_1 + \rho u_1^2/2 = h_2 + \rho u_2^2/2 \quad [\text{JKg}^{-1}] \qquad (3.3)$$

where h is the specific enthalpy. Subscripts 1 refer to the unshocked state and subscripts 2 refer to the shocked state. The coordinate system in which the velocities are given is assumed to be moving with the shock front as shown in figure 3.3.

To solve for the four variables additional information is obtained from the ideal gas equation and the specific enthalpy as a function of temperature. For an ideal gas;

$$P = \rho R_s T \qquad (3.4)$$

where T is the temperature and R_s is the specific gas constant given by

$$R_s = 10^3 R/\bar{M} \qquad [\text{JKg}^{-1}\text{ K}^{-1}] \qquad (3.5)$$

where $\bar{M}$ is the average molecular mass in Kg mol^{-1} units. Therefore, the ideal gas equation can be rewritten as:

$$P = 10^3 \rho RT/\bar{M}. \qquad [Pa] \qquad (3.6)$$

Also for an ideal gas the molar enthalpy, H, is given by:

$$H = C_p(T) \qquad [J] \qquad (3.7)$$

where specific heat, C_p, is constant at short times or low temperatures. The molar enthalpy is related to the specific enthalpy, h, by:

$$h(T) = 10^3 H(T)/\bar{M}. \qquad [JKg^{-1}] \qquad (3.8)$$

The values of H as a function of temperature are known from thermodynamic tables.

If pressure, density and temperature for the unshocked state are known, the specification of the shock strength is sufficient with the above equations, to determine the equilibrium state behind the shock front.

By eliminating all variables but pressure and density from above equations, the relationship for an ideal gas is:

$$P_2/P_1 = (\rho_2 - \mu^2\rho_1)/(\rho_1 - \mu^2\rho_2) \qquad (3.9)$$

where

$$\mu^2 = (\gamma - 1)/(\gamma + 1) \qquad (3.10)$$

and γ is the ratio of specific heats C_p/C_v. For an ideal gas the specific heats at constant pressure and constant volume are independent of temperature. Similarly the expression for the equilibrium temperature behind the shock front for an ideal gas is:

$$T_2/T_1 = (P_2/P_1)[(P_1 + \mu^2 P_2)/(P_2 + \mu^2 P_1)]. \qquad (3.11)$$

The common practice is to express these expressions in terms of Mach Number, M_s

$$M_s = v_s/a \qquad (3.12)$$

where v_s is the shock velocity and a is the speed of sound in the test gas, given by:

$$a = (\gamma R_s T)^{\frac{1}{2}}. \qquad (3.13)$$

Substituting for M_s in the expressions for the ratios:

$$P_{21} = P_2/P_1 = \{[2\gamma M_s^2 - (\gamma - 1)]/(\gamma + 1)\} \qquad (3.14)$$

$$T_{21} = T_2/T_1 = \{2\gamma M_s^2 - [(\gamma - 1)/(\gamma + 1)]\} \{[(\gamma - 1)M_s^2 + 2]/[(\gamma + 1)M_s^2]\} \qquad (3.15)$$

A similar expression can also be written for the density ratio:

$$\rho_{21} = \rho_2/\rho_1 = [(\gamma + 1)M_s^2]/[(\gamma - 1)M_s^2 + 2]. \qquad (3.16)$$

Therefore for an ideal gas by evaluating, a, from equation (3.13) for the usual laboratory ambient temperature and the measurement of the shock velocity values of P_{21}, T_{21} and ρ_{21} can be obtained from expressions (3.14), (3.15) and (3.16). So having measured the initial conditions P_2, T_2, and ρ_2 the conditions behind the shock front can be determined.

3.4 Modification of Shock Parameters for Gases with Active Vibrations

The shock parameters determined from equations derived in the previous section are only true for gases having constant specific heats such as; monatomic gases, frozen gases and for weak shocks in some diatomic and polyatomic gases.

In the 'frozen' shocked gas it is assumed that the translational and rotational degrees of freedom are relaxed together with the weaker vibrations in a polyatomic molecule. In this case:

$$h_2 - h_1 = C_p(T_2 - T_1) \tag{3.17}$$

where C_p only contains contributions from the active degrees of freedom and is constant with temperature hence the procedure becomes the same as before.

If the temperature rise in the shock encompasses a region in which vibrations become active such that the attainment of equilibrium within the vibrational levels is much slower than that of the translational and rotational degrees of freedom, relaxed gas, then enthalpy contains contributions from the vibration and is no longer a simple function of the temperature:

$$h = f(T). \tag{3.18}$$

In this case the shock equations can not be solved explicitly and an iterative procedure is used to determine the shocked gas conditions. The method requires the knowledge of the temperature dependence of the enthalpy for the individual gases. This is achieved by polynomial curve fitting to the H(T) values obtained from J.A.N.A.F. tables;

$$H = a + bT + cT^2 + dT^3 \tag{3.19}$$

The shock parameters are initially obtained for the frozen state using equations (3.14), (3.15) and (3.16) then these values in conjunction with the coefficients obtained from equation (3.19) are used as the starting values for the iteration process. The difference obtained in the enthalpy is then used to make new estimated values for temperature, pressure and density behind the shock front. This completes the first iteration and a new one starts to calculate the enthalpy difference for the new estimated temperature. The process stops when consistent values are obtained for the conditions behind the shock front.

Non uniform flow, caused by the formation of boundary layer behind the shock front, can also give rise to changes in the density and temperature. Pedley[59] studied the buildup of a boundary layer in our system, and suggested that the effect is reasonably small and can be ignored. In this study, no corrections were made for either the boundary layer or the shock attenuation effects in the temperature and density behind the shock front since their presence in the present apparatus was shown[59] to be negligible.

The shock parameters for both the frozen and the relaxed states are determined by computer for our system. The program is adopted from Millikan[62].

For everyday use of finding shock parameters for each experiment a table of T_2, ρ_{21} and P_{21} was compiled for the expected range of M_s.

The values of the computed shock parameters used in the determination of the shocked gas behaviour gave results which agreed with the predicted models (Chapter 4) hence confirming their validity.

3.5 Laboratory and Gas Particle Times

Figure 3.4a shows the coordinates known as Laboratory coordinates for a fixed observation station. In the laboratory coordinates the shock wave is moving with velocity v_s into stationary test gas and the gas particles are following the shock front with velocity v_p. Therefore, the gas being observed at the observation station has actually been at the shock condition for a longer period than which the observer sees. This effect is known as the compression of the observation time and is illustrated in figure 3.4c.

The particle time, t_p, is the time taken for the gas particles to reach the observer, during which the gas has travelled the distance $v_p t_p$ and the shock wave $v_s t_p$. The laboratory time, t_L, is the time since the shock has passed the observer travelling the distance $v_s t_L$. Thus;

$$v_s t_p = v_p t_p + v_s t_L \tag{3.20}$$

$$t_p/t_L = v_s/(v_s - v_p). \tag{3.21}$$

Now for the shock fixed coordinates (see figure 3.4b) the flow velocities are;

$$u_1 = v_s \tag{3.22}$$

$$u_2 = (v_s - v_p). \tag{3.23}$$

For conservation of mass across the shock front,

$$u_1/u_2 = \rho_2/\rho_1 \tag{3.1}$$

hence it follows;

$$t_p/t_L = \rho_{21} \tag{3.24}$$

Figure 3.4 Coordinate systems

(a) Laboratory coordinate

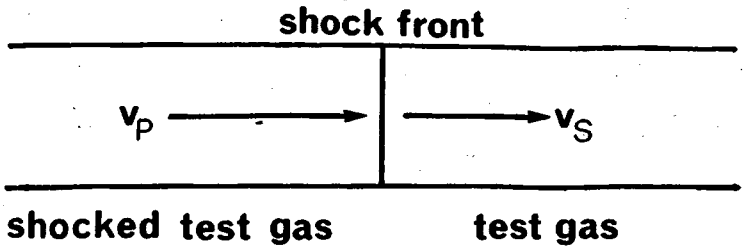

(b) Shock fixed coordinate

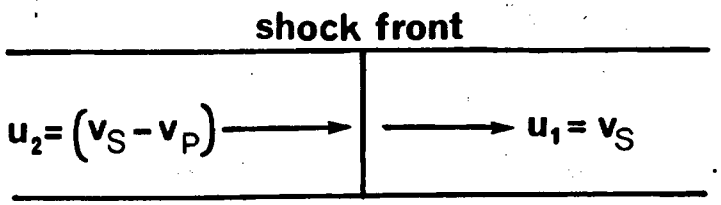

(c) The compression of the observation time

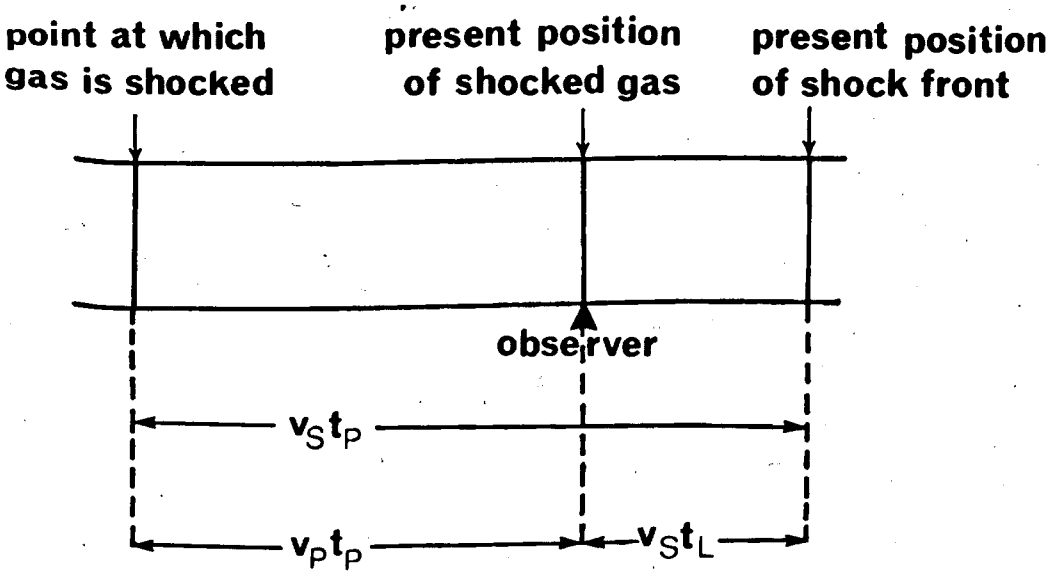

and

$$v_p = v_s(1 - 1/\rho_{21}). \tag{3.25}$$

Therefore, when rate processes are measured, the time measured in the laboratory should be multiplied by the density ratio across the shock front to obtain the true rate referred to the gas molecules.

CHAPTER FOUR

4. The Kinetic Analysis of Reaction Profiles

In this chapter the kinetic equations are developed which describe the collisional quenching of the two excited singlet states of molecular oxygen; $O_2(a^1\Delta_g)$ and $O_2(b^1\Sigma_g^+)$ in both the room temperature and in the high temperature studies of 634 nm and 762 nm emissions. Also outlined is the computer program, based on these equations, which is used for the analysis of the shock regimes. The chapter concludes with a discussion on the reliability of kinetic data obtained.

4.1 Room Temperature Kinetics

Kinetic equations are derived for the determination of the rate constants for collisional quenching of $O_2(a^1\Delta_g)$ and $O_2(b^1\Sigma_g^+)$ by an additive, M, at room temperature by monitoring the emissions of singlet molecular oxygen at 634 nm and 762 nm in a flowing discharge.

4.1.1 The Collisional Quenching of $O_2(a^1\Delta_g)$

$O_2(a^1\Delta_g)$ is generated 1.60 m upstream of the observation station in the discharge and removed by collisional quenching and wall deactivation:

$$O_2(a^1\Delta_g) + M \xrightarrow{k_d^M} O_2(\chi^3\Sigma_g^-) + M \qquad (4.1)$$

$$O_2(a^1\Delta_g) + \text{Wall} \xrightarrow{k_W} O_2(\chi^3\Sigma_g^-). \qquad (4.2)$$

$O_2(a^1\Delta_g)$ is also removed by emission of radiation by the dimol emission. (4.3), by the single molecule transition (4.4) and by the energy pooling reaction (4.5);

$$2O_2(a^1\Delta_g) \longrightarrow 2O_2(\chi^3\Sigma_g^-) + h\nu \ (\lambda = 634 \text{ nm}) \qquad (4.3)$$

$$O_2(a^1\Delta_g) \longrightarrow O_2(\chi^3\Sigma_g^-) + h\nu \ (\lambda = 1270 \text{ nm}) \qquad (4.4)$$

$$2O_2(a^1\Delta_g) \xrightarrow{k_p} O_2(b^1\Sigma_g^+) + O_2(\chi^3\Sigma_g^-). \qquad (4.5)$$

Reactions (4.3) and (4.4), the forbidden radiative processes, are very slow[5] in comparison with reactions (4.1) and (4.2). The loss due to the energy pooling reaction (4.5) is insignificant under our conditions where the concentration of $O_2(a^1\Delta_g)$ is low[63]. Therefore, the rate of change of $O_2(a^1\Delta_g)$ concentration is determined by reactions (4.1) and (4.2) and can be written as:

$$\begin{aligned} d[O_2(a^1\Delta_g)]/dt &= -k_d^M[O_2(a^1\Delta_g)][M] - k_W[O_2(a^1\Delta_g)] \\ &= -k_d'[O_2(a^1\Delta_g)] \end{aligned} \qquad (4.6)$$

where k_d' is the overall pseudo first order rate constant for the deactivation of $O_2(a^1\Delta_g)$.

It has been shown by Whitlow and Findley[64] that the intensity of the dimol emission varies with the square of the concentration of $O_2(a^1\Delta_g)$:

$$^{634}I \propto [O_2(a^1\Delta_g]^2.$$

Experiments, in which the emissions from $O_2(a^1\Delta_g)$ at 634 nm and 1270 nm are compared over a range of pressures, have verified the squared relationship in our system[15].

In the flow tube there is a decay of excited state molecules along the tube. By monitoring ^{634}I along the tube the first order decay constant, α_L, for the dimol emission is obtained:

$$\ln {}^{634}I/{}^{634}I_o = 2 \ln[O_2(a^1\Delta_g)]/[O_2(a^1\Delta_g)]_o = -\alpha_L L \qquad (4.7)$$

where $^{634}I_o$ is the emission intensity at the reference station and ^{634}I is that at a point along the tube, distance L, from the reference station.

Therefore, from equation (4.7):

$$[O_2(a^1\Delta_g)] = [O_2(a^1\Delta_g)]_o \exp(-\alpha_L L/2) \qquad (4.8)$$

$$d[O_2(a^1\Delta_g)]/dl = (-\alpha_L/2)\{[O_2(a^1\Delta_g)]_o \exp(-\alpha_L L/2)\} \qquad (4.9)$$

$$d[O_2(a^1\Delta_g)]/dl = (-\alpha_L/2)/[O_2(a^1\Delta_g)]. \qquad (4.10)$$

The decay rate in equation (4.6) is related to that with distance by:

$$d[O_2(a^1\Delta_g)]/dt = d[O_2(a^1\Delta_g)]/dl \times dl/dt \qquad (4.11)$$

where dl/dt is the linear flow velocity, v. Hence, substituting in equation (4.11):

$$d[O_2(a^1\Delta_g)]/dt = (-\alpha_L/2)[O_2(a^1\Delta_g)]v \qquad (4.12)$$

and from equations (4.12) and (4.6) it follows that

$$k'_d = \alpha_L v/2. \qquad (4.13)$$

The deactivation of $O_2(a^1\Delta_g)$ is measured along the tube by observing the change in the intensity of the dimol emission as a function of length. In practice it is easier to follow the comparatively intense emission (see page 67) from $O_2(b^1\Sigma_g^+)$ which also has been shown[59] to vary with the square of $O_2(a^1\Delta_g)$ concentration

From equation (4.8) is follows:

$$\ln [O_2(a^1\Delta_g)]/[O_2(a^1\Delta_g)]_o = (-\alpha_L/2)L \qquad (4.14)$$

defining equation (4.14) in terms of emission intensity:

$$\ln {}^{634}I/{}^{634}I_o = (-\alpha_L/2)L \qquad (4.15)$$

or

$$\ln {}^{762}I/{}^{762}I_o = (-\alpha_L/2)L. \qquad (4.16)$$

The slope of the ln plot of intensity against distance should give the value of α_L. k'_d is then found by multiplying the decay constant by the linear flow velocity of the gas along the tube.

From equations (4.6) and (4.13), k'_d for oxygen alone:

$$k'_d = \alpha_L v/2 = k_d^{O_2}[O_2] + k_W^o \qquad (4.17)$$

and for oxygen plus an additive M:

$$k'_d = \alpha_L v/2 = k_d^{O_2}[O_2] + k_d^M[M] + k_W \qquad (4.18)$$

therefore, for constant O_2 concentration:

$$\Delta k'_d = k_d^M[M] + (k_W^o - k_W) \qquad (4.19)$$

where k_W^o and k_W are the wall deactivation rate constants in the absence and presence of M.

Hence, from equation (4.19) the second order rate constant, k_d^M, for quenching of $O_2(a^1\Delta_g)$ by M can be determined for a set of values of $\Delta k'_d$ at a known [M].

Figure 4.1a shows the variation of emission intensity as a function of distance along the tube for oxygen and oxygen plus quencher M, for M = HCl. The difference in the slopes provides the value of $\Delta k'_d$ in combination with the linear flow velocity.

Figure 4.1b shows a plot of $\Delta k'_d$ against [HCl] which is a straight line plot passing through the origin, indicating that the intercept is zero and that the deactivation at wall should be almost

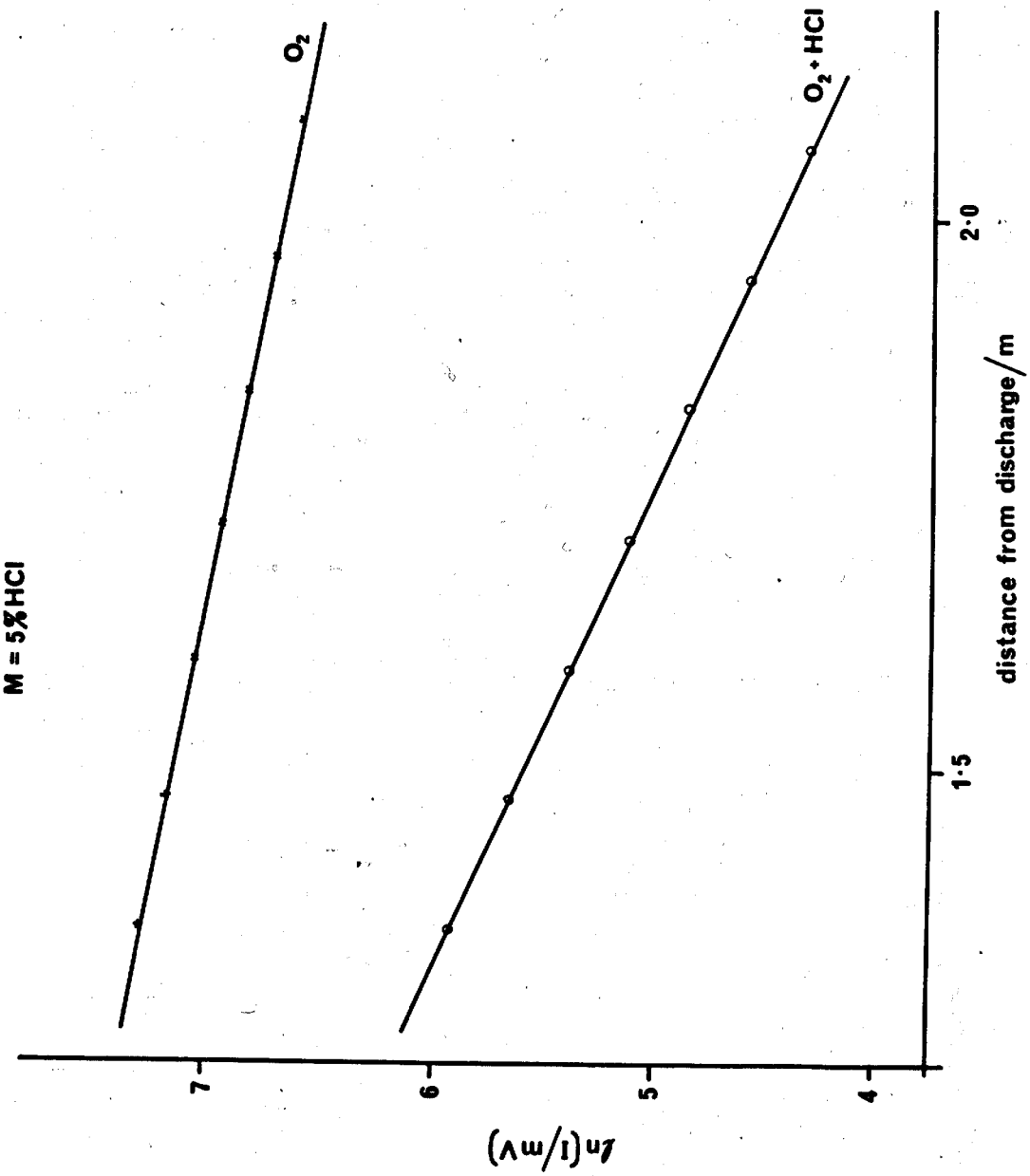

Figure 4.1a The variation of emission intensity as a function of distance along the tube

M = 5% HCl

Figure 4.1b A plot of first order rate constant, $\Delta k'_d$ vs. $[M]$. The slope gives the second order rate constant, k_d^M, for the quenching of $O_2(a^1\Delta_g)$ by M, M = HCl

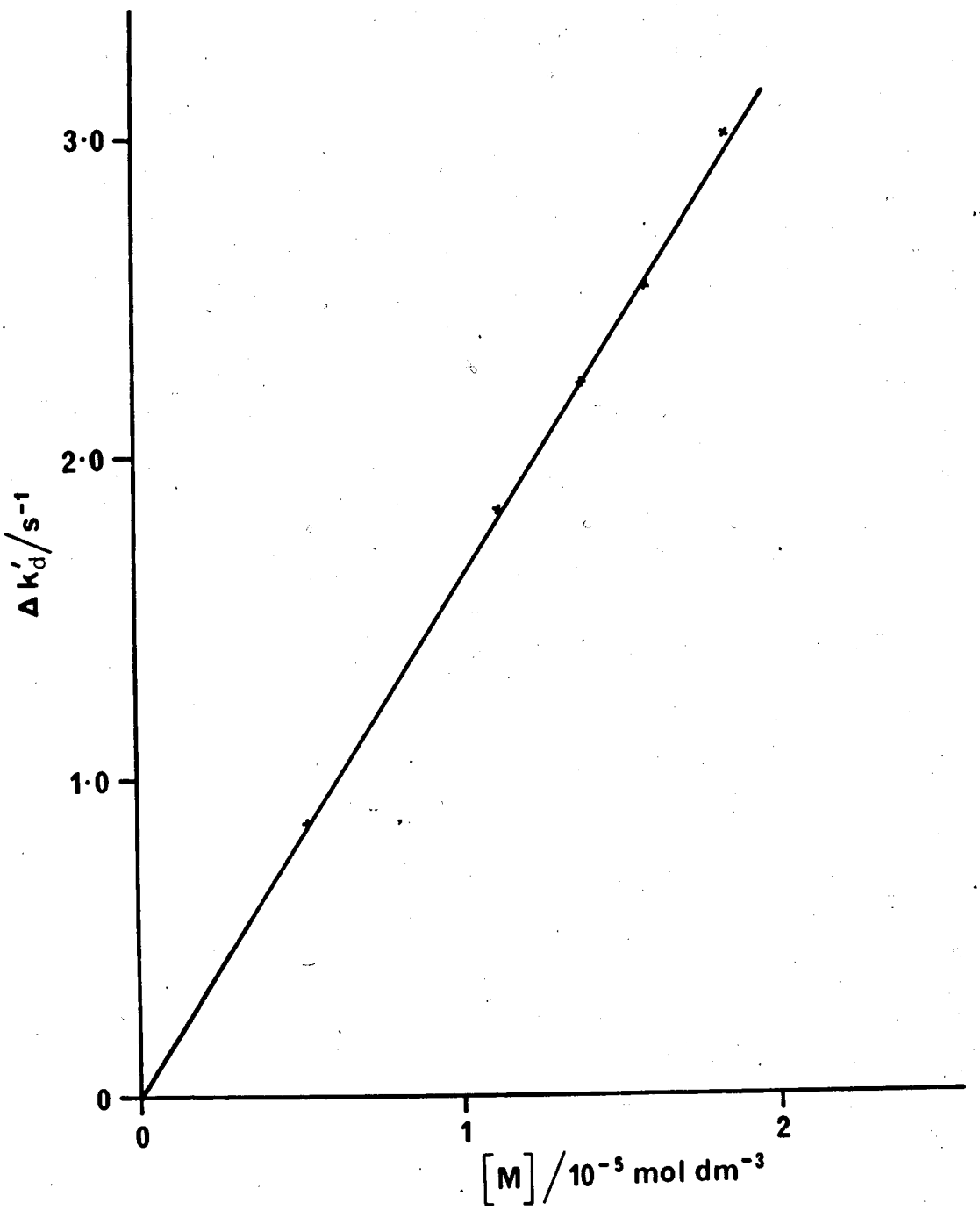

the same in the presence and absence of the quencher. Therefore, the gradient gives the value of k_d^{HCl} directly.

The values of $k_d^{O_2}$ and k_W have been measured previously[63] and during the present study these were frequently checked and found that the agreement was good. This is discussed further in chapter 5.

4.1.2 The Collisional Quenching of $O_2(b^1\Sigma_g^+)$

$O_2(b^1\Sigma_g^+)$ is produced from the energy pooling reaction (4.5) and is deactivated by collisional and wall quenching:

$$2O_2(a^1\Delta_g) \xrightarrow{k_p} O_2(b^1\Sigma_g^+) + O_2(\chi^3\Sigma_g^-) \qquad (4.5)$$

$$O_2(b^1\Sigma_g^+) + M \xrightarrow{k_q^M} O_2(a^1\Delta_g) + M \qquad (4.20)$$

$$O_2(b^1\Sigma_g^+) + \text{Wall} \xrightarrow{k_W} O_2(a^1\Delta_g \text{ or } \chi^3\Sigma_g^-) \quad . \qquad (4.21)$$

and also by radiative process:

$$O_2(b^1\Sigma_g^+) \longrightarrow O_2(\chi^3\Sigma_g^-) + h\nu \ (\lambda = 762 \text{ nm}). \qquad (4.22)$$

In the presence of an additive, M, the concentration of $O_2(b^1\Sigma_g^+)$ at any point along the tube is determined by the steady state between reactions (4.5), (4.20) and (4.21). Compared with these reactions the radiative emission is very slow[5] and can be ignored. Hence, the rate of change of $O_2(b^1\Sigma_g^+)$ concentration is given by:

$$d[O_2(b^1\Sigma_g^+)]/dt = k_p[O_2(a^1\Delta_g)]^2 - k_q^M[O_2(b^1\Sigma_g^+)][M] - k_W[O_2(b^1\Sigma_g^+)] \quad . \qquad (4.23)$$

For a steady flow the concentration of $O_2(b^1\Sigma_g^+)$ is constant so $d[O_2(b^1\Sigma_g^+)]/dt = 0$. Hence, rearranging equation (4.23):

$$[O_2(b^1\Sigma_g^+)] = \{k_p[O_2(a^1\Delta_g)]^2/(k_q^M[M] + k_W)\}. \qquad (4.24)$$

For oxygen alone equation (4.24) can be rewritten as:

$$[O_2(a^1\Delta_g)]^2/[O_2(b^1\Sigma_g^+)] = (k_q^{O_2}[O_2] + k_W^o)/k_p \qquad (4.25)$$

and for oxygen plus an additive M:

$$[O_2(a^1\Delta_g)]^2/[O_2(b^1\Sigma_g^+)] = (k_q^{O_2}[O_2] + k_q^M[M] + k_W)/k_p \qquad (4.26)$$

since;

$$^{762}I \propto [O_2(b^1\Sigma_g^+)]$$

and

$$^{634}I \propto [O_2(a^1\Delta_g)]^2$$

equations (4.25) and (4.26) can be rewritten in terms of the respective emission intensities, I, as:

$$\phi_o = {}^{634}I_o/{}^{762}I_o = a'(k_q^{O_2}[O_2] + k_W^o)/k_p \qquad (4.27)$$

$$\phi_M = {}^{634}I_M/{}^{762}I_M = a'(k_q^{O_2}[O_2] + k_q^M[M] + k_W)/k_p \qquad (4.28)$$

where a' is a constant.

Combination of (4.27) and (4.28) gives the linear expression:

$$f(\phi_M,\phi_o) = \{(k_q^{O_2}[O_2] + k_W^o)(\phi_M - \phi_o)/\phi_o\} - (k_W - k_W^o) \qquad (4.29)$$
$$= k_q^M[M].$$

In expression (4.29), k_W and k_W^o are the wall constants in the presence and absence of M and are determined from equation (4.30)

given by Derwent and Thrush[65] :

$$k_W = 1/\{[r^2(P_1/P_0)]/(8D_0) + (2r/\gamma\bar{C})\} \qquad (4.30)$$

where r is the radius of the flow tube; D_o is the diffusion coefficient of $O_2(b^1\Sigma_g^+)$ at atmospheric pressure, P_o; γ is the wall efficiency; P_1 is the downstream pressure; and $\bar{C}$ is the mean velocity of $O_2(b^1\Sigma_g^+)$. The values of $k_q^{O_2}$ is also known[9].

Therefore, the quenching rate constant, k_q^M, can be determined from expression (4.29) for a set of measured values of ϕ_o and ϕ_M at a known [M], see figure 4.2; an example of a plot for HCl. The plot is linear passing through the origin so the slope gives the rate constant for quenching directly.

The emission of $O_2(b^1\Sigma_g^+)$ may be used to follow the concentration of $O_2(a^1\Delta_g)$ since from equation (4.24):

$$[O_2(b^1\Sigma_g^+)] \propto [O_2(a^1\Delta_g)]^2$$

hence, for a constant oxygen pressure;

$$^{762}I \propto [O_2(b^1\Sigma_g^+)] \propto [O_2(a^1\Delta_g)]^2.$$

Figure 4.3 shows a first order plot of the decay of $O_2(a^1\Delta_g)$ along the tube by observing both the $O_2(b^1\Sigma_g^+)$ and the dimol emission. This illustrates that both have identical gradients.

4.2 High Temperature Kinetics

The kinetic equations are derived along the same lines as at room temperature but the rate constants now refer to reactions taking place at the shock temperature in particle time.

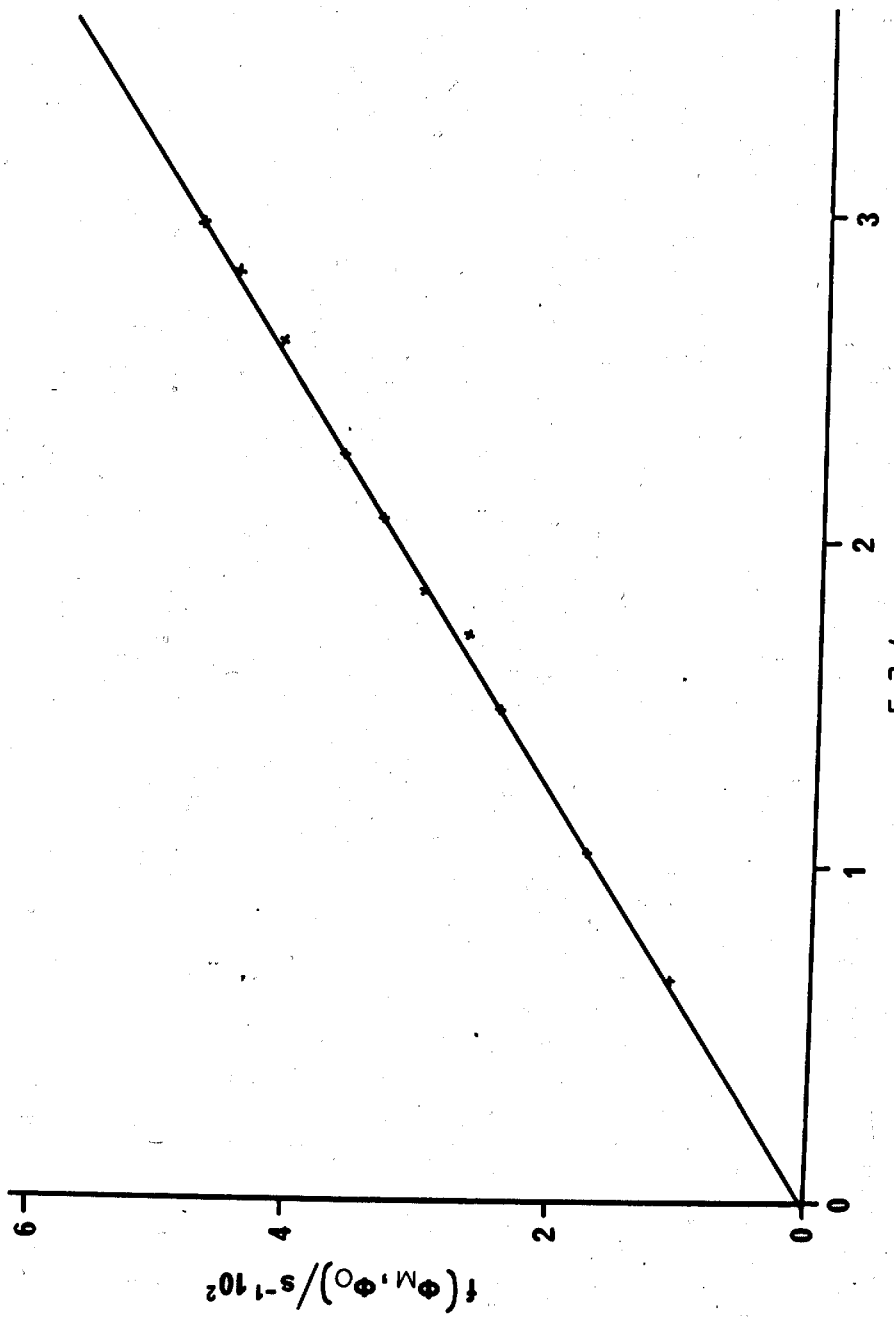

Figure 4.2 Plot of $f(\Phi_M, \Phi_O)$ vs. $[M]$. The slope gives the rate constant, k_q^M, for the quenching of $O_2(b^1\Sigma_g^+)$ by M, M=HCl

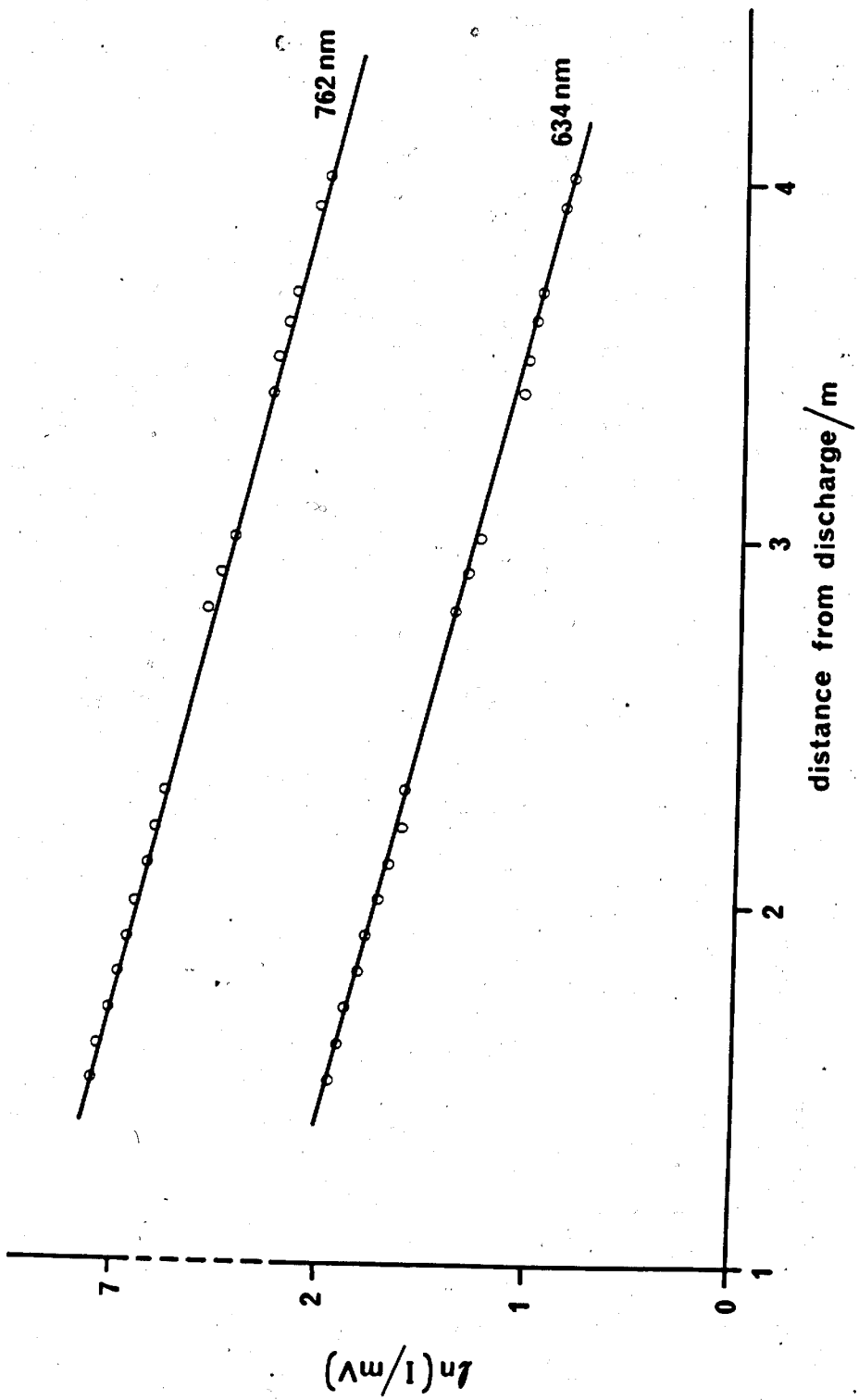

Figure 4.3 First order plot of the decay of emission intensity, I, against distance along the tube

4.2.1 The Collisional Quenching of $O_2(a^1\Delta_g)$

Analogously with (4.6) the concentration change for $O_2(a^1\Delta_g)$ at high temperature in particle time, t_p, (see section 3.5) is:

$$d[O_2(a^1\Delta_g)]/dt_p = - k_d^M[O_2(a^1\Delta_g)][M] - k_W[O_2(a^1\Delta_g)]. \qquad (4.31)$$

The wall constant, k_W, at the shock temperature, T_2, can be ignored since the increase in pressure and temperature render it insignificant compared to k_d^M at T_2. So integrating equation (4.31):

$$\int_{[O_2(a^1\Delta_g)]_0}^{[O_2(a^1\Delta_g)]_{t_p}} \frac{1}{[O_2(a^1\Delta_g)]}\, d[O_2(a^1\Delta_g)] = \int_0^{t_p} - k_d^M[M]dt_p$$

$$\ln[O_2(a^1\Delta_g)]_{t_p}/[O_2(a^1\Delta_g)]_0 = -k_d^M[M]t_p$$

$$[O_2(a^1\Delta_g)]_{t_p}/[O_2(a^1\Delta_g)]_0 = \exp(- k_d^M[M])t_p \qquad (4.32)$$

where $[O_2(a^1\Delta_g)]_0$ is the concentration at any point in the tube immediately after the shock and $[O_2(a^1\Delta_g)]_{t_p}$ is that after time t_p. The value of $[O_2(a^1\Delta_g)]_0$ also varies with distance along the tube in the pre-shock flow due to the concentration gradient and this appears as a variation with time in the post-shock flow. $[O_2(a^1\Delta_g)]_0$ is then related to the initial post-shock concentration of $O_2(a^1\Delta_g)$ at the observation station, $[O_2(a^1\Delta_g)]_0^o$ by the first order decay equation:

$$[O_2(a^1\Delta_g)]_0 = [O_2(a^1\Delta_g)]_0^o \quad \exp(- \alpha_t t_p/2) \qquad (4.33)$$

and so:

$$[O_2(a^1\Delta_g)]_{t_p}/[O_2(a^1\Delta_g)]_0^o = \exp(- k_d^M[M] - \alpha_t/2)t_p. \qquad (4.34)$$

Replacing the concentration ratio with the intensity ratio for the same photomultiplier and noting that the emission intensity, ^{634}I, varies with the square of $O_2(a^1\Delta_g)$ concentration:

$$^{634}I_{t_p} / {}^{634}I_0^o = \exp(-2k_d^M[M] - \alpha_t)t_p \qquad (4.35)$$

$$\ln {}^{634}I_{t_p} / {}^{634}I_0^o = -(2k_d^M[M] + \alpha_t)t_p. \qquad (4.36)$$

Therefore the rate constant for the quenching of $O_2(a^1\Delta_g)$ can be determined by plotting the measured intensity against particle time and measuring the increase of the gradient from that of the pre-shock values, α_L, figure 4.4.

The post-shock decay, α_t, is related to the pre-shock decay constant, α_L, by considering equation (4.10) representing the change in concentration of $O_2(a^1\Delta_g)$ along the tube at room temperature;

$$d[O_2(a^1\Delta_g)]/dl = (-\alpha_L/2)[O_2(a^1\Delta_g)]. \qquad (4.10)$$

In a shock tube, the post-shock decay mirrors the concentration gradient of $O_2(a^1\Delta_g)$ before the arrival of the shock provided that no reaction occurs during the time it takes the shock heated gas to pass the observation station. In other words, one obtains a snapshot of the condition of the gas upstream as it is swept past the observation station.

By analogy with (4.10) the concentration change for $O_2(a^1\Delta_g)$ at high temperature in particle time, t_p, is:

$$d[O_2(a^1\Delta_g)]/dt_p = (-\alpha_t/2)[O_2(a^1\Delta_g)] \qquad (4.37)$$

$$d[O_2(a^1\Delta_g)]/dt_p = d[O_2(a^1\Delta_g)]/dl \times dl/dt_p \qquad (4.38)$$

where dl/dt_p is the particle velocity (see section 3.5). From equations (4.37), (4.10) and (3.25) it follows:

Figure 4.4 Measurement of the rate of quenching of $O_2(a^1\Delta_g)$ behind the shock front

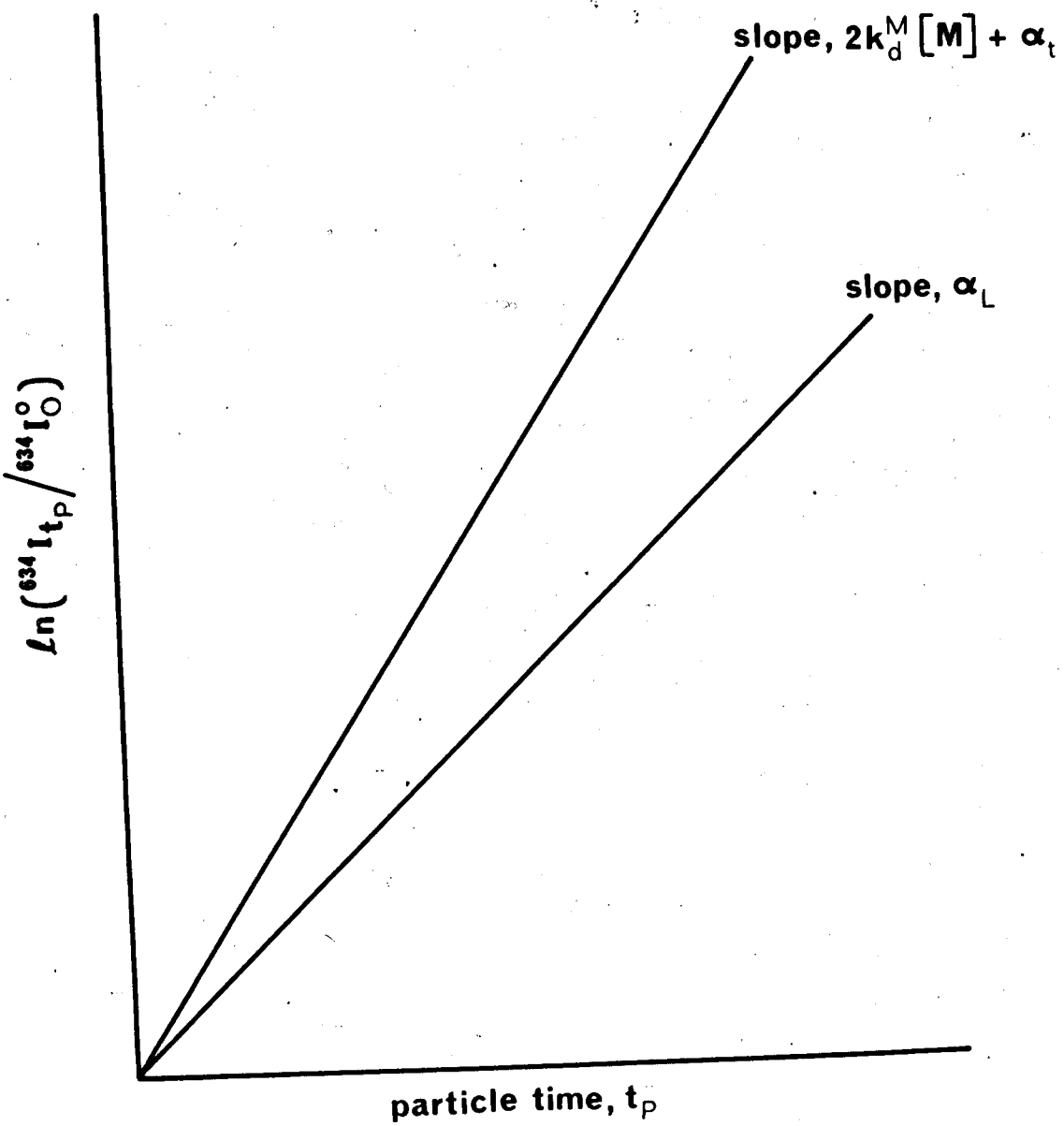

$$d[O_2(a^1\Delta_g)]/dt_p = (-v_s\alpha_L/2)(1 - 1/\rho_{21})[O_2(a^1\Delta_g)] \quad (4.39)$$

$$\alpha_t = v_s\alpha_L(1 - 1/\rho_{21}). \quad (4.40)$$

The measured pre- and post-shock slopes, corrected for shock compression, are similar if there is no appreciable deactibation of $O_2(a^1\Delta_g)$ at the high temperature during the observation time. Hence for

$$2k_d^M[M] << v_s\alpha_L(1 - 1/\rho_{21})$$

equation (4.35) reduces to:

$$^{634}I_{t_p}/{}^{634}I_0^o = \exp(-\alpha_t t_p). \quad (4.41)$$

If the dimol emission reaction is a simple collisional process, then the immediate post-shock emission intensity from the heated gas; $^{634}I_0^o$, can be related to that from the cool gas, $^{634}I_{psg}$, by:

$$^{634}I_0^o = {}^{634}K\ {}^{634}I_{psg}\ \rho_{21}^2\ T_{21}^{\frac{1}{2}} \quad (4.42)$$

where ^{634}K is a constant for any enhancement in the emission with rise in temperature and would be unity in the case of a simple collisional process.

Combination of equation (4.42) and (4.35) relates the observed post-shock glow at the observation station, $^{634}I_{t_p}$, to that observed pre-shock, $^{634}I_{psg}$:

$$^{634}I_{t_p} = {}^{634}K\ {}^{634}I_{psg}\ \rho_{21}^2\ T_{21}^{\frac{1}{2}} \exp(-2k_d^M[M] - \alpha_t)t_p. \quad (4.43)$$

If there is no appreciable deactivation of $O_2(a^1\Delta_g)$ at the high temperature then equation (4.43) reduces to:

$$^{634}I_{t_p} = {}^{634}K\ {}^{634}I_{psg}\ \rho_{21}^2\ T_{21}^{\frac{1}{2}} \exp(-\alpha_t t_p). \quad (4.44)$$

Equation (4.44) predicts an instantaneous rise of emission intensity at the shock front followed by a decay, see figure 4.5a.

This can be compared to the observed post-shock behaviour shown in figure 4.5b; which shows the emission intensity of the shocked gas as a function of time for the dimol emission at 634 nm.

Four zones can be distinguished:

(a) the beginning of the trace is a measure of the pre-shock glow, I_{psg};

(b) the rapid rise at the shock front is due to the increase in density and temperature;

(c) the fall off which reflects the decay of excited species along the tube before the shock; and finally

(d) which is the fall off in emission at the contact surface.

All these observations are in accordance with the predicted model except that the actual rise at the shock front is not vertical due to the effect of the finite slit width characterised by a rise time of, t_s. To compensate for this equations (4.43) and (4.44) must be integrated to allow for, t_s. Therefore, the final expressions for the observed intensity dependence on time are;

$$ {}^{634}I_{t_p} = {}^{634}K \; {}^{634}I_{psg} \; \rho_{21}^{2} \; T_{21}^{\frac{1}{2}} \int_{t_p - t_s}^{t_p} [\exp(-2k_d^M[M] - \alpha_t)t_p]dt_p/t_s \qquad (4.45) $$

and

$$ {}^{634}I_{t_p} = {}^{634}K \; {}^{634}I_{psg} \; \rho_{21}^{2} \; T_{21}^{\frac{1}{2}} \int_{t_p - t_s}^{t_p} \exp(-\alpha_t t_p)dt_p/t_s \qquad (4.46) $$

Figure 4.5 The comparison of the observed post-shock behaviour with that predicted for 634 nm emission

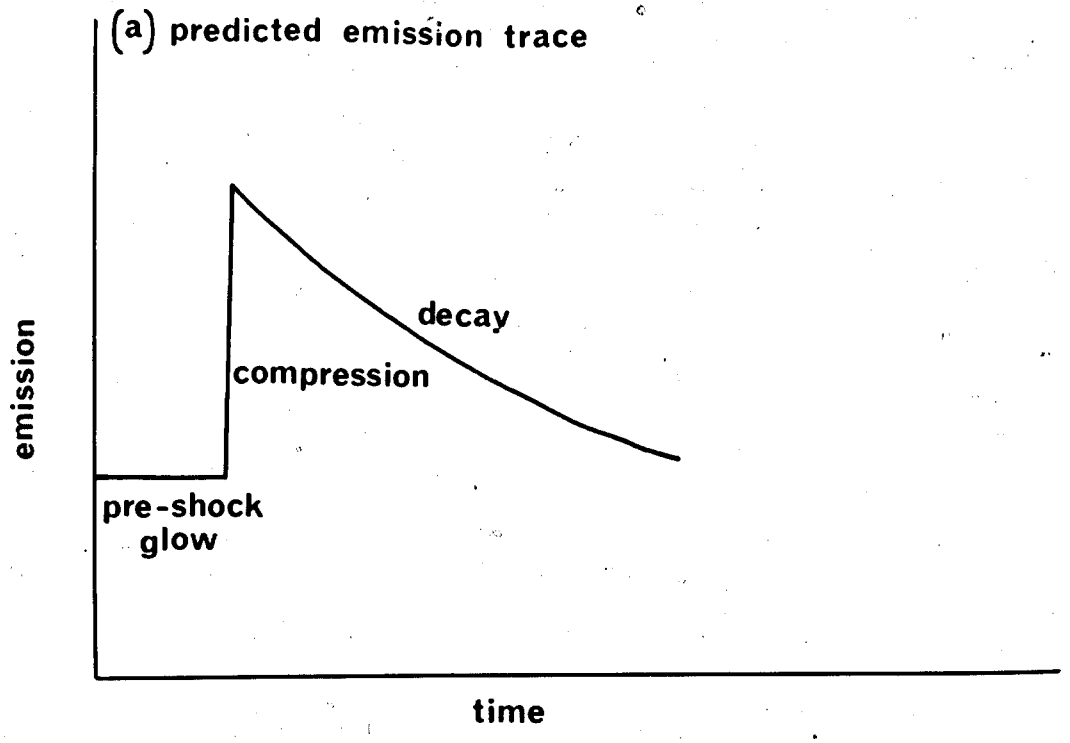

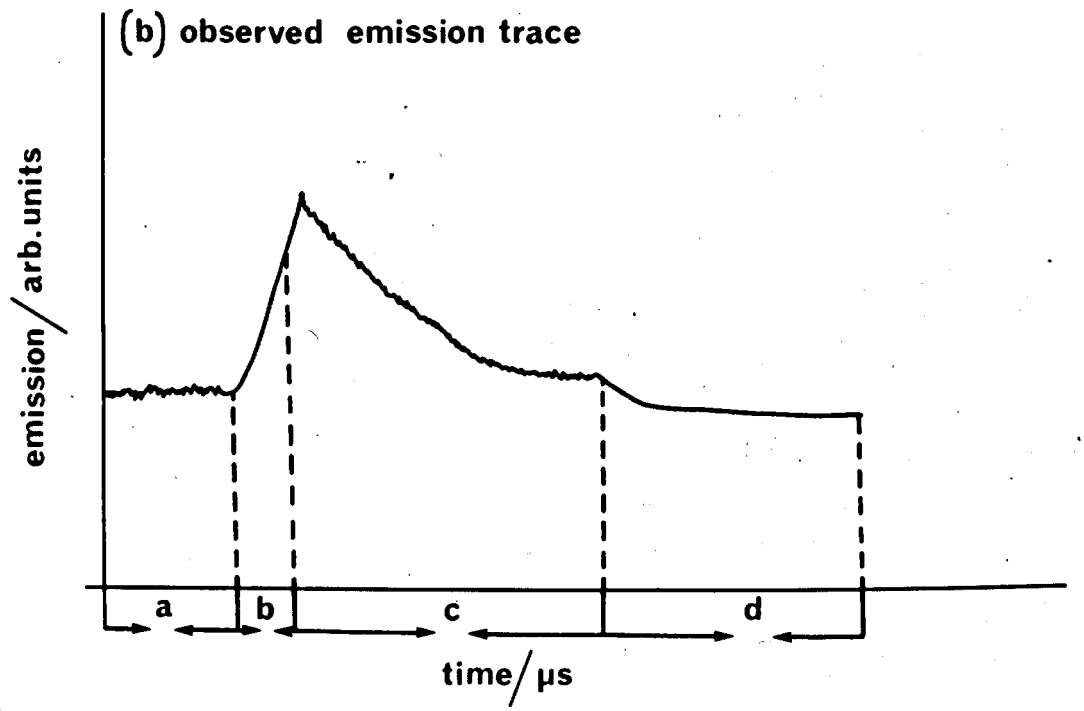

While expressions (4.45) and (4.46) can be integrated explicitly, they are actually integrated numerically using Simpson's rule, as this allows corrections to be made for the effect of vibrational relaxation in the oxygen during the period of the experiment which modifies the concentrations. Correction for non-ideal behaviour in the flow can also be made when it is required. In these experiments vibrational relaxation is complete so correction is unnecessary and it has been shown[59] that corrections for non-ideal flow are not needed.

Figure 4.6a shows an example of the fitted shock trace for a system with no deactivation of $O_2(a^1\Delta_g)$ at high temperature. The full line through the experimental points is the fit obtained using equation (4.46). The fit for each run gives values of α_t, t_s and ^{634}K. The comparison of the post-shock decay and the measured pre-shock decay, corrected for shock compression, has shown that the two values are always similar (Chapter 6).

Figure 4.6b shows an example of the fitted shock trace for a system with deactivation of $O_2(a^1\Delta_g)$ at high temperature. The full line passing through the points is the fit obtained by equation (4.45) which includes the decay at high temperature. The broken line, which does not pass through the points, shows the simple predication from the room temperature measurement of the pre-shock decay, suitably corrected for the shock compression. The fit for each experiment gives values of α_t, t_s, and ^{634}K. The quenching rate constant for $O_2(a^1\Delta_g)$, k_d^M, is then determined from the difference of the decay slopes. This is discussed further in Chapter 6.

All these considerations show that the shape of the shock trace obtained at 634 nm is in agreement with the predicted model hence confirming the adopted kinetic schemes.

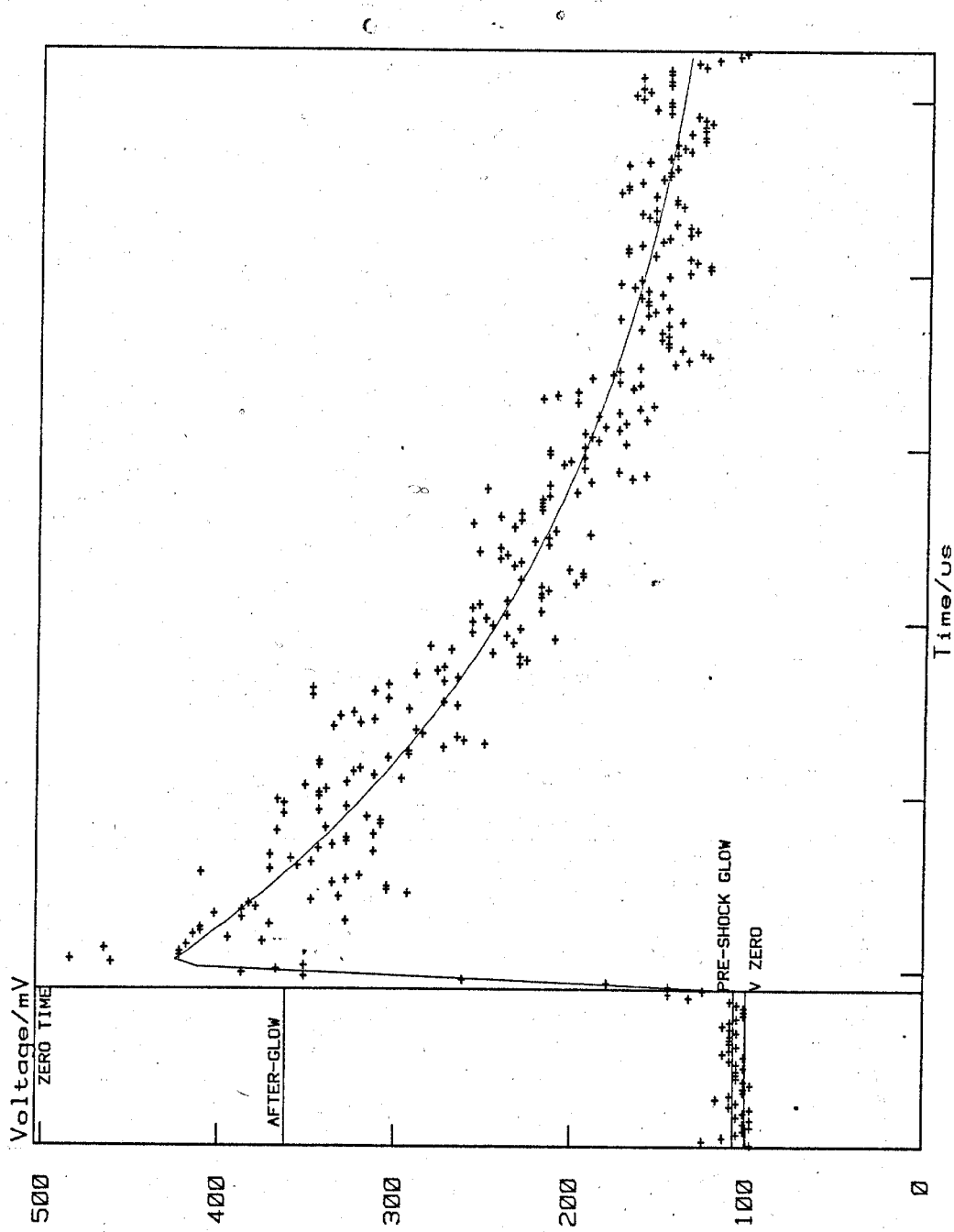

Figure 4.6a A fitted shock trace at 634 nm emission without deactivation of $O_2(a^1\Delta_g)$ at high temperature

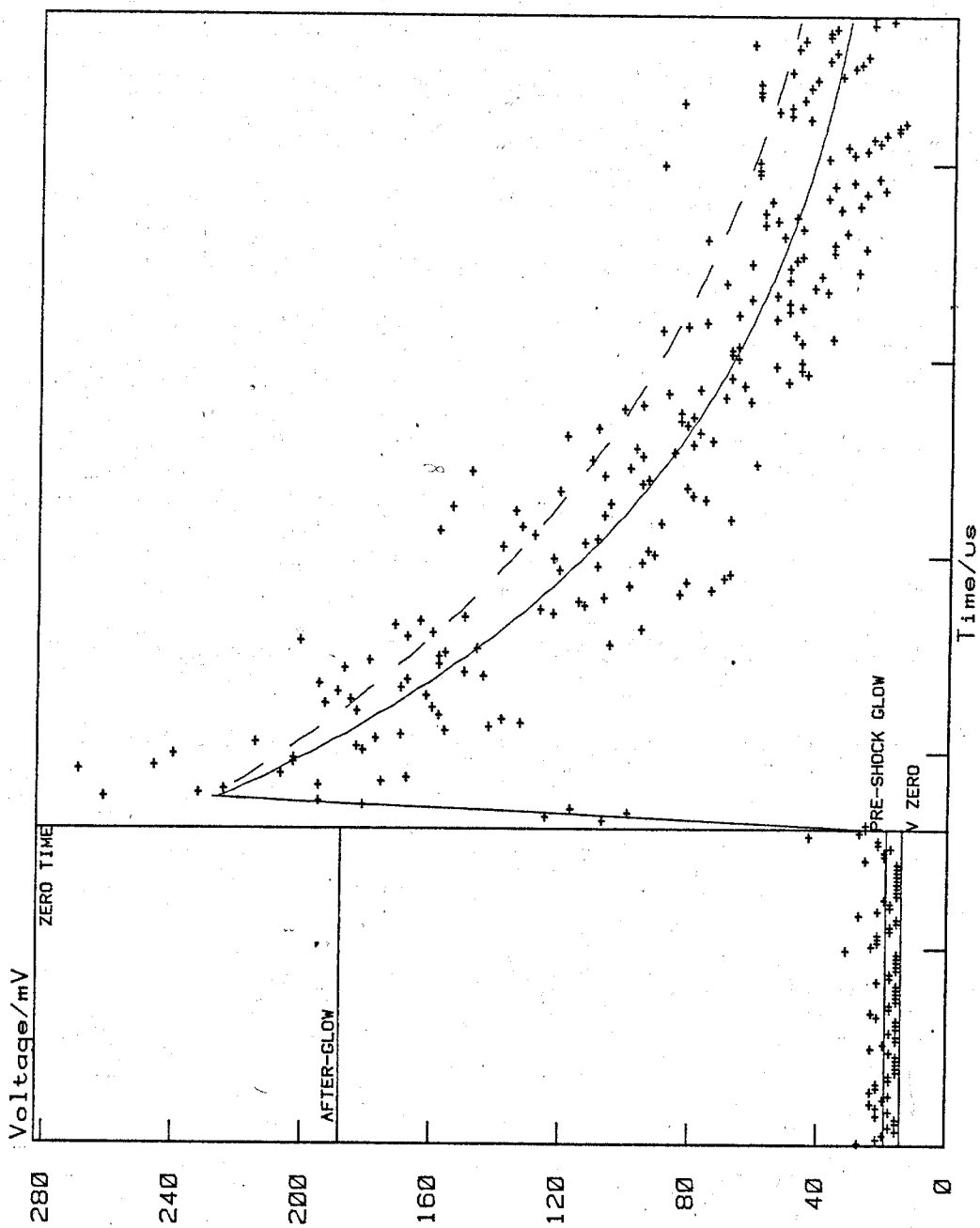

Figure 4.6b A fitted shock trace at 634 nm emission with deactivation of $O_2(a^1\Delta_g)$ at high temperature

The fitting which is obtained by using interactive computer graphics and non-linear least squares is outlined in section 4.2.3.

4.2.2. The Collisional Quenching of $O_2(b^1\Sigma_g^+)$

(a) With no deactivation of $O_2(a^1\Delta_g)$ at high temperature

The treatment which follows assumes that the decay in emission seen as the shock passes the observation station is purely a reflection of the decay prior to the shock and no $O_2(a^1\Delta_g)$ is removed by collisional quenching in time, t_p, that it takes the section of the gas to reach the observation station.

Analogously to the room temperature, T_1, treatment the formation and removal of $O_2(b^1\Sigma_g^+)$ at the new temperature, T_2, is governed by the pooling (4.5) and the quenching (4.20) reactions:

$$d[O_2(b^1\Sigma_g^+)]/dt_p = k_p[O_2(a^1\Delta_g)]^2 - k_q^M[O_2(b^1\Sigma_g^+)][M]. \qquad (4.47)$$

Assuming that $[O_2(b^1\Sigma_g^+)] << [O_2(a^1\Delta_g)]$ equation (4.47) can be integrated:

$$\int_{[O_2(b^1\Sigma_g^+)]_0}^{[O_2(b^1\Sigma_g^+)]_{t_p}} d[O_2(b^1\Sigma_g^+)]/(k_p[O_2(a^1\Delta_g)]^2 - k_q^M[O_2(b^1\Sigma_g^+)][M]) = \int_0^{t_p} dt_p \qquad (4.48)$$

and so

$$\ln\{(k_p[O_2(a^1\Delta_g)]^2 - k_q^M[M][O_2(b^1\Sigma_g^+)]_{t_p})/(k_p[O_2(a^1\Delta_g)]^2 - k_q^M[M][O_2(b^1\Sigma_g^+)]_0)\} = -k_q^M[M]t_p \qquad (4.49)$$

$$[O_2(b^1\Sigma_g^+)]_{t_p}/[O_2(b^1\Sigma_g^+)]_0 = -\{(k_p[O_2(a^1\Delta_g)]^2/k_q^M[M][O_2(b^1\Sigma_g^+)]_0)\exp(k_q^M[M]t_p)\}$$

$$+ \{\exp(k_q^M[M]t_p)\} +$$

$$\{k_p[O_2(a^1\Delta_g)]^2/k_q^M[M][O_2(b^1\Sigma_g^+)]_0\} \qquad (4.50)$$

where $[O_2(b^1\Sigma_g^+)]_0$ is the concentration at any point in the tube immediately after the shock and $[O_2(b^1\Sigma_g^+)]_{t_p}$ is that after time, t_p.

At equilibrium $t_p \to \infty$ so equation (4.50) simplifies to:

$$[O_2(b^1\Sigma_g^+)]_{t_p} = \{k_p[O_2(a^1\Delta_g)]^2/k_q^M[M]\} \qquad (4.51)$$

which is similar to that at room temperature (4.24). Here, the wall constant is omitted since the increase in pressure and temperature render it insignificant compared to k_q^M.

Equations (4.24) and (4.51) can be rewritten as:

$$\{[O_2(a^1\Delta_g)]^2\}_{T_1}/\{[O_2(b^1\Sigma_g^+)][M]\}_{T_1} = \{(k_q^M + k_W/[M]\}_{T_1}/\{k_p\}_{T_1} \qquad (4.52)$$

$$\{[O_2(a^1\Delta_g)]^2\}_{T_2}/\{[O_2(b^1\Sigma_g^+)][M]\}_{T_2} = \{k_q^M\}_{T_2}/\{k_p\}_{T_2}. \qquad (4.53)$$

Combination of equations (4.52) and (4.53) gives the enhancement factor, ^{762}K, which is defined as the ratio of the pre- and post-shock values of the pooling and the quenching rate constants:

$$^{762}K = \{(k_p/k_q^M)\}_{T_2}/\{k_p/(k_q^M + k_W/[M])\}_{T_1}. \qquad (4.54)$$

On the right hand side of equation (4.50) the concentration of the excited states and M occur only as a ratio which is the same as that in the pre-shock but being increased by a factor of density ratio. Hence, rearranging for ^{762}K equation (4.50) gives:

$$[O_2(b^1\Sigma_g^+)]_{t_p}/[O_2(b^1\Sigma_g^+)]_0 = {}^{762}K + (1 - {}^{762}K)\exp(-k_q^M[M]t_p). \quad (4.55)$$

It must be recalled that the fall in the concentration of excited state in the pre-shock is reflected in the post-shock behaviour. As the immediate post-shock concentration, $[O_2(b^1\Sigma_g^+)]_0$, is related to the initial post-shock concentration of $O_2(b^1\Sigma_g^+)$ at the observation station, $[O_2(b^1\Sigma_g^+)]_0^o$, by the first order decay equation:

$$[O_2(b^1\Sigma_g^+)]_0 = [O_2(b^1\Sigma_g^+)]_0^o \exp(-\alpha_t t_p) \quad (4.56)$$

then the combination of (4.55) and (4.56) gives;

$$[O_2(b^1\Sigma_g^+)]_{t_p}/[O_2(b^1\Sigma_g^+)]_0^o = \{{}^{762}K + (1 - {}^{762}K)\exp(-k_q^M[M]t_p)\} \exp(-\alpha_t t_p). \quad (4.57)$$

Replacing the concentration ratio with the emission intensity ratio:

$${}^{762}I_{t_p}/{}^{762}I_0^o = \{{}^{762}K + (1 - {}^{762}K)\exp(-k_q^M[M]t_p)\}\exp(-\alpha_t t_p). \quad (4.58)$$

The immediate post-shock glow at the observation station, ${}^{762}I_0^o$, is related to the pre-shock glow, ${}^{762}I_{psg}$, by:

$${}^{762}I_0^o = {}^{762}I_{psg}\,\rho_{21}. \quad (4.59)$$

Hence, the observed post-shock glow at the observation station, ${}^{762}I_{t_p}$, can be related to that observed in the pre-shock, ${}^{762}I_{psg}$, by combining equations (4.58) and (4.59):

$$^{762}I_{t_p} = {}^{762}I_{psg}\,\rho_{21}\{{}^{762}K + (1 - {}^{762}K)\exp(-k_q^M[M]t_p)\}\exp(-\alpha_t t_p). \quad (4.60)$$

Figure 4.7a shows the predicted shock regime given by equation (4.60) where the rapid increase in the emission intensity at the shock front is followed by relaxation zone then the decay.

Figure 4.7b shows an observed shocked gas behaviour for emission at 762 nm. Five zones can be distinguished in the shock trace; (a) the steady pre-shock glow, $^{762}I_{psg}$, from the room temperature steady state concentration of $O_2(b^1\Sigma_g^+)$; (b) the rapid rise at the shock front due to compression; (c) the relaxation to the new steady state at the high temperature, that is the curvature up to the peak; (d) the decay due to the fall in the concentration of $O_2(b^1\Sigma_g^+)$ along the tube and finally region (e) the complete quenching of the emission due to the arrival of the contact surface.

The comparison shows that the observed shocked gas behaviour is in accordance with the predicted model given by equation (4.60). But once again the rise at the shock front is not vertical so equation (4.60) needs to be modified for this effect by introducing the integration time, t_s:

$$^{762}I_{t_p} = {}^{762}I_{psg}\,\rho_{21}\int_{t_p-t_s}^{t_p}\{{}^{762}K + (1 - {}^{762}K)\exp(-k_q^M[M]t_p)\}\exp(-\alpha_t t_p)dt_p/t_s. \quad (4.61)$$

Equation (4.61) is integrated numerically, using Simpson's rule. The experimental points are fitted to equation (4.61) using interactive

Figure 4.7 The comparison of the observed post-shock behaviour with that predicted for 762 nm

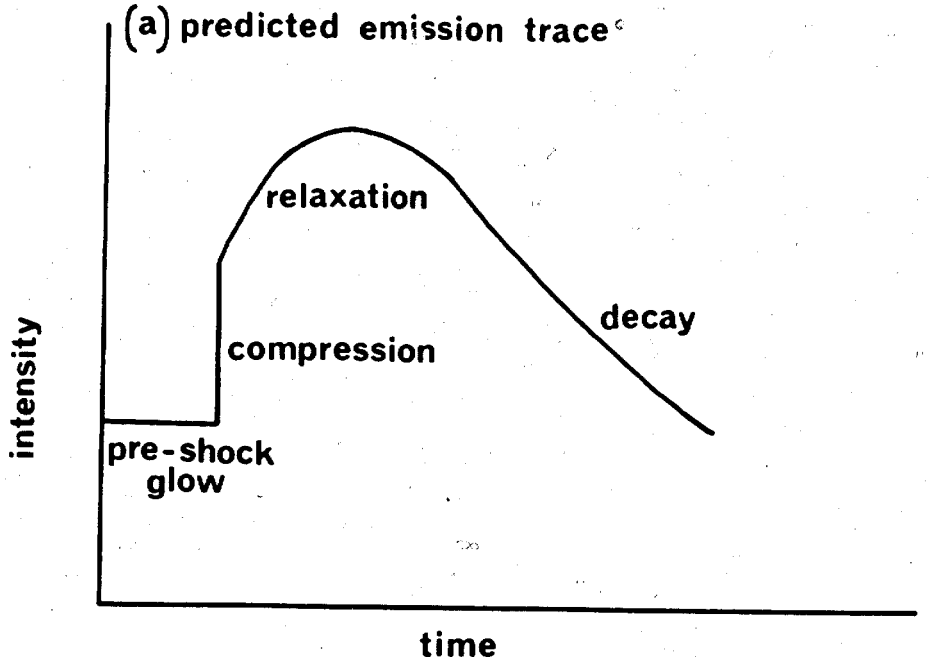

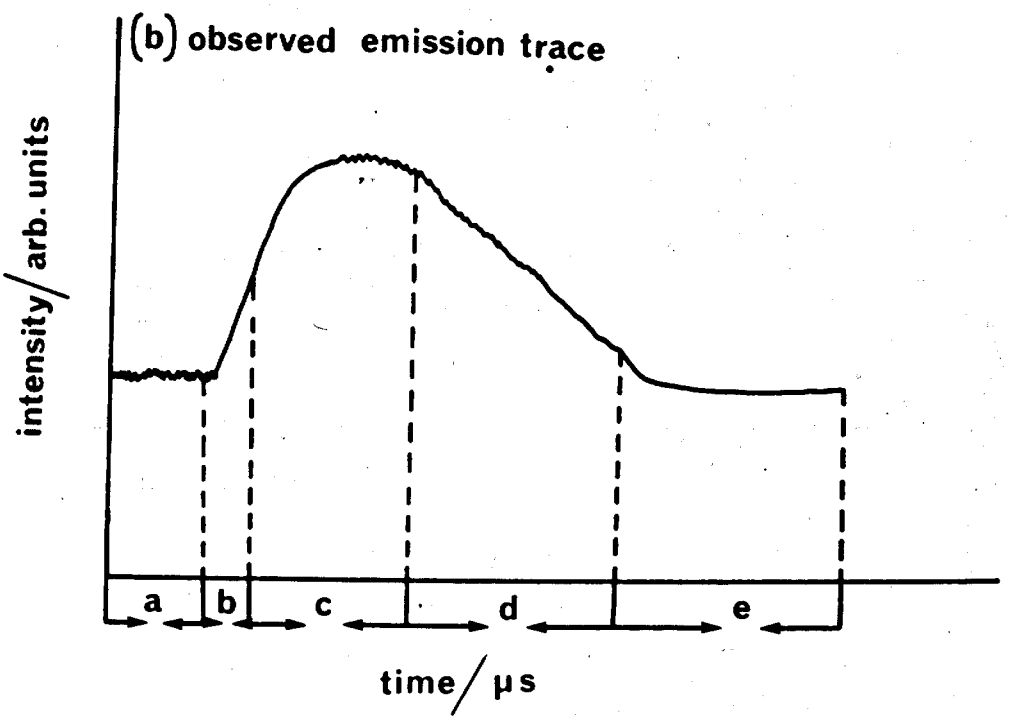

graphics. An example of the fit is shown by the full line in figure 4.8a; the fit for each run gives values of α_t, t_s, k_q^M and ^{762}K.

(b) With deactivation of $O_2(a^1\Delta_g)$ at high temperature

To account for the deactivation of $O_2(a^1\Delta_g)$ by M at the shock temperature it is necessary to rework the rate equations. Now, at a point in the post-shock gas, the steady state $O_2(b^1\Sigma_g^+)$ is determined by the energy pooling reaction (4.5), the quenching reaction (4.20), and the concentration change for $O_2(a^1\Delta_g)$ at that point. The wall reaction can be neglected in the post-shock analysis. So the rate of formation of $O_2(a^1\Sigma_g^+)$ is as before, given by equation (4.47). Equation (4.47) can be rewritten as:

$$d[O_2(b^1\Sigma_g^+)]/dt_p + k_q^M[O_2(b^1\Sigma_g^+)][M] = k_p[O_2(a^1\Delta_g)]^2. \qquad (4.47)$$

To account for the deactivation of $O_2(a^1\Delta_g)$ by M at high temperature, $[O_2(a^1\Delta_g)]$ can be represented as a function of time at a point in the flow (see section 4.2.1) by:

$$[O_2(a^1\Delta_g)]_{t_p} = [O_2(a^1\Delta_g)]_0 \exp(- k_d^M[M])t_p \qquad (4.32)$$

where $[O_2a^1\Delta_g)]_0$ is the concentration at any point in the tube immediately after the shock and $[O_2(a^1\Delta_g)]_{t_p}$ is that after time t_p. $[O_2(a^1\Delta_g)]_0$ also varies with distance along the tube in the pre-shock flow due to the concentration gradient and it was shown previously (section 4.2.1) that this variation with distance in the pre-shock is reflected in the post-shock as a function of time given by equation:

$$[O_2(a^1\Delta_g)]_0 = [O_2(a^1\Delta_g)]_0^o \exp(- \alpha_t t_p/2) \qquad (4.33)$$

Figure 4.8a A fitted shock trace at 762nm emission without deactivation of $O_2(a^1\Delta_g)$ at high temperature

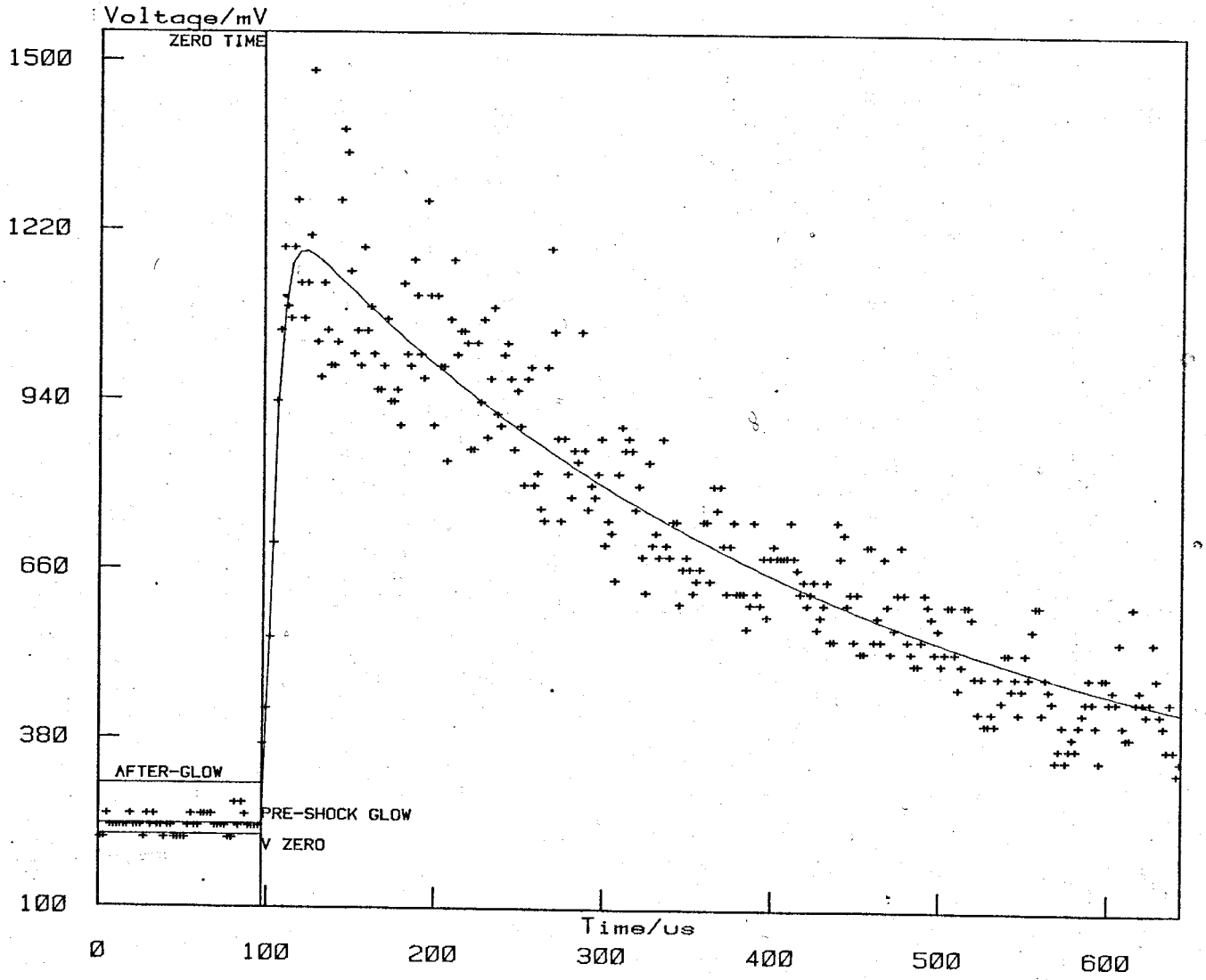

where $[O_2(a^1\Delta_g)]_0^o$ is the initial post-shock concentration at the observation station. Hence, the combination of equations (4.32) and (4.33) gives the actual concentration of $O_2(a^1\Delta_g)$ as a function of time at a point in the flow:

$$[O_2(a^1\Delta_g)]_{t_p} / [O_2(a^1\Delta_g)]_0^o = \exp(- k_d^M[M] - \alpha_t/2)t_p . \qquad (4.34)$$

If equations (4.47) and (4.34) are combined and integrated with the condition that at the observation station the initial post-shock concentration of $O_2(b^1\Sigma_g^+)$ is $[O_2(b^1\Sigma_g^+)]_0^o$, then:

$$[O_2(b^1\Sigma_g^+)]_{t_p} / [O_2(b^1\Sigma_g)]_0^o = \{^{762}K \exp(- k_d^M[M]t_p) + (1 - {}^{762}K)\exp(- k_q^M[M]t_p)\} \times \exp(- \alpha_t t_p) \qquad (4.62)$$

where ^{762}K is the enhancement factor defined as:

$$^{762}K = \{k_p/(k_q^M - k_d^M)\}_{T_2} / \{k_p/(k_q^M - k_d^M + k_W/[M])\}_{T_1} . \qquad (4.63)$$

As before, for the same photomultiplier the concentration ratio can be replaced by the intensity ratio, which is then integrated to allow for the finite slit width, characterised by a time, t_s; the final expression for the observed intensity as a function of time is:

$$^{762}I_{t_p} = {}^{762}I_{psg}\, \rho_{21} \int_{t_p - t_s}^{t_p} \{^{762}K \exp(- 2k_d^M[M]t_p) + (1 - {}^{762}K)\exp(- k_q^M[M]t_p)\} \exp(- \alpha_t t_p)dt_p/t_s . \qquad (4.64)$$

This equation predicts a shocked gas behaviour similar to that shown for equation (4.60), figure 4.7a. The observed behaviour is also similar to that shown in figure 4.7b. However, it should be noted that here the observed post-shock decay is not only due to the

reflection of the fall in $[O_2(a^1\Delta_g)]$ pre-shock, but also it is due to the deactivation of $O_2(a^1\Delta_g)$ by the quencher at high temperature.

Once again equation (4.64) is integrated numerically using Simpson's rule. For each run the experimental points are fitted to equation (4.64) using interactive graphics. An example of the fit is shown by the full line in figure 4.8b. The broken line, which does not pass through the points, is that which uses the decay value under pre-shock conditions. The fit gives values of α_t, t_s, k_d^M, k_q^M and ^{762}K.

These various considerations for the analysis of 762 nm shock traces show that the kinetic schemes followed are correct as they agree with the predicted models.

4.2.3 Analysis of the Kinetic Data by Interactive Computer Graphics and Non-Linear least squares

The equations developed in the previous sections are translated[66] into an interactive computer graphics program for use on the G.E.C. 4082 system with an HP 2647 graphics terminal.

The analysis proceeds by fitting the traces to equations derived in the previous sections. The aim is to evaluate the best values of K, k_q^M, α_t and t_s for each experiment. α_t can be compared with the known pre-shock decay, α_L, to yield k_d^M if they are found not to be the same. ^{762}K, k_q^M and k_d^M yield the rate constant, k_p.

Interactive graphics is used to select reasonable values to start the numerical fitting by non-linear least squares. These initial values are obtained from visual or by partial fits of the data. Also the interactive nature of the program allows the operator to stay in contact with the processing and to exercise a considerable

Figure 4.8b A fitted shock trace at 762nm emission with deactivation of $O_2(a^1\Delta_g)$ at high temperature

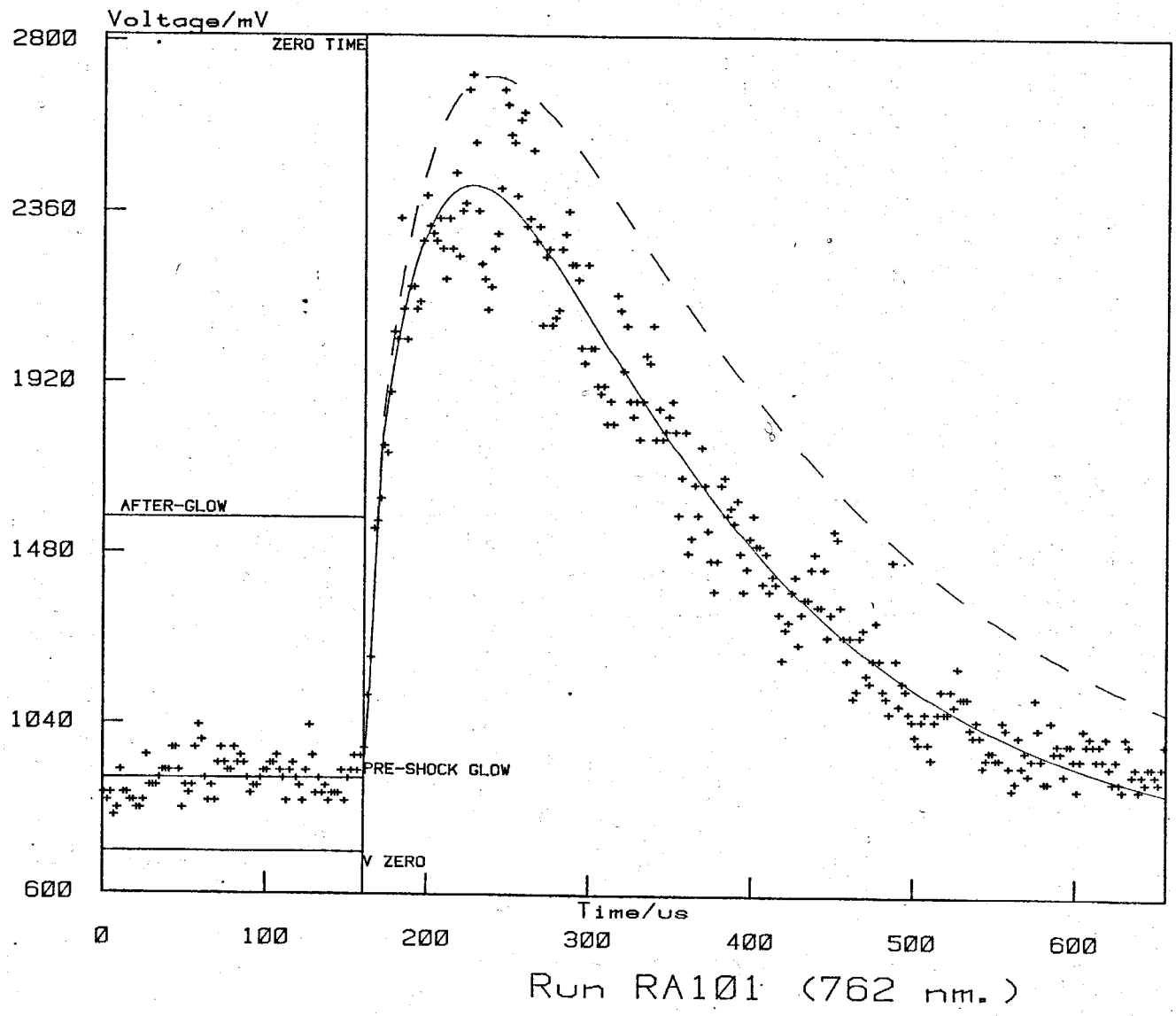

degree of control over the multi-stage analysis. A variety of options are offered at each stage so the effect of variations of values or data can be explored.

The final optimisation of the parameters is achieved by use of a non-linear least squares fitting routine similar to that of the traditional "blind" method of computer analysis. However, the use of interactive graphics allows the operator to check the goodness of the fit by non-linear least squares.

The digitized input data from the transient recorder can also be edited prior to analysis to remove erroneous data or unnecessary points; such as large spikes in the region of the contact surface, or long flat regions at the end of the hot flow time, to improve both the fitting and the display. This is more efficient than the traditonal method.

Therefore, the use of interactive computer graphics for the analysis of the data allows the experimenter to develop a feel for the understanding of the data, the validity of the analysis and the precision and accuracy of the results.

The program consists of numerous sub-routines, a simplified flow diagram is shown in Figure 4.9. The operation of the main sub-routines will now be described.

1. Transfer

The digitized shock trace, 1024 points, already stored on magnetic tape together with the run number, sweep speed and voltage sensitivity is transferred to G.E.C. 4082, via HP 2647, where the coordinates of all the points in millivolts and microseconds are calculated and stored in a disc file with the run parameters to be called up for analysis by the main program graph.

Figure 4.9 A simplified flow diagram for the interactive computer graphics analysis

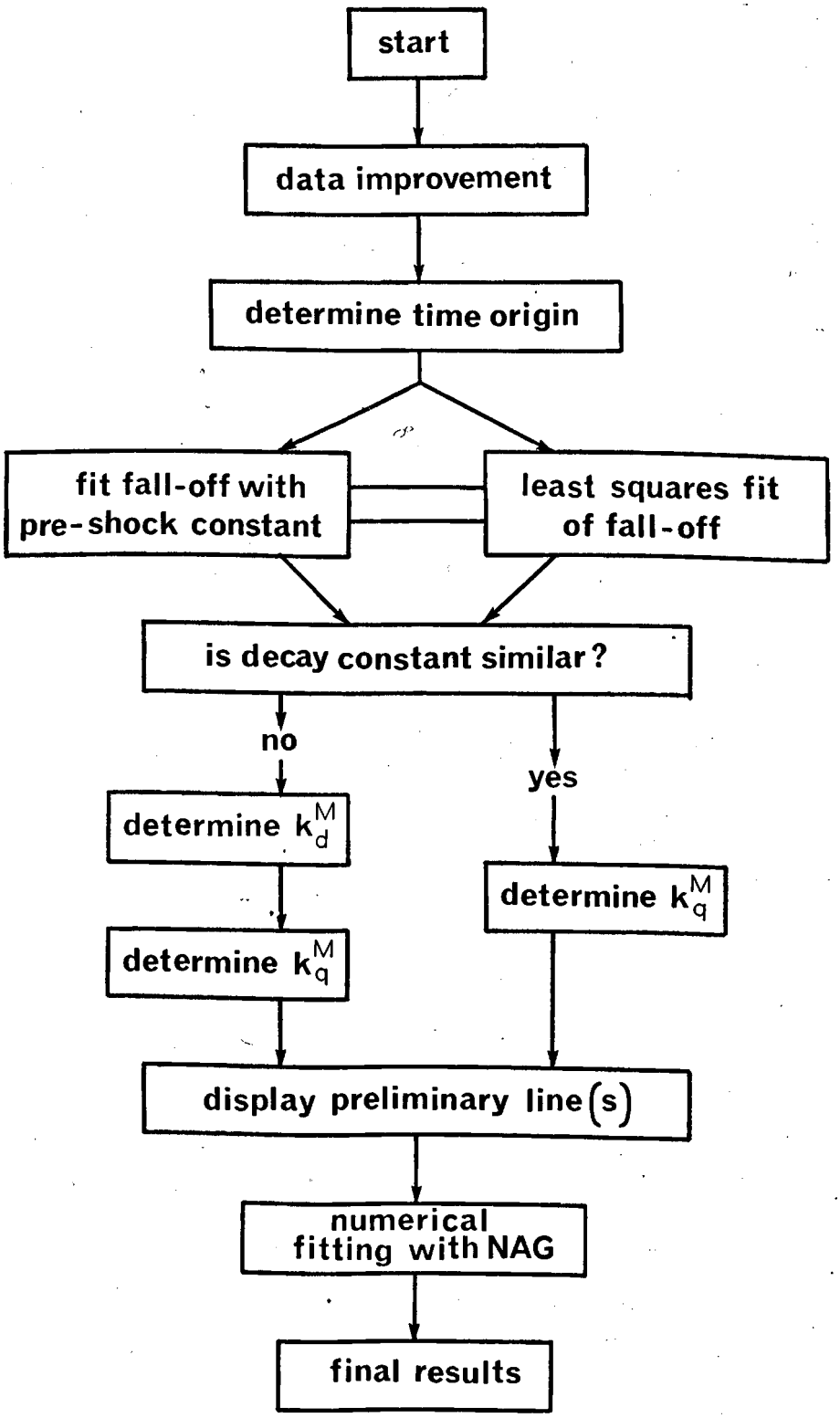

2. Graph

This is a multi-stage program run in conjunction with HP 2647 for display, visual tracking and setting of certain parameters. The time origin is set using the graphics cursor at the start of the sharp rise at the shock front. In the same way the beginning of the decay region is set depending upon the emission being analysed. For traces where there is a relaxation, this is set after the relaxation zone. A decay line is then displayed over the points, it may be one predicted from the pre-shock or calculated from the trace by a non-linear least squares. At this stage a value for the decay is displayed on the screen. This allows the experimenter to see if the value displayed corresponds to that predicted from the room temperature measurement. If the two values are found to be similar, no deactivation of $O_2(a^1\Delta_g)$ at high temperature, the analysis is continued and a fit is obtained for the shock trace. Typical examples are shown in figures 4.6a and 4.8a for shock traces at 634 nm and 762 nm respectively. However, if the two values are found to be different then the analysis is changed to a sub-routine which includes the kinetic scheme for the deactivation of $O_2(a^1\Delta_g)$ at high temperature. Figures 4.6b and 4.8b show typical examples for the shocks analysed at 634 nm emission and 762 nm emission respectively. As can be seen, the difference is illustrated by two lines of decay. The upper one, which does not pass through the experimental points, is that predicted by the normal model in which the only high temperature reactions are the formation and removal of $O_2(b^1\Sigma_g^+)$ and the fall is due to the pre-shock concentration gradient. The lower line, through the points, is the result fitted with a model which includes deactivation of $O_2(a^1\Delta_g)$ by M at high temperature.

The ratio of the observed after glow to that predicted from the pre-shock glow, K, is obtained by extrapolation of the fitted decay curve to zero time.

The parameters to be fitted are chosen depending upon the emission trace analysed, up to four independent variables can be fitted. Each parameter can be omitted or a pre-determined value typed in for it.

The integration of the kinetic expressions is done numerically using Simpson's rule. The values of the parameters are improved by an iterative non-linear least squares routine. Generally after 3 to 10 iterations consistent values are obtained.

The final results, the fitted trace and the run parameters are plotted for each experiment and all the information is recorded on a magnetic tape for permanent storage.

4.3 Reliability of the Discharge Flow Shock Tube Data

The reliability of the measured fundamental parameters; time, voltage, pressure and velocity was outlined in chapter 2. Below is given an assessment of kinetic data obtained for the quenching of singlet molecular oxygen using the combined discharge flow shock tube apparatus.

To obtain the room temperature kinetic data, the nature of the apparatus used demands that the measurements should be made some way from the discharge and so any interference from stray light and short lived species generated in the discharge is reduced to minimum. Comparison with previously reported data has shown that, where the measurements are made along way from the discharge, reliable results with better precision are obtained. This also provides good

evidence that the discharge flow system is under control. Least squares analysis is used for the determination of the rate constants at room temperature and the error limits given are for 2σ (95% confidence) limits.

In contrast to the low temperature data, high temperature shock wave data are often characterized by a considerable scatter since shock experiments are imprecise because they are necessarily unique. For a slow shock the scatter of the experimental points about the fitted best line can be as high as ± 20% but may be as low as ± 5% for a fast shock. Hence, to improve the precision a large number of shock experiments are performed. Error limits are not shown for individual points on the plots of the high temperature rate constants but uncertainties of ± 15% are estimated from the scatter on the graph.

In these experiments the computer optimization of the analysis of data via interactive graphics and non-linear least squares are found invaluable for calculating the best values for the various parameters to fit the data. However, these are treated with great caution as the best fit may not be the true fit if the kinetic models adopted for the reaction mechanism are not correct. In consequence, this is frequently checked by allowing the computer to optimise the fit of the function to the data around it for a fixed pre-determined value of one of the parameters. For example the decay value measured in the pre-shock flow. It was in the course of these cross-checks that the deactivation of $O_2(a^1\Delta_g)$ at high temperature was noticed, since the decay predicted from that measured in the pre-shock flow could not have been fitted to that observed at high temperature.

These various considerations and the good fits obtained for the shocked gas behaviour indicate that the combined apparatus is working and that the analysis is providing reliable high temperature data.

CHAPTER FIVE

5 Room-Temperature studies of the Collisional Quenching of both $O_2(a^1\Delta_g)$ and $O_2(b^1\Sigma_g^+)$

5.1 Introduction

Before the high temperature behaviour of the quenching reactions of singlet molecular oxygen by the chosen quenchers could be studied it was necessary to measure their quenching rate constants at room temperature in the pre-shock flow.

The quenching rate constants which can be measured in the discharge flow section of this apparatus are in the range of 10^3 - 10^8 dm^3 mol^{-1} s^{-1}. Both the lower and the upper limits depend on the quenching efficiency of the quencher used relative to that of O_2. This limits the number of additives which can be studied at room temperature by the requirements of a measurable change in the emission intensity.

The quenchers studied; NH_3, NO, HCl and SO_2, were chosen for the high temperature work as described in Chapter 6. The present chapter describes the room temperature study of these quenching systems. The determination and the practical aspects of the quenching rate constants for $O_2(a^1\Delta_g)$ and $O_2(b^1\Sigma_g^+)$ are described separately and the results obtained are compared with previously reported values.

5.2 Determination of the Room Temperature Rate constants for the Quenching of $O_2(a^1\Delta_g)$ by NH_3, NO, HCl and SO_2

5.2.1 Experimental

The decrease in concentration of $O_2(a^1\Delta_g)$ along the tube was measured by monitoring the voltage output from the movable photomultiplier fitted either with a 634 nm filter or a 762 nm filter. For a set initial pressure the first measurements were taken in pure oxygen for the decay of $O_2(a^1\Delta_g)$ as a function of distance. Then the flow was mixed with a stream of the quencher M, M = NH_3, NO, HCl and SO_2, to give 5% by volume mixture of M in O_2. After the flow had stabilized the new decay of $O_2(a^1\Delta_g)$ with distance along the tube was measured. A series of experiments for each quenching system were performed in the pressure range of 3 - 12 torr (linear flow velocity of 1 - 1.6 ms^{-1}).

5.2.2 Treatment of $O_2(a^1\Delta_g)$ Room Temperature Results

In an oxygen/M mixture, M = NH_3, NO, HCl and SO_2 the quenching reactions are:

$$O_2(a^1\Delta_g) + O_2 \xrightarrow{k_d^{O_2}} O_2(\chi^3\Sigma_g^-) + O_2 \qquad (5.1)$$

$$O_2(a^1\Delta_g) + M \xrightarrow{k_d^{M}} O_2(\chi^3\Sigma_g^-) + M \qquad (4.1)$$

$$O_2(a^1\Delta_g) + \text{Wall} \xrightarrow{k_W} O_2(\chi^3\Sigma_g^-) \qquad (4.2)$$

It was shown in Chapter 4 (section 4.1.1) that by measuring the decay of $O_2(a^1\Delta_g)$ along the flow tube, for oxygen, and oxygen plus the quencher, M, the quenching rate constant for M could be determined from equation (4.19):

$$\Delta k'_d = k_d^M[M] + (k_W - k_W^o). \qquad (4.19)$$

Figure 5.1 shows a typical plot for the variation of emission intensity as a function of distance, for oxygen and oxygen plus M. In this example M = NH_3. The difference in the slopes of the two plots gives the value of $\Delta k'_d$ in combination with the linear flow velocity. Plotting $\Delta k'_d$ against known [NH_3], figure 5.2, gives the second order rate constant, $k_d^{NH_3}$, for the quenching of $O_2(a^1\Delta_g)$ by NH_3.

In equation (4.19), the wall correction term in the presence of M, $(k_W - k_W^o)$, which is considered to depend only on the change in initial pressure was found to be negligible for $x_M \leq 0.05$ since the plot of equation (4.19) gave a straight line passing through the origin (see figure 5.2). This indicates that the wall deactivation in the presence and absence of M is nearly the same.

The rate constant for quenching of $O_2(a^1\Delta_g)$ by O_2, $k_d^{O_2}$, and by the wall, k_W^o, have been previously measured in this laboratory[63]. The value of $k_d^{O_2}$ is $(0.94 \pm 0.03) \times 10^3$ dm^3 mol^{-1} s^{-1} and $k_W^o = 0.11$ s^{-1} at 295 K. These were checked frequently during the present study and found to be the same within the experimental error.

5.2.3 Results

The results of the experiments performed with M = NH_3, HCl and NO are listed in table 5.1. Figure 5.2 shows a plot of the first order rate constant, $\Delta k'_d$, against concentration of quencher M. The slope of each line gives the second order rate constant for the quenching of $O_2(a^1\Delta_g)$ by M;

Figure 5.1 The variation of emission intensity with distance along the tube for M = NH_3

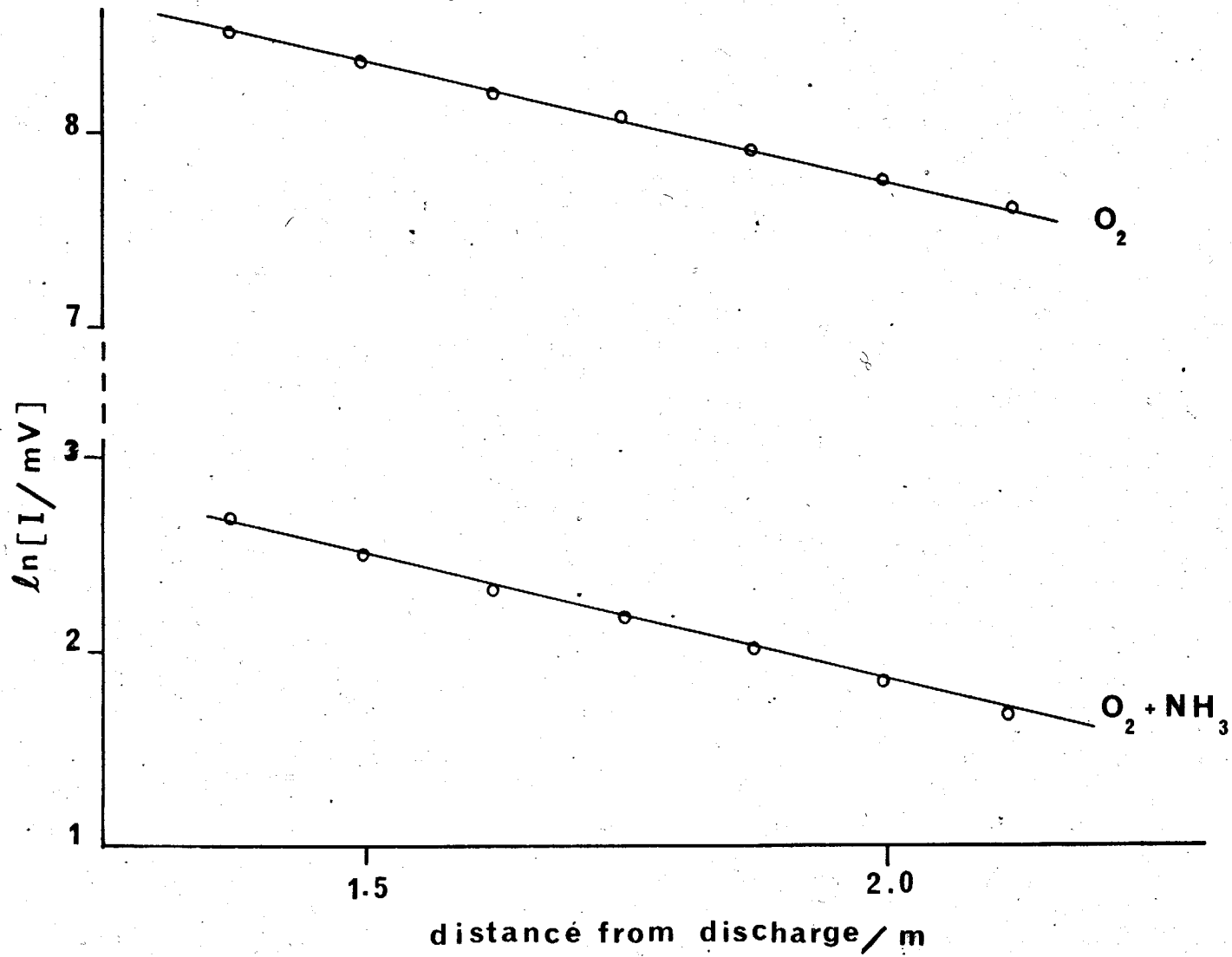

Table 5.1. Results for the Quenching of $O_2(^1\Delta_g)$ by M at 295 K

Run No.	P_1 /torr	LFV /ms^{-1}	$\Delta 2k_d^*/s^{-1}$	[M]/mol$dm^{-3}10^{-5}$
(a) M = NH_3				
R 1	5.88	1.70	0.17	1.64
RA 1	6.04	1.74		
R 2	6.58	1.52	0.21	1.85
RA 2	6.83	1.54		
R 3	5.42	1.84	0.16	1.50
RA 3	5.50	1.91		
R 4	4.88	2.04	0.14	1.35
RA 4	4.97	2.11		
(b) M = NO				
R 5	6.64	2.15	0.56	1.48
RA 5	5.46	1.92		
R 6	6.21	1.61	0.76	1.73
RA 6	6.37	1.65		
R 7	6.83	1.46	0.74	1.92
RA 7	7.08	1.48		
R 8	5.38	1.85	0.66	1.53
RA 8	5.63	1.86		
(c) M = HCl				
R 9	5.79	1.72	2.50	1.63
RA 9	5.96	1.76		
R 10	5.09	1.96	2.21	1.43
RA 10	5.22	2.01		
R 11	6.45	1.54	3.03	1.81
RA 11	6.62	1.58		
R 12	4.05	2.46	1.84	1.13
RA 12	4.14	2.54		

Figure 5.2 R.T. Quenching of $O_2(a^1\Delta_g)$ by M
M = NH_3, NO and HCl

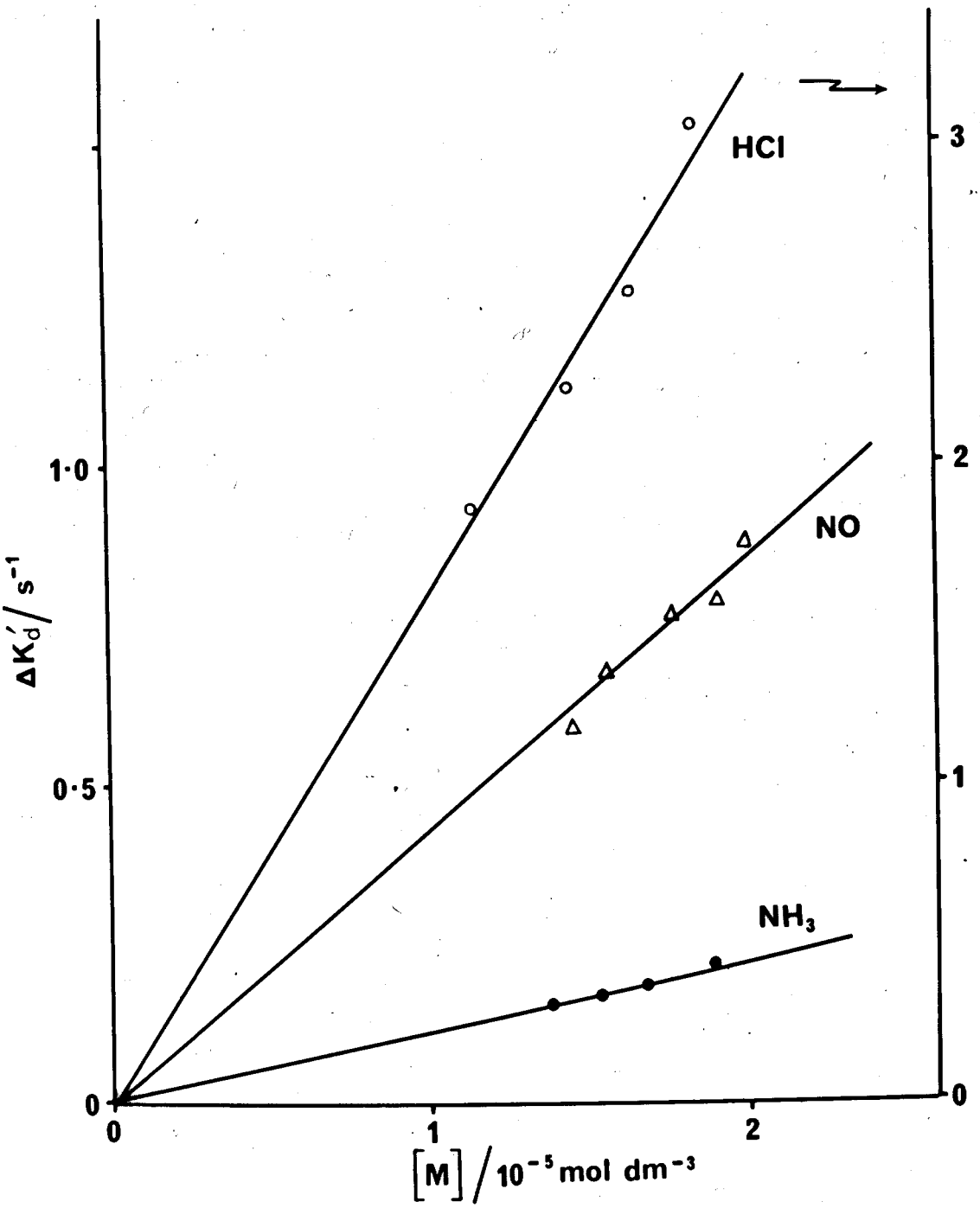

$$k_d^{NH_3}/dm^3\ mol^{-1}\ s^{-1} = (5.37 \pm 0.14) \times 10^3$$

$$k_d^{NO}/dm^3\ mol^{-1}\ s^{-1} = (2.10 \pm 0.28) \times 10^4$$

$$k_d^{HCl}/dm^3\ mol^{-1}\ s^{-1} = (8.00 \pm 0.34) \times 10^4.$$

The error limits are 2σ (95% confidence limits).

Experiments to measure the rate constant for quenching of $O_2(a^1\Delta_g)$ by SO_2 at room temperature were found to be unsuccessful as SO_2 proved to be a poor quencher of $O_2(a^1\Delta_g)$ at room temperature with a rate constant which was too slow to be measured directly in our system. However, at high temperature the quenching of $O_2(a^1\Delta_g)$ by SO_2 was measurable as its quenching rate increased with temperature. The high temperature data obtained for the rate constant was found to fit the Arrhenius equation (see figure 6.11). Hence, a value for the quenching rate constant at room temperature could be estimated by extrapolating the high temperature data. The extrapolated value is:

$$k_d^{SO_2}/dm^3\ mol^{-1}\ s^{-1} = 3 \times 10^3$$

5.2.4 Discussion

The values of the rate constants for quenching of $O_2(a^1\Delta_g)$ by NH_3, NO, HCl and SO_2 are listed in table 5.2 together with previous results. The value for NO agrees well with previous determinations, and that for NH_3 is similar to the estimate of Leiss et al.[70]. The new value for HCl shows that it is a better quencher than NO and NH_3, in keeping with its highly polar character. SO_2 is a poorer quencher, but still more efficient than quenchers like CO_2 and N_2O studied

Table 5.2. Rate Constants for the Quenching of $O_2(^1\Delta_g)$ at 295 K

Quencher, M	k_d^M/dm^{3}mol^{-1}s^{-1}	Ref.
NH_3	(5.37 0.14)x10^3	this work
	(2.65 0.28)x10^3	70
NO	(2.10 0.28)x10^4	this work
	(1.50 0.14)x10^4	67
	(2.7 0.9) x10^4	69
	2.7 x10^4	68
HCl	(8.00 0.34)x10^4	this work
SO_2	3 x10$^{3a)}$	this work

a) Extrapolated value.

previously[10,56] in this laboratory. Previous studies showed that their quenching rate constants at room temperature were too slow to be measured in our system. In contrast to SO_2 the quenching of $O_2(a^1\Delta_g)$ by N_2O and CO_2 was also unmeasurable at high temperatures. The room temperature rate constants reported for CO_2 and N_2O in the literature are 220 $dm^3\ mol^{-1}\ s^{-1}$ and 45 $dm^3\ mol^{-1}\ s^{-1}$ respectively[71,72].

5.3 Determination of the Room Temperature Rate constants for the Quenching of $O_2(b^1\Sigma_g^+)$ by NH_3, NO, HCl and SO_2.

5.3.1 Experimental

The quenching rate constant, k_q^M, was measured for M = NH_3, NO, HCl and SO_2. Experiments were performed at various mixture compositions in the pressure range of 3 - 12 torr and total flow rate of 28 mls^{-1} at STP.

The intensity ratios; ϕ_M and ϕ_o [see equation (4.29)] were measured by positioning the two photomultipliers opposite one another at the observation station. One was fitted with a 762 nm filter and the other with a 634 nm filter. For a steady flow of discharged oxygen at initial pressure of P_1 the first measurement was taken then the desired percentage of the additive, M, was introduced to the flowing oxygen gas and after the flow had restabilized the new pressure and emission intensities were noted. A series of experiments were performed for each quenching system by varying the pressure and the mole fraction of the additive, M, between 0 and 0.2.

5.3.2 Treatment of $O_2(b^1\Sigma_g^+)$ Room Temperature Results

In an oxygen/M mixture, M = NH_3, NO, HCl and SO_2, the quenching reactions are:

$$O_2(b^1\Sigma_g^+) + O_2 \xrightarrow{k_q^{O_2}} O_2(a^1\Delta_g) + O_2 \qquad (5.2)$$

$$O_2(b^1\Sigma_g^+) + M \xrightarrow{k_q^{M}} O_2(a^1\Delta_g) + M \qquad (4.20)$$

$$O_2(b^1\Sigma_g^+) + \text{Wall} \xrightarrow{k_W} O_2(a^1\Delta_g \text{ or } \chi^3\Sigma_g^-). \qquad (4.21)$$

It was shown in Chapter 4 (section 4.1.2) that by simultaneous measurement of emission intensities at 762 nm and 634 nm from $O_2(b^1\Sigma_g^+)$ and $O_2(a^1\Delta_g)$ in the presence and absence of added gas, M, a quenching rate constant for the additive could be determined from equation (4.29);

$$f(\phi_M,\phi_o) = \{(k_q^{O_2}[O_2] + k_W^o)(\phi_M - \phi_o)/\phi_o\} - (k_W - k_W^o)$$

$$= k_q^M[M] \qquad (4.29)$$

where $f(\phi_M,\phi_o)$ represents the ratio of emission intensities at 762 nm and 634 nm with and without the added gas, M. The wall constant in the absence of M, k_W^o, is determined from equation (4.30) given by Derwent and Thrush [65]. In this apparatus at 295 K equation (4.30) can be written as:

$$k_W = 1/(5.2 \times 10^{-3}\ P_1 + 1.16 \times 10^{-2}).\ [s^{-1}] \qquad (4.30)$$

where P_1 is the total pressure in torr.

The small correction in the presence of the quencher, $(k_W - k_W^o)$,

is considered to depend on the change in initial pressure, P_1, where the mole fraction, $x_M < 0.2$. The rate constant for the quenching by oxygen, $k_q^{O_2}$, at this temperature is taken as 1×10^5 dm^3 mol^{-1} s^{-1} in our system (see discussion, 5.3.4). Therefore, k_q^M can be determined from equation (4.29) for a set of measured values of ϕ_M and ϕ_o at known [M].

For M = NH_3, figure 5.3 shows a plot of $f(\phi_{NH_3},\phi_o)$ against concentration of NH_3 at various mixture compositions. The range was obtained by varying the pressure and the mole fraction of NH_3 between 0 and 0.1; each point was obtained by measuing ϕ_{NH_3} and ϕ_o at a single point in the tube. The plot is linear passing through the origin so the slope gives the rate constant, $k_q^{NH_3}$, for the quenching of $O_2(b^1\Sigma_g^+)$ by NH_3 directly.

5.3.3 Results

The results of the experiments performed with M = NH_3, NO, HCl and SO_2 are listed in tables 5.3 - 5.6. Figures 5.3 - 5.6 show plots of $f(\phi_M,\phi_o)$ against concentration of quencher M [equation (4.29)]. The slope of each line gives the rate constant, k_q^M for the quenching of $O_2(b^1\Sigma_g^+)$ by each gas. The results obtained by least squares are:

$$k_q^{NH_3}/dm^3\ mol^{-1}\ s^{-1} = (7.05 \pm 0.10) \times 10^8$$

$$k_q^{NO}/dm^3\ mol^{-1}\ s^{-1} = (1.70 \pm 0.13) \times 10^7$$

$$k_q^{HCl}/dm^3\ mol^{-1}\ s^{-1} = (1.60 \pm 0.20) \times 10^7$$

$$k_q^{SO_2}/dm^3\ mol^{-1}\ s^{-1} = (2.50 \pm 0.50) \times 10^5.$$

The error limits are 2σ (95% confidence limits).

Table 5.3. Results for the Quenching of $O_2(b^1\Sigma_g^+)$ by NH_3 at 295 K

(a) 3% NH_3, 97% O_2

Expt. No. R1

P_1/torr	$\Phi_{NH_3}/10^{-1}$	$\Phi_{O_2}/10^{-3}$	$f(\Phi_{NH_3}, \Phi_{O_2})/s^{-1}10^4$	$[NH_3]$/moldm^{-3} 10^{-5}
4.30	2.66	2.94	0.47	0.72
4.33				
4.88	2.63	2.86	0.49	0.80
4.92				
5.63	2.88	2.92	0.54	0.93
5.71				
6.62	3.60	3.04	0.68	1.09
6.66				
7.03	3.64	3.07	0.70	1.16
7.12				
7.53	3.89	3.04	0.77	1.24
7.61				
8.07	4.00	2.98	0.83	1.33
8.15				
8.81	4.54	3.18	0.96	1.46
8.94				
9.93	4.67	3.24	1.00	1.64
10.06				
11.38	5.00	2.45	1.54	1.88
11.55				

Table 5.3 continued

P_1/torr	$\Phi_{NH_3}/10^{-1}$	$\Phi_{O_2}/10^{-3}$	$f(\Phi_{NH_3}, \Phi_{O_2})/s^{-1}10^4$	$[NH_3]$/moldm$^{-3}10^{-5}$
10.26	5.00	2.21	1.61	1.70
10.35				
9.36	5.56	2.54	1.47	1.54
9.44				

(b) 5% NH_3, 95% NH_3

Expt. No. R2

4.77	5.50	3.04	0.95	1.23
4.51				
4.92	5.67	3.03	0.99	1.35
4.97				
5.42	6.25	2.94	1.16	1.51
5.54				
5.79	6.00	2.90	1.14	1.60
5.88				
6.37	6.40	2.91	1.24	1.78
6.54				
6.66	6.52	1.25	1.25	1.85
6.79				

Table 5.3 continued

P_1 torr	$\Phi_{NH_3}/10^{-1}$	$\Phi_{O_2}/10^{-3}$	$f(\Phi_{NH_3}, \Phi_{O_2})/s^{-1}10^4$	$[NH_3]$/mol $dm^{-3}10^{-5}$
7.03	7.78	2.98	1.53	1.96
7.20				
7.66	8.57	2.86	1.82	2.13
7.82				
8.32	8.33	3.02	1.74	2.32
8.52				
9.23	10.00	3.05	2.19	2.58
9.48				

(c) 7% NH_3, 93% O_2

Expt. No. R3

4.01	6.67	2.82	1.24	1.56
4.10				
5.59	7.50	2.53	1.62	2.19
5.75				
6.33	7.89	2.61	1.71	2.49
6.54				
7.41	8.57	2.55	2.02	2.92
7.66				
8.48	8.00	2.62	1.95	2.32
8.43				
9.06	10.00	2.40	2.75	3.56
9.35				

Figure 5.3 R.T. Quenching of $O_2(b^1\Sigma_g^+)$ by NH_3

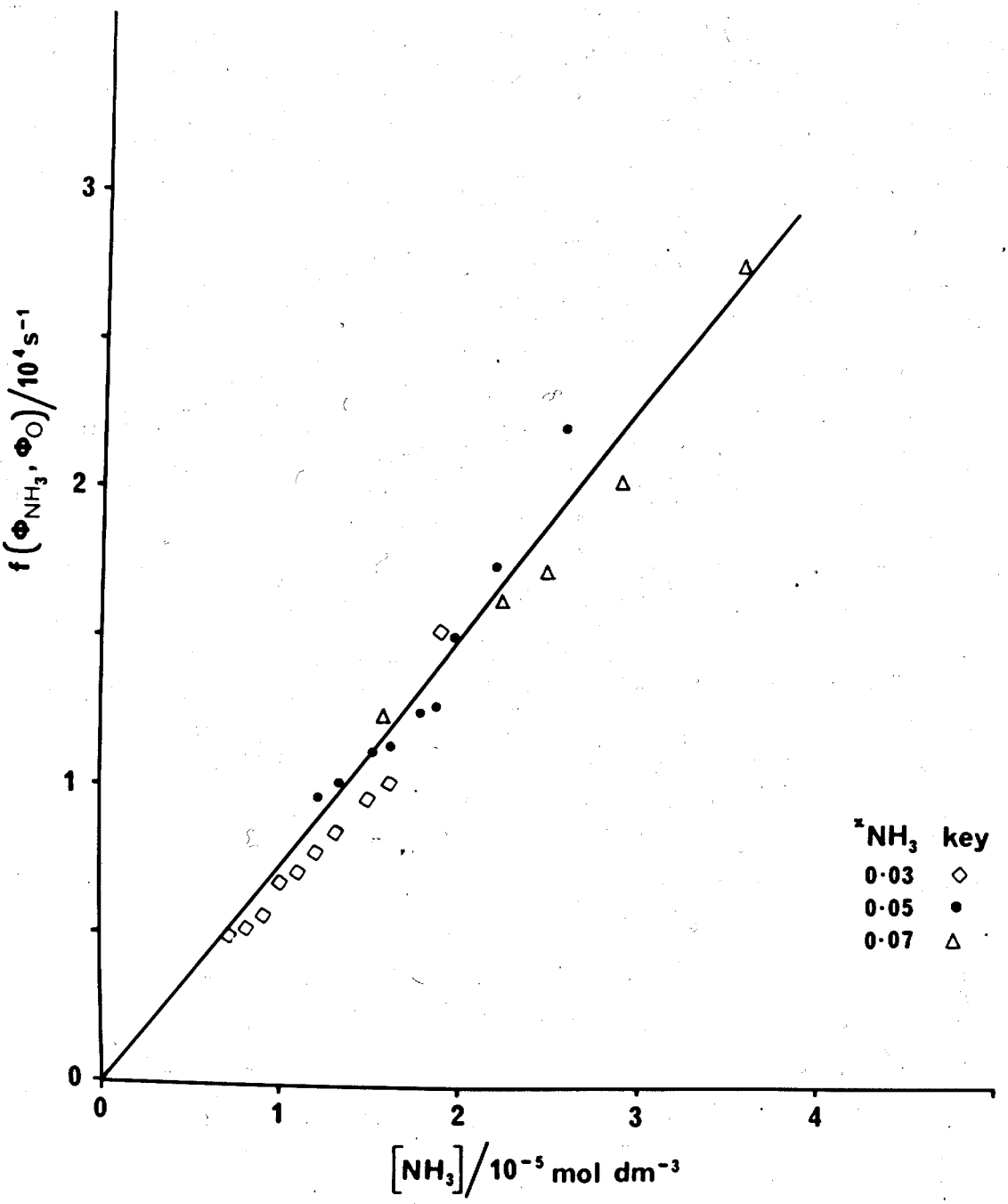

Table 5.4. Results of the Quenching of $O_2(b^1\Sigma_g^+)$ by NO at 295 K

(a) 3% NO, 97% O_2

Expt. No. R4

P_1/torr	$\Phi_{NO}/10^{-3}$	$\Phi_{O_2}/10^{-3}$	$f(\Phi_{NO}, \Phi_{O_2})/s^{-1}10^2$	$[NO]/moldm^{-3}10^{-5}$
4.22	14.52	4.34	1.24	0.71
4.30				
4.39	14.70	4.30	1.28	0.73
4.47				
4.88	15.73	4.36	1.40	0.82
4.97				
5.30	16.28	4.42	1.46	0.87
5.30				
5.63	16.35	4.40	1.50	0.94
5.71				
5.96	17.76	4.50	1.65	0.99
6.08				
6.25	17.14	4.45	1.62	1.03
6.29				
6.70	18.91	4.57	1.83	1.12
6.83				
7.37	19.82	4.57	2.01	1.22
7.45				

Table 5.4 continued

P_1/torr	$\Phi_{NO}/10^{-3}$	$\Phi_{O_2}/10^{-3}$	$f(\Phi_{NO}, \Phi_{O_2})s^{-1}10^2$	$[NO]/moldm^{-3}10^{-5}$
7.95	21.43	4.68	2.23	1.33
9.11				
8.57	22.83	4.72	2.48	1.44
8.77				
9.06	23.30	4.78	2.58	1.51
9.23				
10.26	26.41	4.82	3.20	1.72
10.51				
(b) 5% NO, 95% O_2				
Expt. No. R5				
4.97	22.26	4.17	2.33	1.37
5.05				
5.30	23.62	4.32	2.43	1.48
5.46				
5.88	25.00	4.28	2.69	1.64
6.04				
6.62	26.88	4.32	3.02	1.86
6.87				
7.04	26.00	4.35	2.94	1.97
7.28				
7.53	29.00	4.44	3.37	2.08
7.70				

Table 5.4 continued

P_1 torr	$\Phi_{NO}/10^{-3}$	$\Phi_{O_2}/10^{-3}$	$f(\Phi_{NO}, \Phi_{O_2})/s^{-1}10^2$	$[NO]/moldm^{-3}10^{-5}$
8.28 8.53	32.88	4.47	4.02	2.31
8.53 8.86	32.81	4.56	3.96	2.40
9.02 9.23	33.33	4.37	4.38	2.51
9.19 9.52	34.10	4.59	4.29	2.58
9.65 10.02	38.71	4.61	5.08	2.71
10.18 10.51	40.00	4.65	5.37	2.85
11.51 11.75	44.44	4.75	6.37	3.18
4.06 4.22	20.70	4.16	2.09	1.14

Figure 5.4 R.T. Quenching of $O_2(b\,^1\Sigma_g^+)$ by NO

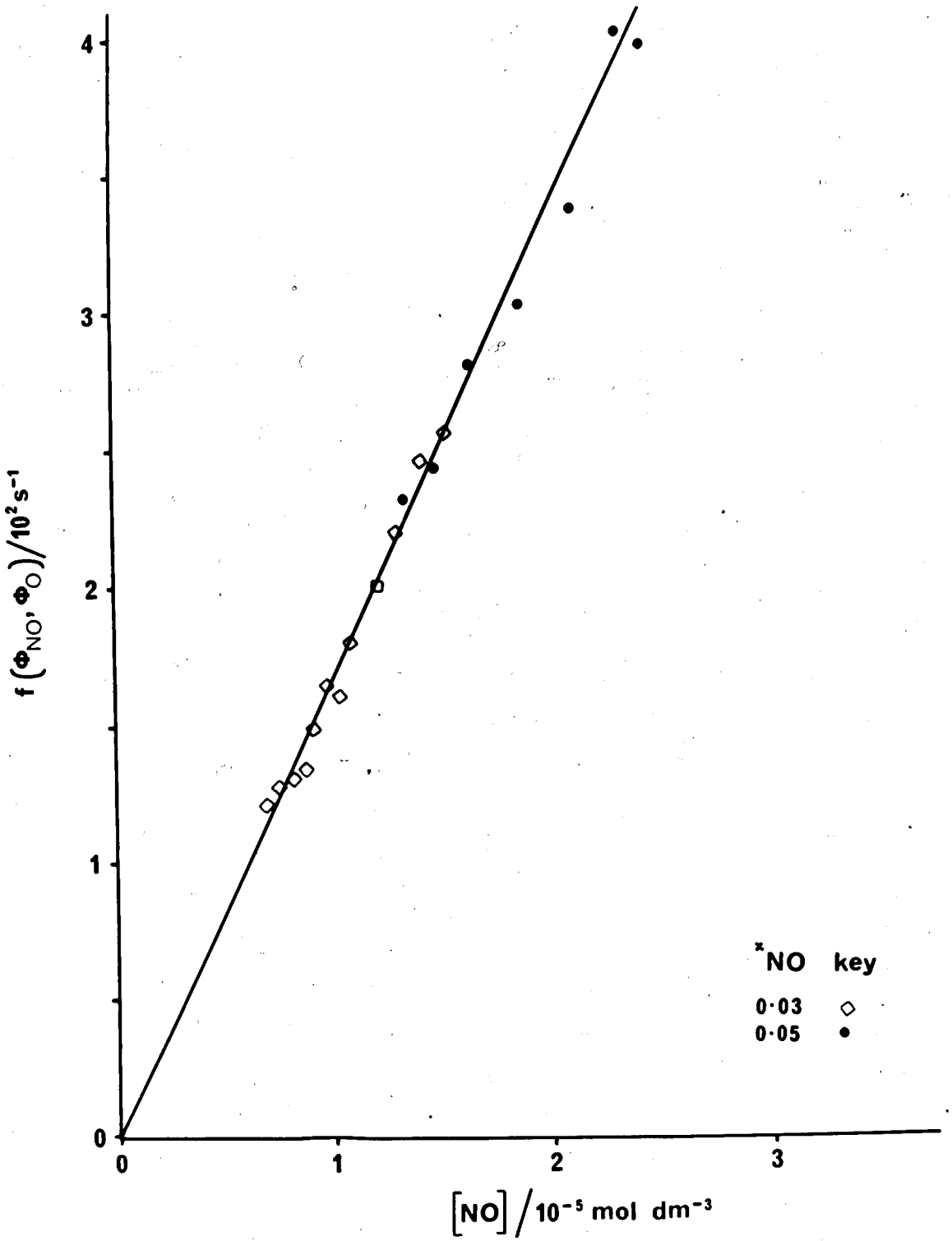

Table 5.5. Results for the Quenching of $O_2(b^1\Sigma_g^+)$ by HCl at 295 K

(a) 3% HCl, 97% O_2

Expt. No. R6

P_1/torr	$\Phi_{HCl}/10^{-3}$	$\Phi_{O_2}/10^{-3}$	$f(\Phi_{HCl}, \Phi_{O_2})/s^{-1}10^2$	[HCl]/moldm$^{-3}10^{-5}$
4.26 4.34	12.28	3.94	1.12	0.71
4.76 4.80	12.77	3.98	1.18	0.79
5.25 5.30	13.68	4.00	1.32	0.87
5.71 5.84	14.50	3.97	1.47	0.96
6.37 6.45	15.58	4.16	1.57	1.06
6.87 6.95	16.41	4.34	1.63	1.14
7.38 7.50	17.62	4.38	1.82	1.23
7.95 8.07	18.63	4.63	1.89	1.32
8.48 8.61	20.10	4.71	2.10	1.41

Table 5.5 continued

P_1/torr	$\Phi_{HCl}/10^{-3}$	$\Phi_{O_2}/10^{-3}$	$f(\Phi_{HCl}, \Phi_{O_2})/s^{-1}10^2$	$[HCl]/moldm^{-3}10^{-5}$
10.22	25.33	5.34	2.67	1.71
10.43				
9.39	22.78	5.07	2.37	1.55
9.48				
(b) 5% HCl, 95% O_2				
4.43	22.38	4.36	2.20	1.24
4.55				
3.89	17.30	4.21	1.65	1.11
4.06				
4.92	19.56	4.45	1.84	1.39
5.09				
(c) 7% HCl, 93% O_2				
Expt. No. R7				
4.84	28.00	4.97	2.49	1.92
5.01				
5.38	31.64	5.10	2.85	2.11
5.51				

Table 5.5 continued

P_1/torr	$\Phi_{HCl}/10^{-3}$	$\Phi_{O_2}/10^{-3}$	$f(\Phi_{HCl}, \Phi_{O_2})/s^{-1}10^2$	$[HCl]/moldm^{-3}10^{-5}$
5.88 6.08	35.62	5.15	3.31	2.73
6.74 6.87	40.73	5.07	4.10	2.63
7.04 7.28	42.12	5.17	4.23	2.79
7.41 7.70	45.11	4.88	4.98	2.95
7.74 8.07	44.66	5.03	4.86	3.09
8.36 8.69	45.40	4.95	5.22	3.22
9.35 9.68	52.83	5.46	5.88	3.71
10.10 10.51	51-25	5.00	6.57	4.03

Table 5.5 continued

P_1/torr	$\Phi_{HCl}/10^{-3}$	$\Phi_{O_2}/10^{-3}$	$f(\Phi_{HCl}, \Phi_{O_2})/s^{-1}10^{2}$	$[HCl]/mol\,dm^{-3}10^{-5}$
(d) 9% HCl, 91% O_2				
Expt. No. R8				
4.05	32.79	4.61	3.23	2.08
4.22				
4.43	32.54	4.50	3.31	2.26
4.59				
5.05	36.94	4.52	3.88	2.59
5.25				
6.66	45.04	4.34	5.44	3.42
6.95				
5.51	39.26	4.32	4.45	2.81
5.71				
7.32	48.72	4.66	5.96	3.77
7.66				

Figure 5.5 R.T. Quenching of $O_2(b^1\Sigma_g^+)$ by HCl

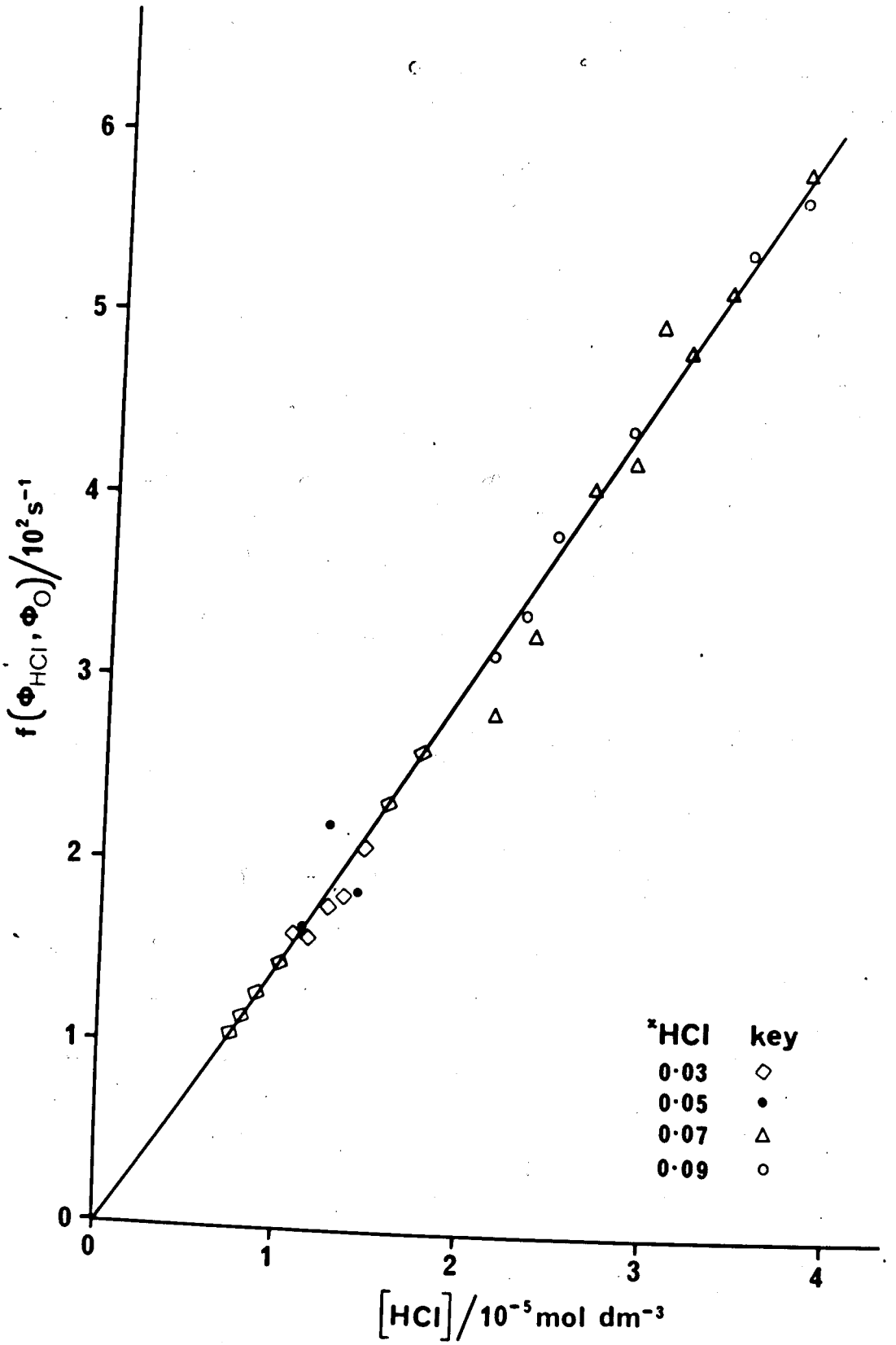

Table 5.6. Results for Quenching of $O_2(b^1\Sigma_g^+)$ by SO_2 at 295 K

(a) 10% SO_2, 90% O_2

Expt. No. R9

P_1/torr	$\Phi_{SO_2}/10^{-3}$	$\Phi_{O_2}/10^{-3}$	$f(\Phi_{SO_2}, \Phi_{O_2})/s^{-1}10$	$[SO_2]$/moldm$^{-3}10^{-5}$
4.38 4.63	6.53	5.55	1.04	2.52
5.30 5.71	6.56	5.64	1.02	3.11
5.67 6.04	6.59	5.68	0.99	3.29
6.37 6.83	6.84	5.77	1.17	3.71
7.16 7.74	6.92	5.84	1.21	4.21
7.70 8.12	7.02	5.89	1.28	4.52
8.03 8.73	7.06	5.92	1.32	4.75
8.53 9.19	7.21	6.04	1.31	5.00
8.82 9.56	7.32	6.09	1.42	5.20
9.11 10.22	7.43	6.13	1.57	5.56

Table 5.6 continued

(b) 15% SO_2, 85% O_2

Expt. No. R10

P_1/torr	$\Phi_{SO_2}/10^{-3}$	$\Phi_{O_2}/10^{-3}$	$f(\Phi_{SO_2}, \Phi O_2)/s^{-1}10$	$[SO_2]$/moldm$^{-3}10^{-5}$
5.13 5.64	6.54	5.69	0.97	4.59
5.42 5.96	6.57	5.55	1.16	4.86
5.84 6.45	6.68	5.60	1.24	5.26
6.30 6.95	6.78	5.62	1.33	5.67
6.62 7.49	6.94	5.68	1.46	6.11
7.12 8.03	7.04	5.77	1.49	6.55
7.49 8.48	7.15	5.83	1.55	6.92
7.82 8.81	7.17	5.86	1.54	7.19
8.23 9.27	7.25	5.94	1.56	7.56
8.77 9.76	7.45	5.89	1.86	7.97

Table 5.6 continued

(c) 20% SO_2. 80% O_2

Expt. No. R11

P_1/torr	$\Phi_{SO_2}/10^{-3}$	$\Phi_{O_2}/10^{-3}$	$f(\Phi_{SO_2}, \Phi_{O_2})/s^{-1}10$	$[SO_2]$ /moldm$^{-3}10^{-5}$
4.47 4.92	6.54	5.44	1.26	5.36
4.88 5.34	6.55	5.51	1.18	5.81
5.30 6.04	6.75	5.51	1.45	6.57
5.79 6.62	6.80	5.56	1.46	7.21
6.21 7.20	7.00	5.61	1.64	7.83
6.62 7.78	7.15	5.60	1.85	8.46
7.28 8.61	7.40	5.71	2.01	9.36
3.64 3.81	6.42	5.57	0.90	4.14
4.38 4.72	6.53	5.56	1.06	5.13

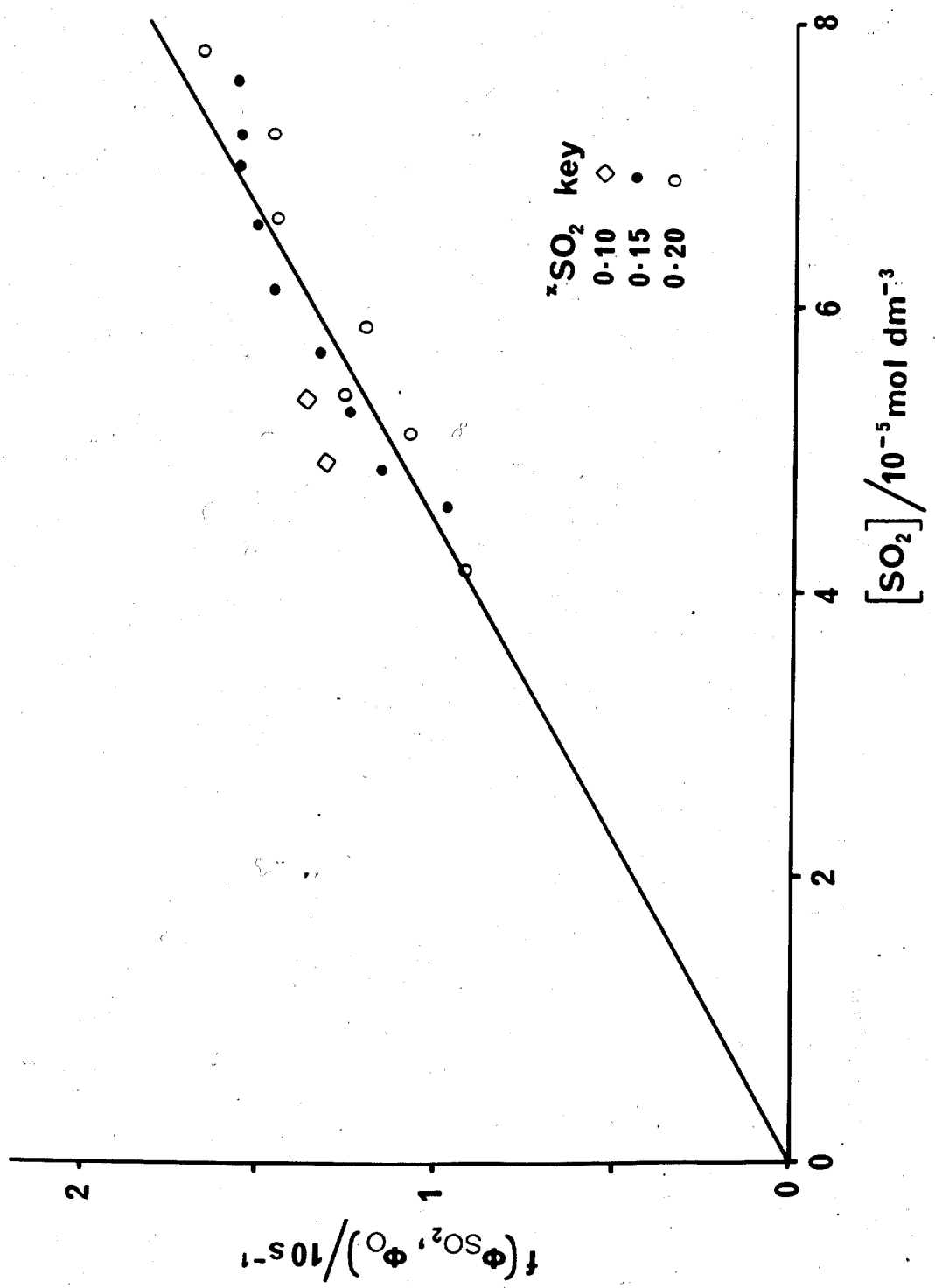

Figure 5.6 R.T. Quenching of $O_2(a\,^1\Sigma_g^+)$ by SO_2

5.3.4 Discussion

The values of the rate constants for quenching of $O_2(b^1\Sigma_g^+)$ by NH_3, NO, HCl and SO_2 are listed in table 5.7 together with previous results. The measurements all rely on the value taken for quenching by oxygen itself, which is estimated by Pedley[59] to be 1×10^5 dm^3 mol^{-1} s^{-1} in our apparatus. This can be compared with a value of 2.6×10^4 dm^3 mol^{-1} s^{-1} reported by Thomas and Thrush[73] for a completely water free system. Considering that the best value[74] reported for the quenching of $O_2(b^1\Sigma_g^+)$ by water is 2.4×10^9 dm^3 mol^{-1} s^{-1}, indicates that the water vapour content in our apparatus is $\sim$ 30 ppm despite drying the gases used and thorough pumping prior to each experiment. Having $\sim$ 30 ppm water vapour in our system does not seem unreasonable considering the large volume of the apparatus and that it is frequently opened to the atmosphere for cleaning. Therefore, we cannot use the value reported by Thomas and Thrush since it is not possible in our system to take the extreme precautions for drying the oxygen gas that they used. Also treating the data with higher and lower values of $k_q^{O_2}$ led to curvature and inconsistencies between mixtures of different composition and only the value of 1.0×10^5 dm^3 mol^{-1} s^{-1} for $k_q^{O_2}$ gave consistent results and the straight lines passing through the origin.

It can be seen (table 5.7) that the results for NH_3 and NO are in broad agreement with the previous work, although they tend to be lower than the earlier values. This can be expected since in our apparatus the observations are made a long way from the discharge, and hence are probably freer from extraneous interference.

The values for HCl and SO_2 are much lower than previous estimates. SO_2 is a poor quencher, and so any measurement is likely

Table 5.7. Rate Constants for the Quenching of $O_2(b^1\Sigma_g^+)$ at 295 K

Quencher, M	$k_q^M/dm^3 mol^{-1} s^{-1}$	Ref.
NH_3	$(7.05 \pm 0.10) \times 10^8$	this work
	$(1.00 \pm 0.12) \times 10^9$	30
	$(1.20 \pm 0.30) \times 10^9$	77
	$(1.81 \pm 0.30) \times 10^9$	75
	1.3×10^9	48
	1.1×10^9	69
	5.2×10^7	76
NO	$(1.70 \pm 0.13) \times 10^7$	this work
	2.4×10^7	75
	3.3×10^7	69
	2.5×10^7	76
	0.93×10^7 b)	50
HCl	$(1.60 \pm 0.20) \times 10^7$	this work
	$(7.8 \pm 2.4) \times 10^7$	30
	$(4.4 \pm 1.0) \times 10^7$	77
	$(4.0 \pm 2.0) \times 10^7$	78
	5.3×10^6 b)	50
SO_2	$(2.50 \pm 0.50) \times 10^5$	this work
	$(1.80 \pm 0.60) \times 10^6$	75
	4.0×10^5 b)	49

b) Calculated value

to be increased by impurity effects. HCl is an awkward gas to handle and to be sure of its concentration. However, in this study three different mixture compositions were examined and as figure 5.5 shows the results are well consistent for the various mixtures. These various considerations together with the good results obtained for quenching of $O_2(b^1\Sigma_g^+)$ by CO_2 and N_2O, studied previously in this laboratory[10,56], indicate that in our apparatus reliable results are obtained.

Braithwaite et al.[50] have calculated rate constants for a number of quenchers by considering long range forces. While quite good agreement with experiment was obtained for HD, D_2, CO and N_2, the values, given in table 5.7, were lower for NO and HCl than the best experimental estimates. It is interesting to see how near the present results are to their predicted values. Kear and Abrahamson[49] calculated a value for the quenching of $O_2(b^1\Sigma_g^+)$ by SO_2 using a model based on short range forces, the present experimental value is also close to their prediction. These theoretical approaches are outlined in Chapter 7 and have been discussed in relation to the high temperature results obtained in this work which at present seem to offer a better understanding of these energy transfer processes.

5.4 Conclusion

The linearity of the plots obtained for both $O_2(a^1\Delta_g)$ and $O_2(b^1\Sigma_g^+)$ indicate that the room temperature conditions in the present apparatus are stable and reliable results are obtained for the quenching rate constants. The fact that the plots are linear show that the mercury surface is an effective way of removing atomic

oxygen from the discharged products across the pressure range used.

The comparison of the results obtained with those reported previously has shown that the agreement is good. This provides additional conformation for the value of $k_q^{O_2}$ in our apparatus and hence the estimated water vapour content.

CHAPTER SIX

6 High Temperature Studies of the Collisional Quenching of $O_2(a^1\Delta_g)$ and $O_2(b^1\Sigma_g^+)$

6.1 Introduction

It has been suggested[49] that vibrational excitation of the quencher is important in the quenching mechanism of $O_2(a^1\Delta_g)$ and $O_2(b^1\Sigma_g^+)$, and that evidence for such electronic to vibrational energy transfer could come from the relative magnitude of the quenching rate constants with various quenchers. The theoretical approaches for calculating the rates, consider either short[49] or long[50] range interactions. Although some success has been achieved with these approaches, a comparison of the two theories with the experimental values reported is not satisfactory, nor can the temperature dependence of the rate constants be easily predicted.

The present study was undertaken to provide experimental data on the temperature dependence of the quenching reactions of $O_2(a^1\Delta_g)$ and $O_2(b^1\Sigma_g^+)$ with various quenchers since the high temperature behaviour may indicate the nature of the interactions which lead to energy transfer.

The range of quenching rate constant which can be measured in the present apparatus is 10^5-10^9 dm^3 mol^{-1} s^{-1}, where the lower limit is determined by the maximum hot-flow time which can be recorded and the upper limit by the shortest relaxation time that can be followed (section 6.4). This in combination with practical considerations such as toxicity, chemical reactivity and stability limits the choice of quenchers which can be studied in this apparatus.

The collisional deactivation of $O_2(b^1\Sigma_g^+)$ by CO_2, N_2O, N_2, O_2 and Ar has been examined[56] before in this laboratory. For both O_2 and N_2 the rate constants increased with temperature but neither set of results could be fitted to Arrhenius or Landau-Teller[8] temperature dependence. However, for quenchers N_2O and CO_2 the rate constants were found to fall with an increase in temperature. For Ar the reaction rate increased too slowly to be measured in our apparatus. In these experiments it was also found that the temperature dependence of the rate constants for quenching of $O_2(a^1\Delta_g)$ by these gases is too small and could not have been measured within the time scale of the experiments.

These previous studies seem to suggest that the quenchers of $O_2(b^1\Sigma_g^+)$ can be classified into two groups; poor quencher at room temperature which display an increase of rate constant with temperature, and more efficient quenchers for which the rate constant decreases at high temperatures.

The quenchers studied in this work; NH_3, NO, HCl, SO_2, were chosen systematically and in view of the previously examined quenchers where different temperature dependences for quenching were observed.

It seemed worthwhile to study NH_3 which is a still more efficient quencher at room temperature but for which Kohse-Hoighaus[30] have reported a slight positive temperature dependence of the rate constant between 210-350 K. Thereafter, it was decided to extend the work to moderate quenchers; NO, HCl and finally to SO_2 which is a poor quencher of $O_2(b^1\Sigma_g^+)$ at room temperature. In the course of these studies it was found that there was an appreciable deactivation of $O_2(a^1\Delta_g)$ at high temperatures and that we were able to measure the rate constants for the quenching of $O_2(a^1\Delta_g)$ by NO, HCl and SO_2.

The two species, $O_2(a^1\Delta_g)$ and $O_2(b^1\Sigma_g^+)$, show quite different temperature dependences for quenching; the rate constants for $O_2(a^1\Delta_g)$ are Arrhenius in form, while those for $O_2(b^1\Sigma_g^+)$ either decrease or are independent of temperature and fit with the previous results for other quenchers (Chapter 7).

The determination of the results for $O_2(a^1\Delta_g)$ and $O_2(b^1\Sigma_g^+)$ are described separately in this chapter. The results obtained are discussed in the next chapter.

6.2 Experimental

The temperature dependence of the rate constants for the quenching of $O_2(a^1\Delta_g)$ and $O_2(b^1\Sigma_g^+)$ by NH_3, NO, HCl and SO_2 are measured between 600 K and 1200 K using the discharge flow/shock tube system. The operational procedure is as described in Chapter 2.

In this apparatus two emission traces are recorded for any one shock. For these experiments the emissions monitored were at two wavelengths, 762 nm and 634 nm. Before each shock the change in concentration of $O_2(a^1\Delta_g)$ along the tube was measured using the movable photomultiplier. Experiments were performed at various mixture compositions with total flow rate of 28 mls^{-1} giving a total pressure of 6 torr ($\sim$ 800 Pa) and linear flow velocity of $\sim$ 1.6 ms^{-1}.

6.3 Treatment of $O_2(a^1\Delta_g)$ High Temperature Results

As described in Chapter 4 data on the collisional quenching of $O_2(a^1\Delta_g)$ by various quenchers can be obtained either from the high temperature behaviour of the emission at 634 nm or 762 nm. The behaviour of the 634 nm emission is described below, that of the 762 nm emission in the next section.

As shown in Chapter 4 the emission trace displays the main three zones that were predicted by the developed kinetic model given by equation (4.45).

$$^{634}I_{t_p} = {}^{634}K\,{}^{634}I_{psg}\,\rho_{21}^{2}\,T_{21}^{\frac{1}{2}}\int_{t_p-t_s}^{t_p}[\exp(-2k_d^M[M]-\alpha_t)t_p]dt_p/t_s. \qquad (4.45)$$

Analysis by computer graphics (Chapter 4) yields values for the integration time, t_s, the enhancement factor, ^{634}K, and the post-shock decay constant, α_t. It is from the decay zone that the overall quenching rate constant, k_d^M is obtained for the quenching of $O_2(a^1\Delta_g)$ provided that the post-shock decay constant obtained by the fitting, α_t, is greater than that measured in the pre-shock flow, α_L, which has been suitably corrected for the shock compression. Thus, k_d^M, the pseudo first order rate constant for quenching of $O_2(a^1\Delta_g)$ is obtained from the difference in decay given by:

$$k_d^M = (\alpha_t-\alpha_L)/\rho_{21} \qquad [s^{-1}] \qquad (6.1)$$

The overall rate constant, k_d^M, is related to the quenching rate constants of the gases present in the system by:

$$k_d^M = [k_d^{O_2}(1-x) + k_d^{NO}x]\rho_2 \qquad [s^{-1}] \qquad (6.2)$$

Here, for example, the system under study is a mixture of oxygen and nitric oxide and x is the mole fraction of nitric oxide.

Previous studies[15] have shown that $k_d^{O_2}$ is too small to measure under the shock conditions and can be neglected hence the value of k_d^{NO} is simply given by:

$$k_d^{NO} = k_d^M/\rho_2 x \qquad [dm^3\ mol^{-1}\ s^{-1}] \qquad (6.3)$$

If the post-shock decay constant, α_t, is found to be the same as that measured in the pre-shock, α_L, then the quenching of $O_2(a^1\Delta_g)$ at the shock temperature is not large enough to be measured and shock traces are analysed by equation (4.46) as described in Chapter 4.

$$^{634}I_{t_p} = {}^{634}K \; {}^{634}I_{psg} \; \rho_{21}^2 \; T_{21}^{\frac{1}{2}} \int_{t_p - t_s}^{t_p} \exp(-\alpha_t t_p) dt_p / t_s . \qquad (4.46)$$

The fit for each run gives values of α_t, ^{634}K, and t_s.

In this work NH_3 results are analysed using equation (4.46) and those for NO, HCl and SO_2 using equation (4.45).

6.3.1 Results

(a) NH_3

A series of shocks into mixtures containing 3, 5 and 7% NH_3 were carried out. The run parameters are listed in Appendix 1. Figure 6.1a shows a typical high temperature emission trace at 634 nm from a mixture containing NH_3. The three regions expected can be seen; the steady pre-shock glow, the rapid rise at the shock front and the decay. The traces were analysed using equation (4.46) by interactive computer graphics as described in Chapter 4. An example of the fit is shown by the full line in figure 6.2. The results obtained, α_t, ^{634}K and t_s, are listed in table 6.1.

The post-shock decay constant, α_t, given by the fitting is compared with the value predicted from the pre-shock measurement of the concentration gradient along the tube, α_L, and is found to be similar (table 6.1). The similarity of pre- and post-shock decay rates indicate that there is no appreciable deactivation of

Figure 6.1 Traces of the Shock Emission.

R 209, NH_3 / O_2

a_ 634 nm

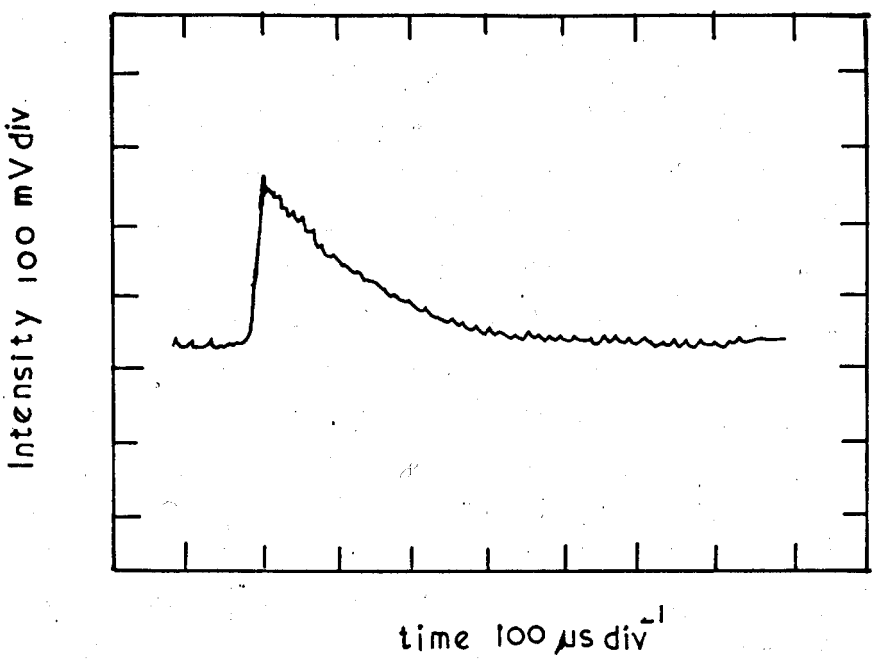

b_ 762 nm (RA 209)

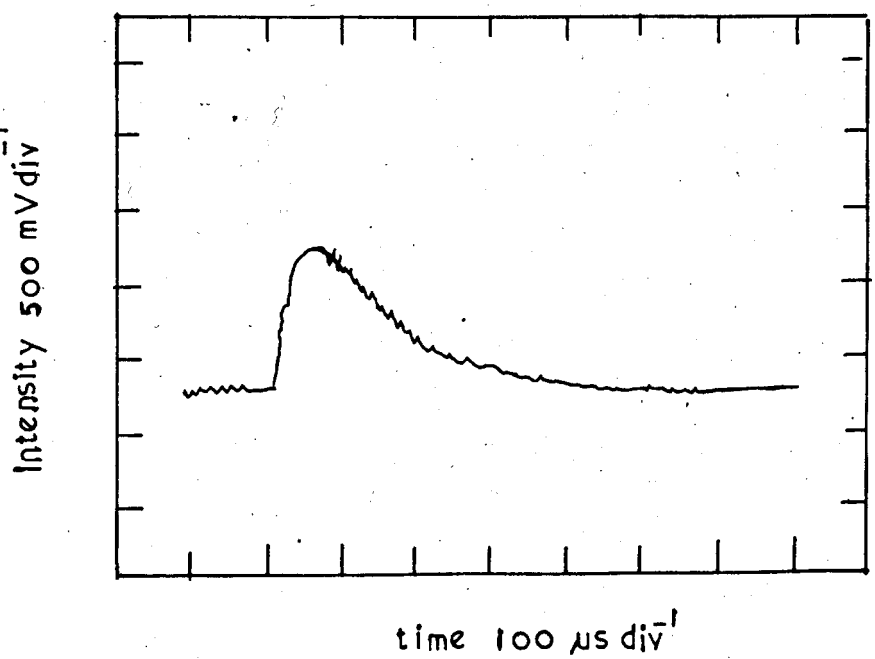

Note: no base lines indicated.

RESULTS

fitted	Ratio (K)	: 1.0930E+00	
	err.	: 2.3103E-01	
fitted	Decay Constant	:-3.0000E-03	us-1
		:-7.0958E-03	cm-1
	err.	: 4.7341E-01	
	(Pre-shock decay	: 3.0863E-03	us-1)
fitted	Integration Time	: 1.0179E+01	us
	err.	: 1.4537E+00	

RUN DATA

Oxygen	: 97.000	%
NH3	: 3.000	%
Shock Speed	: 1.147	mm us-1
Initial Pressure	: 6.790	torr
P21	: 14.410	
Initial Temperature	: 294.000	K
T2	: 901.000	K
Density Ratio, R021	: 4.686	
Xzero	: 89.400	us
Yzero	: 100.452	mV
Decay*1000	: 7.300	cm-1
Pre-shock glow, PSG	: 6.800	mV
Afterglow	: 261.398	mV

FITTING :NAG : incomplete.
Iterations: 1 : 540 points.
Sum of the Squares : 5.6184E+05

* * *

Figure 6.2 A fitted shock trace for O_2/NH_3 at 634 nm emission

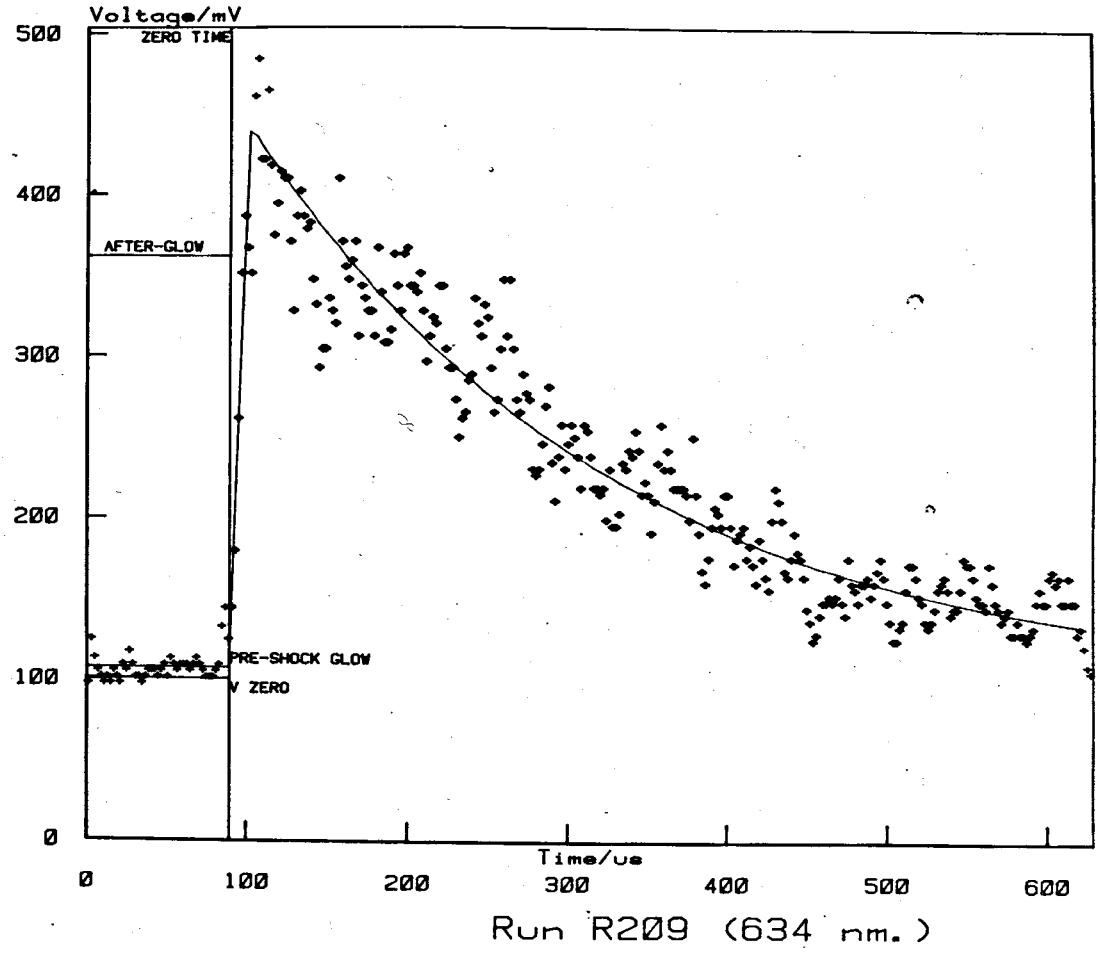

Table 6.1. Analysis of 634 nm Emission Traces, NH_3 Results

Run No.	T_2 /K	^{634}K	α_t /$\mu s^{-1} 10^{-3}$	α_L /$\mu s^{-1} 10^{-3}$	t_s /μs
		3% NH_3. 97% O_2			
R216	602	1.11	2.30	2.35	27
R213	699	0.87	2.60	2.70	18
R212	732	1.02	2.30	2.20	20
R211	876	1.26	3.40	3.30	15
R210	883	1.11	3.30	3.20	9
R209	901	1.09	3.00	3.08	10
R208	998	1.17	4.10	4.00	8
R214	1031	1.12	3.80	3.70	15
R215	1135	1.75	3.20	3.10	11
		5% NH_3, 95% O_2			
R224	754	1.27	2.30	2.20	16
R225	846	1.32	2.60	2.50	20
R226	906	1.32	2.60	2.60	18
R206	1039	1.38	3.00	2.90	12
R207	1114	1.65	2.90	3.00	10
		7% NH_3, 93% O_2			
R220	747	1.13	2.30	2.40	14
R219	833	1.32	2.60	2.50	11
R218	883	1.37	3.00	3.11	12
R217	956	1.37	2.90	3.00	14

$O_2(a^1\Delta_g)$ by NH_3 at high temperatures within the timescale of our experiment ($\sim$ 400 μs). In this respect NH_3 is similar in quenching behaviour to CO_2, N_2O, N_2 and O_2 studied previously in this laboratory.

(b) NO

A series of shocks into mixtures containing 3, 5, 8% NO were performed. The run parameters are listed in Appendix 2. Figure 6.3a shows a typical 634 nm emission trace. It displays the expected shape; the steady pre-shock glow, the rapid rise at the shock front and the fall in emission, which in the earlier study (i.e. NH_3) has simply reflected the decrease in concentration of $O_2(a^1\Delta_g)$ along the tube in the pre-shock flow. There, the observed decay could be predicted from that measured in the pre-shock flow, but in these experiments with NO as a quencher, the post-shock decay rate, α_t, was found to be greater than that predicted, α_L (table 6.2). So as described in Chapter 4 equation (4.45) was used for the analysis of the shock traces. A typical fit obtained is shown in figure 6.4. The difference in decay is illustrated by the two lines. The upper one, which does not pass through the experimental points, is the decay simply predicted from the room temperature measurement of the pre-shock decay. The lower line, through the points, is the result fitted with equation (4.45) which includes deactivation of $O_2(a^1\Delta_g)$ by NO at high temperature.

The values of pre- and post-shock decay constants together with the overall quenching rate constant, k_d^M, and NO quenching rate constant, k_d^{NO}, are listed in table 6.2.

Figure 6.5 shows a logarithm plot of k_d^{NO} against temperature as can be seen it increases with temperature. It was found that a plot of high temperature data for k_d^{NO} vs. 1/T showed a reasonable

Figure 6.3 Traces of the Shock Emission.

NO/O_2 mixture.

a_634 nm (R101)

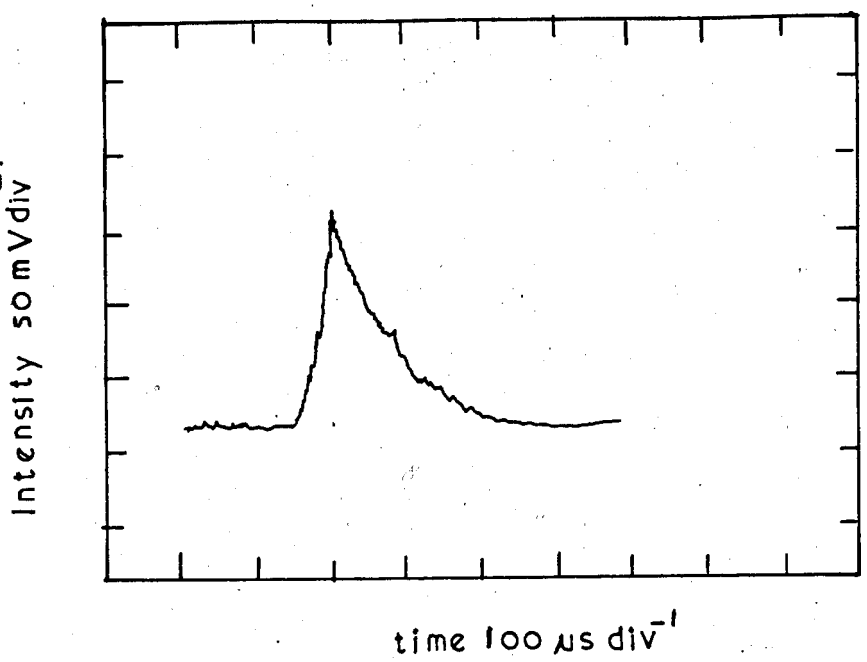

b_762 nm (RA101)

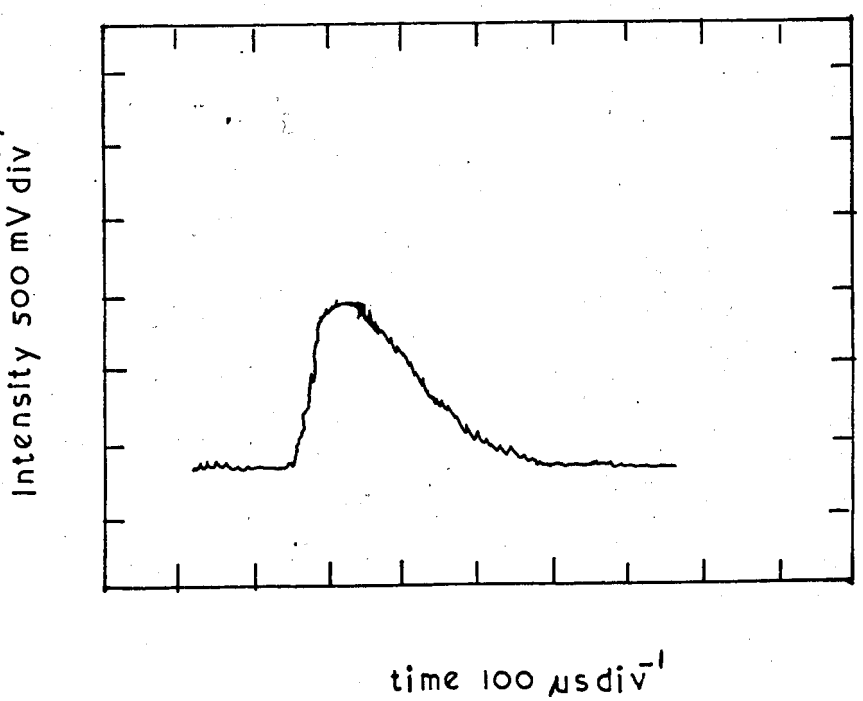

RUN NUMBER R101 03 JUL 1981
634.nm DELTA-NO

RESULTS

fitted	Ratio (K)	: 1.2728E+00	
	err.	: 1.3272E-01	
fitted	Delta Decay Const.	: 1.5177E-03	us-1
	err.	: 3.2997E-01	
	(Total Decay	:-6.1370E-03	us-1)
	(Pre-shock decay	:-4.6193E-03	us-1)
fitted	Integration Time	: 1.5931E+01	us
	err.	: 1.3426E+00	

RATE CONSTANTS (in l mol-1 s-1)

fitted	Delta decay: kd	: 2.0309E+05	
	err.	: 1.7966E+08	

RUN DATA

Oxygen	: 95.000	%
NO	: 5.000	%
Shock Speed	: 1.128	mm us-1
Initial Pressure	: 6.620	torr
P21	: 13.990	
Initial Temperature	: 295.000	K
T2	: 899.000	K
Density Ratio, R021	: 4.557	
Xzero	: 160.600	us
Yzero	: 14.064	mV
Pre-shock glow, PSG	: 4.800	mV
Afterglow	: 174.007	mV

FITTING	:NAG	: complete.
Iterations:	5	: 415 points.
Sum of the Squares		: 2.0644E+05

* * *

Figure 6.4 A fitted shock trace for O_2/NO at 634 nm emission

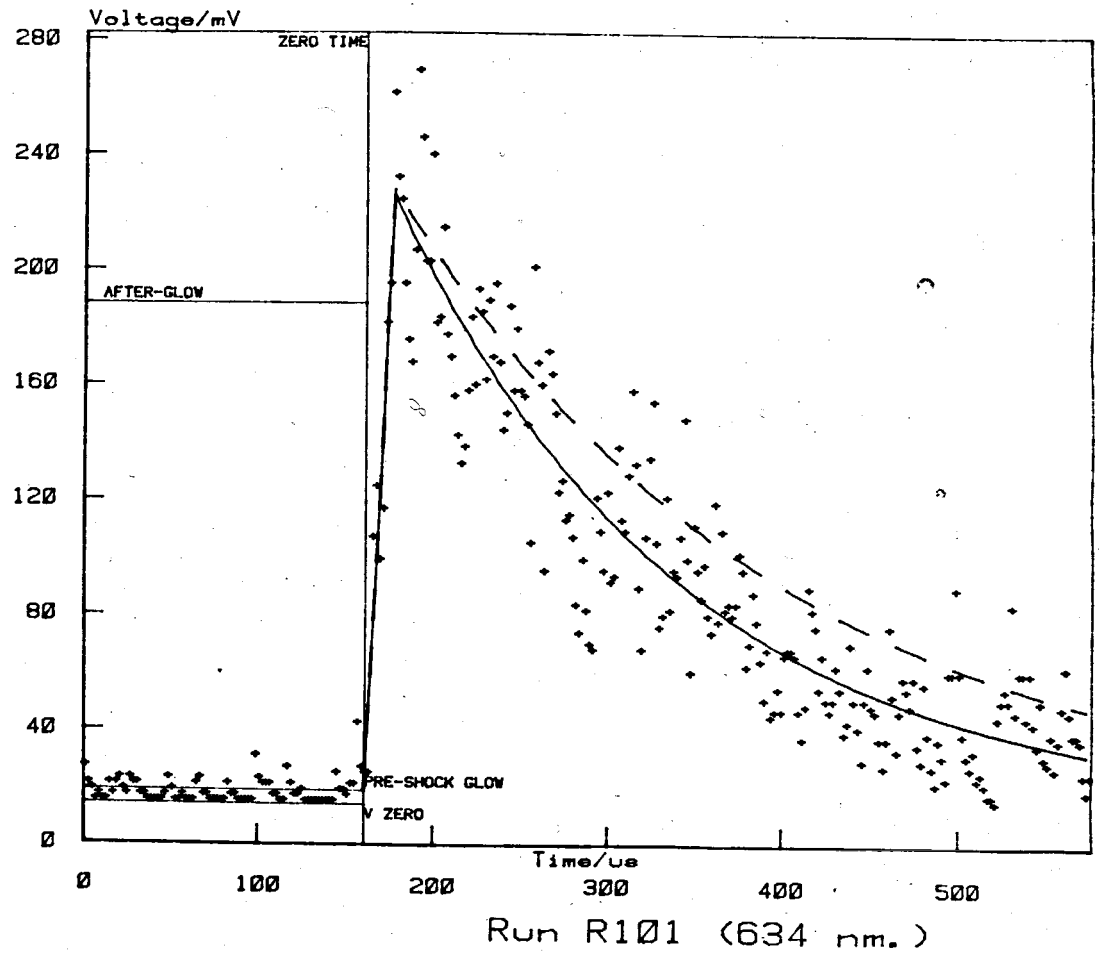

Table 6.2. Analysis of 634 nm Emission Traces, NO Results

Run No.	T_2 /K	^{634}K	α_t /$\mu s^{-1} 10^{-3}$	α_L /$\mu s^{-1} 10^{-3}$	t_s /μs	k_d^M /$dm^3 mol^{-1} s^{-1} 10^5$	k_d^{NO} /$dm^3 mol^{-1} s^{-1} 10^6$
			3% NO, 97% O_2				
R 85	703	0.92	4.15	3.12	22	1.43	2.40
R 104	805	1.00	4.97	4.26	21	1.02	1.69
R 88	895	1.10	6.17	4.06	20	2.96	4.94
R 107	916	1.05	5.92	4.41	19	1.91	1.91
R 106	977	1.19	6.77	5.03	23	2.05	3.43
R 87	987	1.23	7.15	5.58	23	1.85	3.10
R 105	1065	1.06	7.28	5.26	17	2.22	3.69
R 86	1133	1.18	8.56	6.61	18	2.03	3.37
			5% NO, 95% NO				
P 59	683	0.91	4.47	3.82	17	1.21	1.21
R 103	710	1.03	4.95	3.21	17	3.08	3.08
R 96	831	1.07	5.53	4.10	20	2.09	2.10
R 101	899	1.27	6.14	4.62	16	2.03	2.03
R 97	916	1.28	6.63	5.04	16	2.10	2.10
R 102	937	1.27	6.20	4.92	19	1.63	1.63
R 100	1016	1.23	7.48	5.44	16	2.43	2.43
R 99	1068	1.20	8.63	6.35	19	2.60	2.60
P 60	1088	1.10	10.28	7.37	12	3.26	3.26
			8% NO, 92% O_2				
R 95	762	0.94	4.91	3.85	20	1.97	1.23
R 93	806	1.14	5.48	4.13	10	2.19	1.37
R 91	832	1.22	6.21	4.53	14	2.63	1.64
R 92	941	1.30	6.73	5.42	15	1.81	1.13
R 94	951	1.34	7.56	5.33	15	3.06	1.91

Figure 6.5 Rate Constant for Quenching of $O_2(a\,^1\Delta_g)$ by NO

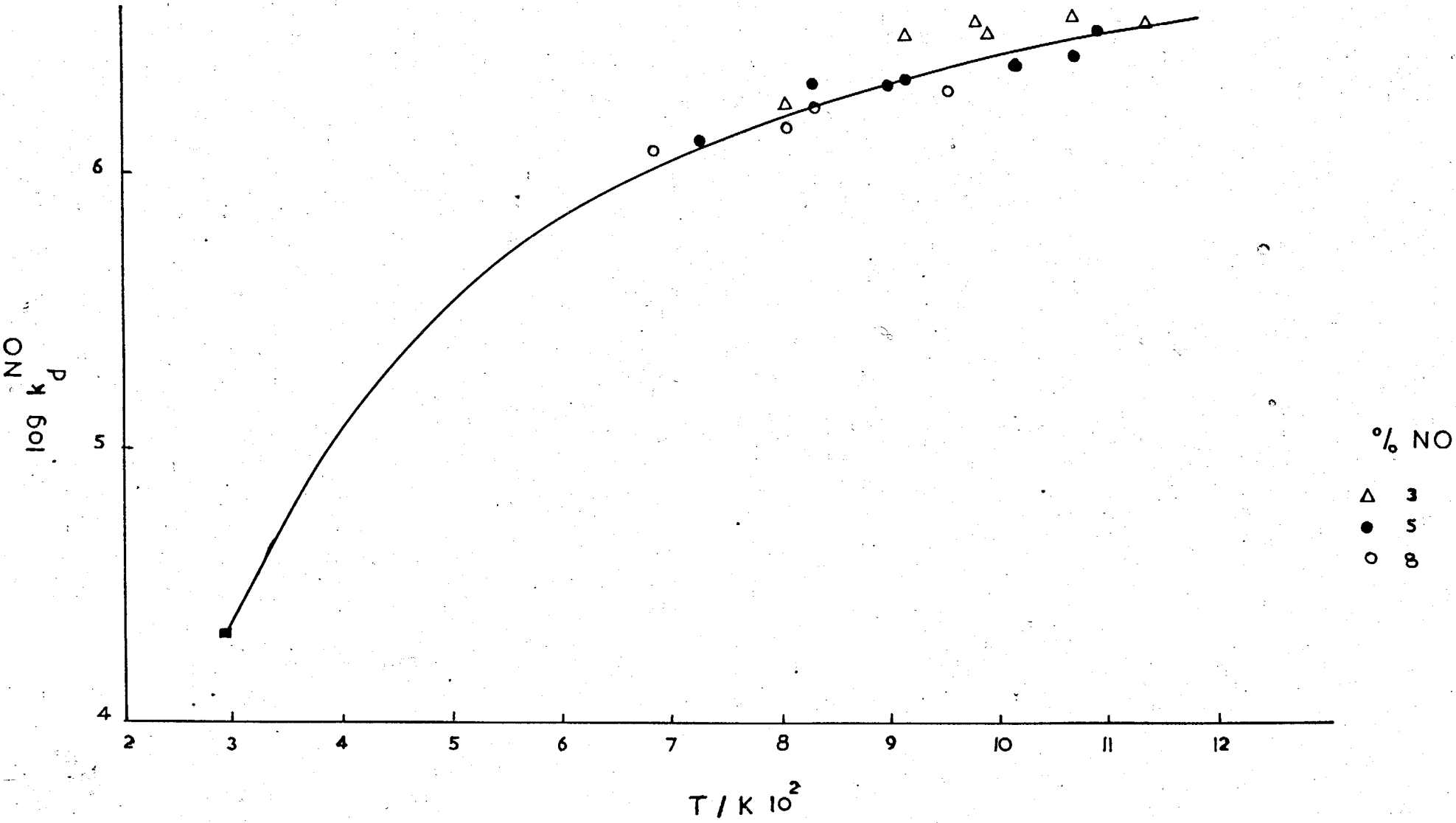

Figure 6.6 Arrhenius Plot of the Rate Constant for Quenching of $O_2(a^1\Delta_g)$ by NO

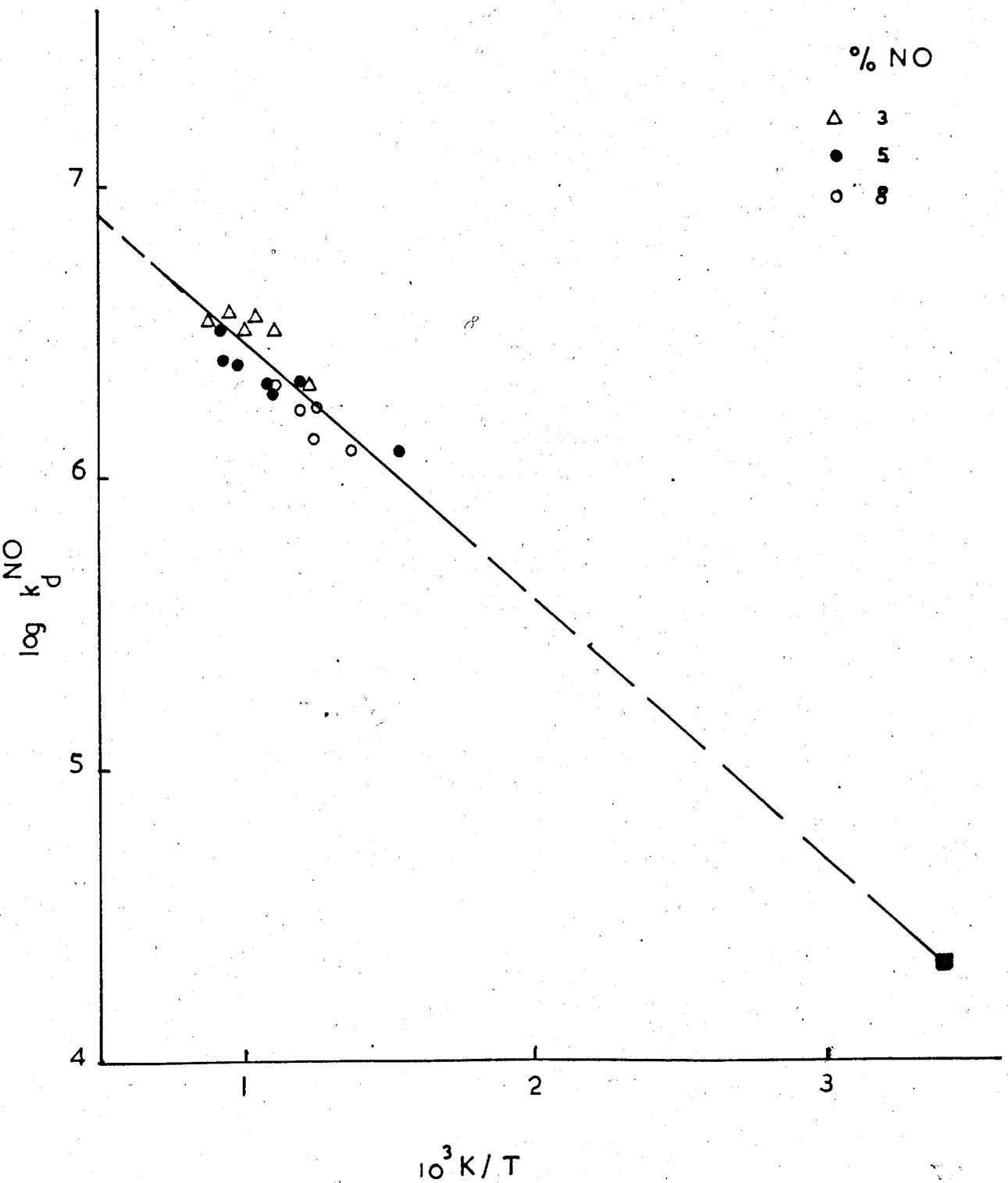

Arrhenius behaviour, figure 6.6. Also shown in figure 6.6 is the measured room temperature rate constant (Chapter 5). Extrapolation to room temperature although long shows the value obtained experimentally to be within the error limits. Hence, it is reasonable to include this point in the fitting to obtain the overall Arrhenius equation:

$$k_d^{NO} / dm^3\ mol^{-1}\ s^{-1} = (1.90 \pm 0.02) \times 10^7 \exp[-(2030 \pm 50)/T]. \quad (6.4)$$

The similarity between the results for differing mixtures (figure 6.6) shows the validity of neglecting $k_d^{O_2}$ at high temperatures [equation (6.3)].

(c) HCl

A series of shock experiments were performed on mixtures containing 3, 5 and 7% HCl. The run parameters are listed in Appendix 3. The form of the dimol emission was similar to that described for NO (figure 6.3a). So the shock traces were fitted using equation (4.45). Table 6.3 gives the values for pre- and post-shock decay constants together with k_d^M and k_d^{HCl}.

The values of k_d^{HCl} are plotted against temperature in figure 6.7. It can be seen that they increase with temperature. This positive temperature dependence was found to be simple Arrhenius form. Figure 6.8 shows an Arrhenius plot of k_d^{HCl} for runs made with three different mole fractions of HCl. These high temperature values are extrapolated to the measured room temperature rate constant (Chapter 5). The room temperature value is $(8.00 \pm 0.34) \times 10^4$ dm^3 mol^{-1} s^{-1} and the Arrhenius equation obtained between 295 K and 1140 K by least squares analysis is

$$k_d^{HCl} / dm^3\ mol^{-1}\ s^{-1} = (2.34 \pm 1.0) \times 10^7 \exp[-(1660 \pm 180)/T] \quad (6.5)$$

Table 6.3. Analysis of 634 nm Emission Traces, HCl Results

Run No.	T_2 /K	^{634}K	α_t /$\mu s^{-1}10^{-3}$	α_L /$\mu s^{-1}10^{-3}$	t_s /μs	k_d^M /$dm^3 mol^{-1} s^{-1} 10^5$	k_d^{HCl} /$dm^3 mol^{-1} s^{-1} 10^6$
			3% HCl, 97% O_2				
R 347	599	0.88	3.63	3.32	17	0.65	1.09
R 348	630	0.83	3.88	3.54	17	0.67	1.12
R 336	678	1.94	7.61	4.05	16	5.96	9.95
R 346	705	0.97	5.69	4.50	16	2.03	3.38
R 345	707	0.93	5.56	4.16	17	2.40	4.00
R 344	725	0.89	5.06	4.37	18	1.12	1.87
R 334	730	1.19	5.74	4.43	12	2.00	3.33
R 343	789	1.07	6.42	4.48	13	3.00	5.00
R 337	804	0.90	6.43	6.16	16	3.46	5.70
R 341	838	1.09	6.30	4.83	17	2.01	3.35
R 340	893	0.84	6.15	4.85	19	1.57	2.62
R 339	964	1.18	11.25	6.83	15	5.36	8.94
R 342	1038	1.25	9.15	7.41	14	1.93	3.23
			5% HCl, 95% O_2				
R 329	629	1.04	4.85	3.710	17	2.26	2.26
R 350	735	0.94	5.32	4.55	18	1.22	1.22
R 332	825	1.13	7.82	4.15	15	5.08	5.08
R 349	860	0.97	5.60	5.07	15	0.71	0.71
R 330	891	1.33	8.53	5.50	18	3.97	3.97
R 331	994	1.25	11.46	8.25	14	3.74	3.74
R 351	947	1.06	9.93	8.13	19	2.14	2.14
R 355	1021	1.29	11.65	6.80	12	5.35	5.35
R 353	1032	1.32	11.32	8.04	13	3.49	3.49
R 352	1046	1.20	11.78	8.39	11	3.61	3.61
R 356	1112	1.30	11.28	7.33	10	4.25	4.25
R 354	1172	1.34	14.30	8.28	10	6.28	6.28

Table 6.3 continued

7% HCl, 93% O_2

Run No.	T_2 /K	$634/T_2$ K	α_t /$\mu s^{-1} 10^{-3}$	α_L /$\mu s^{-1} 10^{-3}$	t_s /μs	k_d^M /$dm^3 mol^{-1} s^{-1} 10^5$	k_d^{HCl} /$dm^3 mol^{-1} s^{-1} 10^6$
R 364	605	0.99	4.58	3.22	15	2.81	2.00
R 363	683	1.01	5.45	3.97	17	2.46	1.76
R 362	701	0.96	6.58	4.33	15	3.63	2.60
R 361	743	0.87	6.65	5.12	16	2.31	1.65
R 360	778	1.04	8.19	5.94	20	3.22	2.30
R 359	818	1.08	8.59	5.73	21	3.87	2.76
R 358	880	1.11	7.78	6.58	18	1.53	1.09
R 357	958	1.18	7.65	6.36	10	1.53	1.09

Figure 6.7 Rate Constant for Quenching of $O_2(a\,^1\Delta_g)$ by HCl

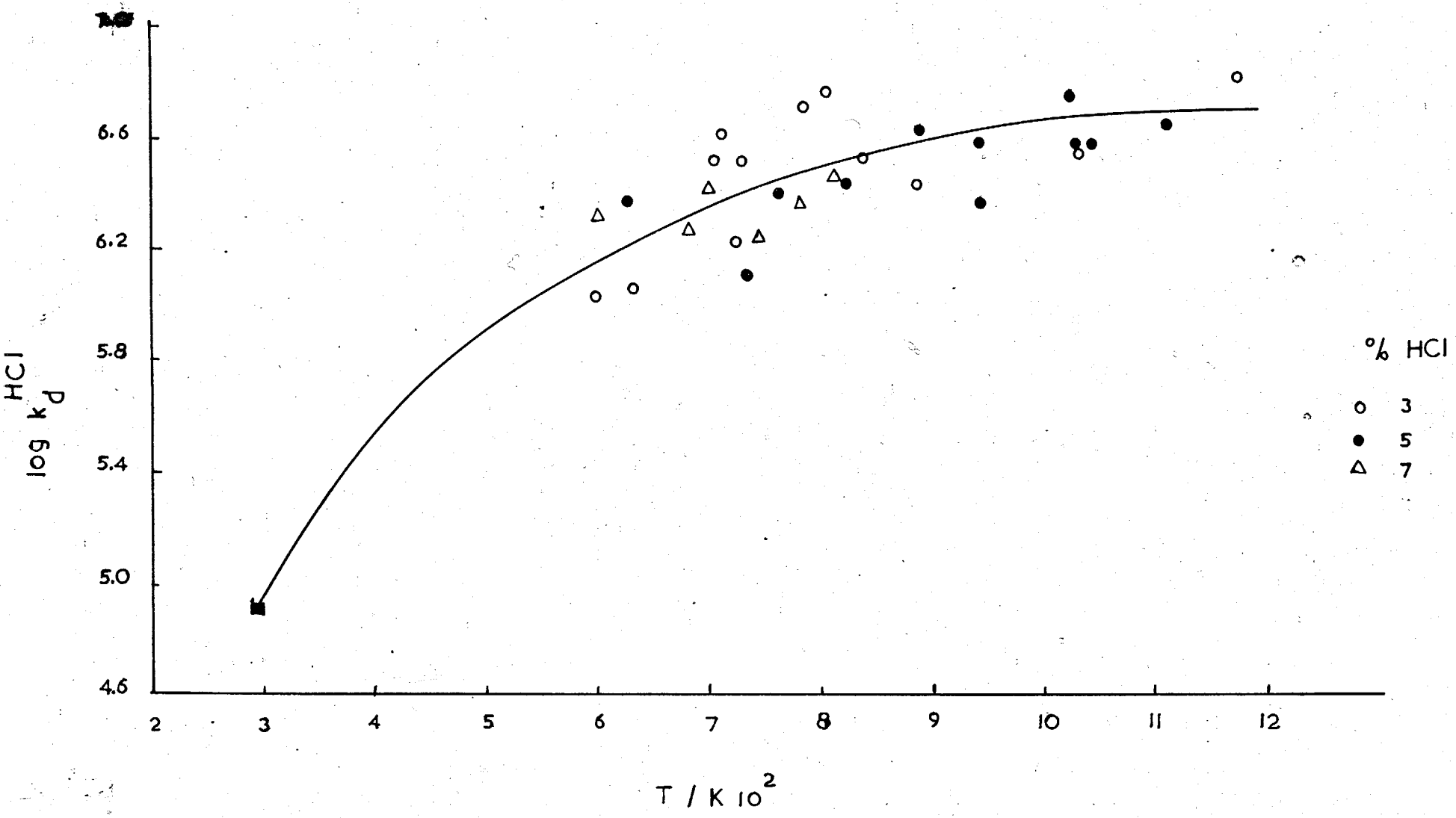

Figure 6.8 Arrhenius Plot of the Rate Constant for Quenching of $O_2(a^1\Delta_g)$ by HCl

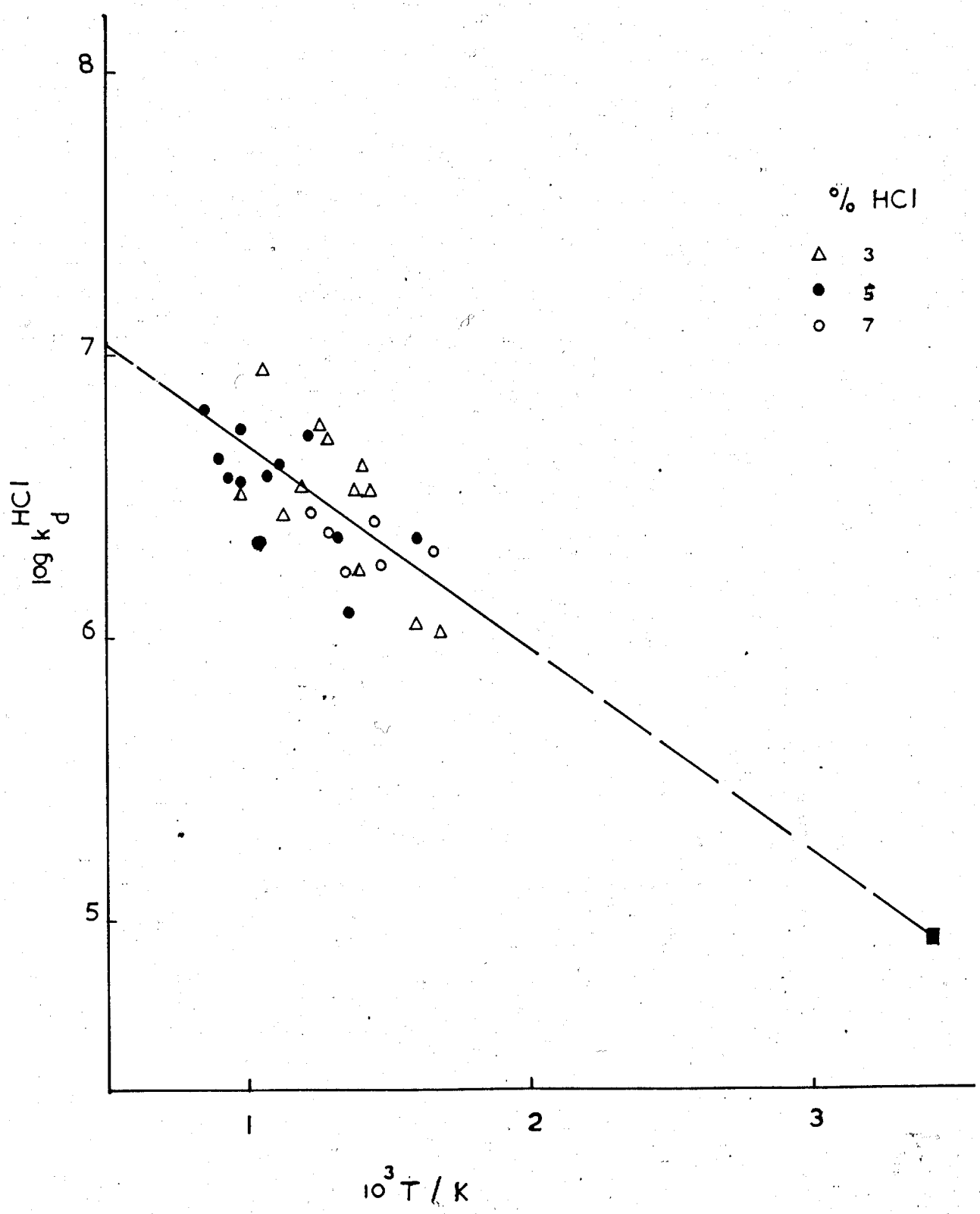

(d) $\underline{SO_2}$

A series of shocks into mixtures containing 10, 15 and 20% SO_2 were carried out. The run parameters are listed in Appendix 4. A typical 634 nm emission trace is shown in figure 6.9a. The high temperature behaviour was found to be similar to that observed for NO or HCl, so the shock traces were analysed using equation (4.45), as described previously, to yield values for k_d^M and $k_d^{SO_2}$. The results are listed in table 6.4. The values of $k_d^{SO_2}$ are plotted against temperature in figure 6.10. It can be seen that they increase with temperature. A plot of $\log.k_d^{SO_2}$ against 1/T is shown in figure 6.11. It displays a reasonable Arrhenius behaviour. Extrapolating to room temperature enables us to estimate a value for the rate constant since we could not measure it at room temperature (Chapter 5). The overall Arrhenius equation obtained by a least squares fitting is:

$$k_d^{SO_2}/dm^3\ mol^{-1}\ s^{-1} = (8.90 \pm 3.45) \times 10^6 \exp[-(2370 \pm 90)/T] \qquad (6.6)$$

(e) $\underline{\text{The Enhancement Factor, } {}^{634}K}$

Figure 6.12 shows a plot of the enhancement factor, ^{634}K against temperature for differing mixtures of all quenchers studied in this work. As it can be seen the values of ^{634}K are approximately equal to one for temperatures up to $\sim$ 1000 K. This is expected if the dimol emission is a simple collisional process [equation (4.42)]. However, above 1000 K there is systematic increase in ^{634}K. This observation has been studied further in this work and is discussed in Chapter 8.

Figure 6.9 Traces of the Shock Emission.

SO_2 / O_2 mixture.

a_ 634 nm (R446)

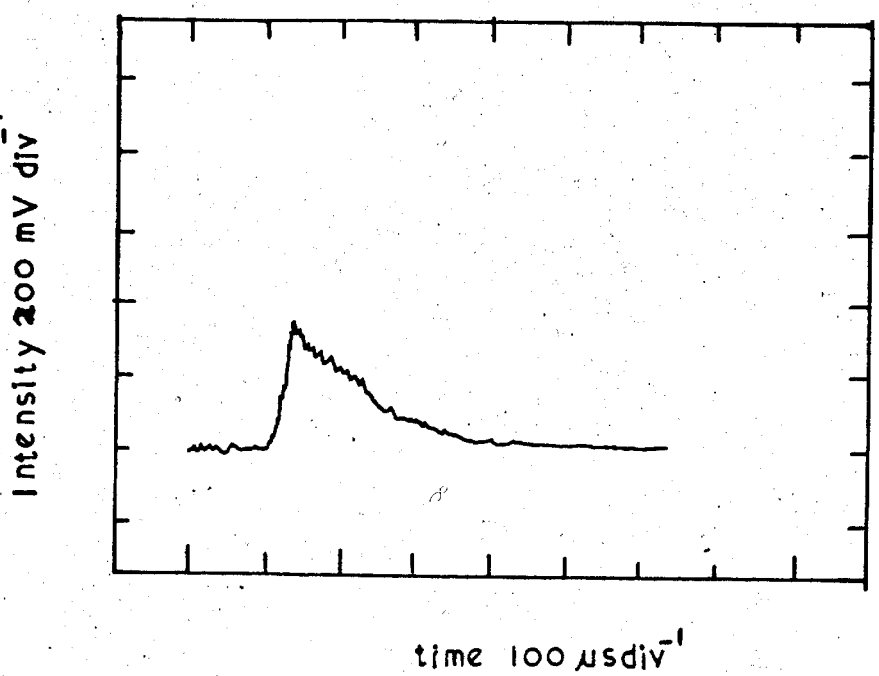

b_ 762 nm (RA 446)

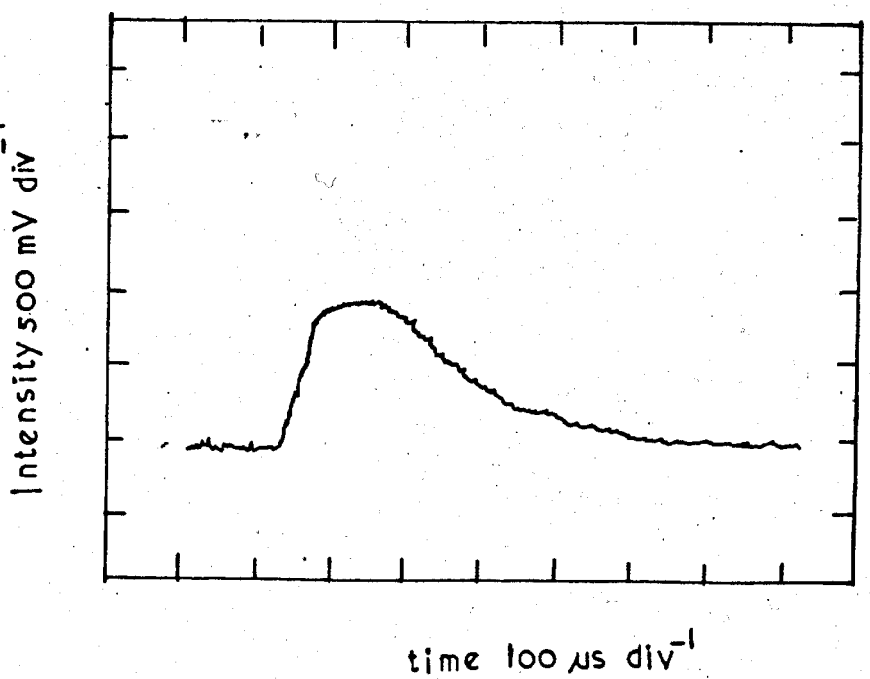

Table 6.4. Analysis of 634 nm Emission Traces, SO_2 Results

Run No.	T_2 /K	^{634}K	α_t /$\mu s^{-1} 10^{-3}$	α_L /$\mu s^{-1} 10^{-3}$	t_s /μs	k_d^M /$dm^3 mol^{-1} s^{-1} 10^5$	$k_d^{SO_2}$ /$dm^3 mol^{-1} s^{-1} 10^5$
			10% SO_2, 90% O_2				
R 403	663	0.87	2.47	2.16	19	0.64	3.21
R 402	673	0.94	2.49	2.01	23	0.96	4.83
R 404	753	0.83	2.93	2.24	21	1.16	5.79
R 407	764	0.98	3.35	2.57	27	1.19	5.98
R 405	776	0.93	3.36	2.88	18	0.82	4.08
R 408	786	0.94	3.22	2.99	21	0.39	1.93
R 410	836	0.98	3.39	2.80	24	0.93	4.63
R 412	863	1.12	4.03	3.09	16	1.35	6.78
R 411	884	1.09	4.23	3.21	18	1.47	7.35
R 417	943	1.07	4.47	3.58	14	1.21	6.06
R 415	946	1.09	4.66	3.60	17	1.49	7.43
R 413	988	1.17	4.96	3.74	16	1.60	8.00
R 419	989	1.06	5.12	3.87	16	1.57	7.85
R 416	1063	1.11	5.50	4.02	15	1.75	8.75
R 421	1102	1.36	6.34	4.16	14	2.68	13.39
R 423	1070	1.18	4.93	3.92	16	1.26	6.28
R 418	1122	1.13	6.61	4.07	13	2.87	14.37
R 422	1130	1.14	5.93	4.19	13	2.04	10.21
R 420	1206	1.19	6.54	4.67	13	2.07	10.34
			15% SO_2, 85% O_2				
R 431	663	0.96	1.94	1.62	20	0.81	2.69
R 432	706	1.09	2.26	1.55	17	1.61	5.37
R 429	764	1.02	2.61	1.96	16	1.37	4.58
R 424	792	1.05	2.82	2.08	23	1.50	5.00
R 425	809	1.10	3.15	2.41	24	1.33	4.42
R 430	812	1.07	2.94	2.27	15	1.31	4.37
R 426	865	1.09	3.22	2.55	16	1.18	3.93
R 433	934	1.10	3.67	2.72	20	1.60	5.31
R 434	967	1.15	4.17	3.10	18	1.66	5.54
R 427	1004	1.18	4.36	2.79	13	2.41	8.04
R 436	1052	1.45	5.24	3.51	15	2.61	8.66
R 435	1081	1.24	5.07	3.45	13	2.33	7.77

Table 6.4 continued

20% SO_2, 80% O_2

Run No.	T_2 /K	634_K	α_t /$\mu s^{-1} 10^{-3}$	α_L /$\mu s^{-1} 10^{-3}$	t_s /μs	k_d^M /$dm^3 mol^{-1} s^{-1} 10^5$	$k_d^{SO_2}$ /$dm^3 mol^{-1} s^{-1} 10^5$
R 439	731	1.21	1.93	1.55	16	1.02	2.54
R 437	814	1.23	2.68	1.62	19	2.39	5.97
R 442	846	1.20	3.13	2.03	14	2.34	5.84
R 438	853	1.31	2.95	2.08	25	1.86	4.65
R 443	919	1.30	3.52	2.32	11	2.34	5.84
R 444	1063	1.36	4.11	2.75	17	2.36	5.92
R 445	1067	1.43	4.73	2.69	19	3.53	8.82
R 446	1136	1.47	5.16	3.05	16	3.35	8.34

Figure 6.10 Rate Constant for Quenching of $O_2(a^1\Delta_g)$ by SO_2

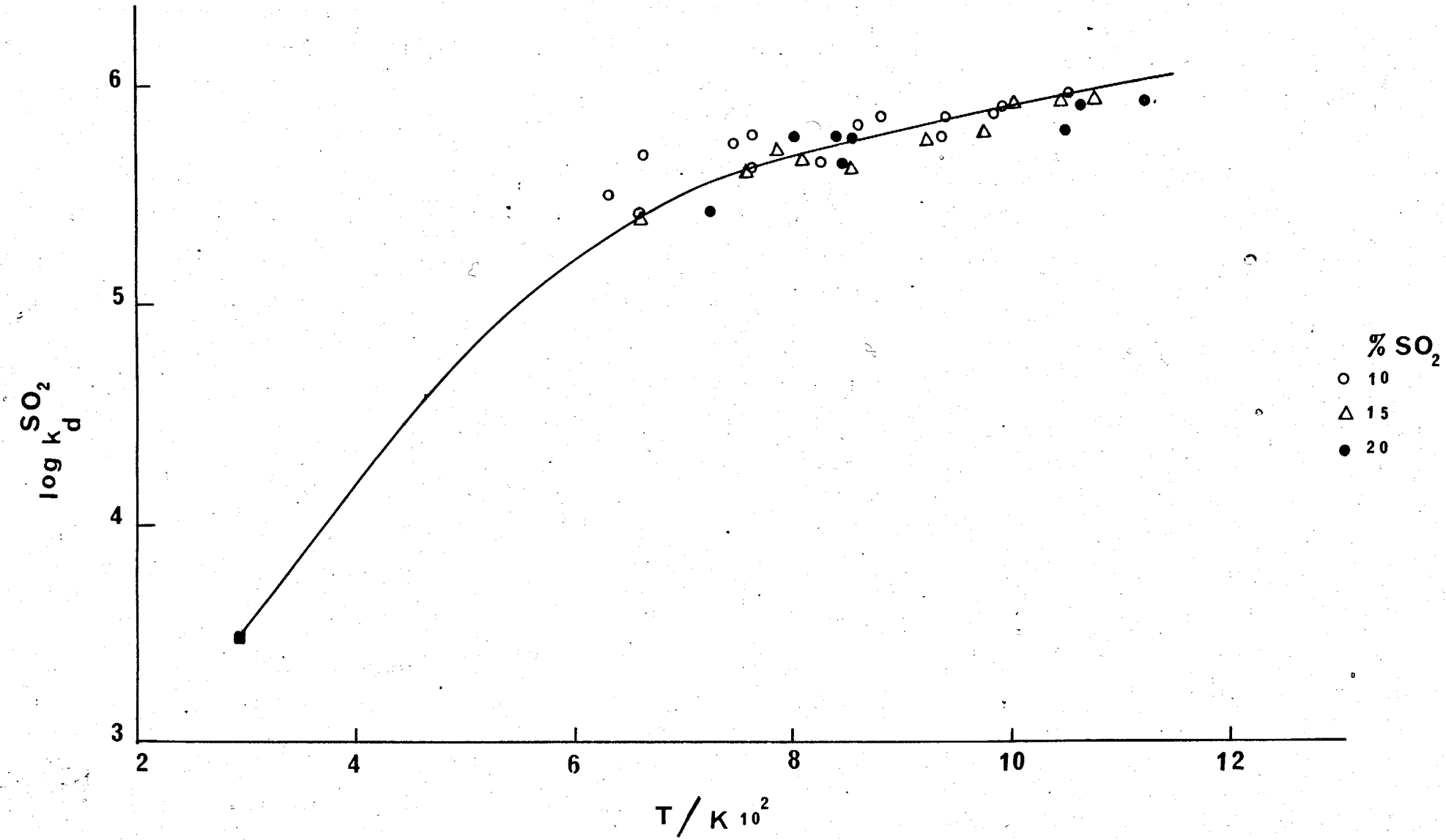

Figure 6.11 Arrhenius Plot of the Rate Constant for Quenching of $O_2(a^1\Delta_g)$ by SO_2

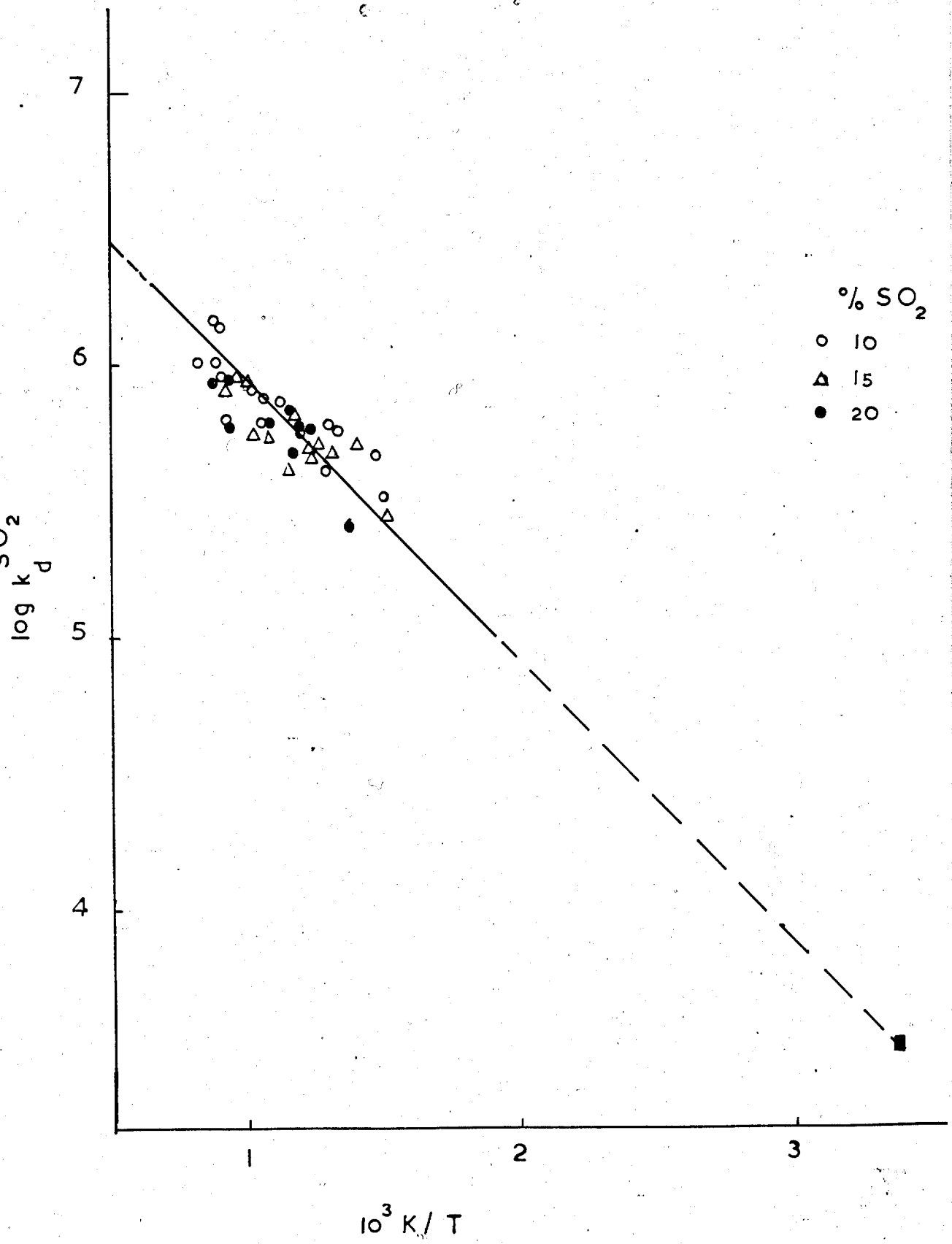

Figure 6.12 Variation of ^{634}K with Temperature

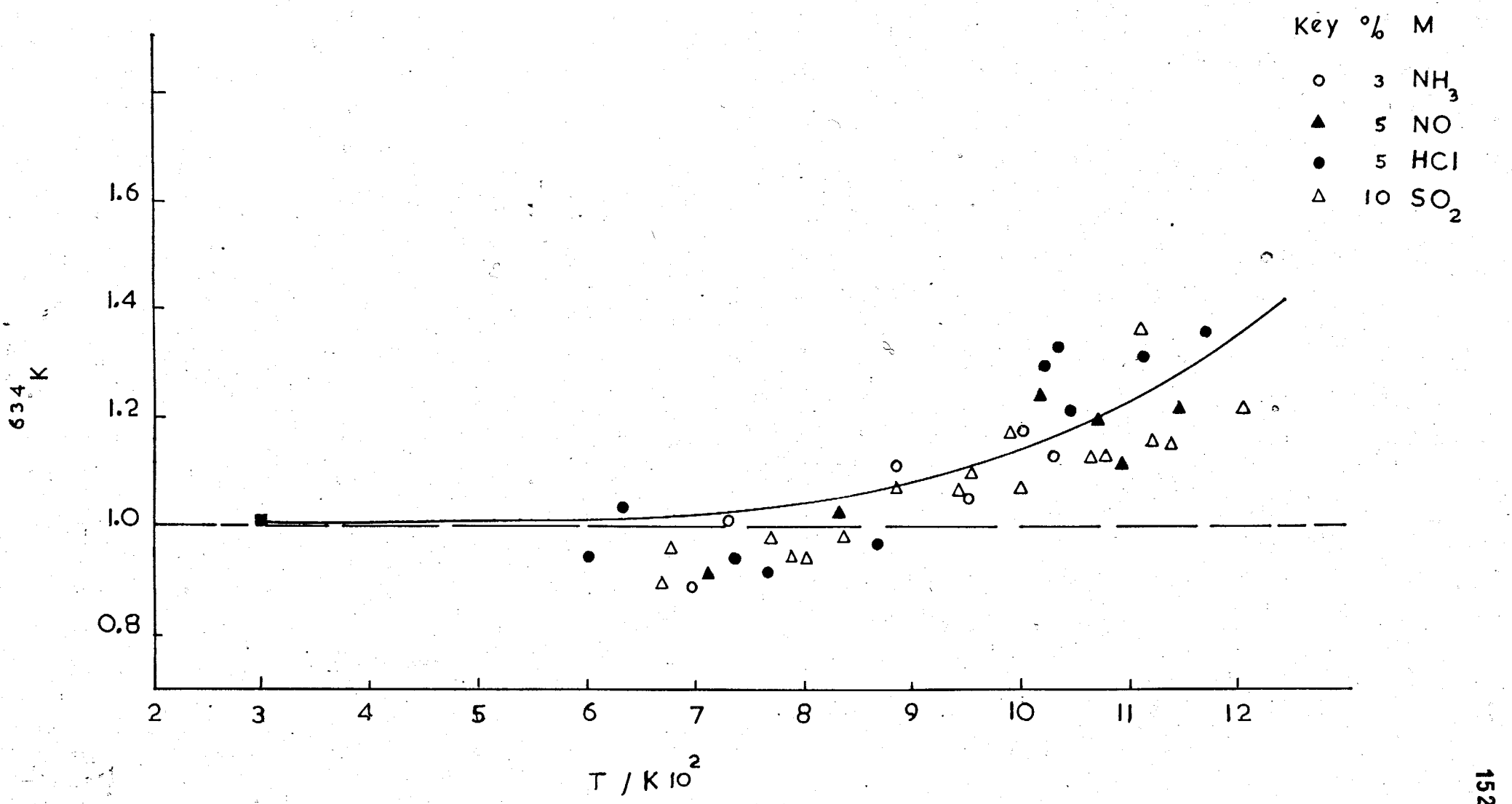

6.4 Treatment of $O_2(b^1\Sigma_g^+)$ High Temperature Results

Data on the collisional quenching of $O_2(a^1\Sigma_g^+)$ is obtained from the high temperature behaviour of the emission at 762 nm:

$$O_2(b^1\Sigma_g^+) \rightarrow O_2(\chi^3\Sigma_g^-) + h\nu \ (\lambda = 762 \text{ nm}). \qquad (4.22)$$

As described in Chapter 4 the emission trace displays the four zones that were predicted by the developed kinetic model given by equation (4.60):

$$^{762}I_{t_p} / {}^{762}I_{psg}\ \rho_{21} = \{{}^{762}K + (1 - {}^{762}K)\ \exp(-\ k_q^M[M]t_p)\}\ \exp(-\ \alpha_t t_p). \qquad (4.60)$$

It is from the relaxation zone and the enhancement factor, ^{762}K, that the experimental rate constants are obtained for the collisional quenching reaction (4.20) and the energy pooling reaction (4.5):

$$O_2(b^1\Sigma_g^+) + M \xrightarrow{k_q^M} O_2(a^1\Delta_g) + M \qquad (4.20)$$

$$2O_2(a^1\Delta_g) \xrightarrow{k_p} O_2(b^1\Sigma_g^+) + O_2(\chi^3\Sigma_g^-). \qquad (4.5)$$

The relaxation time, τ_{rel}, observed in the relaxation zone where the level of emission intensity relaxes to the new equilibrium level at the high temperature is defined as

$$\tau_{rel} = 1/k_q^M[M]. \qquad [s] \qquad (6.7)$$

Equation (4.60) can be rewritten in terms of relaxation time as:

$$^{762}I_{t_p} / {}^{762}I_{psg}\ \rho_{21} = \{{}^{762}K + (1 - {}^{762}K)\ \exp(-\ t_p)(\tau_{rel})\}\ \exp(-\ \alpha_t t_p). \qquad (6.8)$$

In equation (6.8) if we assume that there is no exponential decay along the tube (see figure 6.13) then for a completed relaxation process ($t_p = \infty$) the ratio of emission intensities will be given by:

$$^{762}I_{t_p} / ^{762}I_{psg} = \rho_{21} \, ^{762}K \qquad (6.9)$$

in the other extreme if t_p is very short ($t_p = o$) then,

$$^{762}I_{t_p} / ^{762}I_{psg} = \rho_{21} \qquad (6.10)$$

and so relaxation measurements will not be possible. In other words, if the ratio of rate constants for the reactions forming and removing $O_2(b^1\Sigma_g^+)$ at the two temperatures, ^{762}K, [equation (4.54)] is equal to unity then relaxation cannot be measured. It was shown in Chapter 4 that the enhancement factor, ^{762}K, is given by:

$$^{762}K = \{(k_p/k_q^M)\}_{T_2} / \{k_p/(k_q^M + k_W/[M])\}_{T_1}. \qquad (4.54)$$

Thus the overall collisional quenching rate constant, k_q^M, at the shock temperature, T_2, is determined from the measurement of relaxation time, and this value together with the value of ^{762}K and the known room temperature, T_1, rate constants (Chapter 5) give the rate constant for the energy pooling reaction, k_p, at temperature T_2.

These calculations are carried out in the process of the computer graphics analysis (Chapter 4) when the experimental points are fitted to equation (4.61) for no deactivation of $O_2(a^1\Delta_g)$ at high temperature (section 4.2.2a). The fit gives values of t_s, k_q^M, α_t and ^{762}K. The pooling rate constant, k_p, is determined from k_q^M and ^{762}K using equation (4.54) as described above. However, if $O_2(a^1\Delta_g)$ is

Figure 6.13 The 762 nm Trace assuming no decay.

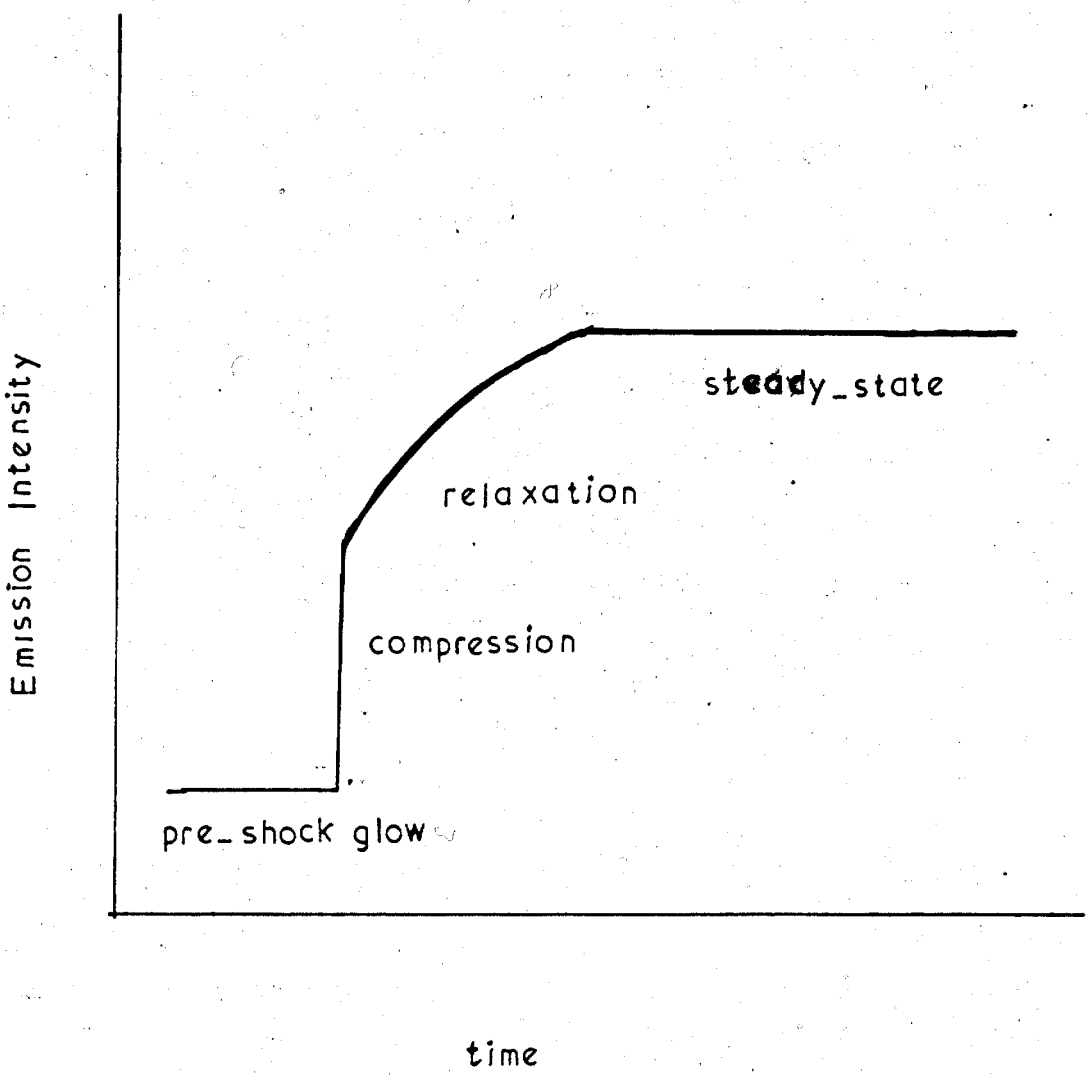

deactivated at high temperature (section 4.2.2b) then equation (4.64) is used for the fitting which also yields the value of k_d^M from the decay zone as described in section 6.3. In this case the value of k_p is determined from equation (4.63). The values of k_d^M obtained from 762 nm emission trace are always found to be the same as those obtained from 634 nm emission trace.

From the value of overall quenching rate constant, k_q^M, given by the fitting the rate constant for the quenching gas, for example NO, is determined from the equation:

$$k_q^{NO} = [k_q^M \rho_2 - k_q^{O_2}(1 - x)]/x \qquad (6.11)$$

where x is the mole fraction of the quencher studied, in this case NO. The values of $k_q^{O_2}$, for pure oxygen, are known from previous study[9].

In this work NH_3 results are analysed by the normal model, with no deactivation of $O_2(a^1\Delta_g)$ at high temperature, using equation (4.61). The results for NO, HCl and SO_2 are analysed using the modified model, equation (4.64), which includes deactivation of $O_2(a^1\Delta_g)$ at high temperature.

6.4.1 Results

The run parameters for the results of 762 nm emission given below are the same as those listed for 634 nm (section 6.3.1) since both emission wavelengths were recorded simultaneously for each shock experiment.

(a) NH_3

A typical high temperature 762 nm emission trace from a mixture containing NH_3 is shown in figure 6.1b. The four regions expected can be seen; the steady glow from the cool gas, the rapid rise at

the shock front, the relaxation zone and the decay. It can be seen from 6.1b that the relaxation zone is short.

As there is no deactivation of $O_2(a^1\Delta_g)$ at high temperature (section 6.3.1a), equation (4.61) was used for the analysis. An example of the fit is shown by the full line in figure 6.14. The results obtained are listed in table 6.5. The post-shock decay constant, α_t, obtained is compared with that obtained from 634 nm emission trace and with the value predicted from the pre-shock measurements (table 6.1) to check the procedure. It can be seen that the values are similar.

The experimental records for NH_3 were strikingly different from those obtained with NO or HCl, presented later in this section. The emission level was much higher and gave a large value to ^{762}K, the enhancement factor. There are two reasons for the large value of ^{762}K in the presence of NH_3. First, the pre-shock glow is depressed because NH_3 is an efficient quencher at room temperature (table 5.7); second, the overall quenching rate constant, k_q^M, scarcely changes with temperature in comparison to the pooling rate constant, k_p, so that the concentration of $O_2(a^1\Sigma_g^+)$ at high temperature is relatively much higher. Thus, as can be seen by comparing figure 6.14 with figure 6.18, a fitted shock trace from O_2/NO mixture, the initial jump is small compared with the height of the maximum emission. Therefore, the large enhancement factors in the presence of NH_3 indicate that the quenching rate constant k_q^M must decrease with temperature (equation 4.54).

Figure 6.15 shows the values of ^{762}K plotted against temperature for three different mole fractions of NH_3. It can be seen that data fall on three separate lines. The lines are drawn by eye through the points.

RESULTS

fitted	Quenching Const.	: 1.9836E-01	us-1	
		: 5.2531E+00	us	
	err.	: 9.1065E+00		
fitted	Ratio (K)	: 1.2321E+01		
	err.	: 4.6000E-01		
fitted	Decay Constant	:-2.9341E-03	us-1	
		:-6.9387E-03	cm-1	
	err.	: 7.0946E-01		
	(Pre-shock decay	:-3.0869E-03	us-1)	
fitted	Integration Time	: 4.3142E+00	us	
	err.	: 1.4600E+00		

RATE CONSTANTS (in l mol-1 s-1)

fitted	Quenching : kq	: 2.3407E+07	
	err.	: 4.0578E+07	
	log kq	: 7.3693	
fitted	Pooling : kp	: 1.5519E+05	
	err.	: 4.1565E+03	
	log kp	: 5.1909	

RUN DATA

Oxygen	:	97.000	%
NH3	:	3.000	%
Shock Speed	:	1.147	mm us-1
Initial Pressure	:	6.790	torr
P21	:	14.410	
Initial Temperature	:	294.000	K
T2	:	901.000	K
Density Ratio, RO21	:	4.686	
Xzero	:	96.900	us
Yzero	:	219.698	mV
Decay*1000	:	-7.300	cm-1
Pre-shock glow, PSG	:	18.100	mV
Afterglow	:	84.816	mV

FITTING	:NAG	: complete.
Iterations:	10	: 547 points.
Sum of the Squares		: 3.8119E+06

* * *

Figure 6.14 A fitted shock trace for O_2/NH_3 at 762 nm emission

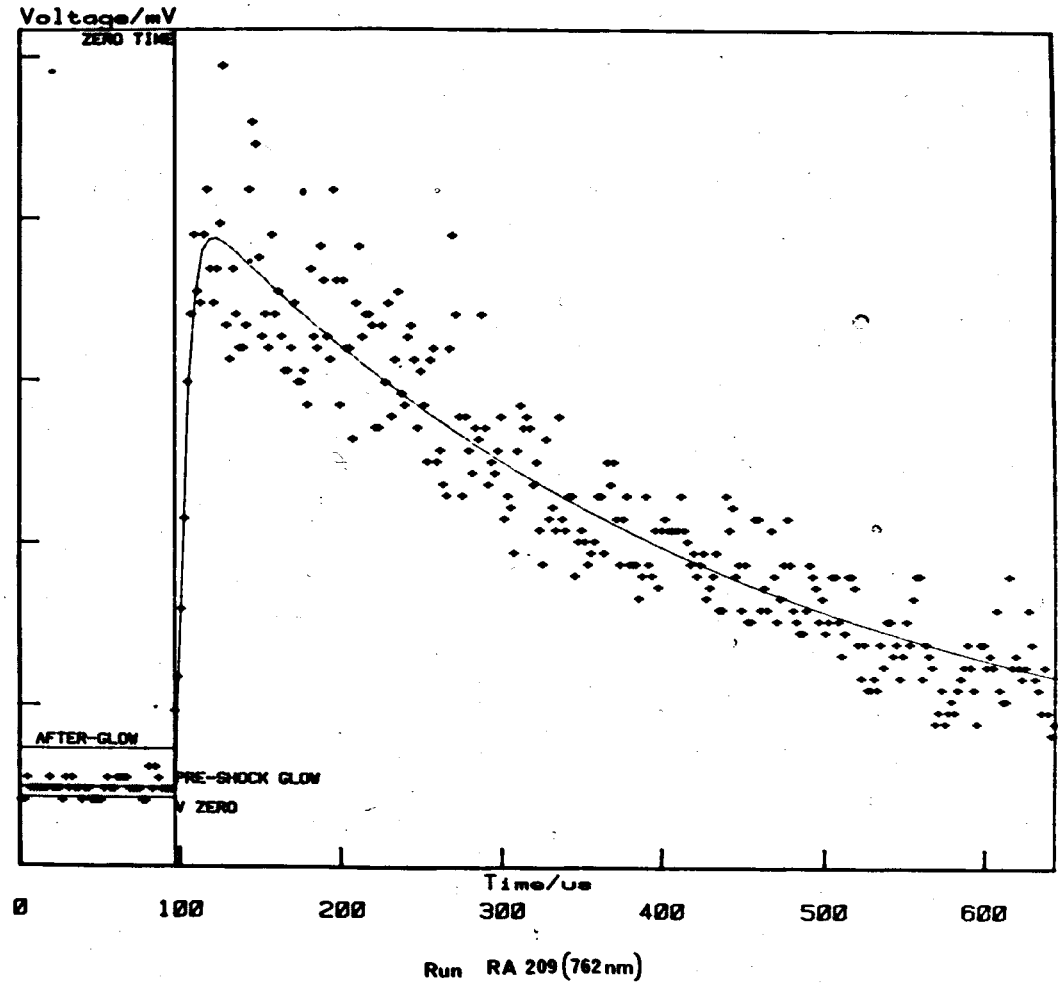

Table 6.5. Analysis of 762 nm Emission Traces, NH_3 Results

Run No.	T_2 /K	^{762}K	α_t /$\mu s^{-1} 10^{-3}$	t_s /μs	τ_{rel} /μs	k_q^M /$dm^3 mol^{-1} s^{-1} 10^7$ Fitted	cal.	$k_q^{NH_3}$ /$dm^3 mol^{-1} s^{-1} 10^8$	k_p /$dm^3 mol^{-1} s^{-1} 10^5$
					3% NH_3, 97% O_2				
RA 216	602	2.80	2.40	3	9	1.05	1.00	9.21	0.11
RA 213	699	3.92	2.69	2	4	3.76	3.08	9.85	0.80
RA 212	732	4.36	2.19	8	7	2.22	3.19	10.18	0.52
RA 211	876	11.43	3.31	6	7	1.95	2.12	6.33	1.20
RA 210	883	10.25	2.95	3	6	2.11	2.40	7.41	1.16
RA 209	901	12.32	2.93	4	5	2.34	2.19	6.49	1.55
RA 208	998	20.34	4.09	3	7	1.58	1.78	4.82	1.74
RA 214	1031	32.22	3.70	1	7	1.52	1.24	2.99	2.63
RA 215	1135	44.79	3.18	3	8	1.37	1.18	2.46	3.30
					7% NH_3, 93% O_2				
RA 220	747	6.90	2.31	14	6	2.90	5.00	7.10	0.47
RA 219	833	13.00	2.50	4	4	3.86	3.82	5.20	1.16
RA 218	883	16.12	3.03	5	5	3.18	3.50	4.71	1.18
RA 217	956	23.49	2.91	11	6	2.88	3.10	4.10	1.56

Table 6.5 continued

5% NH_3, 95% O_2

Run No.	T_2 /K	762/K	α_t /$\mu s^{-1} 10^{-3}$	t_s /μs	τ_{rel} /μs	k_q^M/$dm^3 mol^{-1} s^{-1} 10^7$ Fitted	cal.	$k_q^{NH_3}$ /$dm^3 mol^{-1} s^{-1} 10^8$	k_p /$dm^3 mol^{-1} s^{-1} 10^5$
RA 201	630	3.27	2.29	5	4	5.93	4.72	9.26	0.63
RA 200	665	3.310	1.84	11	8	2.80	5.36	10.52	0.30
RA 224	754	6.53	2.31	8	5	4.00	4.00	7.60	0.83
RA 223	802	10.08	2.77	13	6	2.63	3.00	5.77	0.86
RA 225	846	12.14	2.62	10	8	2.32	3.05	5.72	0.91
RA 222	786	16.93	2.89	12	7	2.00	2.37	4.31	1.10
RA 226	906	18.12	2.57	8	5	2.73	2.50	4.47	1.60
RA 205	1005	25.72	3.23	11	7	2.07	2.37	4.12	1.72
RA 228	1013	34.07	2.02	4	7	1.96	1.81	3.00	2.16
RA 227	1030	41.78	3.25	1	7	1.82	1.60	2.51	2.47
RA 206	1039	35.31	2.94	2	7	1.78	1.92	3.17	2.04
RA 207	1114	55.49	2.80	2	7	1.72	1.50	2.18	3.09

Figure 6.15 A Plot of the Enhancement Factor, ^{762}k, vs. Temperature for NH_3

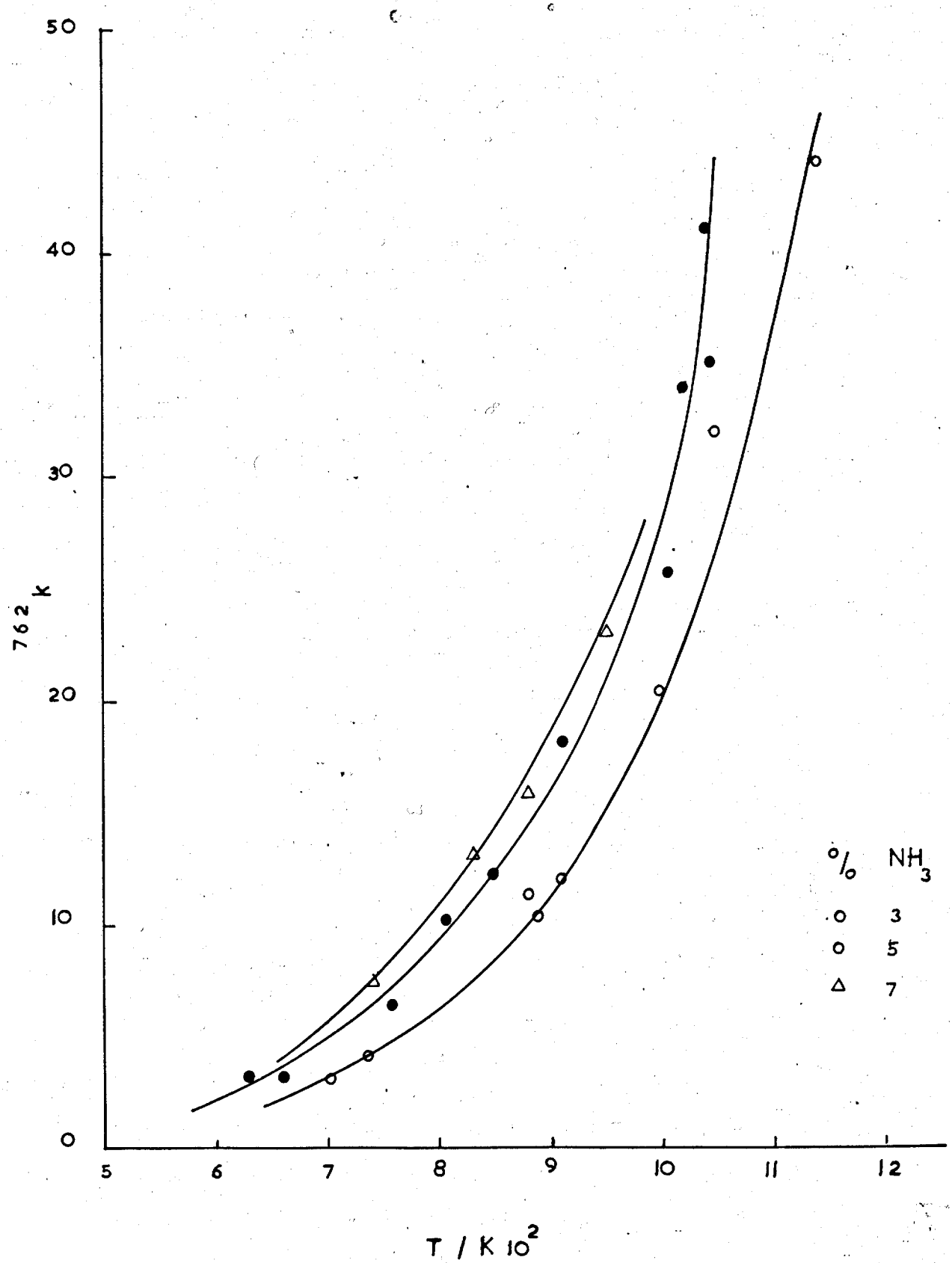

In these experiments, the relaxation time, τ_{rel}, [equation (6.7)] was found to be rapid and comparable to the integration time, t_s, so that the non-linear least squares fitting (Chapter 4) gave poor results for the two parameters. But it was found that if the value of t_s was fixed, calculated from shock speed and the slitwidth, during the fitting then reliable values could be obtained for k_q^M. To check this, the k_q^M values were also recalculated using equation (4.54), from ^{762}K (which is unaffected by the relaxation zone since it is determined from the back extrapolation of the decay to the time of arrival of the shock front) and known values[79] of k_p, which is independent of the additive (section 6.4.1e).

The results from the two procedures for the three mixtures are plotted against each other in figure 6.16. As can be seen the results are well correlated and fall on the same line passing through the origin with the slope equal to unity. The scatter, by the standards of shock tube experiments, is small. Therefore, this indicates that both methods give correct results and that the numerical analysis is producing reliable results.

Figure 6.17 gives the final results for the quenching of $O_2(b^1\Sigma_g^+)$ with NH_3 as a function of temperature the points from all mixture fall on a single line indicating the validity of equation (6.11). The notable features are the slight maximum and the fall in the rate constant with temperature.

(b) NO

Figure 6.3b shows a typical shocked gas trace at 762 nm. It displays the expected shape. The results obtained from the 634 nm emission traces (section 6.3.1b) indicated that $O_2(a^1\Delta_g)$ was deactivated by NO at high temperature so here the traces were analysed using equation 4.64. An example of the fit obtained is shown by the

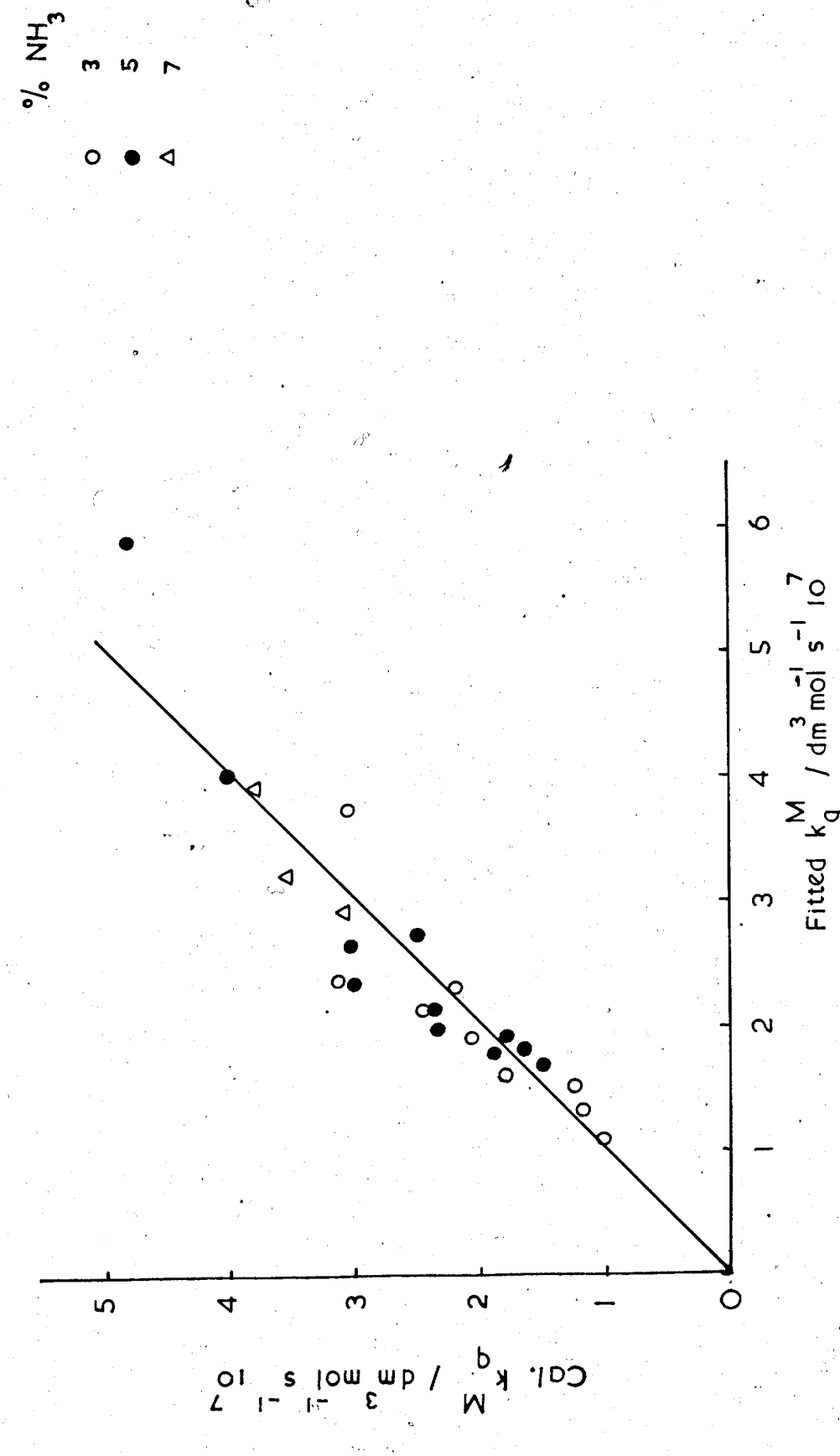

Figure 6.16 A Plot of Cal. k_q^M vs. Fitted k_q^M

Figure 6.17 Log. of Rate Constants for Quenching of $O_2(b^1\Sigma_g^+)$ by NH_3 and NO

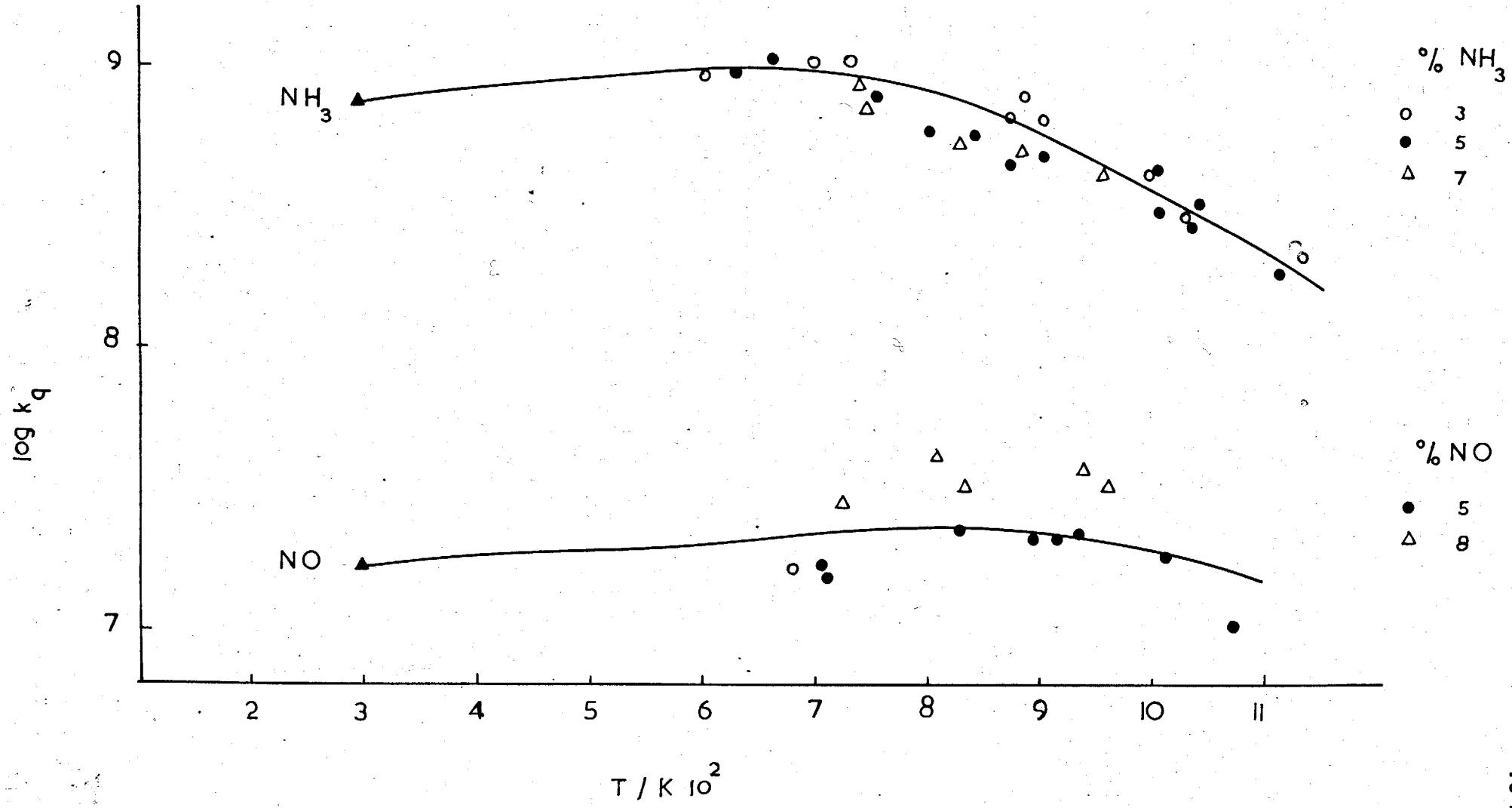

lower line passing through the points in figure 6.18. The upper line which does not pass through the points is that predicted by the normal model in which the only high temperature reactions are the formation and removal of $O_2(b^1\Sigma_g^+)$ and the fall is due to the pre-shock concentration gradient. For all runs the post-shock decay was found to agree well with the values obtained from the 634 nm emission traces.

In these experiments it was found that the relaxation was rapid and so comparable to the integration time. This meant that once again the relaxation constants obtained were not accurately determined by the fitting of the relaxation zone. So as before the method of calculation was reversed and estimated k_q^M from the measured enhancement factor ^{762}K, the known values of k_d^M (obtained from the 634 nm emission traces) and the energy pooling rate constant, k_p, with equation (4.63). The results obtained are listed in table 6.6. It can be seen that the enhancement factor, ^{762}K, rises from 2.6 at 638 K to 5.8 at 1088 K in mixtures containing 5% NO. This rise in ^{762}K is small in comparison to that obtained for NH_3 (Table 6.5).

Figure 6.17 shows a plot of the logarithm of the rate constant for quenching of $O_2(b^1\Sigma_g^+)$ by NO, k_q^{NO}, against temperature. The line through the points is drawn by eye. However, while the scatter of the points is reasonable it is systematic for the two mixtures shown, since the points for x = 0.05 lie below those for x = 0.08. Further experiments with a weaker mixture (x = 0.03) confirmed this, but the overall second order rate constants, k_q^M, were so close to the values for $k_q^{O_2}$ that sensible values for k_q^{NO} could not be determined. Thus there is a slight concentration dependence, additional to that implied

RUN NUMBER RA101 30 JUN 1981
762.nm SIGMA-NO

RESULTS

fitted	Quenching Const.	: 1.7651E-02	us-1
		: 5.6656E+01	us
	err.	: 3.2273E+02	
fitted	Ratio (K)	: 4.1154E+00	
	err.	: 1.4499E-01	
fitted	Delta Decay Const.	: 1.7000E-03	us-1
	err.	: 1.0006E-01	
	(Total Decay	:-6.3193E-03	us-1)
	(Pre-shock decay	:-4.6193E-03	us-1)
fitted	Integration Time	: 9.3664E+00	us
	err.	: 1.3742E+00	

RATE CONSTANTS (in l mol-1 s-1)

fitted	Quenching : kq	: 2.3619E+06	
	err.	: 1.3454E+07	
fitted	Pooling : kp	: 1.0460E+05	
	err.	: 2.5555E+03	
fitted	Delta decay: kd	: 2.2748E+05	
	err.	: 1.3390E+07	

RUN DATA

	Oxygen	: 95.000	%
	NO	: 5.000	%
	Shock Speed	: 1.128	mm us-1
	Initial Pressure	: 6.620	torr
	P21	: 13.990	
	Initial Temperature	: 295.000	K
	T2	: 899.000	K
	Density Ratio, RO21	: 4.557	
	Xzero	: 160.600	us
	Yzero	: 708.699	mV
	Pre-shock glow, PSG	: 189.000	mV
	Afterglow	: 861.273	mV
FITTING	: NAG	: complete.	
	Iterations: 10	: 495 points.	
	Sum of the Squares	: 5.7691E+06	

* * *

Figure 6.18 A fitted shock trace for O_2/NO at 762 nm emission

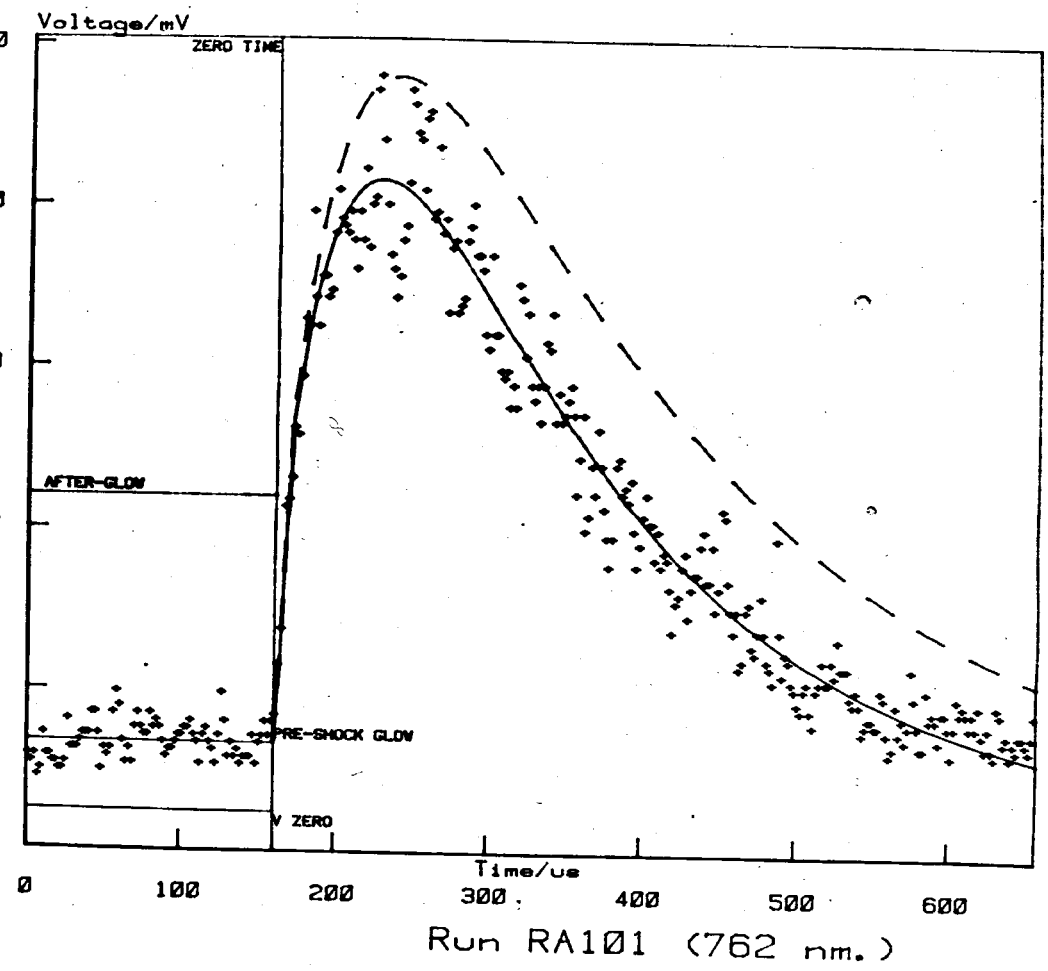

Table 6.6. Analysis of 762 nm Emission Traces, NO Results

Run No.	T_2 /K	^{762}K	t_s /μs	τ_{rel} /μs	k_q^M(cal.) /$dm^3 mol^{-1} s^{-1} 10^6$	k_q^{NO} /$dm^3 mol^{-1} s^{-1} 10^7$	k_p /$dm^3 mol^{-1} s^{-1} 10^5$
				5% NO, 95% O_2			
PA 59	683	2.60	20	94	1.95	1.72	0.60
RA 103	710	3.30	18	89	1.95	1.53	0.67
RA 96	831	3.28	18	55	3.11	2.42	0.95
RA 101	899	4.11	10	56	3.41	2.16	1.05
RA 97	916	3.96	14	41	3.41	2.01	1.43
RA 102	937	3.94	9	34	3.68	2.14	1.60
RA 100	1016	4.31	9	27	4.16	1.86	2.17
RA 99	1068	5.00	3	22	4.13	0.95	2.98
PA 60	1088	5.78	2	22	3.90	-	3.31
				8% NO, 92% O_2			
RA 95	762	2.56	10	33	3.82	2.99	1.09
RA 93	806	2.69	15	22	5.05	4.16	1.50
RA 91	832	3.28	11	31	4.61	3.46	1.23
RA 92	941	3.73	12	19	5.66	3.88	2.15
RA 94	951	4.30	8	23	5.20	3.23	1.90

in equation (6.11). The possibility of a termolecular reaction between NO and $O_2(b^1\Sigma_g^+)$ similar to that for the ground state molecule was considered, but it was found that the effect would be negligible for any reasonable rate constant. Figure 6.17 shows that the rate constant for quenching of $O_2(b^1\Sigma_g^+)$ by NO is nearly independent of temperature with a slight fall above 1000 K.

(c) HCl

The form of shock trace obtained for O_2/HCl mixture was similar to that observed for O_2/NO mixture (see figure 6.3b). 634 nm results indicated that $O_2(a^1\Delta_g)$ was deactivated at high temperature (section 6.3.1c) so here the shock traces were analysed using equation (4.64). A fitted shock trace was similar to that shown for NO (figure 6.18).

In these experiments the relaxation was rapid so k_q^M values were determined by the same method adopted for the O_2/NO system.

The values obtained by the fitting for ^{762}K together with quenching rate constants, k_q^{HCl}, are listed in table 6.7. Figure 6.19 shows a logarithm plot of k_q^{HCl} against temperature. It can be seen that k_q^{HCl} increases slightly with temperature.

(d) SO_2

A typical shocked gas emission trace at 762 nm is shown in figure 6.9b. It displays the expected zones. Compared to figure 6.3b, O_2/NO mixture, the relaxation zone is very long. The shock traces were fitted to equation (4.64) and the results obtained are listed in table 6.8. As can be seen the relaxation time, τ_{rel}, is long varying in the range of 40-120 μs depending on the shock temperature and this shows also in the low values of the overall quenching rate constant, k_q^M, obtained by the fitting. This is also indicated by the small size of the enhancement factors which are in the range of 1-2.5 depending on the shock temperature.

Table 6.7. Analysis of 762 nm Emission Traces, HCl Results

Run No.	T_2 /K	^{762}K	t_s /μs	τ_{rel} /μs	k_q^M(cal.) /$dm^3 mol^{-1} s^{-1} 10^6$	k_q^{HCl} /$dm^3 mol^{-1} s^{-1} 10^7$	k_p /$dm^3 mol^{-1} s^{-1} 10^5$
				3% HCl, 97% O_2			
RA 347	599	1.20	14	45	1.87	3.47	0.32
RA 336	678	2.93	14	60	1.69	1.83	1.19
RA 346	705	1.47	11	73	2.69	4.76	0.60
RA 345	707	1.90	10	70	2.23	3.16	0.30
RA 344	725	1.25	17	40	3.30	6.51	1.10
RA 341	838	1.64	15	33	3.92	6.58	1.22
RA 340	893	1.78	13	45	4.14	6.09	0.90
RA 339	964	2.68	11	40	3.86	3.34	1.25
RA 342	1038	2.35	11	27	4.86	4.56	1.72
				5% HCl, 95% O_2			
RA 334	730	2.67	15	42	2.45	2.21	0.30
RA 350	736	1.46	11	60	4.37	6.00	0.30
RA 349	860	2.05	13	50	4.80	5.53	0.34
RA 351	947	2.73	12	43	4.82	4.32	0.90
				7% HCl, 93% O_2			
RA 362	701	1.334	19	21	5.61	6.31	0.96
RA 361	743	1.49	14	36	5.94	6.51	0.60
RA 360	778	2.23	10	40	4.72	4.53	0.50

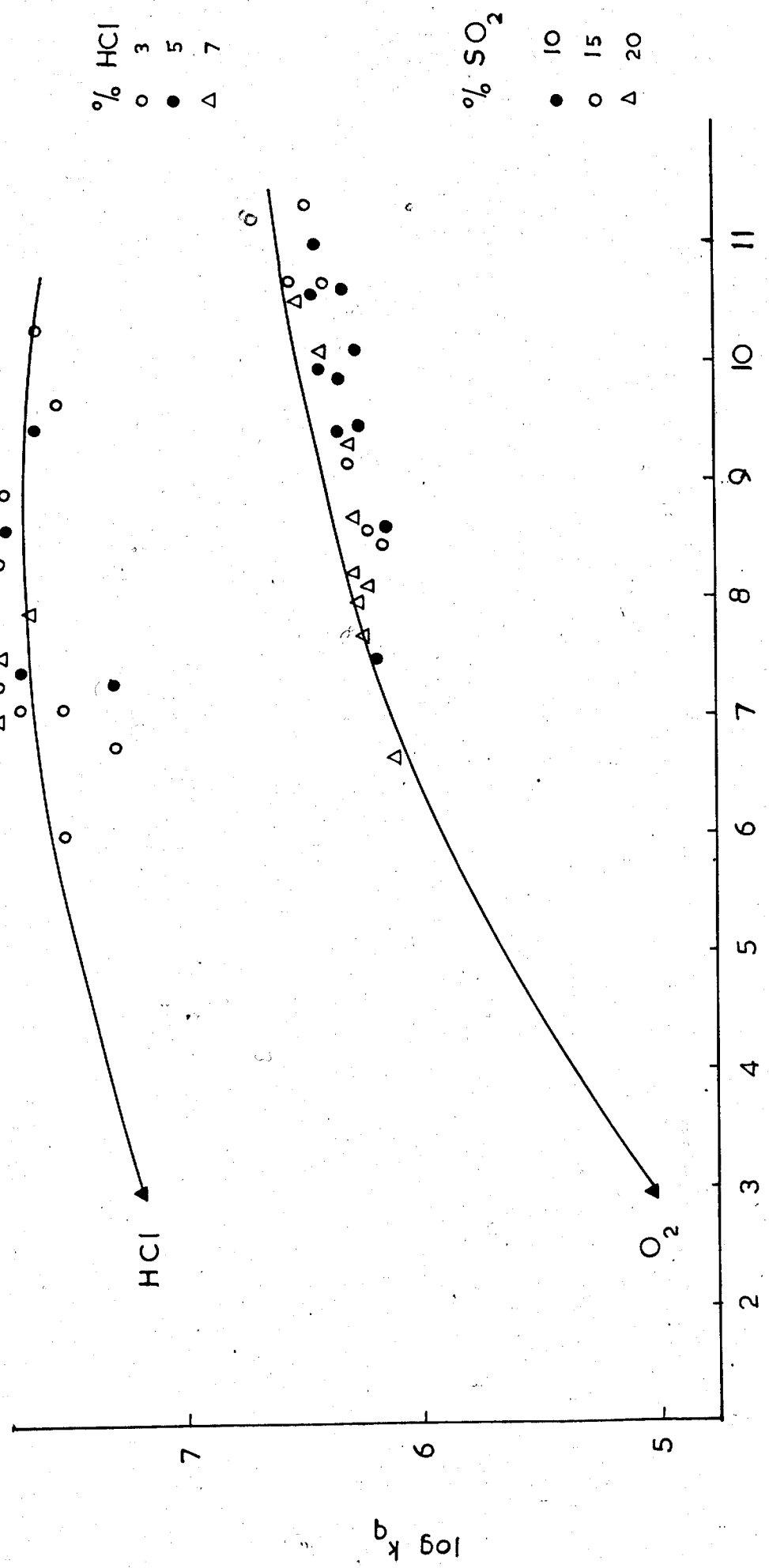

Figure 6.19 Log. of Rate Constants for Quenching of O_2 ($b^1\Sigma_g^+$) by HCl and O_2

Table 6.8. Analysis of 762 nm Emission Traces, O_2 Results

Run No.	T_2 /K	^{762}K	t_s /μs	τ_{rel} /μs	k_q^M(Fitted) /$dm^3 mol^{-1} s^{-1} 10^6$	$k_q^{O_2}$ /$dm^3 mol^{-1} s^{-1} 10^6$	k_p /$dm^3 mol^{-1} s^{-1} 10^5$
					10% SO_2, 90% O_2		
RA 404	753	1.18	14	124	1.36	1.52	1.00
RA 412	863	2.04	13	123	1.17	1.31	1.42
RA 417	943	1.95	11	76	1.80	2.00	2.04
RA 415	946	1.70	7	86	1.62	1.81	1.67
RA 413	988	1.90	12	65	2.00	2.22	2.38
RA 419	989	1.54	10	56	2.22	2.47	2.16
RA 414	1012	1.61	13	81	1.60	1.77	1.56
RA 416	1063	1.74	11	67	1.78	1.96	1.92
RA 423	1070	1.30	13	40	3.14	3.50	2.60
RA 421	1102	1.63	12	50	2.48	2.76	2.47
RA 418	1122	1.40	9	24	4.75	5.28	4.43
RA 422	1130	1.71	11	54	2.16	2.41	2.22
RA 420	1206	2.04	10	62	1.78	1.98	2.10
					15% SO_2, 85% O_2		
RA 431	663	1.67	14	215	1.17	1.37	1.10
RA 432	706	1.72	14	132	1.72	2.02	1.64
RA 429	764	1.67	10	138	1.54	1.81	1.41
RA 424	792	2.13	14	120	1.70	2.00	1.94
RA 425	809	2.15	14	130	1.40	1.65	1.71
RA 430	812	1.67	12	136	1.43	1.68	1.30
RA 426	865	2.06	13	115	1.53	1.80	1.80

Table 6.8 continued

Run No.	T_2 /K	^{762}K	t_s /μs	τ_{rel} /μs	k_q^M(Fitted) /$dm^3 mol^{-1} s^{-1} 10^6$	$k_q^{O_2}$ /$dm^3 mol^{-1} s^{-1} 10^6$	k_p /$dm^3 mol^{-1} s^{-1} 10^5$
					15% SO_2, 85% O_2		
RA 433	934	1.87	7	97	1.74	2.04	1.76
RA 434	976	1.90	15	88	1.76	2.07	1.88
RA 427	1004	2.08	7	70	2.21	2.60	2.52
RA 431	1052	2.23	6	58	2.58	3.03	3.10
RA 435	1081	2.23	9	90	1.60	1.90	1.92
					20% SO_2, 80% O_2		
RA 439	731	1.85	18	137	1.91	2.40	1.88
RA 437	814	2.37	12	140	1.62	2.02	1.87
RA 442	846	2.46	12	180	1.18	1.50	1.35
RA 438	853	2.50	12	160	1.37	1.71	1.68
RA 443	919	2.25	7	100	1.95	2.43	2.25
RA 444	1063	2.27	8	78	2.23	2.80	2.58
RA 445	1067	2.53	9	83	2.08	2.60	2.51
RA 446	1136	2.6	8	72	2.18	2.73	2.83

As shown before (section 6.4) for a binary mixture the observed quenching rate constant, k_q^M, should be the sum of two contributions:

$$k_q^M = k_q^{O_2} x_{O_2} + k_q^{SO_2} x_{SO_2} \quad [dm^3\ mol^{-1}\ s^{-1}] \qquad (6.11)$$

and so for each point $k_q^{SO_2}$ can be determined using the previously[9] determined values for pure oxygen, $k_q^{O_2}$. However, in these experiments the values obtained for k_q^M were less than the corresponding values for $k_q^{O_2}$. For a mixture containing SO_2 the overall quenching rate constant, k_q^M, rises from 1.3×10^6 $dm^3\ mol^{-1}\ s^{-1}$ at 750 K to 1.8×10^6 $dm^3\ mol^{-1}\ s^{-1}$ at 1200 K, the corresponding values for pure oxygen are 1.5×10^6 $dm^3\ mol^{-1}\ s^{-1}$, and 5.0×10^6 $dm^3\ mol^{-1}\ s^{-1}$ respectively. This means that at high temperatures the self quenching by O_2 is much faster than that by SO_2 and that the room temperature quenching rate constant of $O_2(b^1\Sigma_g^+)$ by SO_2, $k_q^{SO_2}$, (table 5.7) is little changed with increasing temperature. Therefore, it is justifiable to consider SO_2 as diluent and calculate values for $k_q^{O_2}$ from equation (6.11) and neglect the SO_2:

$$k_q^{O_2} = k_q^M / x_{O_2}. \qquad (6.12)$$

$k_q^{O_2}$ values obtained this way are plotted against temperature in figure 6.19. The full line in figure 6.19 represents the best line through the previously determined values[9] of $k_q^{O_2}$. All values agree within their combined error limits, table 6.9. The errors are taken from the scatter about the best lines through the points for each set of the results and correspond to 2σ limits (approx. ± 20%). The agreement is encouraging considering that the results are obtained from the study of different binary mixtures. The previous values[9] were determined

Table 6.9. Rate Constants for the Quenching $O_2(b^1\Sigma_g^+)$ by O_2 at various Temperatures

T_2 /K	$k_q^{O_2}$ (previous work) /$dm^3 mol^{-1} s^{-1}$	$k_q^{O_2}$ (this work) /$dm^3 mol^{-1} s^{-1}$
295 a)	$(0.10\pm0.01)\times10^6$	$(0.10\pm0.01)\times10^6$
700	$(1.26\pm0.25)\times10^6$	$(1.35\pm0.27)\times10^6$
800	$(1.74\pm0.34(\times10^6$	$(1.74\pm0.34)\times10^6$
900	$(2.40\pm0.48)\times10^6$	$(2.20\pm0.44)\times10^6$
1000	$(3.16\pm0.63)\times10^6$	$(2.51\pm0.50)\times10^6$

a) Room Temperature value determined by Pedley[59].

from the study of O_2/N_2 mixtures.

(e) The Energy Pooling Reaction

The rate constant, k_p, for the energy pooling reaction (4.5) is determined from the overall quenching rate constants; k_q^M, k_d^M and the enhancement factor, ^{762}K, for each run by using equation (4.63) and the values of the room temperature rate constants determined in the pre-shock experiments. However, for a quenching system with no deactivation of $O_2(a^1\Delta_g)$ at high temperature k_p is determined from equation (4.54). Thus to determine k_p at high temperature it is necessary only to know the overall quenching rate constants, not the individual contributions. This implies that the accuracy of k_p values depend on the quality of the fitting of the relaxation zone. Where relaxation is very fast less accurate values for k_p might be obtained by the analysis. This is why the previous values of k_p were used in recalculation of k_q^M in the case of NO and HCl as the quenchers.

Figure 6.20a shows a typical plot of k_p against temperature for all mixtures of NH_3. The line drawn through the points is the best line through previous[79] measurements in O_2/N_2 mixtures. It can be seen that points lie on or very close to the line. The similarity between the results for various mixtures shows that there is no composition dependence. This would be expected from eqution (4.5).

Figure 6.20b shows a plot of k_p against temperature for differing mixtures of all quenchers studied in this work. It can be seen that k_p is independent of the additive. The striking agreement between the previous measurements and the current work indicates the validity of the kinetic scheme and the nature of the energy pooling reaction (Chapter 7).

Figure 6.20a Temperature Dependence of the Energy Pooling reaction for NH_3 / O_2 mixtures

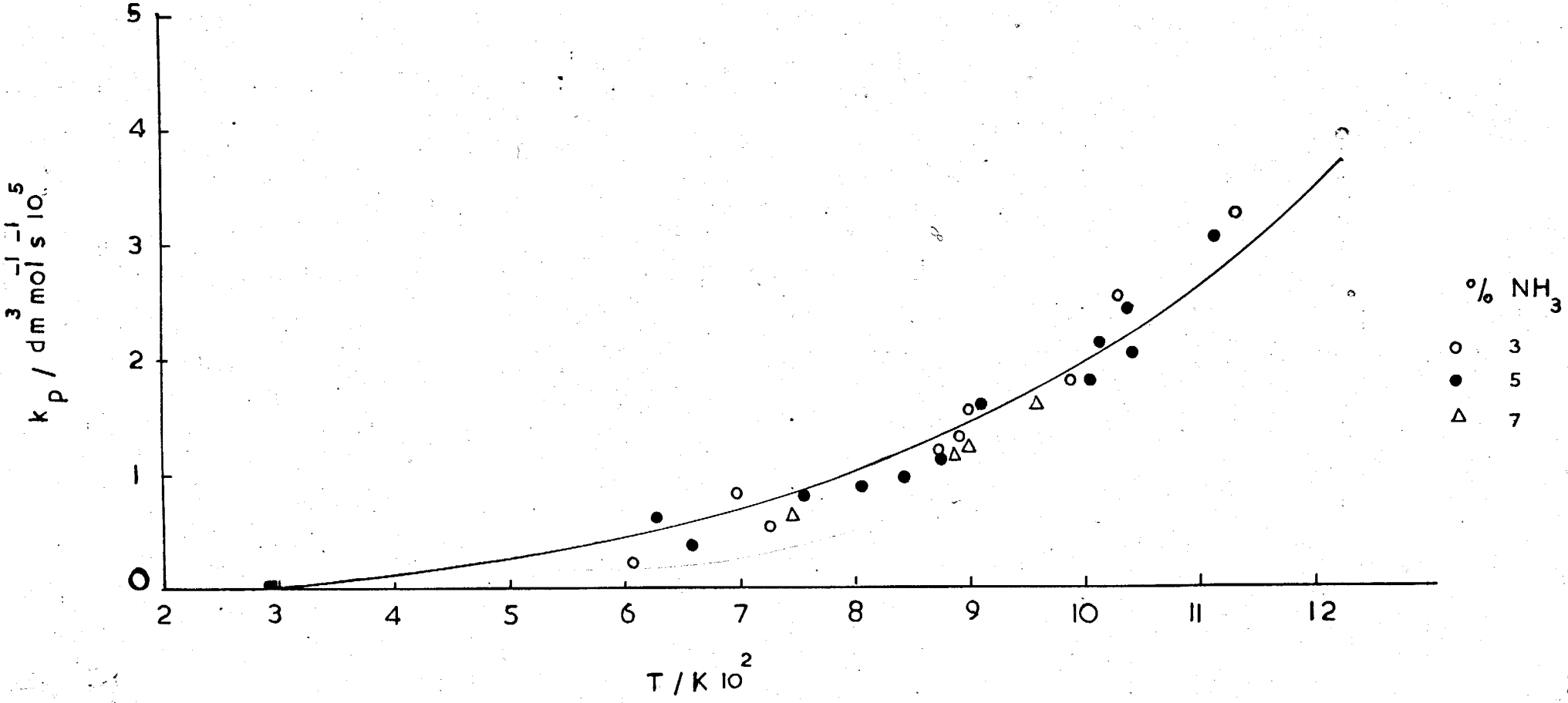

Figure 6.20b Temperature Dependence of the Energy Pooling Rate Constant for M = NH_3, NO, HCl and SO_2

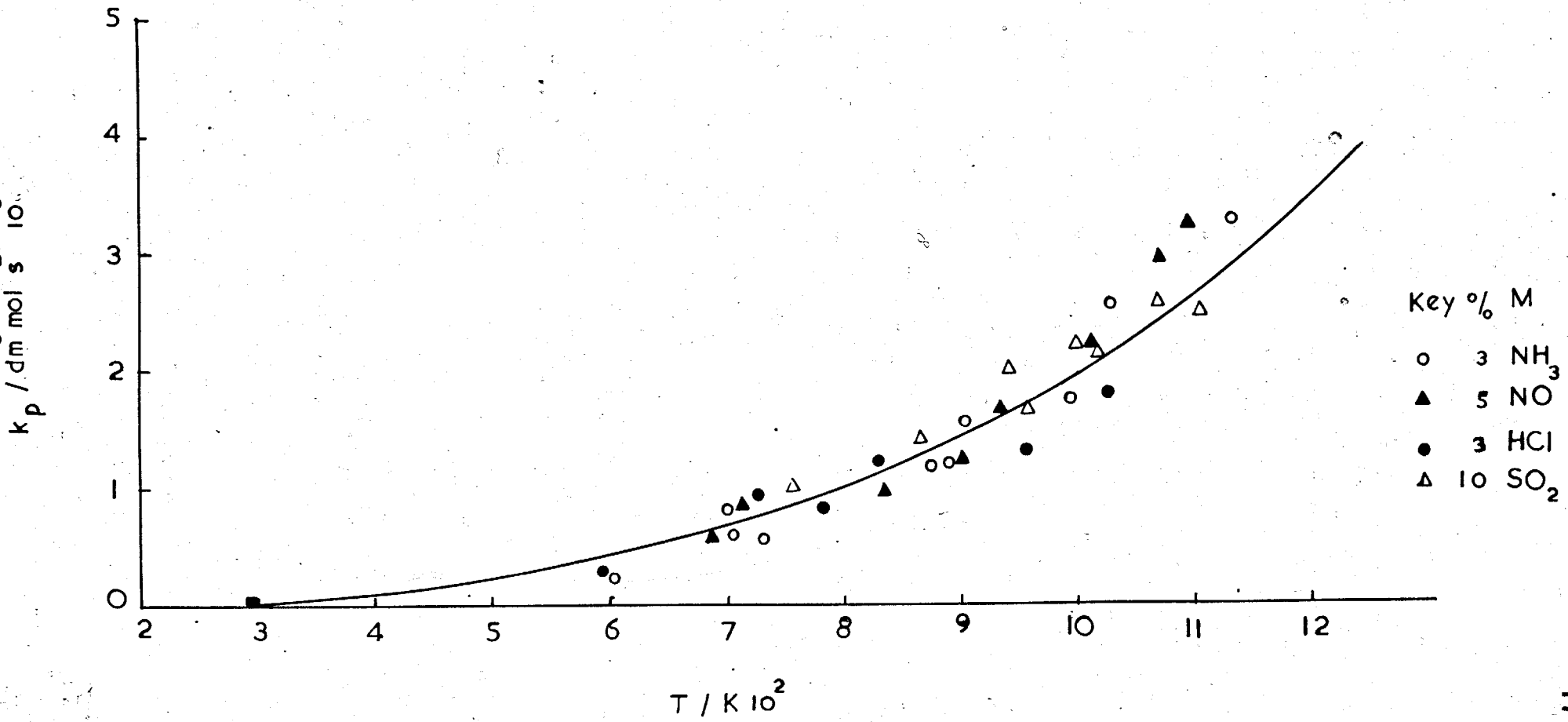

6.5 Additional Emissions

Evidence was obtained for an extra emission at high temperatures in mixtures of O_2/NO, O_2/NH_3 and O_2/HCl.

In mixtures O_2/NO and O_2/NH_3 the new emission appeared at temperatures above 1150 K whereas for O_2/HCl mixtures it appeared at temperatures greater than 1050 K.

In each case the form of the trace for 634 nm emission changed so that the emission intensity began to rise again at times greater than 200 μs. A similar but smaller rise was also noticed at 762 nm. For a typical example see figure 6.21a.

To help identify the source of the glow experiments were carried out on undischarged oxygen plus each individual quencher. The new emission at longer times appeared here too, though the emission from $O_2(a^1\Delta_g)$ and $O_2(b^1\Sigma_g^+)$ was absent. For a typical example see figure 6.21b.

The anomalous emission grew more rapidly and extensively as the temperature was increased.

Thus the new emission lies on the short wavelength side of 762 nm and appears in mixtures of undischarged O_2 and NO, NH_3, HCl at high temperatures.

A further glow was observed after a shock into HCl/O_2 mixtures followed by passing excited molecular oxygen through the tube. This blue green emission (see plate 3) was sufficiently intense to be seen with the naked eye and persisted for $\sim$ 15 minutes. Preliminary experiments to determine the origin of this glow by artificial reproduction, for example by passing discharged oxygen over various metal compounds (e.g. $AlCl_3$, $HgCl_2$, Hg_2Cl_2) was unsuccessful. Also a spectrum of the emission recorded by a Hilger prism spectrograph was unrewarding due to the low resolution.

Figure 6.21 Traces of the Shock Emission at Higher Temperatures showing the extra-emission for the NO / O_2 mixture.

a - 634 nm (R 64, T_2 = 1334 K)

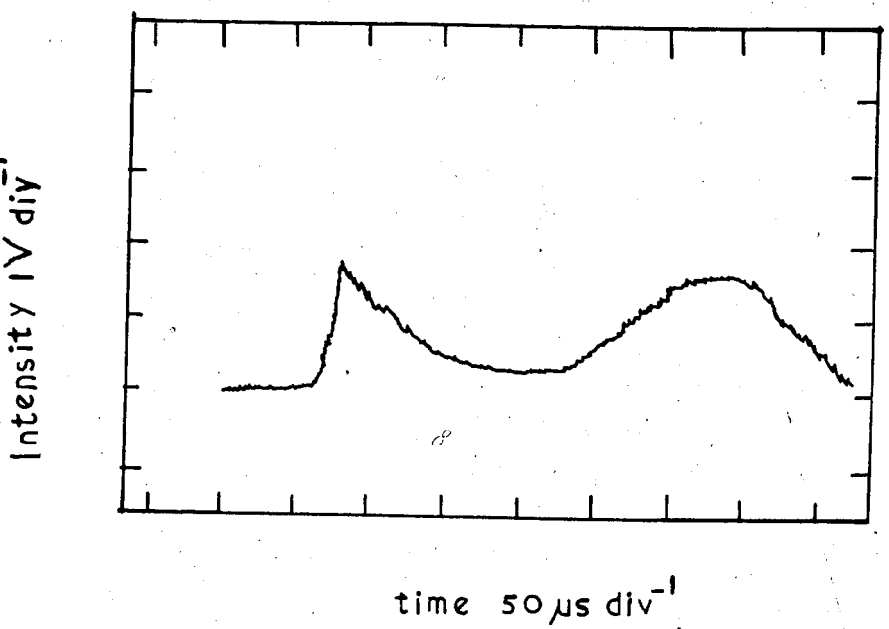

b - 634 nm (RA 64, Discharge off)

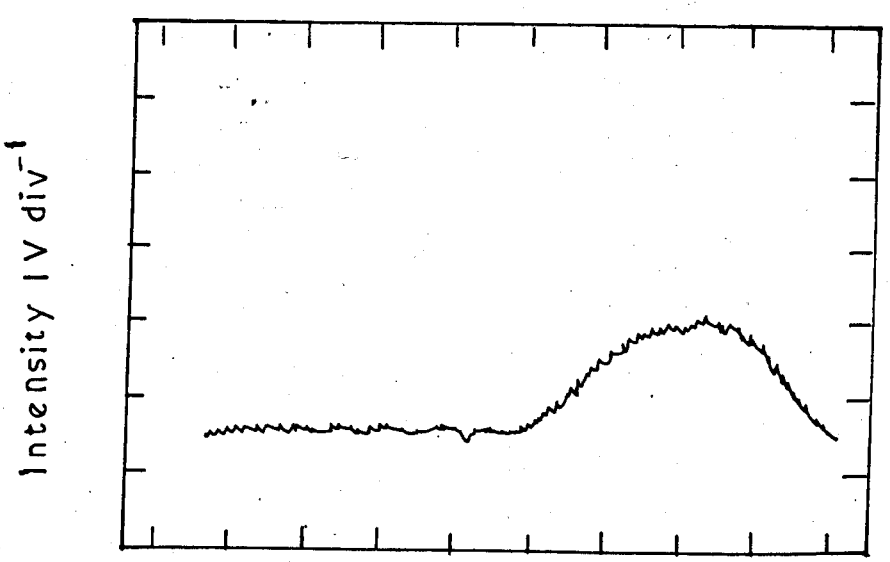

Plate 3

The discharge flow/shock tube, looking towards the discharge. The blue green emission is the glow observed after a shock into HCl/O_2 mixtures followed by passing excited molecular oxygen through the tube. Pieces of aluminium diaphragm carried by the shock are also visible near the end plate.

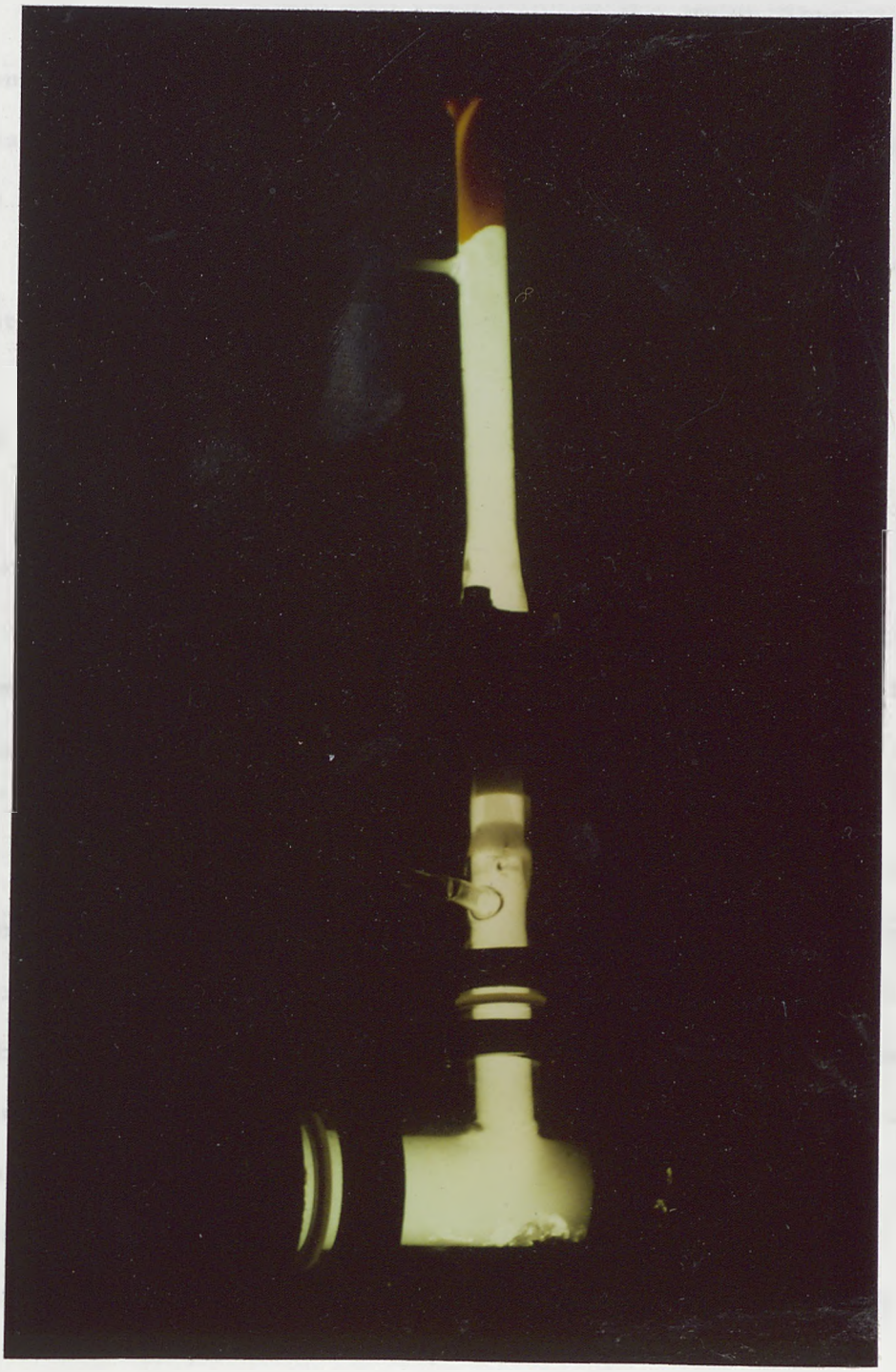

CHAPTER SEVEN

7 Temperature Dependence of the Rate Constants for the Quenching of Singlet Molecular Oxygen by NH_3, NO, HCl and SO_2.

7.1 Introduction

In this chapter the temperature dependences seen for the quenching of singlet molecular oxygen by NH_3, NO, HCl and SO_2 (Chapter 6) and their possible mechanisms in terms of energy transfer are discussed.

Initially the theoretical approaches to quenching in these systems are briefly reviewed.

7.2 The Theoretical Approaches

Kear and Abrahamson[49] developed an approach by considering short range interactions for the energy transfer from $O_2(b^1\Sigma_g^+)$ and calculated quenching rate constants for a variety of quenchers at room temperature. They imagined that the transfer is taking place when the excited molecule and quencher are very close together, on the repulsive part of the intermolecular potential curve.

In their calculations of the quenching rate constant for $O_2(b^1\Sigma_g^+)$ by various quenchers they assumed a value of unity for the electronic matrix element for the $O_2(b^1\Sigma_g^+ \rightarrow a^1\Delta_g)$ transition which, of course, could be too high since this transition is forbidden. Consequently, the calculated rate constants appear to represent upper limits, although the actual predictions gave values which were lower than the experimental values. This approach is similar to the Swartz, Slawsky and Herzfeld (SSH) treatment of vibrational relaxation[8]

and appears to give largely a positive dependence of rate constant on temperature.

Ogryzlo and co-workers[50] have approached the modelling of the quenching of $O_2(b^1\Sigma_g^+)$ from a different direction by considering long range forces. They assumed that for the more efficient quenchers, the energy transfer process occurred at greater intermolecular separation via long range attractive interactions between the transition quadrupole of oxygen and the transition dipoles or quadrupoles of the quencher. The actual predictions gave values which were low but nearer the experimental values than those predicted by Kear and Abrahamson.

A complication in these approaches is the distribution of the electronic energy released between the vibrational modes of $O_2(a^1\Delta_g)$ and the quencher. But here, these theoretical studies stress the importance of the conversion of electronic energy into vibrational energy and assume near resonance between the energy released and the vibrational energy spacing in the quencher favours the energy transfer.

Ogryzlo et al.[51,52] having calculated rate constants for quenching of $O_2(b^1\Sigma_g^+)$ by diatomic molecules at room temperature, which were slightly lower than those observed experimentally, next chose to study the temperature dependence of the quenching of $O_2(b^1\Sigma_g^+)$ by the same model. They studied the quenching of $O_2(b^1\Sigma_g^+)$ by HBr in the temperature range of 170 - 393 K. In comparing their predicted quenching rate constants with the experimental values (see figure 7.1) they suggested that the short range interactions may also contribute to the quenching process. So rate constants were also calculated using the short range interaction model. As can be seen in figure 7.1 the short range interactions lead to a positive temperature dependence while the long range interactions gave a negative temperature

Figure 7.1 Results of Ogryzlo et al.[52]

o Experimental Data

An Arrhenius Plot of the Rate Constant for Quenching of $O_2(b^1\Sigma_g^+)$ by HBr.

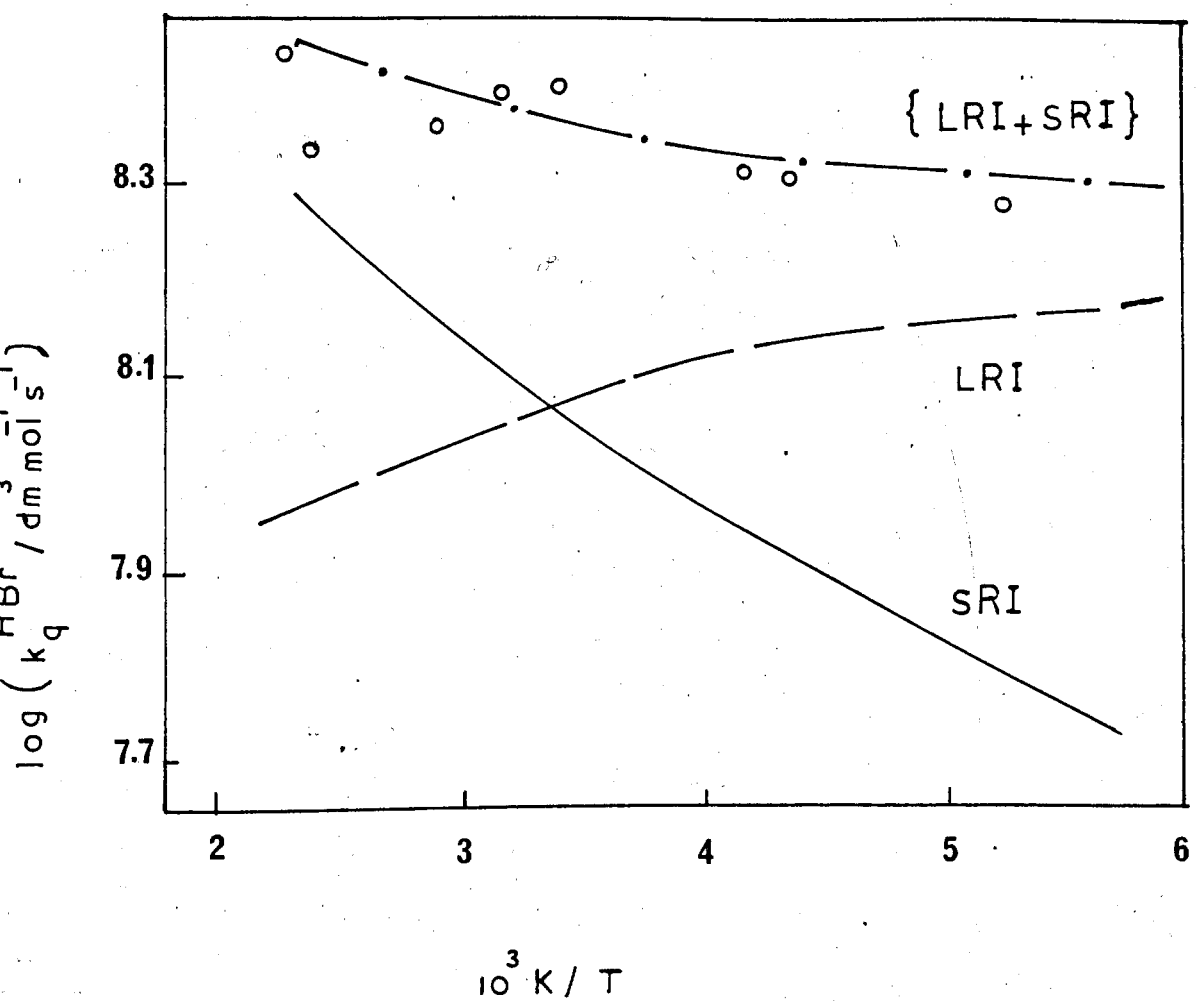

dependence. It was found that the experimental behaviour was best reproduced by adding together the results of the both theoretical approaches. Therefore, they came to the conclusion that both long and short range interactions were important in a given quenching process.

Parmenter and his coworkers[80,81] have developed an alternative long range approach in which energy transfer takes place by formation of a collision complex [A* - M] between the excited species, A*, and the quencher, M.

$$A^* + M \rightarrow [A^* - M] \rightarrow A + M. \qquad (7.1)$$

The correlation is between the cross section, σ, for a reaction of an excited state A* with a series of additives M at a given temperature:

$$\ell n\sigma_M = \text{const.} + \varepsilon(A^*M)/KT \qquad (7.2)$$

where K is the Boltzmann's constant and ε is the well depth energy in the attractive potential curve for the complex between A* and M.

The model is shown to hold for electronic, rotational and vibrational relaxation for both monoatomic and polyatomic molecules provided that the interactions leading to the state change involve predominately attractive forces. Also resonances specific to certain M partners, but not others, must be absent.

While the well depth $\varepsilon(A^*M)$ is not known, they assumed that it can be approximated by:

$$\varepsilon(A^*M) = [\varepsilon(A^*A^*)\varepsilon(MM)]^{\frac{1}{2}} \qquad (7.3)$$

where $\varepsilon(A^*A^*)$ is the well depth between excited species A* and $\varepsilon(MM)$ is that for partners M. Parmenter et al.[80] give well depths for a

large number of quenchers.

The model predicts a straight line relationship between the cross section or rate constant and the well depth for a series of added gases M which collisionally deactivate A*, if the conditions mentioned earlier are met. The correlation may also be used to predict the temperature dependence of the quenching with a specific quencher, equation (7.2), and appears to give a negative dependence of rate constant on temperature.

There are also two main empirical correlations for quenching in these systems. Davidson and Ogryzlo[48] plotted the logarithm of the rate constants for quenching of $O_2(b^1\Sigma_g^+)$ and $O_2(a^1\Delta_g)$ against the highest fundamental vibrational frequency of the quencher, and found a good correlation for the quenching of both species by homonuclear diatomic molecules. The general trend observed was that the quenching efficiency increased with increasing value of the fundamental vibration frequency of the quencher. Based on this they suggested that the quenching process involves the conversion of the electronic excitation energy of singlet molecular oxygen into vibrational excitation in the quencher.

Thomas and Thrush[45,77] having studied the quenching of both $O_2(b^1\Sigma_g^+)$ and $O_2(a^1\Delta_g)$ with a variety of quenchers at room temperature were able to determine the fraction of quenching steps, α_v, which resulted in population of a particular vibrational level in the quenching molecule. Using the statistical theory, they were able to predict the probability of a particular level, P_v, of the quencher being populated in the quenching process. From these data they constructed a surprisal plot, plotting $\ln(\alpha_v/P_v)$ against the fraction of energy released going into vibration, that showed a linear

relationship for the quenching of both $O_2(b^1\Sigma_g^+)$ and $O_2(a^1\Delta_g)$. By this surprisal analysis they also were able to estimate that $\sim$ 25% of the energy released went into translation and rotation. Based on this evidence, they suggested that resonance quenching paths were not particularly favoured, that the quenching mechanism was not specific and that therefore quenching probably occurred on the repulsive part of the intermolecular potential. This partly conflicts with the suggestion of Davidson and Ogryzlo, that the quenching rate constant can be simply related to the ability of the quencher to become vibrationally excited.

This introduction has briefly reviewed the theoretical and emperical studies associated with the quenching of singlet molecular oxygen. Taken together these various studies suggest that the short range interaction will lead to a positive temperature dependence and long range interaction to a negative temperature dependence. Whether resonance exchange is important for the distribution of energy in these transitions is not clear.

In the next section the temperature dependences observed in this work are discussed.

7.3 Discussion of the High Temperature Results

In this section the experimental results obtained in this work for the quenching of $O_2(a^1\Delta_g)$ and $O_2(b^1\Sigma_g^+)$ by NH_3, NO, HCl and SO_2 as a function of temperature (Chapter 6) are discussed in relation to the theoretical predictions outlined in the previous section and the various other experimental data reported in the literature.

7.3.1 Discussion of $O_2(a^1\Delta_g)$ High Temperature Results

It was shown in Chapter 6 that the rate constants for the quenching of $O_2(a^1\Delta_g)$ by NO, HCl and SO_2 increased with temperature and that each set of results could be fitted between 295 K and 1100 K to the simple Arrhenius equations (figure 7.2):

$$k_d^{NO} /dm^3\ mol^{/1}\ s^{-1} = (1.90\pm0.20) \times 10^7 exp[-(2030\pm50)/T)] \quad (6.4)$$

$$k_d^{HCl} /dm^3\ mol^{-1}\ s^{-1} = (2.34\pm1.00) \times 10^7 exp[-(1660\pm180)/T] \quad (6.5)$$

$$k_d^{SO_2} /dm^3\ mol^{-1}\ s^{-1} = (8.90\pm3.45) \times 10^6 exp[-(2370\pm90)/T] \quad (6.6)$$

The exponential parameters correspond to activation energies of 16.9 kJ mol^{-1}, 13.8 kJ mol^{-1} and 19.7 kJ mol^{-1} for quenching by NO, HCl and SO_2 respectively. There are few studies of the temperature dependence of the quenching reactions with which to compare these values, but the observed activation energies and the pre-exponential factors are similar to those found in chemical reaction of $O_2(a^1\Delta_g)$ with various olefins[82].

The sharp increase of rate with temperature suggests that the energy transfer in this quenching reactions take place at short distances where the intermolecular potential is repulsive in form.

Ogryzlo and Thrush[83] used infrared spectroscopy to study the vibrational energy distribution produced in NO by the quenching of $O_2(a^1\Delta_g)$ in the gas-phase, and concluded that transfer occurs preferentially into the v=4 state of NO:

$$O_2(a^1\Delta_g)_{v=0} + NO_{v=0} \rightarrow O_2(\chi^3\Sigma_g^-)_{v=0} + NO_{v=4} \ .\ \Delta H = 6.53\ kJ\ mol^{-1} \quad (7.4)$$

Later Thomas and Thrush[77] in their surprisal analysis, discussed in the previous section, indicated that for most quenchers the energy

Figure 7.2 Arrhenius Plots of the Rate Constants for Quenching of $O_2(a^1\Delta_g)$ by HCl, NO and SO_2

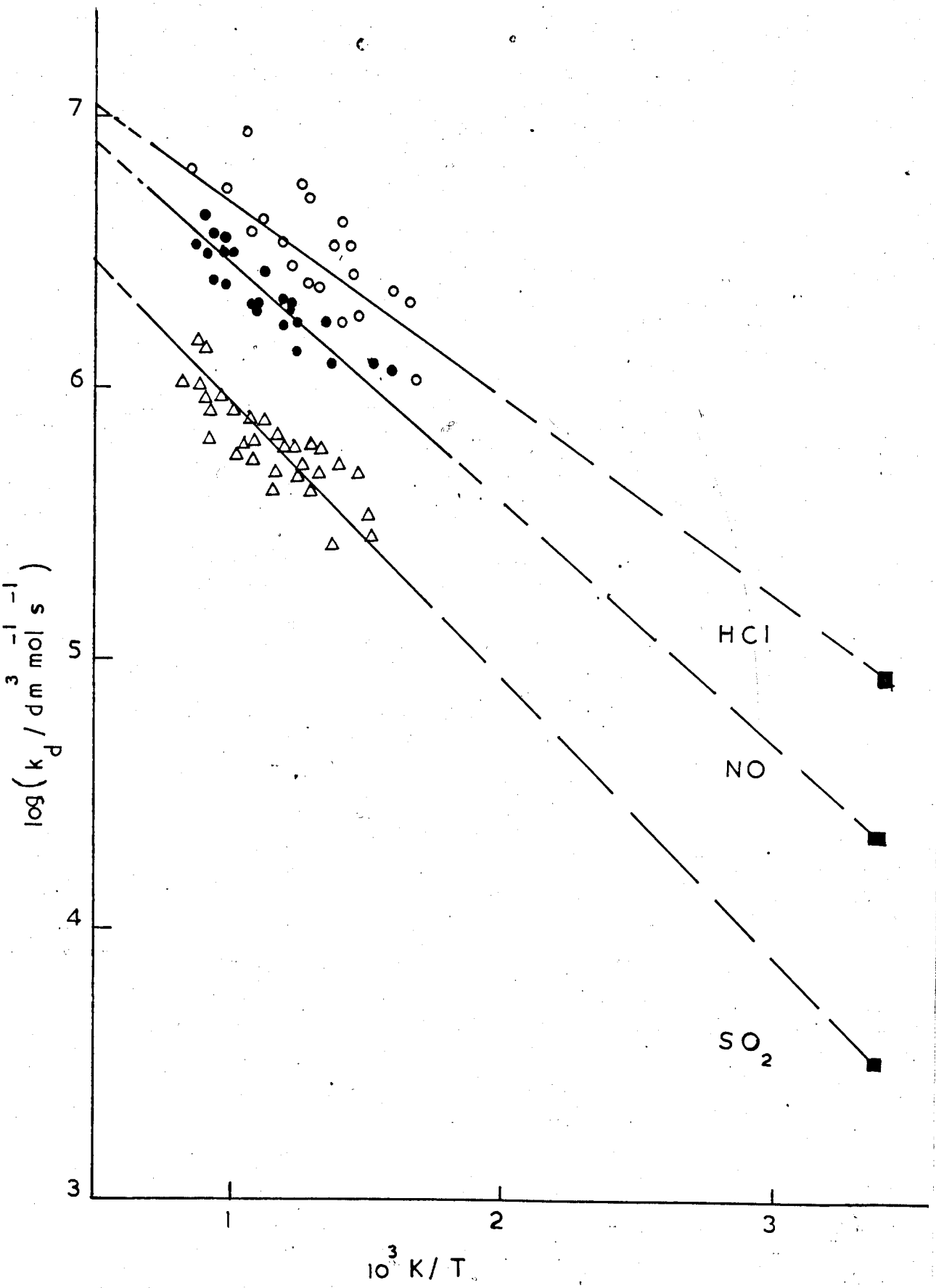

transfer is non-specific. But they also found an exception to this rule, the quenching of $O_2(a^1\Delta_g)$ by NO which predominantly populated both the v=2 and v=4 levels of the quencher. It was therefore suggested that the quenching occurs on the repulsive part of the intermolecular potential as the present temperature dependence of NO also indicates.

However, while our results for HCl and SO_2 are also consistent with the final conclusion, it is hard to understand why the quenching of $O_2(a^1\Delta_g)$ by NH_3 and by several other quenchers studied previously[9,10] in this laboratory (N_2, O_2, CO_2 and N_2O) does not increase measurably with temperature as well, unless the reaction is specific in some way to NO, HCl and SO_2. For these quenchers the observed Arrhenius behaviour implies that there is a favoured channel at $\sim$ 17 kJ above the already excited energy level. Therefore, we can deduce that an activation energy is required to facilitate the energy transfer. However, with polyatomic and diatomic molecules there can be several energy transfer channels at all levels and so it is hard to see why one should be favoured in the case of SO_2, NO and HCl. This perhaps points to a mechanism dependent on a larger interaction potentials with NO, HCl and SO_2 at high temperatures.

7.3.2. Discussion of $O_2(b^1\Sigma_g^+)$ High Temperature Results

Temperature dependences of the rate constants for quenching of $O_2(b^1\Sigma_g^+)$ by NH_3, NO, HCl and O_2 are shown in figure 7.3 together with the results of previous studies[9,10] with other quenchers in this laboratory. The lines for the other quenchers are 'best' lines through the previous results. It can be seen that there is a simple correlation of the type of temperature dependence and the room temperature quenching efficiency. The most efficient quenchers (NH_3,CO_2 and N_2O) show a

Figure 7.3 Plot of the log. of the Rate Constants for Quenching of $O_2(b^1\Sigma_g^+)$ by NH_3, HCl, NO and O_2 against Temperature. Previous results with other gases are also shown.

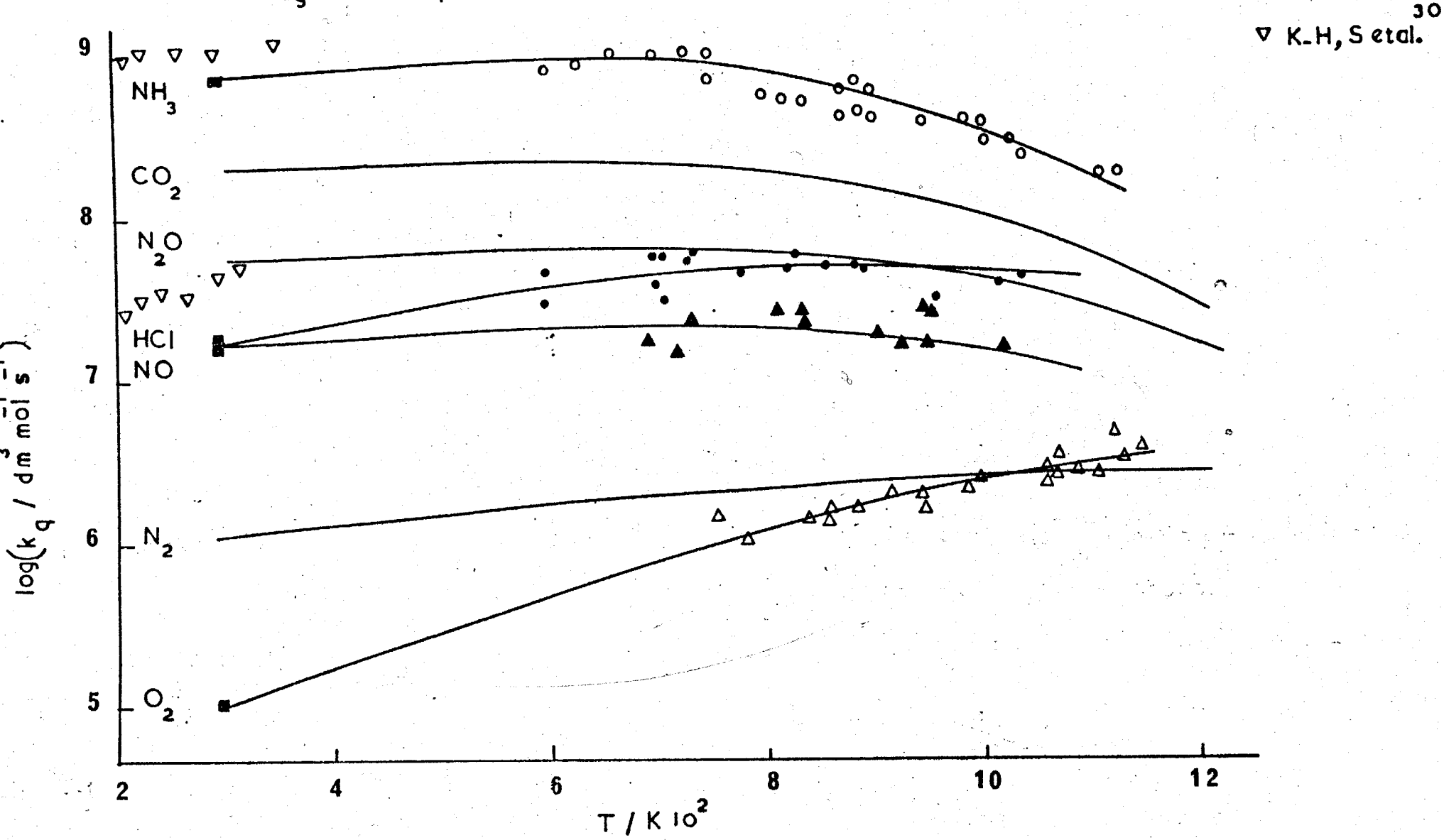

negative dependence of rate constant on temperature and the least (O_2 and N_2) show a positive temperature dependence while the intermediate ones (NO and HCl) are almost temperature independent.

The results for quenching of $O_2(b^1\Sigma_g^+)$ by NH_3 shows that the rate constant rises slightly from (7.50±0.10) x 10^8 dm^3 mol^{-1} s^{-1} at 295 K to a maximum at ∿ 750 K then falls slowly to 2.4 x 10^8 dm^3 mol^{-1} s^{-1} at 1150 K. Also included in figure 7.3 are the five points of Kohse-Hoinghaus and Stuhl[30] obtained recently in the quenching of $O_2(b^1\Sigma_g^+)$ by NH_3 between 200 K and 350 K. They reported their results with a slight positive temperature dependence. Within the combined experimental error limits, the two sets of results combine well with each other and show that when the whole temperature range is taken into account the rate constant does not change appreciably with temperature between 200 K and 750 K. Above 750 K it does decrease. A qualitative picture suggests that the energy transfer at higher temperatures involves a long range mechanism.

For the quenching of $O_2(b^1\Sigma_g^+)$ by NO figure 7.3 shows that rate constant is nearly independent of temperature but falls slightly above 1000 K. It can also be seen that NO, which is a quencher of intermediate efficiency at room temperature, the temperature dependence lies between that of the poor quenchers, O_2 and N_2, where the rate constant increases with temperature, and the efficient quenchers NH_3, CO_2 and N_2O where the rate constants decrease with temperature.

For the quenching of $O_2(b^1\Sigma_g^+)$ by HCl it was found that the rate constant increased slightly with temperature. Figure 7.3 shows the results. Also included in figure 7.3 are the results of Kohse-Hoinghaus and Stuhl[30] who measured the rate constant at six temperatures between 200 K and 350 K using a laser fluorescence method. Within their temperature range they reported a slight positive temperature dependence.

Though we find our room temperature value to be lower than that found by Hoinghaus and Stuhl, the two sets of results fall within the error limits of the experiments. Consequently, when the whole temperature range is taken into account it appears that the rate constant does not vary appreciably with temperature between 200 K and 1000 K. This fits into the pattern discussed before, since HCl occupies an intermediate position being more efficient than O_2 and N_2 and less efficient than CO_2 and NH_3.

Thomas and Thrush[77] have studied the distribution of energy among the vibrational levels of the quencher in the quenching of $O_2(b^1\Sigma_g^+)$, in the surprisal analysis discussed previously. For the quenching with HCl the highest vibration level of the quencher excited was found to be v=2. Of all the quenching processes they studied this was the only process which required more energy than is released in quenching to $O_2(a^1\Delta_g)_{v=0}$;

$$O_2(b^1\Sigma_g^+)_{v=0} + HCl_{v=0} \rightarrow O_2(a^1\Delta_g)_{v=0} + HCl_{v=2} \quad . \Delta H = 5.1 \text{ kJ mol}^{-1} \qquad (7.5)$$

This process is endothermic if $O_2(b^1\Sigma_g^+)_{v=0}$ is quenched to $O_2(a^1\Delta_g)_{v=0}$. By studying the emission spectra they found no evidence for the presence of the necessary concentration of $O_2(b^1\Sigma_g^+)_{v=1}$ nor populated vibrational levels of HCl up to v=4, which would be probable if $O_2(b^1\Sigma_g^+)_{v=0}$ were quenched to $O_2(\chi^3\Sigma_g^-)$. This indicated that the observed rate of excitation of HCl to v=2 was consistent with process (7.5) and that the observation of this level did not imply any deactivation of $O_2(b^1\Sigma_g^+)_{v=0}$ to $O_2(\chi^3\Sigma_g^-)$. They suggested that the energy deficit of 5.1 kJ mol^{-1} was made up from translation and rotation.

Therefore, it was concluded that in a quenching process

involving $O_2(b^1\Sigma_g^+)$ deactivation occurs to $O_2(a^1\Delta_g)$ and not to $O_2(\chi^3\Sigma_g^-)$.

The quenching rate constant of $O_2(b^1\Sigma_g^+)$ by SO_2 could not be determined since the increase with temperature was too slow in comparison to the self quenching of O_2. Therefore, SO_2 was considered as diluent and quenching rate constants were determined for $O_2(b^1\Sigma_g^+)$ by O_2.

As figure 7.3 shows, the rate constant for the quenching of $O_2(b^1\Sigma_g^+)$ by O_2 increases with temperature between 295 K and 1200 K. An arrhenius plot of the results is shown in figure 7.4. It is evident that the Arrhenius plot is not linear. The curved plot suggests that there may be two mechanisms for the energy transfer. At high temperatures, short range repulsive interactions could control the energy transfer while at lower temperatures the transfer may occur via long range attractive interactions. The overall mechanism is consistant with the findings of Ogryzlo et al.[51,52] who concluded that both interations are operative.

In terms of Parmenter's prediction from well depths figure 7.5 shows a plot of the room temperature rate constants for quenching of singlet molecular oxygen by a variety of molecules for which ground state well depths are known. The plot includes NH_3, NO, HCl, SO_2 and O_2 together with the other quenchers studied previously in this laboratory (CO_2, N_2O, N_2).

Two points can be made concerning figure 7.5. Firstly, most of the rate constants for quenching of $O_2(b^1\Sigma_g^+)$ fall on or very close to the line predicted by the theory except O_2, H_2 and D_2. Secondly, none of the values for the quenching of $O_2(a^1\Delta_g)$ fit the line. A common reason for the failure of these quenchers to fit the correlation could be the fact that all show a positive temperature dependence.

Figure 7.4 Arrhenius Plot for Quenching of $O_2(b^1\Sigma_g^+)$ by O_2 and the Energy Pooling Rate Constants.

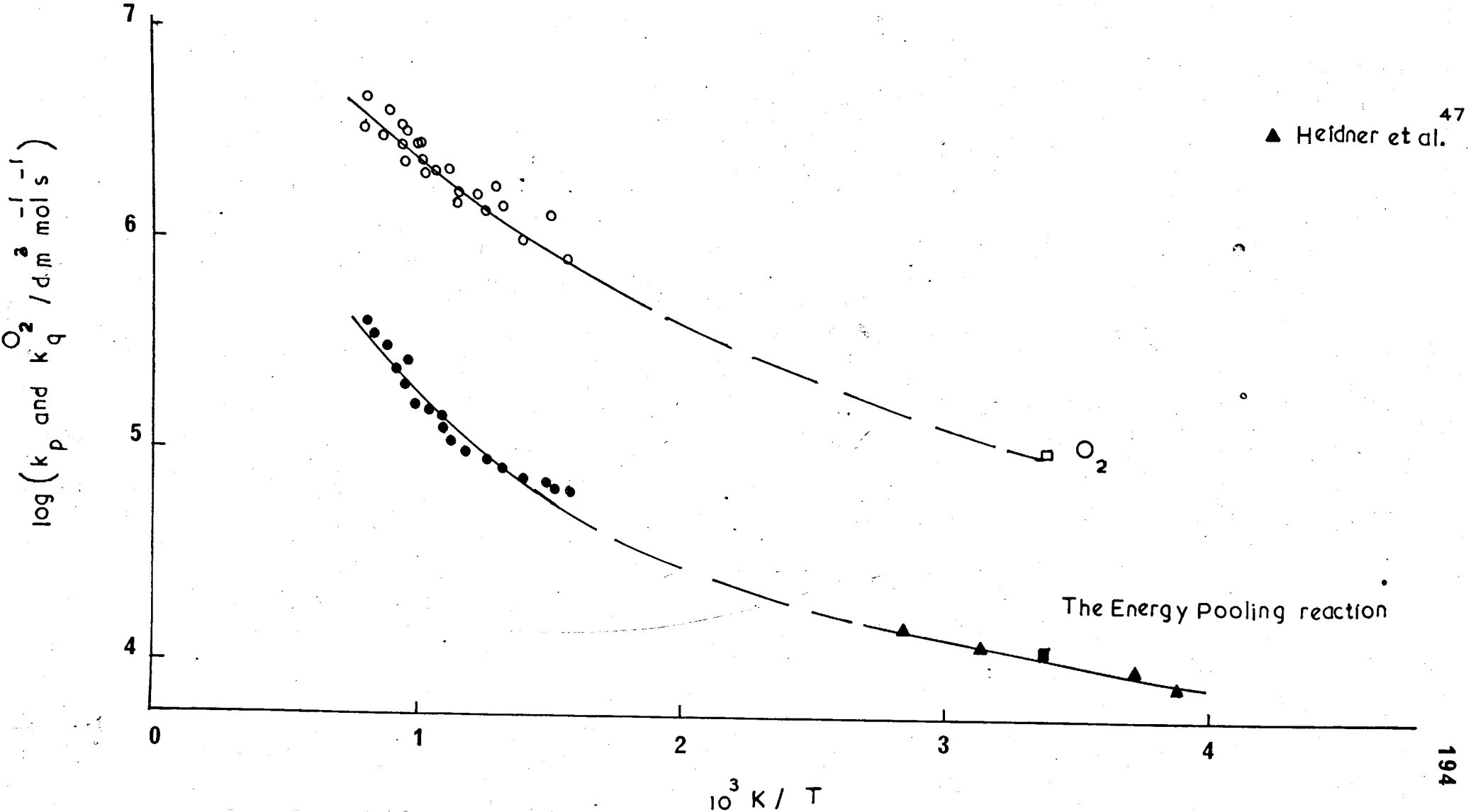

Figure 7.5 Parmenter Plot: the Quenching of $O_2(b^1\Sigma_g^+)$ {•} and $O_2(a^1\Delta_g)$ {▲} by various Quenchers at 295 K.

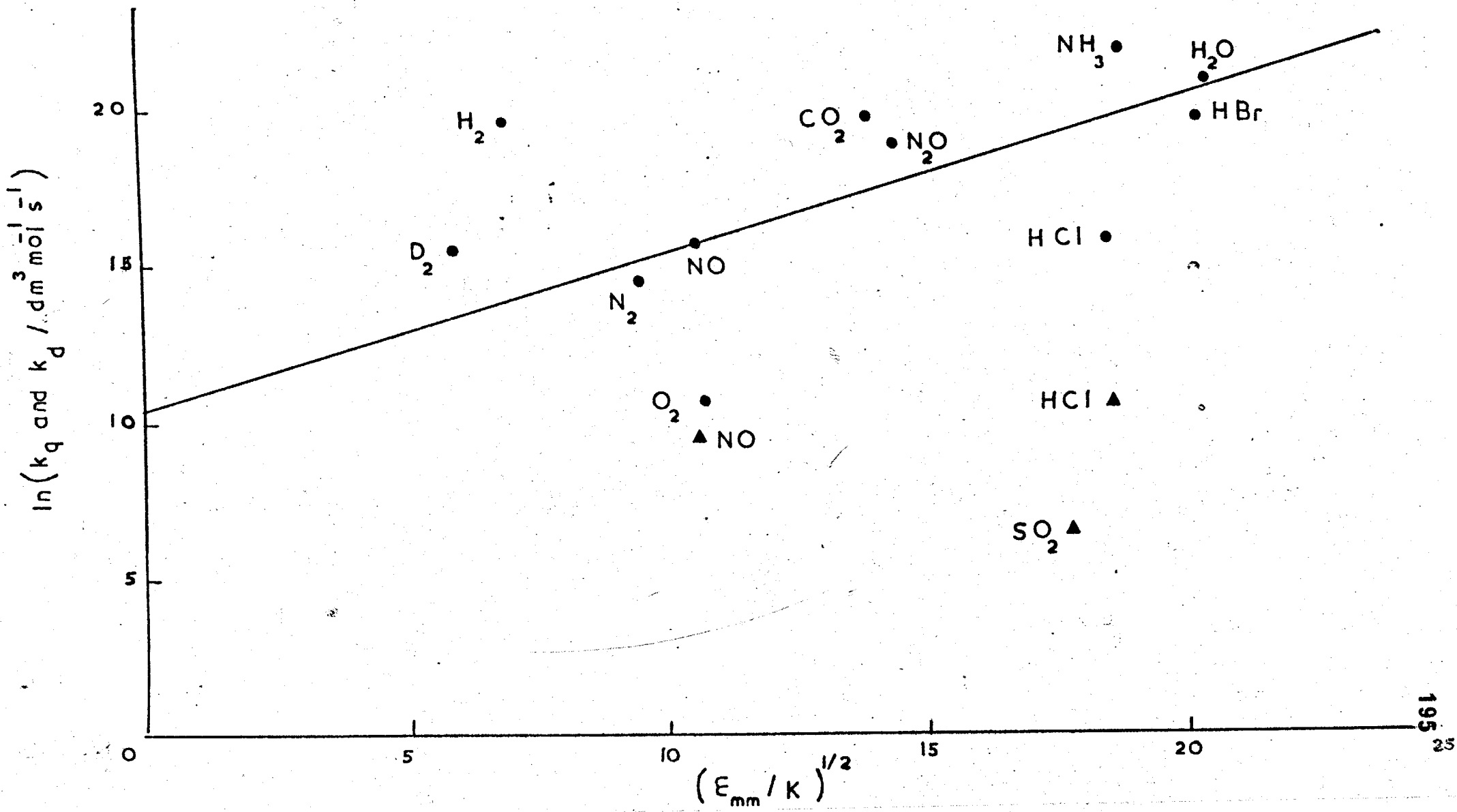

The positive temperature dependences for the quenching of $O_2(b^1\Sigma_g^+)$ by O_2 and $O_2(a^1\Delta_g)$ by NO, HCl and SO_2 have already been discussed. The results of Kohse-Hoinghaus[30] show that the rate constants for the quenching of $O_2(b^1\Sigma_g^+)$ by H_2 and D_2 also increase with temperature.

Thus it seems that at room temperature the Parmenter correlation is valid for the quenching of $O_2(b^1\Sigma_g^+)$ provided that it involves only long range interactions. Once again, for the quenching of $O_2(a^1\Delta_g)$ by NO, HCl and SO_2 the evidence points to a mechanism which perhaps involves specific interactions.

To compare the observed decline in the quenching of $O_2(b^1\Sigma_g^+)$ by NH_3 with the model of Parmenter, a graph of the logarithm of the quenching probability for NH_3 against temperature is plotted, see figure 7.6. The full line presents the 'best' line through the results. Also shown in figure 7.6 is the behaviour predicted by the model, the broken line, using equation (7.2). As can be seen the experimental behaviour differs from that predicted. The decline predicted by the model using Parmenter's well depths is much less than that actually observed. So the observed decrease in reaction rate constant at high temperatures can not be accounted for by the well depths in the interaction potential given in the Parmenter model. This was also found to be the case with CO_2 and N_2O as the quenchers, studied previously[10] in this laboratory.

Therefore, the Parmenter correlation appears to hold at a single temperature although, over a wide temperature range the well depths are not realistic enough to account for the observed decline in the quenching rate constants, so the model is not adequate for the prediction of temperature dependence. However, one should be aware that the model was originally designed for highly efficient quenchers which none of ours are.

Figure 7.6 The Quenching Probability of $O_2(b^1\Sigma_g^+)$ by NH_3 as a Function of Temperature.

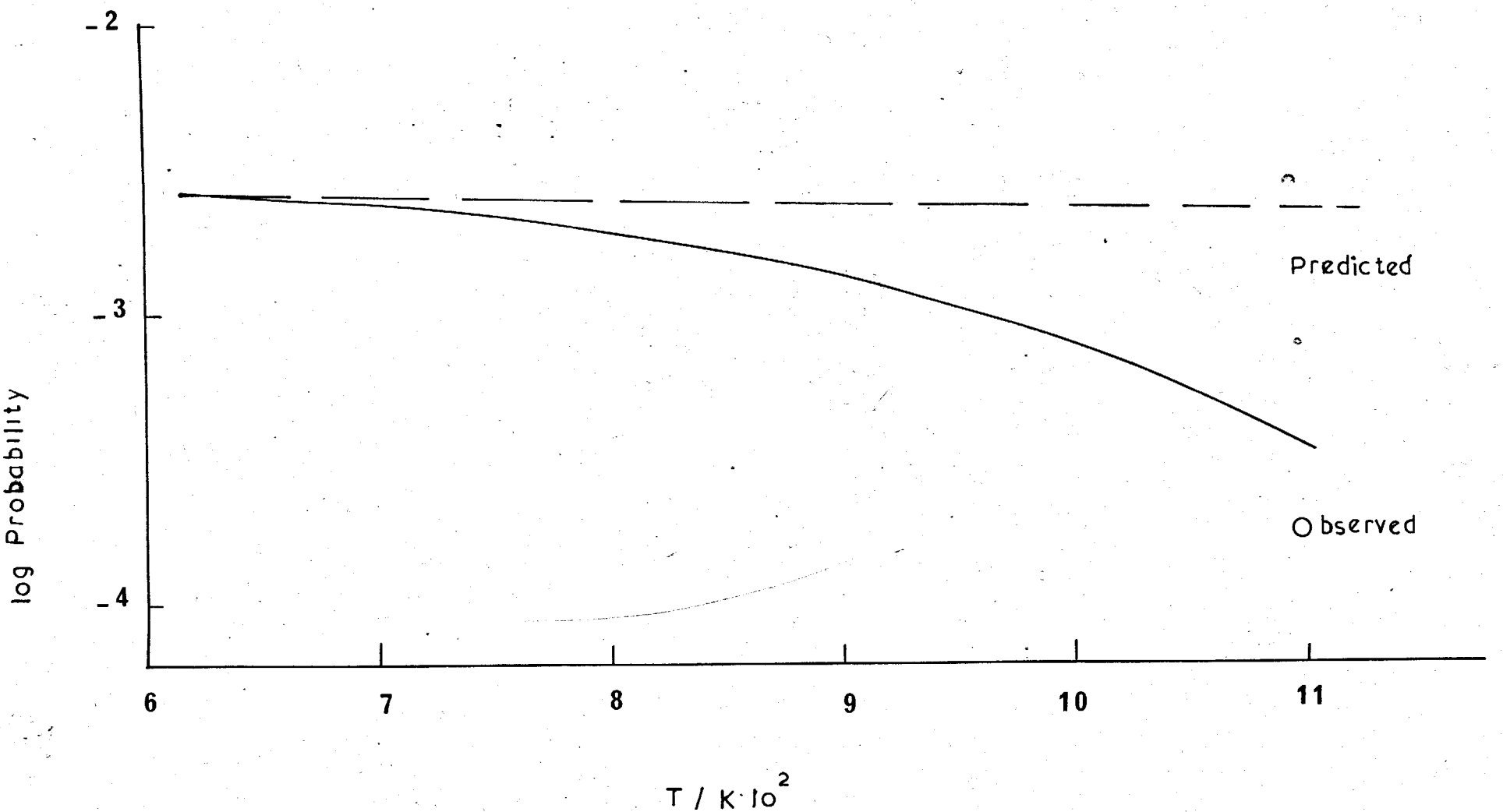

7.3.3 The Energy Pooling Reaction

It was shown in Chapter 6 that the rate constant increased with increasing temperature. An Arrhenius plot of these results is shown in figure 7.4. It can be seen that it has a similar temperature dependence to that observed for the quenching of $O_2(b^1\Sigma_g^+)$ by O_2, also shown in figure 7.4.

Recently Heidner et al.[47] reported results on the temperature dependence of the energy pooling reaction which were obtained in a jacketed flow system between 295 K and 353 K. These are also shown on the Arrhenius plot (figure 7.4) where it can be seen to fit well with our results extrapolated to the room temperature value[65].

Schurath[44] has studied the energy pooling reaction (1.14) by observing the emission from several vibration levels of $O_2(b^1\Sigma_g^+)$ as they formed:

$$2O_2(a^1\Delta_g) \xrightarrow{k_p} O_2(b^1\Sigma_g^+)_{v=n} + O_2(\chi^3\Sigma_g^-) \quad . \quad \Delta H = 1.65 \text{ kJ mol}^{-1} \qquad (1.14)$$

His results showed that v=0 and v=2 transitions were significantly stronger than those expected from the Boltzmann distribution across the vibrational levels of $O_2(b^1\Sigma_g^+)$. However, the overall reaction to v=2, which would be a nearly resonant reaction channel, is thought to be favoured.

The increase in rate constant with temperature which we find, taken with Schurath's work, seems to indicate that the energy pooling reaction is an instance of a near-resonant energy transfer which occurs at short range on the repulsive part of the intermolecular potential curve. Thomas and Thrush[77] in comparing the energy pooling reaction with a variety of quenching reactions, suggested that energy pooling may take place by two parallel mechanisms; one which involves long

range interactions and is nearly resonant, and another involving repulsive short range interactions and giving a more statistical vibrational distribution. Their suggestion partly conflicts with our own and Schurath's findings. However, there is the possibility that the transitions to v=2 and v=0 may have different temperature dependences. This possibility would encompass all three studies. Clearly further investigations are required in order to test the idea.

7.3.4 Concluding Remarks

Although the detailed mechanism of the quenching reactions of $O_2(a^1\Delta_g)$ and $O_2(b^1\Sigma_g^+)$ can not be precisely determined from these experiments, the various results obtained have revealed the following features.

1. The rate constants for the quenching of $O_2(a^1\Delta_g)$ by NO, HCl and SO_2 increase with temperature and the results can be fitted between 295 K and 1100 K to a simple Arrhenius equation (figure 7.2). However, with NH_3 we found no appreciable increase in the rate constant for quenching with temperature, this was also the case with N_2, O_2, CO_2 and N_2O studied[9,10] previously in this laboratory, and so it does seem that the mechanism for quenching by NO, HCl and SO_2 is specific and perhaps points to a mechanism dependent on a larger interaction potential.

2. The results obtained for the quenching of $O_2(b^1\Sigma_g^+)$ by NH_3, NO, and HCl together with the results of the previously examined quenchers show that there is a simple correlation of the type of temperature behaviour and the room temperature quenching efficiency (figure 7.3). The most efficient quenchers show a negative dependence of rate constant

on temperature and the least a positive temperature dependence while the intermediate ones are almost temperature independent. A qualitative picture would suggest that with poor quenchers energy transfer occurs by a short range mechanism on the repulsive part of the intermolecular potential curve, while the efficient quenchers relax by a mechanism which involves long range interactions in the attractive region of the intermolecular potential curve.

3. A comparison is made of the observed decline in rates, for the more efficient quenchers, with the model of Parmenter which unfortunately does not fit, although his suggested correlation of rate constant with well depth is reasonable at room temperature.

4. The rate constant for the energy pooling reaction has been determined from 295 K to 1200 K. The reaction shows a positive temperature dependence. The Arrhenius plot is non-linear (figure 7.4). Based on the temperature behaviour together with some spectroscopic data reported in the literature it is evident that the reaction proceeds via a short range near-resonant mechanism.

5. The temperature dependence of the rate constant for quenching of $O_2(b^1\Sigma_g^+)$ by O_2 obtained from the study of O_2/SO_2 mixtures confirms the behaviour seen previously from the O_2/N_2 mixtures. This confirmation of the results for the quenching by O_2 is important since all other quenching rate constants measured rely on these values. The positive temperature dependence shows a non-linear Arrhenius behaviour (figure 7.4). This indicates that the reaction mechanism must involve repulsive forces but the influence of attractive forces cannot be completely excluded.

6. The studies with mixtures of O_2 and NH_3 have provided a useful check on the validity of our numerical analysis (Chapter 6).

7. For the observed differences between the quenchers of $O_2(a^1\Delta_g)$ and $O_2(b^1\Sigma_g^+)$ there is no general correlation, although some success is achieved by the various theoretical approaches. The present studies of temperature dependence seem to indicate that the mechanisms involved are more complicated and that the results obtained neither can be readily generalised nor be easily predicted with these approaches.

8. An anomalous emission was detected from O_2/NH_3, O_2/HCl and O_2/NO mixtures at temperature above 1200 K. Preliminary tests indicated that the emission was not due to the presence of singlet molecular oxygen. A further glow was also observed after a shock into HCl/O_2 mixtures but in this case it was found that the glow did depend on the presence of singlet molecular oxygen.

CHAPTER EIGHT

The Temperature Dependence of the Dimol Emissions

8.1 Introduction

It was shown in Chapter 4 that if the dimol emission at 634 nm is a simple collisional process then the post-shock glow will be related to that pre-shock by:

$$^{634}I_o = {}^{634}K \; {}^{634}I_{psg} \; \rho_{21}^2 \; T_{21}^{\frac{1}{2}} \qquad (4.42)$$

where ^{634}K is a constant for any enhancement in the emission with rise in temperature and would be unity in the case of a simple collisional process. In equation (4.42); ρ_{21} is the density ratio of shocked (2) to pre-shocked (1) gas, and T_{21} is the temperature ratio.

Figure 6.12 shows that while the original assumption[12] that the dimol emission at 634 nm is a simple collisional process is approximately true (i.e. $^{634}K \cong 1$), there is a further enhancement of the emission at high temperatures.

A similar rise was also seen in the previous studies[57]; it was less well characterised but still noticeable with the other two dimol emissions at 703 nm and 579 nm. At that time the anomalous rise was attributed to an increase in the rate constant with temperature. But this posed difficulties since the rise was not uniform and apparently started rather abruptly near 1000 K. The present results for the quenching of $O_2(a^1\Delta_g)$ by various quenchers (Chapter 6) confirmed this observation since the enhancement factor, ^{634}K, started to increase systematically at temperatures above 1000 K (see figure 6.12).

In view of the anomalous behaviour, it seemed worthwhile to investigate further the temperature dependence of the three dimol emissions of $O_2(a^1\Delta_g)$:

$$O_2(a^1\Delta_g)_{v=0} + O_2(a^1\Delta_g)_{v=0} \rightarrow O_2(\chi^3\Sigma_g^-)_{v=0} + O_2(\chi^3\Sigma_g^-)_{v=0} + h\nu \ (\lambda = 634 \text{ nm}) \qquad (1.10)$$

$$O_2(a^1\Delta_g)_{v=0} + O_2(a^1\Delta_g)_{v=0} \rightarrow O_2(\chi^3\Sigma_g^-)_{v=1} + O_2(\chi^3\Sigma_g^-)_{v=0} + h\nu \ (\lambda = 703 \text{ nm}) \qquad (1.11)$$

$$O_2(a^1\Delta_g)_{v=1} + O_2(a^1\Delta_g)_{v=0} \rightarrow O_2(\chi^3\Sigma_g^-)_{v=0} + O_2(\chi^3\Sigma_g^-)_{v=0} + h\nu \ (\lambda = 579 \text{ nm}). \qquad (1.12)$$

So this chapter reports the variation of visible emission from shock heated $O_2(a^1\Delta_g)$ with temperature. Emissions measured at 634, 703 and 579 nm show an increase with temperature greater than that expected simply from concentration effects on the species preimarily responsible for the transitions. Now the increase is attributed to hot bands overlapping the main transition. From the results rate constants for dimol emissions involving various levels of the upper and lower states are deduced.

In this chapter the reactions studied are written in terms of the vibrational quantum numbers of the upper and lower states, so the above dimol reactions are:

$$(0 + 0) \rightarrow (0 + 0) + h\nu \quad (\lambda = 634 \text{ nm}). \qquad (8.1)$$

$$(0 + 0) \rightarrow (1 + 0) + h\nu \quad (\lambda = 703 \text{ nm}) \qquad (8.2)$$

$$(1 + 0) \rightarrow (0 + 0) + h\nu \quad (\lambda = 579 \text{ nm}). \qquad (8.3)$$

In figure 8.1 tracings of the oscilloscope record of the three emissions are given.

Figure 8.1 Oscillograms showing the time dependence of the various emissions on shock heating.

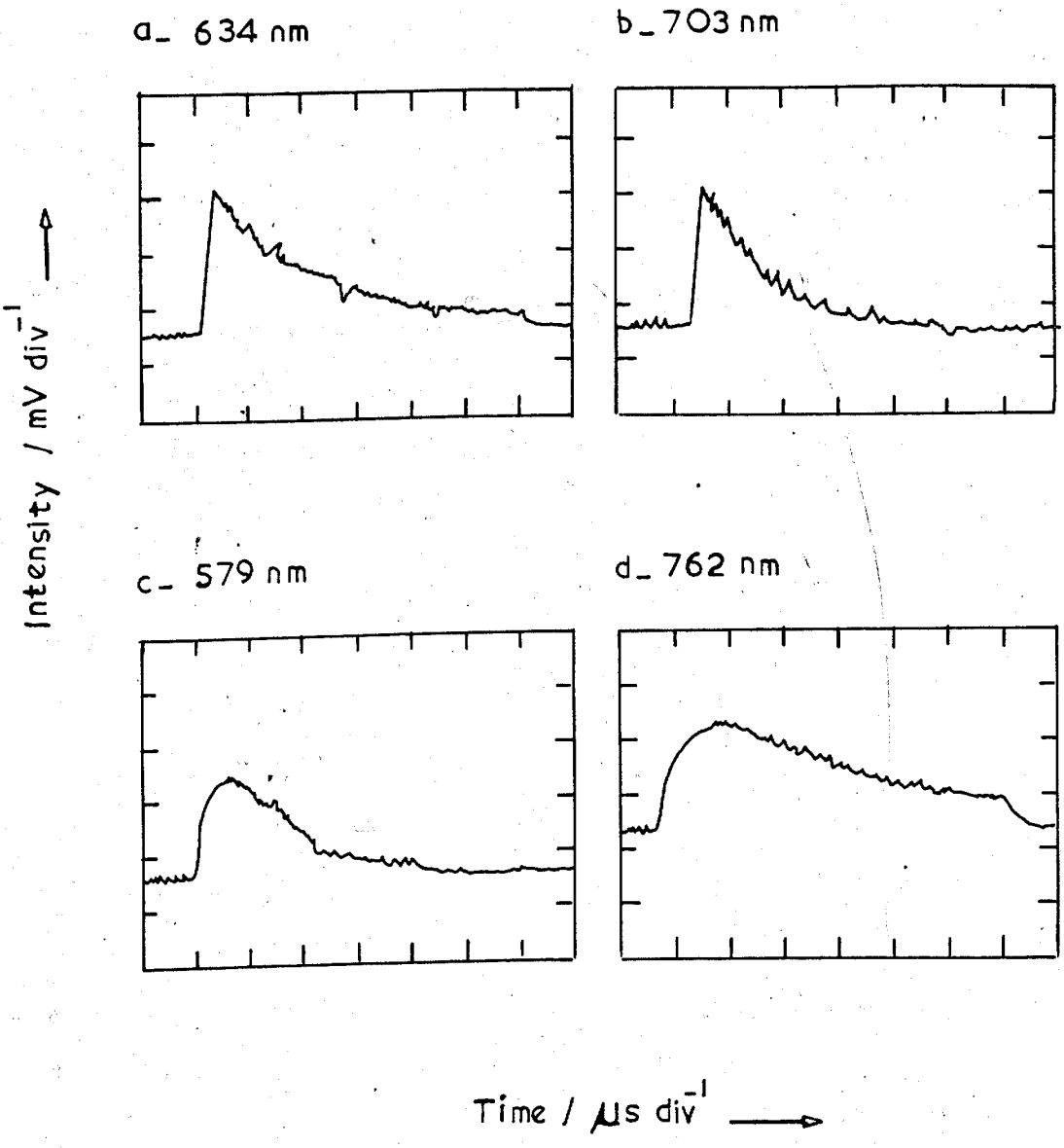

8.2 Experimental

In this work the object was to obtain a comparable series of shocks at various temperatures at each of the three wavelengths. Hence, the experimental procedure described in Chapter 2 was modified.

One photomultiplier with a 634 nm filter was used as a reference throughout the experiments; the other photomultiplier was used for the measurement of pre-shock decay along the tube and to obtain a series of shocked gas traces at each wavelength.

As the emission ratios were measured with a single detector, corrections were unnecessary for the geometry of the system.

The transmission curves of each filter were measured with a Pye-Unicam spectrophotometer. Each of the filters was found to have a maximum transmittance of 40 ± 2% and a half-width of 10 nm.

The fraction of each band seen was estimated by comparing the band area with the filter area. This was done by matching the published dimol spectrum with the measured filter transmission curve and calculating the area of overlap. Dimol spectra were obtained from the following sources; the 634 nm and 703 nm bands from the corrected spectrum of Bader and Ogryzlo[18] obtained in emission, and the 579 nm band from the gas absorption spectrum of Khan and Kasha[17].

Figure 8.2 shows the dimol bands with the transmission curve of each filter superimposed. The transmitted intensity was then calculated as a percentage of the incident intensity for each band. The values obtained are given in table 8.1.

Corrections were also made for the change in photomultiplier sensitivity with wavelength using the manufacturer's data (see table 2.2).

For these measurements singlet molecular oxygen was produced as before (Chapter 2) but then the flow was mixed with a stream of CO_2

Figure 8.2 Filter Transmission and Emission bands:

a_ the 634 nm

b_ the 703 nm

c_ the 579 nm

In each the filter is shown on scale of 2 and the bands are normalized to a scale of 1.

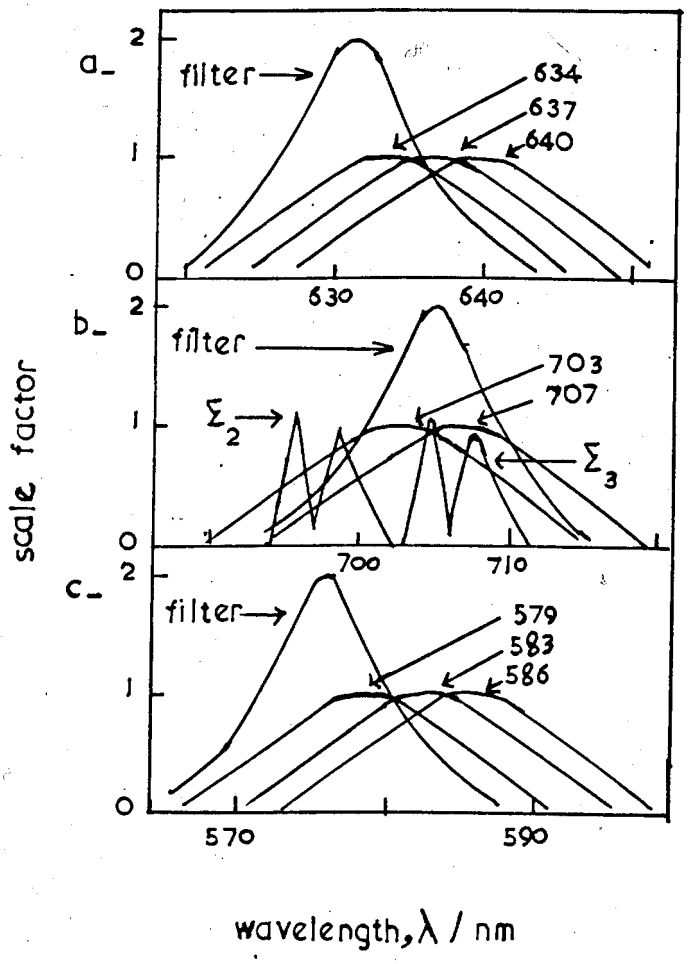

Table 8.1. Filter Transmissions

Filter/nm	Band, λ/nm	Transmittance %
634C	634	26.0
	637	19.0
	640	15.0
703C	703	22.5
	707	17.0
	697	27.8
	706	19.8
703B	703	20.6
	707	19.8
	697	10.8
	706	30.0
579	579	21.4
	583	15.5
	587	10.1

to give a 5% by volume mixture of CO_2 in O_2. The CO_2 was added to speed up vibrational relaxation. This is discussed further in section 8.3.2.

The run parameters are listed in Appendix 5.

8.3 Results

8.3.1 High Temperature Emission Traces

Figure 8.1 shows the emission intensity of the shocked gas as a function of time for the three dimol emissions from the O_2/CO_2 mixture. Also shown in figure 8.1 is the emission from $O_2(b^1\Sigma_g^+)$ at 762 nm for comparison.

Figure 8.1a shows an oscilloscope trace of the 634 nm emission. As can be seen the shocked gas behaviour is similar to that described in Chapter 4.

In figure 8.1b a tracing of the 703 nm emission from shock heated gas is shown. As can be seen it is very similar to that at 634 nm emission. Hence, the kinetic equations derived for the emission at 634 nm (Chapter 4) can be applied to that at 703 nm emission. Consequently the 703 nm shock traces are analysed in a similar manner to those at 634 nm (Chapter 4).

Figure 8.1c shows the high temperature behaviour of the emission at 579 nm. As can be seen the 579 nm emission is markedly different to those at 634 nm and 703 nm. Here we see a relaxation zone. The treatment of the shock trace is shown later. Suffice it to say here that the analysis allows the initial rise, relaxation zone and decay to be fitted as in the case of the 762 emission (Chapter 4) from $O_2(b^1\Sigma_g^+)$, figure 8.1d.

8.3.2 Analysis of the Data

To account for the increase in K with temperature, the data are analysed with a model in which the emission seen is the sum of emission from both the normal and hot bands (a hot band is observed when an already excited vibration is further excited, increase of the population of the initial state, with increasing temperature). To illustrate this an example is given below.

The two bands near 634 nm are:

$$(0 + 0) \xrightarrow{k_0} (0 + 0) + h\nu \ (\lambda = 634 \text{ nm}) \qquad (8.1)$$

$$(1 + 0) \xrightarrow{k_1} (1 + 0) + h\nu \ (\lambda = 637 \text{ nm}). \qquad (8.4)$$

Reaction (8.4) is the first hot band corresponding to the normal band, reaction (8.1). Hence, the filter passes light from both bands and the observed emission, I_{t_p}, at time t_p is:

$$I_{t_p} = k_0\Delta_0^2 + k_1\Delta_1\Delta_0 \qquad (8.5)$$

where Δ_0 and Δ_1 denote the concentrations of $O_2(a^1\Delta_g)_{v=0}$ and $O_2(a^1\Delta_g)_{v=1}$ respectively. k_0 and k_1 are the temperature-independent rate constants and must be multiplied by $T^{\frac{1}{2}}$ to give the normal second order rate constants.

At the shock front the vibrationally cold gas in the pre-shock flow is compressed to give the initial frozen concentrations Δ_0^o and Δ_1^o, and these then relax to the equilibrium values Δ_0^e, Δ_1^e, with a relaxation time τ. Equation (8.5) now becomes:

$$I_{t_p} = k_0[\Delta_0^e + (\Delta_0^o - \Delta_0^e)\exp(-t_p/\tau)]^2$$
$$+ k_1[\Delta_1^e + (\Delta_1^o - \Delta_1^e)\exp(-t_p/\tau)][\Delta_0^e + (\Delta_0^o - \Delta_0^e)\exp(-t_p/\tau)] \quad (8.6)$$

if the relaxation is a simple first order process. Previous studies[57] have shown that the presence of the relaxation zone in the 579 nm emission complicates the analysis. So in the present experiments CO_2 was used to speed up the vibrational relaxation such that to reduce τ to a value which is less than the rise-time of the system. Then, after compression, the emission immediately assumes its equilibrium values so that equation (8.6), with $t_p >> \tau$, becomes:

$$I_{eq} = k_0(\Delta_0^e)^2 + k_1\,\Delta_0^e\Delta_1^e. \quad (8.7)$$

It was shown in Chapter 4 that if the dimol emission reaction is a simple collisional process, then the immediate post-shock emission intensity from the heated gas, I_0, can be related to that from the cool gas, I_{psg}, by:

$$I_0 = I_{psg}(\rho_{21})^2(T_{21})^{\frac{1}{2}} \quad (4.42)$$

where ρ_{21} and T_{21} are the ratios of post- to pre-shock densities and temperatures.

In the pre-shock glow, I_{psg}, virtually all the molecules are in the lowest vibrational state, so that:

$$I_0 = k_0(\Delta_0^o)^2 = k_0\,\Delta_{tot}^2 \quad (8.8)$$

where Δ_{tot} is the total concentration of $O_2(a^1\Delta_g)$.

Now from equations (8.7) and (8.8) the ratio of the equilibrium to the initial emission is:

$$K = I_{eq}/I_0 = (\Delta_0^e/\Delta_{tot})^2[1 + (k_1\Delta_1^e/k_0\Delta_0^e)] \qquad (8.9)$$

where all the concentrations are equilibrium values. The value of K provides a measure of the enhancement of the post-shock emission over that expected from the pre-shock emission.

It was shown in Chapter 4 (section 4.2.1) that the observed emission, I_{t_p}, is related to K by:

$$I_{t_p} = K\, I_{psg}\, \rho_{21}^2\, T_{21}^{\frac{1}{2}} \int_{t_p - t_s}^{t_p} \exp(-\alpha_t t_p)\, dt_p/t_s \qquad (4.46)$$

if there is no appreciable deactivation of $O_2(a^1\Delta_g)$ at high temperature.

As before, in equation (4.46) t_s is the rise-time of the system and α_t is the post-shock decay constant. Once again equation (4.46) is integrated numerically using Simpson's rule. The experimental points for each run are fitted to equation (4.46), first using interactive graphics to obtain a rough fit and then by non-linear least squares to get the best fit. The fitting is described in detail in section 4.2.3. An example of the fit is shown by the full line in figure 8.3. It can be seen to display the expected shocked gas behaviour (see section 4.2.3). The fit for each run gives values of t_s, α_t and K (see Appendix 5 for the results). The post-shock decay, α_t, is compared with that measured in the pre-shock flow with the mobile photomultiplier, suitably corrected for the shock compression; the two values are always found to be similar.

RUN NUMBER R56 11 FEB 1981
634.nm DELTA

RESULTS

fitted Ratio (K)	:	1.5773E+00	
err.	:	1.0737E-01	
fitted Decay Constant	:	-8.0787E-03	μs-1
	:	-9.6499E-03	cm-1
err.	:	2.4429E-01	
fitted Integration Time	:	1.3394E+01	us
err.	:	1.1848E-01	

RUN DATA

Oxygen	:	95.000	%
CO2	:	5.000	%
Shock Speed	:	1.614	mm us-1
Initial Pressure	:	6.620	torr
P21	:	30.200	
Initial Temperature	:	293.000	K
T2	:	1430.000	K
Density Ratio, RO21	:	6.187	
Xzero	:	42.400	us
Yzero	:	354.779	mV
Pre-shock glow, PSG	:	7.100	mV
Afterglow	:	600.416	mV

FITTING

Fitted by NAG	:	complete fit.
No. of iterations	:	5
No. of points	:	319
Sum of the Squares	:	5.2727E+05

* * *

Figure 8.3 A fitted shock trace for O_2/CO_2 at 634 nm emission

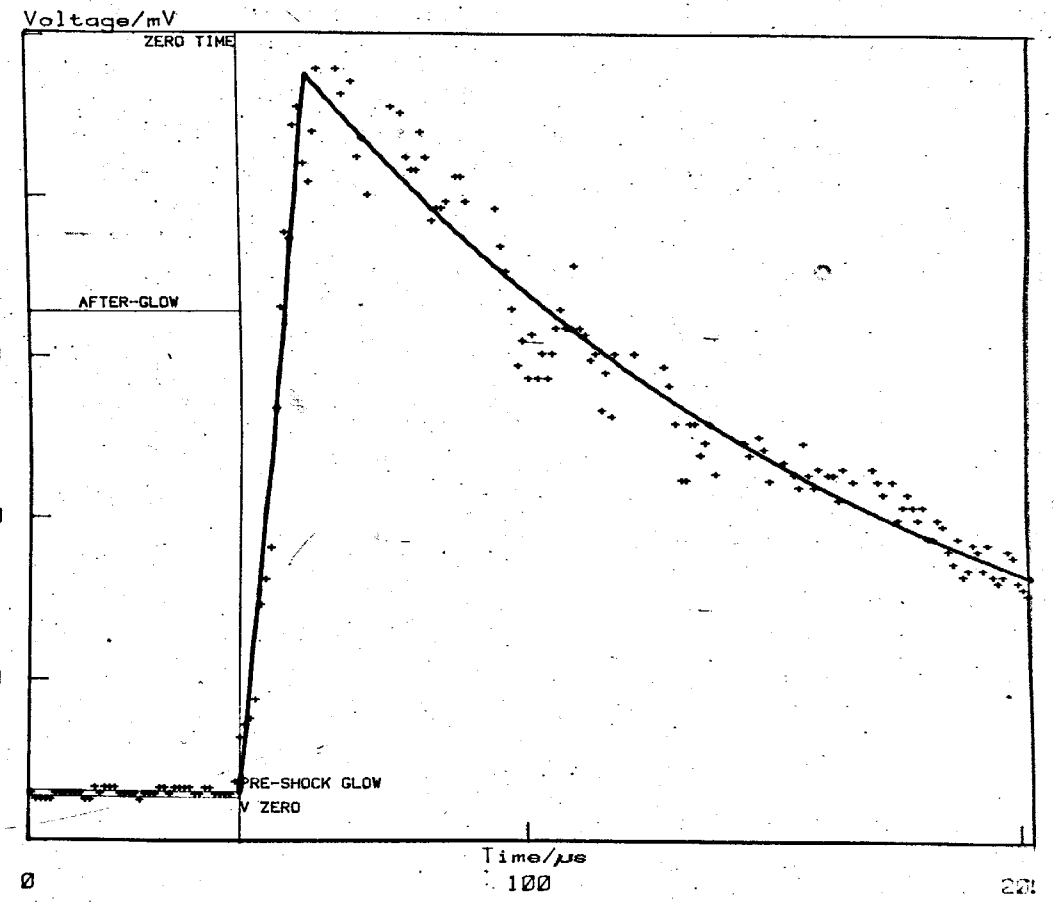

Equation (8.9) can be linearised with respect to temperature to give the ratio of the emission rate constants, k_0/k_1, directly at each temperature for a known value of K.

The concentration ratios can be obtained from the Boltzmann equation[84]:

$$N_j/N = [g_j \exp(- \varepsilon_j/K_B T)]/q \qquad (8.10)$$

where N_j is the population of level j, N is the total population, g_j is the degeneracy of level j, ε_j is the energy of level j; K_B is the Boltzmann constant, and q is the partition function given by:

$$q = \sum_j g_j \exp(- \varepsilon_j/K_B T). \qquad (8.11)$$

For a simple harmonic oscillator equation (8.11) can be approximated by:

$$q = [1 - \exp(- hc\omega/K_B T)]^{-1} \qquad (8.12)$$

where for $O_2(a^1\Delta_g)$

$$hc\omega/K_B = 2131 \text{ K}. \qquad (8.13)$$

Therefore, the concentration ratio from equation (8.10) for $O_2(a^1\Delta_g)$ is:

$$B_v^{\Delta} = \Delta_v/\Delta_{tot} = \exp(- 2131v/T)[1 - \exp(- 2131/T)]. \qquad (8.14)$$

Now substituting for concentration ratios (v=1) in equation (8.9):

$$K = [1 - \exp(- 2131/T)]^2[1 + (k_1/k_0)\exp(- 2131/T)] \qquad (8.15)$$

$$\ln\{\{K/[1 - \exp(- 2131/T)]^2\}-1\} = \ln(k_1/k_0) - 2131/T. \qquad (8.16)$$

Therefore a plot of the left hand side of equation (8.16) against T^{-1} should be a straight line with gradient equal to 2131 K from which the rate constant ratio can be obtained from the intercept.

For these experiments reasonable graphs were obtained but although giving a straight line the gradient was found to be greater than the expected value of 2131 K. So the analysis was enlarged to take into account the second hot bands for the three dimol emissions studied as fundamentals.

(a) The 634 nm Emission

Figure 8.2a shows the transmission curve for the narrow-band filter used in the experiment, together with curves for the possible dimol bands which are listed in table 8.2a. It is assumed that the shapes for the hot bands are similar to those for the normal band, and while the assumption is reasonable it is probably the largest source of error in the intensity estimates.

All the bands in table 8.2a overlap the filter transmission and can add to the observed emission. Still higher hot bands also overlap to a small extent, but these have not been included on the grounds of low relative population and also to keep the number of parameters in the analysis small. The relative populations at 1200 K are also given in table 8.2a for comparison.

Figure 8.4a shows the values of ^{634}K determined from the experimental measurements of emission intensity as a function of temperature.

For the three groups of bands in table 8.2a, ^{634}K can be described by the equation, similar to equation (8.9):

$$^{634}K = (\Delta_0^e/\Delta_{tot})^2[1 + (k_1\Delta_1^e/k_0\Delta_0^e) + (k_2\Delta_2^e/k_0\Delta_0^e] \quad (8.17)$$

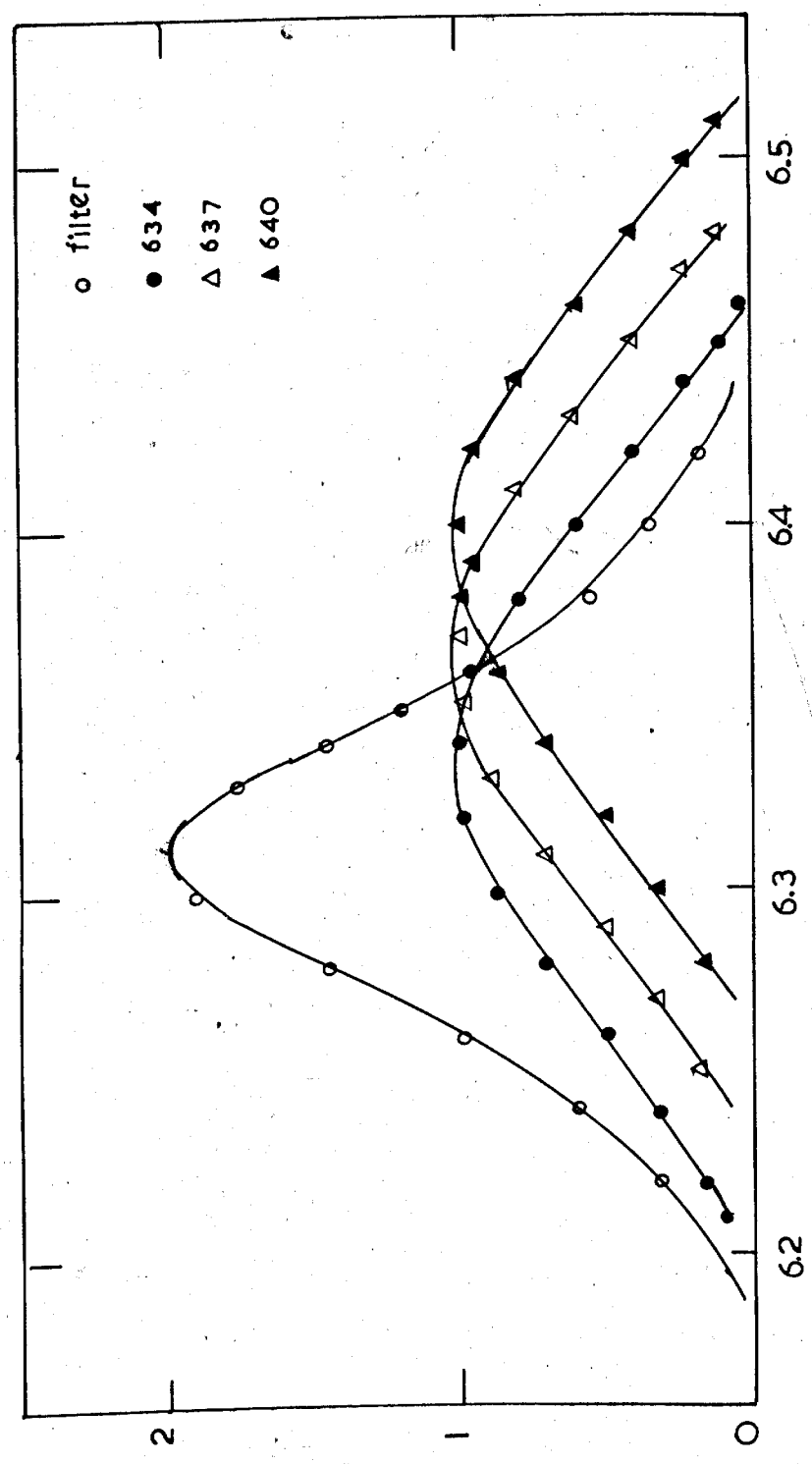

Figure 8.2a Filter 634 nm and the bands

Table 8.2a - Bands at 634 nm

no. of quanta n	transition (v' + v') - (v" + v")	wavelength of maximum, λ/nm	relative population at 1200 K	$\lambda_{k_n}/^{634}k_0$ (measured)	filter factor f_{634}/f_λ	$\lambda_{k_n}/^{634}k_0$ (corrected)
0	(0 + 0) - (0 + 0)	634.3	0.74	1	-	1
1	(1 + 0) - (1 + 0)	637.3	0.12	2.39	1.33	3.18
2	(1 + 1) - (1 + 1)	640.2	0.02	20.3	1.73	35.2
	(1 + 1) - (2 + 0)	639.3				
	(2 + 0) - (1 + 1)	641.3				
	(2 + 0) - (2 + 0)	640.3				

Figure 8.4a Results for 634 nm Emission.

The experimental points show ^{634}K vs. Temperature.

The Full line gives the best fit for eqn. 8.18

The dashed line ⟶ contributions from (0+0→0+0) band.

The dotted line ⟶ the sum of the (0+0→0+0) and (1+0→1+0) bands.

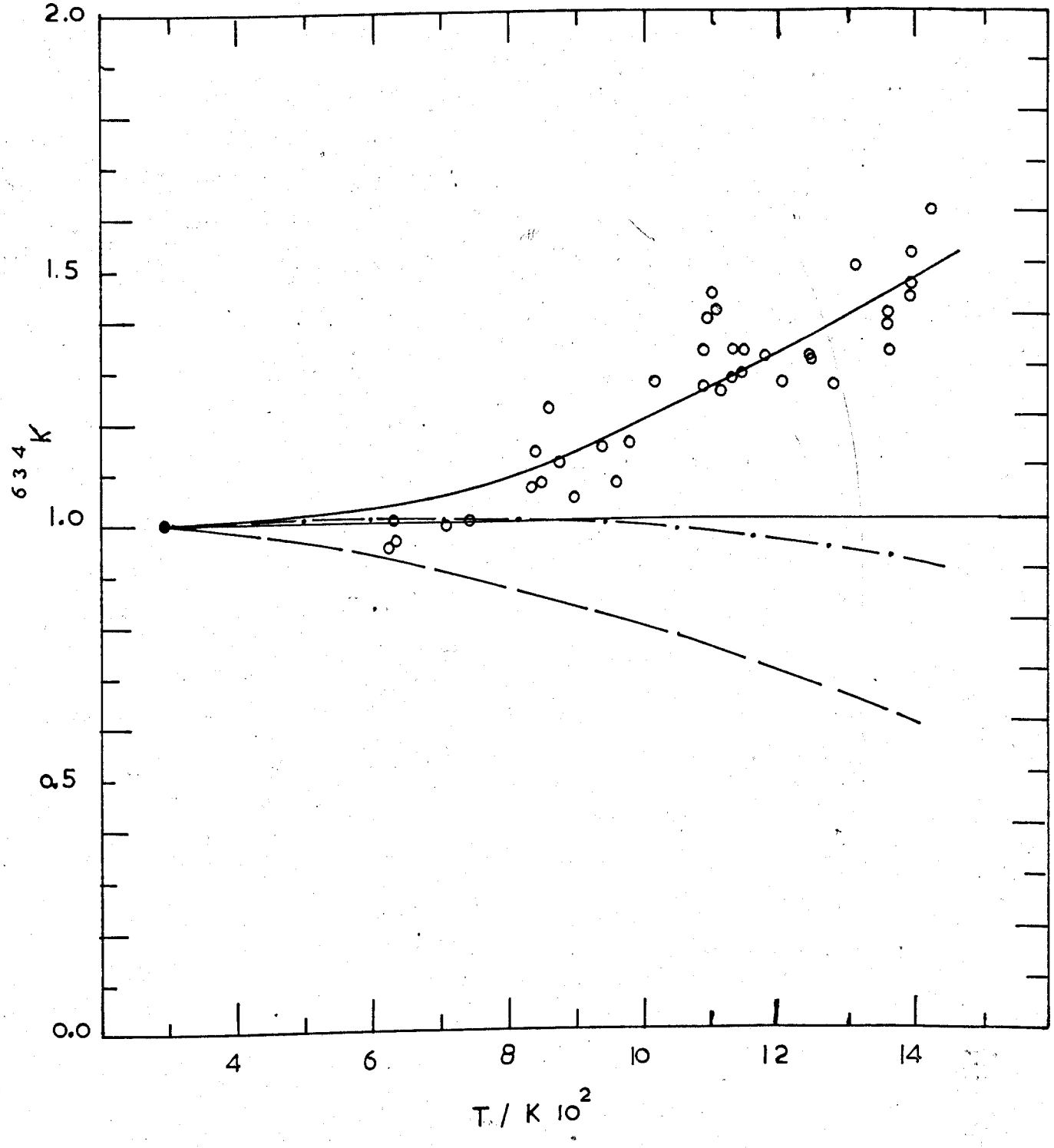

where the concentrations refer to equilibrium values, and k_0, k_1 and k_2 are the rate constants for the three bands. Once again substituting for concentration ratios, given by equation (8.14), equation (8.17) becomes:

$$^{634}K = B_0^{\Delta}[B_0^{\Delta} + (k_1/k_0)B_1^{\Delta} + (k_2/k_0)B_2^{\Delta}]. \qquad (8.18)$$

The final term includes contributions from both of the upper levels (1 + 1 and 2 + 0), the differences due to anharmonicity has been ignored. Thus k_2 is the sum of the rate constants for the four possible transitions (see table 8.2a).

Now equation (8.18) cannot be linearised with respect to temperature, so it has been fitted by non-linear least squares analysis using a NAG routine[85]. The full line in figure 8.4a shows the fit obtained. The heights between the various lines in the figure show the contributions to the emission made from the various bands. At low temperatures only the normal (0 + 0 → 0 + 0) band contributes; as the lowest vibrational level is depopulated at highter temperatures the contribution decreases, while that from the higher bands increases until, at 1400 K, more than half the emission is from the hot bands.

The ratios of the rate constants obtained from the fit are given in table 8.2a and the final column gives the ratio corrected for the differing filter transmissions of the bands. The ratios and the accuracy of the results are discussed later.

(b) The 703 nm Emission

Figure 8.4b shows the measured values of ^{703}K nm emission at temperatures between 600 and 1500 K. Like the 634 nm emission, the emission increases more than expected, but here the increase is double that found for the 634 nm emission to which it might be expected to

Figure 8.4b Results for the 703 nm Emission.

The experimental points are ^{703}K values.

The full line gives the best fit for eqn. 8.23

The dashed line ⟶ contributions from $(0+0 \rightarrow 1+0)$ band.

The dotted line ⟶ the sum of the $(0+0 \rightarrow 1+0)$, the $(1+0 \rightarrow 1+1)$ and $(1+0 \rightarrow 2+0)$ bands.

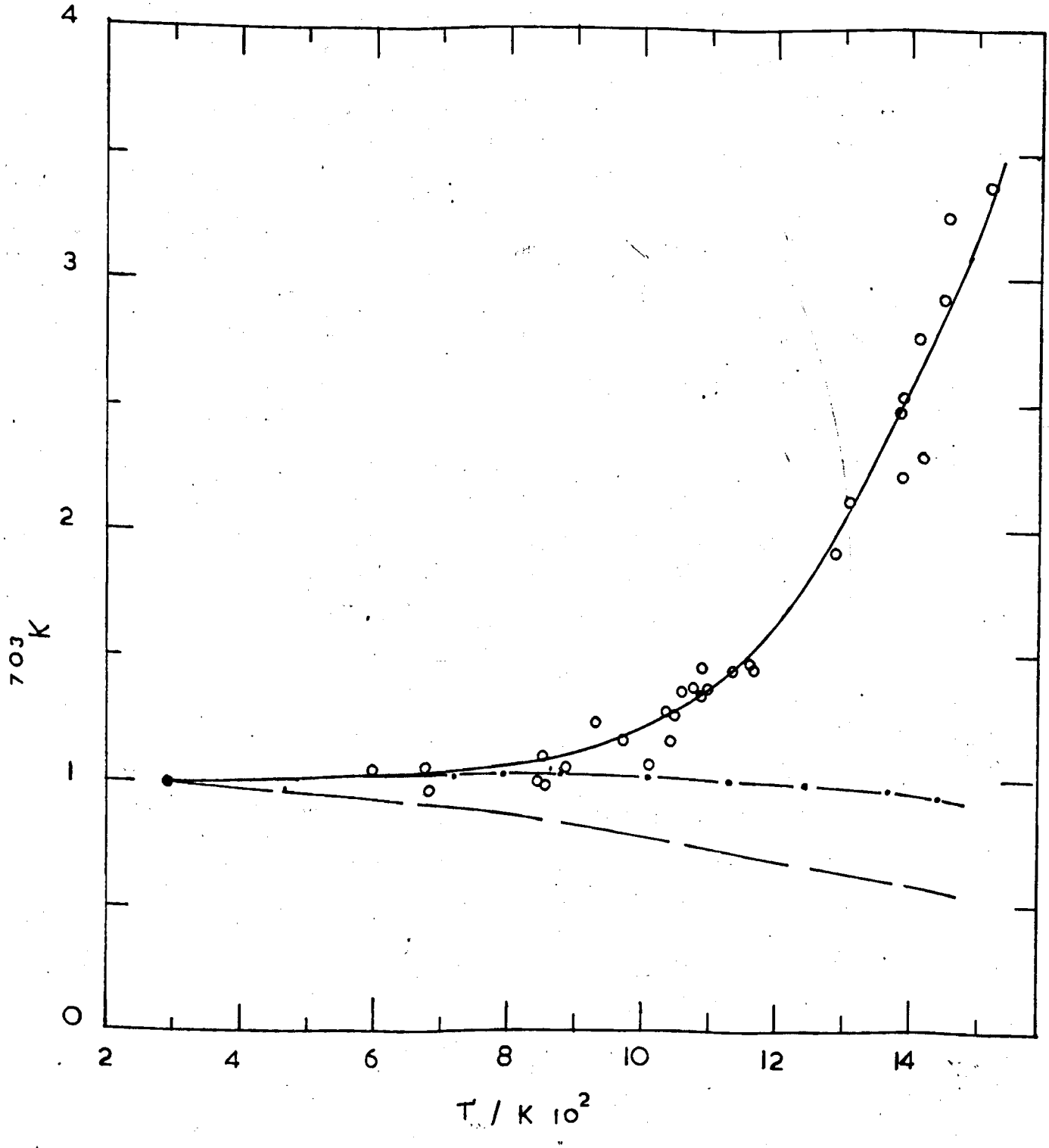

be similar. Examination of the oxygen spectrum in this region shows that not only are there dimol hot bands but also bands from the emission of $O_2(b^1\Sigma_g^+)$; table 8.2b lists these possibilities and figure 8.2b shows the overlap of the various bands with the filter transmission. The envelopes for $O_2(b^1\Sigma_g^+)$ emissions are drawn from the known spectroscopic constants[86] for a temperature of 1200 K. Previous studies[63] have shown that, at our concentrations, $O_2(b^1\Sigma_g^+)_{v=0}$ emission is more intense than that of the dimol emission, so inflation of the ^{703}K value by these bands can be expected.

Following equation (8.7), the emission intensity can be written as:

$$^{703}I = k_0(\Delta_0^e)^2 + k_1\Delta_0^e\Delta_1^e + k_2\Sigma_2 + k_3\Sigma_3 \qquad (8.19)$$

where k_0 and k_1 refer here to the 703 nm emission, k_2 and k_3 are first order rate constants for the $O_2(b^1\Sigma_g^+)$ emission, and Σ_2 and Σ_3 represent the equilibrium concentrations of $O_2(b^1\Sigma_g^+)$ in the second and third vibrational levels.

Following equation (8.9) the enhancement factor, ^{703}K is then:

$$^{703}K = (\Delta_0^e/\Delta_{tot})^2[1 + (k_1\Delta_1^e/k_0\Delta_0^e)] + [(k_2\Sigma_2/(k_0\Delta_{tot}^2T_2^{\frac{1}{2}})] + [k_3\Sigma_3/(k_0\Delta_{tot}^2T_2^{\frac{1}{2}})]. \qquad (8.20)$$

The temperature term $T_2^{\frac{1}{2}}$ is included here since the dimol emission is being compared with $O_2(b^1\Sigma_g^+)$ emission, which is a single molecule transition and would not be expected to show the collisional dependence on temperature that the dimol emissions have (see section 4.2.2).

The constants k_2 and k_3 are related through the known Franck-Condon factors,[87] $k_2/k_3 = 0.711$. The equilibrium concentrations,

Table 8.2b - Bands at 703 nm

no. of quanta n	transition (v' + v') - (v'' + v'')	wavelength of maximum, λ/nm	relative population at 1200 K	$\lambda_{k_n}/^{703}k_0$ (measured)	filter factor f_{703}/f_λ	$\lambda_{k_n}/^{703}k_0$ (corrected)	$\lambda_{k_n}/^{634}k_0$
0	(0 + 0) - (1 + 0)	703.8	0.74	1	-	1	0.83
1	(1 + 0) - (1 + 1)	707.4	0.12	2.59	1.04	2.69	2.24
	(1 + 0) - (2 + 0)	706.2					
		$O_2(^1\Sigma_g^+)_{v'} \rightarrow O_2(^3\Sigma_g^-)_{v''}$ transitions					
2	2 - 1	697.0	-	19.7	1.91	37.5	31.2
	3 - 2	706.1					

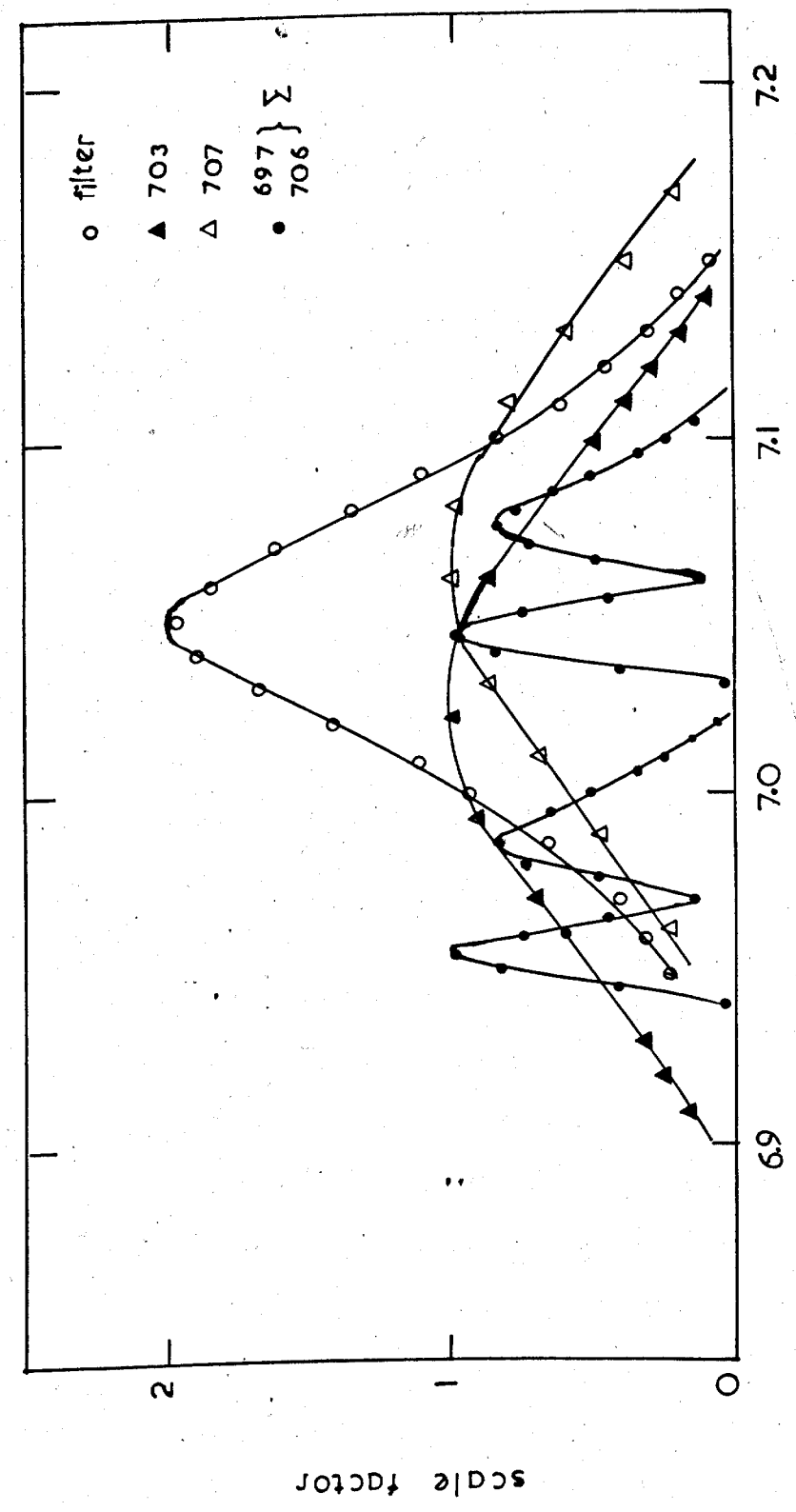

Figure 8.2b Filter 703 nm and the bands.

Σ_2 and Σ_3 are determined from the Boltzmann equation, (8.10), using the characteristic vibrational temperature of $O_2(b^1\Sigma_g^+)$:

$$B_v^{\Sigma} = \Sigma_v/\Sigma_{tot} = \Sigma_{tot}[\exp(-2015v/T)][1 - \exp(-2015/T)] \quad (8.21)$$

where Σ_{tot} is the total concentration of $O_2(b^1\Sigma_g^+)$, which was determined in Chapter 4 (section 4.2.2) by considering a steady state between the energy pooling reaction, (4.5), and the quenching reaction, (4.20). Here, it may be represented as:

$$\Sigma_{tot} = (k_p\Delta_{tot}^2)/(k_q^{O_2}[O_2] + k_q^{CO_2}[CO_2]) = C_\Sigma\Delta^2. \quad (8.22)$$

The values of k_p and k_q have been measured over this temperature range, (Chapter 6) so C_Σ can be determined at each temperature. Thus ^{703}K becomes:

$$^{703}K = B_0^{\Delta}[B_0^{\Delta} + (k_1/k_0)B_1^{\Delta}] + [k_2C_\Sigma/k_0T^{\frac{1}{2}}](B_2^{\Sigma} + \alpha B_3^{\Sigma}). \quad (8.23)$$

The constant α is the ratio of the Franck-Condon factors multiplied by the ratio of the filter factors for the bands.

Once again the rate constant ratios, k_1/k_0, and, k_2/k_0, are determined by fitting the results to equation (8.23) by a non-linear least squares procedure. The full line in figure 8.4b shows the best fit obtained and the heights between the various lines show the contributions made by the two dimol emissions and that from $O_2(b^1\Sigma_g^+)$. At low temperatures only the lowest dimol band produces emission, but at high temperatures the $O_2(b^1\Sigma_g^+)$ emission produces the large increase, and so is responsible for the difference in behaviour between the 703 and 634 nm emissions.

Only one hot dimol band has been included in the analysis although there are others which overlap. When it was attempted to

include the next group of bands, it was found that the term was swamped by the $O_2(b^1\Sigma_g^+)$ term, and the analysis gave unreliable results. Table 8.2b gives the values determined for the rate constant ratios by the analysis.

In order to compare the 703 and 634 nm emissions, the ratios of the emissions were measured in the pre-shock flow in O_2/CO_2 mixtures. For a series of experiments at room temperature the ratio was found to be 0.58. This was corrected for the relative filter transmissions ($f_{703}/f_{634}=1$) and the photomultiplier quantum efficiency ($\phi_{703}/\phi_{634} = 0.70$) so that

$$^{703}k(0 + 0 \rightarrow 1 + 0)/^{634}k(0 + 0 \rightarrow 0 + 0) = 0.83. \quad (8.24)$$

The final column in table 8.2b gives the values of the other bands relative to the 634 nm band.

The rate constant for the emission from $O_2(b^1\Sigma_g^+)$ is determined from the value of $(k_2/^{634}k_0)$ since $^{634}k(0 + 0 \rightarrow 0 + 0)$ has been measured by Fisk and Hays[88] to be 0.0265 $dm^3\ mol^{-1}\ s^{-1}$:

$$k_2 = 0.0265(k_2/^{634}k_0)T_1^{\frac{1}{2}}. \qquad [s^{-1}] \qquad (8.25)$$

Here again the temperature, T_1, is introduced since $^{634}k_0$ is the temperature independent part of the dimol rate constant, whereas the measured value contains the temperature. The value found for k_2 is 0.046 s^{-1}.

(c) The 579 nm Emission

All the dimol bands in this region are hot bands since all come from vibrationally excited $O_2(a^1\Delta_g)$ molecules and so, in the pre-shock flow, the emission is very weak compared with those at 634 nm and 703 nm, but still large enough to be measured at room temperature.

So at the shock front there is a rapid increase in emission due to the increased density and temperature of the shocked gas. It is found to be that which would occur for a dimol emission and is given by:

$$^{579}I_2 = {}^{579}I_1 \, \rho_{21}^2 \, T_{21}^{\frac{1}{2}}. \qquad (8.26)$$

After the instantaneous rise there is a gradual increase to an enhanced level of emission. The other dimol emissions do not show this (see figure 8.1). Following the enhancement there is a decay.

The enhancement observed is shown to be due to vibrational relaxation[56]. Therefore, here the enhancement factor, K, is the ratio of the glow after relaxation to that predicted from the pre-shock glow at 634 nm emission [equation (4.42)]:

$$^{579}K = {}^{579}I_{eq}/{}^{634}I_0 = {}^{579}I_{eq}/{}^{634}I_{psg} \, \rho_{21}^2 \, T_{21}^{\frac{1}{2}}. \qquad (8.27)$$

The pre-shock glow at 634 nm was measured both with the photomultiplier used for the 579 nm measurements and with the reference photomultiplier to obtain a correction factor to account for the difference in sensitivity of the two detectors and filters for the 634 nm emission.

The values of ^{579}K found between 600 and 1500 K are shown in figure 8.4c. Because of the redefinition of K, the values do not extrapolate to K = 1 at room temperature.

Table 8.2c shows the bands in this region and figure 8.2c shows the overlap of filter transmission with the bands. There are no $O_2(b\,^1\Sigma_g^+)$ bands in this region.

The emission intensity is thus:

Figure 8.4c Results for the 579 nm Emission.

The experimental points are ^{579}K values.

The full line ⟶ the fit obtained by eqn. 8.29

The dashed line ⟶ the contributions from $(1+0\rightarrow 0+0)$ band.

The dotted line ⟶ the sum of the $(1+0\rightarrow 0+0)$, and the $(1+1\rightarrow 1+0)$, $(2+0\rightarrow 1+0)$ bands.

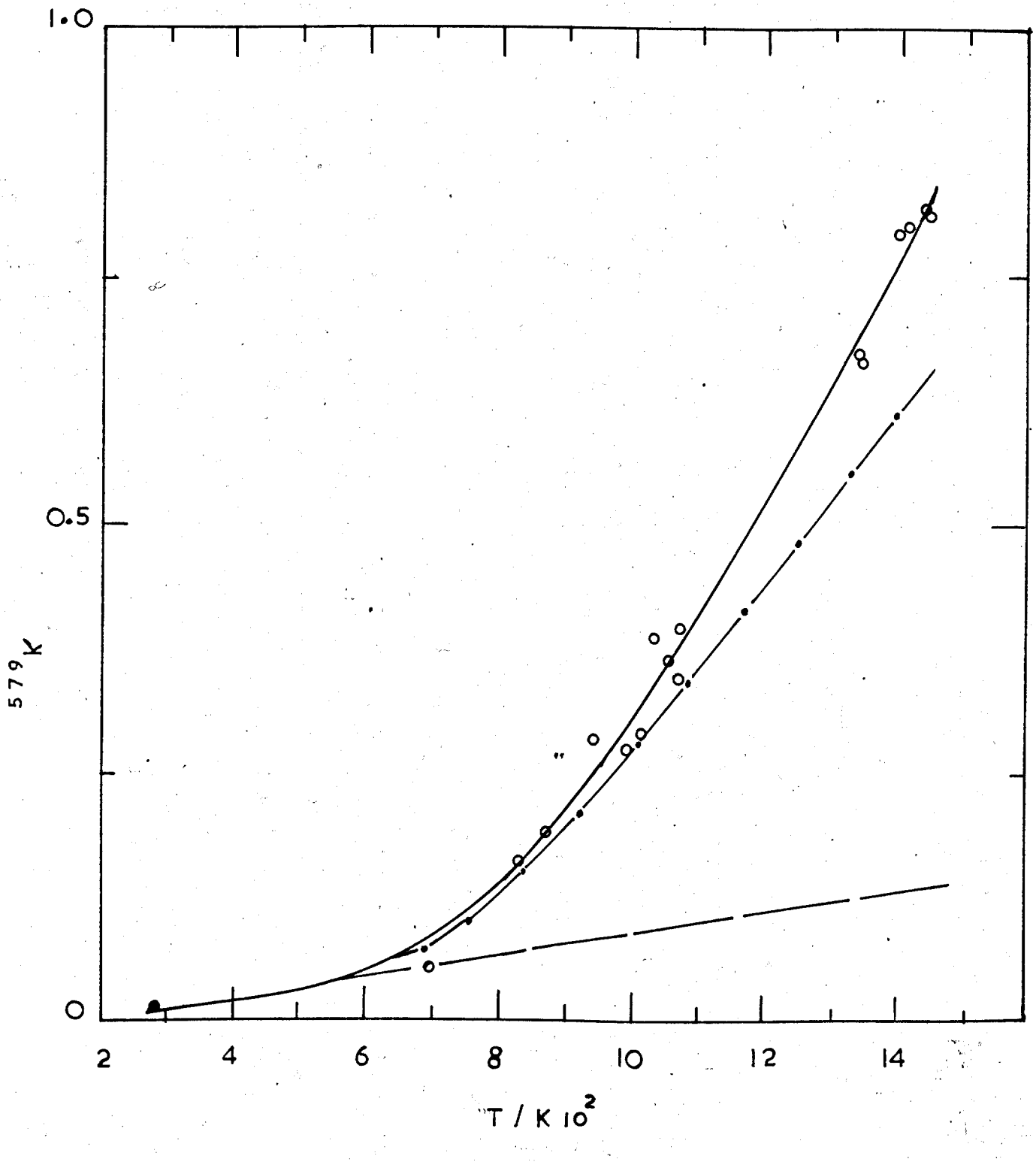

Table 8.2c - Bands at 579 nm

no. of quanta n	transition (v' + v') - (v" - v")	wavelength of maximum, λ/nm	relative population at 1200 K	$\lambda_{k_n/^{579}k_1}$ (measured)	filter factor f_{579}/f_λ	$\lambda_{k_n/^{579}k_1}$ (corrected)	$\lambda_{k_n/^{634}k_0}$
1	(1 + 0) - (0 + 0)	579.8	0.12	1	-	1	0.93
2	(1 + 1) - (1 + 0)	582.2	0.02	17.4	1.38	24.0	22.3
	(2 + 0) - (1 + 0)	583.1					
3	(2 + 1) - (1 + 1)	585.6	0.0035	25.0	2.10	53.0	49.3
	(2 + 1) - (2 + 0)	584.7					
	(3 + 0) - (1 + 1)	587.4					
	(3 + 0) - (2 + 0)	586.5					

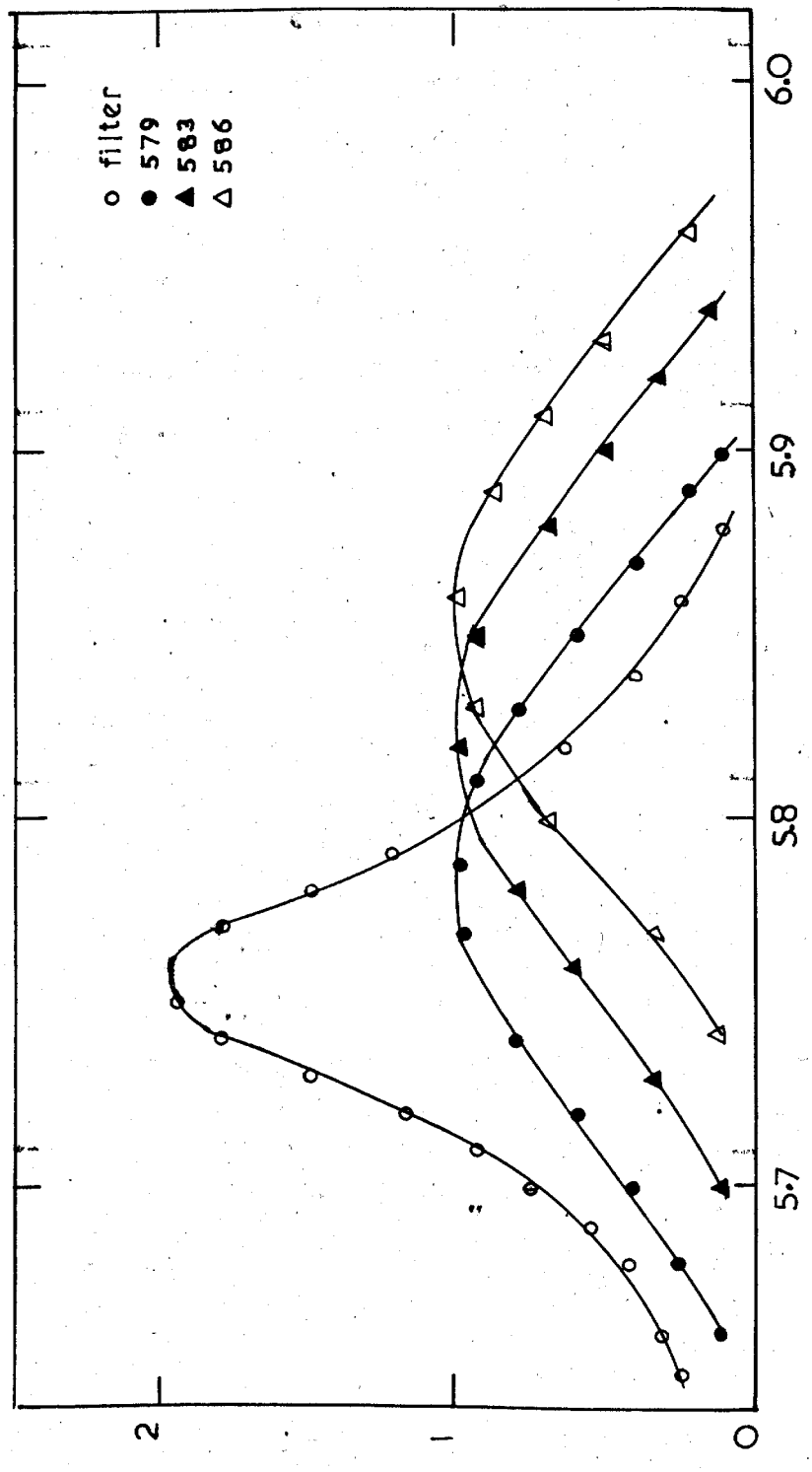

Figure 8.2c Filter 579 nm and bands.

$$^{579}I = k_1 \Delta_1^e \Delta_0^e + k_2 \Delta_1^e \Delta_1^e + k_3 \Delta_1^e \Delta_2^e \qquad (8.28)$$

where the various emissions involving 2 or 3 quanta in the upper state have been combined together. Combining equations (8.27) and (8.28) and replacing the concentration ratios by Boltzmann factors gives:

$$^{579}K = (k_1/^{634}k_0) B_1^{\Delta} [B_0^{\Delta} + (k_2/k_1) B_1^{\Delta} + (k_3/k_1) B_2^{\Delta}] \qquad (8.29)$$

where $^{634}k_0$ refers to the $(0 + 0 \rightarrow 0 + 0)$ transition at 634 nm, and k_1, k_2 and k_3 refer to the emissions at 579 nm.

The data were fitted to equation (8.29) by a non-linear least squares procedure and the best line is shown in figure 8.4c, together with the contributions from the various bands. The ratios of the constants are given in table 8.2c.

The ratio $(^{579}k_1/^{634}k_0)$ was found to be 0.995 from a series of measurements at room temperature. The relative values for 579 nm/634 nm emission constants are then obtained by correcting this value for the photomultiplier efficiency at these wavelengths ($\phi_{579}/\phi_{634} = 1.30$) and for the filter factor ($f_{579}/f_{634} = 0.82$). The final column of the table gives the ratios with respect to the 634 nm $(0 + 0 \rightarrow 0 + 0)$ band.

8.3.3 Rate Constants of the Dimol Emissions

The room temperature rate constants for the dimol emissions studied are calculated from the relative intensities, with respect to the $(0 + 0 \rightarrow 0 + 0)$ band, using the room temperature value for the $(0 + 0 \rightarrow 0 + 0)$ band reported recently by Fisk and Hays[88]. The values are listed in table 8.3 together with the measured relative intensities.

Rate constants at other temperatures can be obtained using that

Table 8.3. Rate Constants of the Dimol Emissions at 295 K

$$O_2(a^1\Delta_g)_{v'} + O_2(a^1\Delta_g)_{v'} \rightarrow O_2(X^3\Sigma_g^-)_{v''} + O_2(X^3\Sigma_g^-)_{v''} + h\nu$$

Transition $(v'+v')-(v''+v'')$	Emission Wavelength, λ/nm	$\lambda k_n / {}^{634}k_o$	Rate constant /$dm^3 mol^{-1} s^{-1}$
(0+0)-(0+0)	634.3	1	0.0265 a)
(1+0)-(1+0)	673.3	3.18	0.084
(1+1)-(1+1)	640.2	35.2	0.933
(1+1)-(2+0)	639.3		
(2+0)-(1+1)	641.3		
(2+0)-(2+0)	640.3		
(0+0)-(1+0)	703.8	0.83	0.023
(1+0)-(1+1)	707.4	2.24	0.059
(1+0)-(2+0)	706.2		
(1+0)-(0+0)	579.8	0.93	0.025
(1+1)-(1+0)	582.2	22.3	0.591
(2+0)-(1+0)	583.1		
(2+1)-(1+1)	585.6	49.3	1.306
(2+1)-(2+0)	584.7		
(3.0)-(1+1)	587.4		
(3.0)-(2+0)	586.5		

a) Base value measured by Fisk and Hays[88].

calculated at room temperature and equation (8.30):

$$\lambda_{k_T} = \lambda_{k_{295}} (T/295K)^{\frac{1}{2}}. \qquad (8.30)$$

The rate constants obtained rely on the base value measured by Fisk and Hays[88] at 295 K. They compared the dimol emission with that from the O + NO reaction and used the latest value of the rate constant for the calibration. Their value appears to confirm the earlier measurements of Gray and Ogryzlo[14] and Falik and Mahan[89] but it is higher than the value of Derwent and Thrush[65].

8.3.4 Discussion

Arnold, Browne and Ogryzlo[74] studied the temperature dependence of the dimol emission at 634 nm between 221 and 475 K and fround that the intensity varied with the square of the concentration of $O_2(a^1\Delta_g)$ and that the rate constant for the (0 + 0 → 0 + 0) band increased with the square root of the temperature. So based on these observations they suggested that the reaction is a simple collisional process with a zero activation energy.

For both the 634 nm and 703 nm emissions up to nearly 1000 K, the present values for the enhancement factor, K, is equal to one as expected for the collisional model hence confirming the collisional nature of the reaction.

In an earlier study[57] the rise in dimol emission at higher temperatures was attributed to an increase in the rate constant with temperature. The present suggestion that the rise observed is due to contributions from hot bands seems more reasonable since they do actually overlap in the wavelength region of the filters and can contribute to the observed emission. However, the earlier suggestion still cannot be completely excluded.

Two hot bands have been observed previously by Goodman and Brus[90]. They used laser radiation near 579 nm to excite oxygen, in solid neon at 4K, to $O_2(a^1\Delta_g)_{v=1}$ state. Emissions observed were near 703 nm from the (1 + 0 → 1 + 1) and (1 + 0 → 2 + 0) bands as well as from the (0 + 0 → 1 + 0) band.

There have been two other estimates of the intensities of dimol transitions in the gas-phase. Whitlow and Findlay[64] found the emission at 703 nm to be comparable to that at 634 nm and so reported a value of 1.05 for ratio, $^{703}k/^{634}k_0$. The present results agree well with this. Khan and Kasha[17] studied the absorption spectra and the ratio $^{579}k_1/^{634}k_0$ estimated from their results is 1.44 in comparison to 0.93 given by the present study. The discrepancy seems reasonable considering the weakness of the transitions.

The results in table 8.3 show that the rate constants for the dimol emissions in any band increase with number of vibrational quanta in the upper state. However, these changes do not reflect the Franck-Condon factors for the single molecule transitions. For example, the ratio of the Franck-Condon factors[87] for 1 → 0/0 → 0 and 0 → 1/0 → 0 transitions of $O_2(a^1\Delta_g)_{v'} \longrightarrow O_2(\chi^3\Sigma_g^-)_{v''}$ are 0.022 and 0.007, and yet in the dimol transitions (1 + 0 → 0 + 0)/(0 + 0 → 0 + 0) and (0 + 0 → 1 + 0)/(0 + 0 → 0 + 0) the rate constants ratios are 0.93 and 0.85. Franck-Condon factors can be a good guide to relative intensities if the electronic part of the transition probability is nearly constant in the region of the transition. It seems that in these cooperative transitions where the electronic part is determined by weak intermolecular forces, the electronic transition probability changes rapidly with distance. So at higher vibrational states the interactions may take place over a greater range of distances giving rise to greater intensities.

The nature of the upper state $[O_2(a^1\Delta_g), O_2(a^1\Delta_g)]$ is not clear.

$[O_2]_2$ has been suggested as the cause of the blue colour of liquid oxygen[91,92]. Arnold et al.[74] concluded from their study of the temperature dependence of the emission that an $[O_2]_2$ complex is not responsible for the emission. The fact that enhancement factor, K, does not decrease with increasing temperature is a further evidence that the emitting species can not be a dimer.

The intensities of these bands have been considered theoretically[93,94] where the models used allow for mixing of the possible transitions due to the intermolecular forces. The suggestion is that the dimol transitions may gain electronic intensity from the very strong $B(^3\Sigma_g^-) \rightarrow \chi(^3\Sigma_g^-)$ transition, which is responsible for the Schumann-Runge band system of O_2. Some success has been achieved with these approaches.

In this study evidence has been presented that the extra temperature dependence of the observed dimol emissions from $O_2(a^1\Delta_g)$ is due to contributions from overlapping hot bands but clearly confirmation requires spectroscopic identification.

8.3.5. Reliability of the Results

The reliability of discharge flow shock tube technique has been discussed in Chapter 4 (section 4.4.3). Below is given an assessment of the spectroscopic data obtained in the present study.

The number of experimental points and the best fits obtained for the data using interactive graphics and non-linear least squares are found invaluable for calculating the relative rate constants with a high precision. However, all the results have been subjected to two correction factors. First, corrections were made for the change of photomultiplier quantum efficiency with wavelength, with relative

values obtained from the manufacturer's data[95]. Since the measurements were made with a single photomultiplier the error is probably not greater than ± 10%.

Second and more important is the correction applied for differences in transmission by the filter. The general shape of the (0 + 0 → 0 + 0) band was obtained from the emission spectrum of Bader and Ogryzlo[18], after correcting their wavelength scale, and it is similar to that seen in absorption by Khan and Kasha[17] and recently by Singh and Koroll[96]. Clearly a shape obtained from spectra taken from a weak emission can hardly give precise values, but the lack of detail in the spectrum reduces the errors in comparative measurements. It is reasonable to assume that the other bands have the same shape, but it is difficult to be certain without knowledge of the spectra. Shapes of several bands can be seen in the work of Goodman and Brus[90] and they are similar, but all the bands are considerably narrowed in the solid at 4K. Taking these sources of error into account we estimate a 95% confidence level at ± 25% of the values listed in table 8.3.

The value estimated for the (2 → 1) transition of the $O_2(a^1\Sigma_g^+)$ emission (0.046 s^{-1}) is subject to a greater error since we had to approximate a line spectrum by an envelope to obtain the filter correction. The value[86,87] for the (0 - 0) band is 0.077 s^{-1}, and when the ratio of the Franck-Condon factors is taken into account, the expected value is about one third of what we find. Considering the approximations involved in comparing the single and dimol transitions the value seems reasonable.

CHAPTER NINE

9 Suggestions for Further Studies

In this chapter some possible further studies of singlet molecular oxygen and other systems using the combined discharge flow shock tube techniques are outlined in the light of the present work.

9.1 Further Studies of Singlet Molecular Oxygen

A study of the temperature dependence of the quenching of $O_2(b^1\Sigma_g^+)$ by HBr and H_2 would allow comparison with previous work[30,52]. These quenching systems have been modelled by Ogryzlo et al.[5,52] using long and short range interactions. The wide temperature range attainable with our discharge flow/shock tube should provide a good test for the theory.

HBr possess the disadvantage of being highly corrosive and with H_2 there is some danger of explosion, especially in the presence of the discharge. So in both cases extreme care should be taken in carrying out the experiments.

It may also be possible to measure the temperature dependence of the quenching of $O_2(a^1\Delta_g)$ by these quenchers if, (a) the pre-shock decay rate is large enough to be measured accurately at room temperature; (b) there is at least 15% increase in decay rate at the shock temperature.

As the potential energy surfaces for the quenching of both $O_2(a^1\Delta_g)$ and $O_2(b^1\Sigma_g^+)$ are unknown it is difficult to determine the precise nature of these reactions solely by inferring to the measured temperature dependences so it would be invaluable to calculate these potential surfaces.

There are several mixed dimol emissions[17] for example:

$$O_2(a^1\Delta_g) + O_2(b^1\Sigma_g^+) \rightarrow 2O_2(\chi^3\Sigma_g^-) + h\nu \ (\lambda = 478 \text{ nm}) \qquad (1.13)$$

and

$$O_2(a^1\Delta_g) + O_2(b^1\Sigma_g^+) \rightarrow O_2(\chi^3\Sigma_g^-)_{v=1} + O_2(\chi^3\Sigma_g^-) + h\nu \ (\lambda = 514 \text{ nm}) \qquad (9.1)$$

that could be studied in this apparatus. The problem here will be due to the low emission intensity and the absence of a sensitive spectrometer. At present a rapid scan spectrometer, consisting of a simple monochromator linked to a charged coupled semiconductor array, is under construction which can be used to study these systems.

This rapid scan spectrometer which is designed to take a spectrum at our light intensities within 200 μs could be also used to identify the additional emissions (section 6.5) seen in this work.

9.2 Studies of Other Systems

Recently Slanger[97] and Ogryzlo et al.[98] have reported emission in the visible region from the recombination of oxygen atoms which has been attributed to several new band systems of molecular oxygen; $^3\Delta_u \rightarrow {}^1\Delta_g$, $^3\Delta_u \rightarrow {}^3\Sigma_g^-$ and $^1\Sigma_u \rightarrow {}^1\Delta_g$. The emission should be visible in our system where we can generate higher concentrations than in a normal discharge and will enable us to study the reactions of oxygen atoms at high temperatures. Already a new discharge flow/shock tube system free of mercury, which can be operated in parallel to the existing one, is constructed to study these reactions.

The initial studies could be of the reaction of oxygen atoms with CF_3I and CH_3I to provide a comparison with the work of Grice[99] who studied these particular reactions with his molecular beam

technique. Once established, the method could be used to study any oxygen atom reactions which are of evident importance in combustion, in the upper atmosphere and in air pollution processes.

This new system can also be used to study further the additional emissions seen at both 762 nm and 634 nm at longer times and higher temperatures in mixtures of O_2/NO, O_2/NH_3 and O_2/HCl. For example, the emission observed in O_2/NO mixtures may be due to chemiluminescence from the reaction between NO and atomic oxygen which has a broad maximum in this region. Here the atomic oxygen may be generated by the decomposition of oxygen itself, and if this is the case then the observation points to a way of studying this decomposition and the similar ones at lower temperatures than hitherto have been possible.

The O + NO system, used for monitoring the concentration of oxygen atoms, is well understood at room temperature[100] but there have been few studies at high temperatures. It was the first reaction to be studied in a discharge flow/shock tube[53] but the reported temperature dependence seems unrealistic. The initial measurements relied only on the initial shock compression and took no account of the system rise time, vibrational relaxation or the variation of concentration along the tube, all of which we have found to be important in obtaining accurate results with our method. So it would be worthwhile to study this reaction in detail at high temperatures.

In the O + NO system, the oxygen atoms are usually produced by reaction of NO with N atoms, generated by passing N_2 through a discharge, and there are many worthwhile studies of the various chemiluminescent processes in the active nitrogen system[101].

Barnes, Becker and Fink[102] have reported studies at room temperature of the electronically excited states of S_2 and SO equivalent to those of O_2. The comparison between the temperature dependences of the rates of these reactions of these states with those for O_2 would be valuable. For example $SO(^1\Delta)$ and $S_2(^1\Delta_g)$ show energy pooling reactions:

$$SO(^1\Delta) + SO(^1\Delta) \rightarrow SO(^1\Sigma) + SO(^3\Sigma) \qquad (9.2)$$

$$S_2(^1\Delta_g) + S_2(^1\Delta_g) \rightarrow S_2(^1\Sigma_g^+) + S_2(\chi^3\Sigma_g^-) . \qquad (9.3)$$

SO and S_2 are formed by discharging sulphur containing compounds e.g. $SOCl_2$ and S_2Sl_2.

References

1. C.S. Foote, Y.C. Chang and R.W. Denny; J. Am. Chem. Soc., 92, 5216, 5218, (1970).
2. H.I. Schiff, Ann. N.Y. Acad. Sci., 171, 188, (1970).
3. J.N. Pitts, A.U. Khan, E.B. Smith and R.P. Wayne, Environ. Sci. Tech., 3, 243, (1969).
4. D.J. Benard, W.E. McDermott, N.R. Pchelkin and R.R. Bousek, Appl. Phys. Lett., 34, 40, (1979).
5. R.P. Wayne, Advan. Photochem., 7, 311, (1969).
6. J. Nicholas, "Chemical Kinetics", Harper and Row, (1976).
7. G.M. Barrow, "Physical Chemistry", McGraw-Hill, (1973).
8. J.D. Lambert, "Vibrational and Rotational Relaxation in Gases", Oxford, (1977).
9. P.M. Borrell, M.D. Pedley, P. Borrell and K.R. Grant, Proc. R. Soc. London, Ser. A, 367, 395 (1979).
10. P.M. Borrell, P. Borrell and K.R. Grant, J. Chem. Phys., 78, 748, (1983).
11. D.R. Kearns, Chem. Rev., 71, 403, (1971).
12. S.J. Arnold, E.A. Ogryzlo and H. Witzke, J. Chem. Phys., 40, 1769, (1964).
13. G. Herzberg, "Spectra of Diatomic Molecules", Van Nostrand, N.Y., (1939).
14. E.W. Gray and E.A. Ogryzlo, Chem. Phys. Lett., 3, 658, (1969).
15. P.M. Borrell, Ph.D. Thesis, University of Keele, (1980).
16. K. Furukawa, E.W. Gray and E.A. Ogryzlo, Ann. N.Y. Acad. Sci., 171, 175, (1970).
17. A.U. Khan and M. Kasha, J. Amer. Chem. Soc., 92, 3293, (1970).

18. L.W. Bader and E.A. Ogryzlo, Disc. Faraday Soc., 37, 46, (1964).

19. R.A. Young and G. Black, J. Chem. Phys., 42, 3740, (1965).

20. R.H. Kummler, M.H. Bartner and T. Baurer, Environ. Sci. Tech., 3, 248, (1969).

21. E. Castellano and H.J. Schumacher, Chem. Phys. Lett., 13, 625, (1972).

22. J. Heicklen, "Atmospheric Chemistry", Acad. Press. N.Y., (1976).

23. R.P. Wayne, Quart. J. Roy. Meteorol. Soc., 93, 395, (1967).

24. E.J. Bowen, Advan. Photochem., 1, 23, (1963).

25. R.P. Steer, J.L. Sprung and J.N. Pitts, Environ. Sci. Tech. 3, 946, (1969).

26. J.A. Davidson, K. Kear and E.W. Abrahamson, J. Photochem., 1, 307, (1972/3).

27. T.C. Frankiewicz and R.S. Berry, J. Chem. Phys., 58, 1787, (1973).

28. L.R. Martin, R.B. Cohen and J.F. Schatz, Chem. Phys. Lett., 41, 394, (1976).

29. S.A. Lawton, S.E. Novick, H.P. Broida and A.V. Phelps, J. Chem. Phys., 66, 1381, (1977).

30. K. Kohse-Hoinghaus and F. Stuhl, J. Chem. Phys., 72, 3720, (1980).

31. I.B.C. Matheson, J. Lee, B.S. Yamanashi and N.L. Wohlbarsht, Chem. Phys. Lett., 27, 355, (1974).

32. "Singlet Oxygen", H.H. Wasserman and R.W. Murray eds., Academic Press, N.Y. (1979).

33. L. Mallett, C.R. Hebd. Seances Acad. Sci., 185, 352, (1927).

34. A.M. Trozzolo and S.R. Fahrenholtz, Ann. N.Y. Acad. Sci., 171, 61, (1970).

35. R.W. Murray and M. Kaplan, J. Am. Chem. Soc., 90, 537, (1968).

36. A.U. Khan, Science, 168, 476, (1970).

37. R.P. Steer, K.R. Darnall and J.N. Pitts, Tetrahedron Lett. 3765, (1969).

38. A.M. Falick, B.H. Mahan and R.J. Myers, J. Chem. Phys., 42, 1837, (1965).

39. I.D. Clark and R.P. Wayne, Proc. Roy. Soc., A316, 539, (1970).

40. S.J. Arnold, M. Kubo and E.A. Ogryzlo, Advan. Chem. Ser., 77, 133, (1968).

41. R.W. Murray and M.L. Kaplan, J. Am. Chem. Soc., 90, 4161, (1968).

42. R.W. Murray and M.L. Kaplan, J. Am. Chem. Soc., 91, 5358, (1969).

43. "Singlet Oxygen-Reactions with Organic Compounds and Polymers", B. Ranby and J.F. Rabek eds., Wiley, (1978).

44. U. Schurath, J. Photochem., 1, 215, (1975).

45. R.G.O. Thomas and B.A. Thrush, Proc. Roy. Soc. London, A356, 307, (1977).

46. R.G. Derwent and B.A. Thrush, Chem. Phys. Lett. 9, 591, (1971).

47. R.F. Heidner III, C.E. Gardner, T.M. Ei-Sayed, G.I. Segal and J.V.V. Kasper, J. Chem. Phys., 74, 5618, (1981).

48. J.A. Davison and E.A. Ogryzlo, "Chemiluminescence and Bioluminscence", M.J. Cormier, D.M. Hercules and J. Lee eds., Plenum Press N.Y., (1973).

49. K. Kear and E.W. Abrahamson, J. Photochem., 3, 409, (1975).

50. M. Braithwaite, J.A. Davidson and E.A. Ogryzlo, J. Chem. Phys., 65, 771, (1976).

51. M. Braithwaite, E.A. Ogryzlo, J.A. Davidson and H.I. Schiff, J. Chem. Soc. Faraday II, 72, 2075, (1976).

52. M. Braithwaite, E.A. Ogryzlo, J.A. Davidson and H.I. Schiff, Chem. Phys. Lett., 42, 158, (1976).

53. R.A. Hartunian, W.P. Thompson and E.W. Hewitt, J. Chem. Phys., 44, 1765, (1966).

54. N. Cohn and R.F. Gross, J. Chem. Phys., 50, 3119, (1969).

55. J.E. Breen, R.B. Quy and G.P. Glass, J. Chem. Phys., 59, 556, (1973).

56. K.R. Grant, Ph.D. Thesis, University of Keele, (1981).

57. P.M. Borrell, P. Borrell and K.R. Grant, J. Chem. Soc. Faraday II, 76, 1442, (1980).

58. C.J. Smith, "The General Properties of Matter", Edward Arnold, Lond., (1953).

59. M.D. Pedley, Ph.D. Thesis, University of Keele, (1978).

60. C.T. Bowman and R.K. Hanson, J. Phys. Chem., 83, 757, (1978).

61. J.A.N.A.F. Thermochemical Tables, The Dow Chemical Company, Michigan, (1965).

62. R.C. Millikan, General Electric Research Report 64-RL-3700C, N.Y. (1964).

63. P. Borrell, P.M. Borrell and M.D. Pedley, Chem. Phys. Lett., 51, 300, (1977).

64. S.H. Whitlow and F.D. Findlay, Can. J. Chem., 45, 2087, (1967).

65. R.G. Derwent and B.A. Thrush, Trans. Faraday Soc., 67, 2036, (1971).

66. P. Borrell, Comput. Chem., 4, 131, (1980).

67. M. Yaron, A. von Engel and P.H. Vidaud, Chem. Phys. Lett. 37, 159, (1976).

68. D.J. Giachardi, G.W. Harris and R.P. Wayne, J. Chem. Soc. Faraday Trans. II, 72, 691, (1976).

69. K.H. Becker, W. Groth and U. Schurath, Chem. Phys. Lett., 8, 259, (1971).

70. A. Leiss, U. Schurath, K.H. Becker and E.H. Fink, J. Photochem., 8, 211, (1978).

71. I.A. McLaren, N.W. Morris and R.P. Wayne, J. Photochem., 16, 311, (1981).

72. F.D. Findlay and D.R. Snelling, J. Chem. Phys., 55, 545, (1971).

73. R.G.O. Thomas and B.A. Thrush, J. Chem. Soc. Faraday Trans. II, 71, 664, (1975).

74. J.S. Arnold, R.S. Browne and E.A. Ogryzlo, Photochem. Photobiol., 4, 963, (1965).

75. R.J. O'Brien Jr. and G.H. Myers, J. Chem. Phys., 53, 3832, (1972).

76. S.V. Filseth, A. Zia and K.H. Welge, J. Chem. Phys., 52, 5502, (1970).

77. R.G.O. Thomas and B.A. Thursh, Proc. Royl. Soc. London, A356, 295, (1977).

78. M.J.E. Gautheir and D.R. Snelling, J. Photochem. 4, 27, (1975).

79. P.M. Borrell, P. Borrell, K.R. Grant and M.D. Pedley, J. Phys. Chem., 36, 700, (1982).

80. H.M. Lin, M. Seaver, K.Y. Tong, A.E.W. Knight and C.S. Parmenter, J. Chem. Phys., 70, 5442, (1979).

81. C.S. Parmenter and M. Seaver, J. Chem. Phys., 70, 5458, (1979).

82. R.D. Ashford and E.A. Ogryzlo, J. Am. Chem. Soc., 97, 3604, (1975).

83. E.A. Ogryzlo and B.A. Thrush, Chem. Phys. Lett., 32, 34, (1973).

84. P.W. Atkins, "Physical Chemistry", Oxford, (1978).

85. Nottingham Algorithms Group (Nottingham, 1972), unpublished work.

86. K.P. Huber and G. Herzberg, "Constants of Diatomic Molecules", Van Nostrant Reinhold, N.Y., (1979).

87. P.H. Krupenie, J. Phys. Chem. Ref. Data, 1, 423, (1972).

88. G.A. Fisk and G.N. Hays, Chem. Phys. Lett., 79, 331, (1981).

89. A.M. Falik and B.H. Mahan, J. Chem. Phys., 47, 4778, (1967).

90. J. Goodman and L.E. Brus, J. Chem. Phys., 67, 4398, (1977).

91. D.L. Heustis, G. Black, S.A. Edelstein and R.L. Sharpless, J. Chem. Phys., 60, 4471, (1974).

92. S.E. Novik and H.P. Broida, J. Chem. Phys., 67, 5975, (1977).

93. V.G. Krishna, J. Chem. Phys., 50, 792, (1969).

94. S.C. Tsai and G.W. Robinson, J. Chem. Phys., 51, 3559, (1969).

95. Photomultipliers (E.M.I. Ltd., Hayes, Middlesex, 1979).

96. A. Singh and G.W. Koroll, unpublished work.

97. T.G. Slanger, Science, 202, 751, (1978).

98. R.D. Kenner, E.A. Ogryzlo and S. Turley, J. Photochem., 10, 199, (1979).

99. R. Grice, Faraday Discuss. Chem. Soc., 67, 16, (1979).

100. A. Fontijn, C.B. Meyer and H.I. Schiff, J. Chem. Phys., 40, 64, (1964).

101. A.N. Wright and C.A. Winkler, "Active Nitrogen", Academic Press, N.Y., (1968).

102. I. Barnes, K.H. Becker and E.H. Fink, Chem. Phys. Lett., 67, 310, (1979).

Appendix 1

Run Parameters for NH_3/O_2

T_1 = 295 K, TOTAL Flow Rate, F_{T_0} = 28 mls^{-1}

(a) 3% NH_3, 97% O_2

Run No.	λ /nm	psg /mV	P_1 /torr	V_s /Kms^{-1}	T_2 /K	P_{21}	ρ_{21}
R 216	634	6.0	6.99	0.826	602	7.35	3.58
RA 216	762	16.1					
R 212	634	7.0	6.62	0.978	732	10.41	4.16
RA 212	762	14.6					
R 211	634	7.4	6.25	1.125	876	13.83	4.62
RA 211	762	19.0					
R 210	634	7.1	6.87	1.129	883	14.08	4.65
RA 210	762	15.6					
R 209	634	6.8	6.79	1.147	901	14.41	4.68
RA 209	762	18.1					
R 208	634	8.3	6.95	1.236	998	16.77	4.92
RA 208	762	21.6					
R 214	634	7.4	6.95	1.265	1031	17.56	4.99
RA 214	762	13.7					
R 215	634	6.8	6.45	1.354	1135	20.16	5.20
RA 215	862	18.1					

(b) 7% NH_3, 93% O_2

R 220	634	6.5	6.45	0.984	747	10.26	4.02
RA 220	762	6.4					
R 219	634	6.4	6.29	1.072	833	12.20	4.29
RA 219	762	6.9					
R 218	634	6.6	6.37	1.120	883	13.33	4.42
RA 218	762	8.0					
R 217	634	7.6	5.54	1.187	956	15.03	4.60
RA 217	762	11.2					

Appendix 1 continued

(c) 5% NH_3, 95% O_2

Run No.	λ /nm	psg /mV	P_1 /torr	$V_{s_{-1}}$ /Kms	T_2 /K	P_{21}	ρ_{21}
R 201	634	8.3	5.63	0.870	630	8.16	3.79
RA 201	762	11.2					
R 224	634	5.7	6.45	0.997	754	10.66	4.14
RA 224	762	8.5					
R 223	634	5.9	6.62	1.046	802	11.78	4.30
RA 223	762	7.3					
R 225	634	6.5	6.55	1.090	846	12.80	4.43
RA 225	762	10.4					
R 222	634	6.3	6.50	1.119	876	13.50	4.51
RA 222	762	7.2					
R 226	634	6.3	5.96	1.147	906	14.21	4.59
RA 226	762	8.7					
R 205	634	8.5	5.71	1.237	1005	16.56	4.82
RA 205	762	15.4					
R 228	634	6.4	5.46	1.243	1013	16.74	4.84
RA 228	762	9.1					
R 227	634	7.0	5.92	1.259	1030	17.15	4.88
RA 227	762	8.9					
R 206	634	8.1	5.67	1.266	1039	17.36	4.89
RA 206	762	13.5					
R 207	634	8.3	5.63	1.331	1114	19.18	5.04
RA 207	762	12.4					

Appendix 2

Run Parameters for NO/O_2

$T_1 = 295$ K, $F_T = 28$ mls^{-1}

(a) 3% NO, 97% O_2

Run No.	λ /nm	psg /mV	P_1 /torr	V_s /Kms^{-1}	T_2 /K	P_{21}	ρ_{21}
R 85	634	4.9	6.62	1.155	918	14.78	4.71
RA 85	762	291.0					
R 104	634	5.1	6.62	1.047	805	12.08	4.39
RA 104	762	281.0					
R 88	634	5.4	6.62	1.067	825	12.55	4.45
RA 88	762	339.0					
R 107	634	6.7	6.62	1.154	916	14.73	4.71
RA 107	762	409.0					
R 106	634	5.02	6.62	1.208	977	16.19	4.85
RA 106	762	264.0					
R 87	634	4.8	6.62	1.218	987	16.44	4.88
RA 87	762	266.0					
R 105	634	5.4	6.62	1.286	1065	18.36	5.05
RA 105	762	278.0					
R 86	634	4.9	6.62	1.343	1133	20.08	5.19
RA 86	762	269.0					

(b) 5% NO, 95% O_2

P 59	634	3.7	6.62	0.909	683	9.0	3.86
RA 59	762	140.0					
R 103	634	5.0	6.62	0.939	710	9.62	3.97
RA 103	762	193.0					
R 96	634	5.1	6.62	1.064	831	12.42	4.37
RA 96	762	209.0					
R 101	634	4.8	6.62	1.128	899	13.99	4.56
RA 101	762	189.0					
R 97	634	4.7	6.62	1.144	916	14.39	4.60
RA 97	762	189.0					
R 102	634	4.8	6.62	1.163	937	14.88	4.65
RA 102	762	202.0					

Appendix 2 continued

(b) 5% NO, 95% O_2

Run No.	λ /nm	psg /mV	P_1 /torr	V_s /Kms^{-1}	T_2 /K	P_{21}	ρ_{21}
R 100	634	4.8	6.62	1.233	1016	16.76	4.83
RA 100	762	202.0					
R 99	634	4.5	6.62	1.278	1068	18.06	4.95
RA 99	762	169.0					
P 60	634	3.7	6.62	1.293	1088	18.52	4.99
PA 60	762	132.0					

(c) 8% NO, 92% O_2

R 95	634	3.6	6.62	0.994	762	9.64	3.89
RA 95	762	93.0					
R 93	634	3.6	6.62	1.026	806	11.43	4.15
RA 93	762	101.0					
R 91	634	3.7	6.62	1.051	832	12.01	4.22
RA 91	762	109.0					
R 92	634	3.6	6.62	1.151	941	14.45	4.50
RA 92	762	103.0					
R 94	634	3.8	6.62	1.160	951	14.68	4.52
RA 94	762	110.0					

Appendix 3

Run Parameters for HCl/O_2

$T_1 = 293$ K, $F_T = 28$ mls^{-1}

(a) 3% HCl, 97% O_2

Run No.	λ /nm	psg /mV	P_1 /torr	V_s /Kms^{-1}	T_2 /k	P_{21}	ρ_{21}
R 347	634	7.2	6.41	0.823	599	7.47	3.65
RA 347	762	437.0					
R 348	634	7.2	6.29	0.862	630	8.21	3.82
RA 348	762	436.0					
R 336	634	5.3	6.66	0.919	678	9.36	4.04
RA 336	762	312.0					
R 346	634	5.9	6.21	0.950	705	10.02	4.16
RA 346	762	364.0					
R 345	634	6.1	6.12	0.952	707	10.06	4.17
RA 345	762	356.0					
R 344	634	6.5	6.17	0.972	725	10.50	4.24
RA 344	762	391.0					
R 334	634	4.9	6.62	0.975	730	10.59	4.25
RA 334	762	174.0					
R 343	634	5.8	5.92	1.041	789	12.05	4.47
RA 343	762	388.0					
R 337	634	5.3	6.87	1.054	804	12.41	4.52
RA 337	762	297.0					
R 341	634	7.3	6.21	1.090	838	13.26	4.63
RA 341	762	448.0					
R 340	634	8.5	6.58	1.143	893	14.61	4.79
RA 340	762	406.0					
R 339	634	6.6	6.08	1.210	964	16.38	4.98
RA 339	762	390.0					
R 342	634	7.3	6.21	1.276	1038	18.25	5.15
RA 342	762	467.0					

Appendix 3 continued

(b) 5% HCl, 95% O_2

Run No.	λ /nm	psg /mV	P_1 /torr	V_s /Kms^{-1}	T_2 /K	P_{21}	ρ_{21}
R 329	634	7.0	6.37	0.859	629	8.17	3.80
RA 329	762	253.0					
R 350	634	5.6	6.25	0.981	736	10.72	4.27
RA 350	762	250.0					
R 332	634	7.0	6.29	1.074	825	12.90	4.58
RA 332	762	224.0					
R 349	634	6.0	6.21	1.108	860	13.77	4.69
RA 349	762	309.0					
R 330	634	6.5	6.12	1.138	891	14.51	4.77
RA 330	762	243.0					
R 331	634	6.2	6.50	1.199	944	15.84	4.91
RA 331	762	217.0					
R 351	634	5.6	6.33	1.191	947	15.92	4.92
RA 351	762	237.0					
R 355	634	5.6	6.37	1.257	1021	17.77	5.09
RA 355	762	189.0					
R 353	634	5.1	6.54	1.267	1032	18.06	5.12
RA 353	762	192.0					
R 352	634	4.8	6.45	1.278	1046	18.41	5.15
RA 352	762	173.0					
R 356	634	5.9	6.08	1.335	1112	20.08	5.29
RA 356	762	203.0					
R 354	634	5.5	6.00	1.384	1172	21.61	5.40
RA 354	762	186.0					

Appendix 3 continued

(c) 7% HCl, 73% O_2

Run No.	λ /nm	psg /mV	P_1 /torr	V_s /Kms^{-1}	T_2 /K	P_{21}	$\hat{\rho}_{21}$
R 364	634	6.0	6.58	0.837	605	7.58	3.67
RA 364	762	136.0					
R 363	634	6.0	6.71	0.920	683	9.43	4.04
RA 363	762	158.0					
R 362	634	5.5	6.66	0.940	701	9.85	4.12
RA 362	762	142.0					
R 361	634	5.1	6.58	0.987	743	10.88	4.29
RA 361	762	142.0					
R 360	634	4.9	6.54	1.024	778	11.73	4.41
RA 360	762	131.0					
R 359	634	4.7	6.54	1.064	818	12.69	4.54
RA 359	762	134.0					
R 358	634	4.9	6.37	1.125	880	14.21	4.73
RA 358	762	153.0					
R 357	634	5.7	6.29	1.189	958	16.15	4.94
RA 357	762	189.0					

Appendix 4

Run Parameters for SO_2/O_2

$T_1 = 295$ K, $F_T = 28$ mls^{-1}

(a) 10% SO_2, 90% O_2

Run No.	λ /nm	psg /mV	P_1 /torr	V_s /Kms^{-1}	T_{21}	p_{21}	ρ_{21}
R 403	634	12.6	7.12	0.821	663	7.87	3.53
RA 403	762	391.0					
R 402	634	12.8	7.16	0.832	673	8.08	3.57
RA 402	762	361.0					
R 404	634	12.6	7.28	0.912	753	9.77	3.86
RA 404	762	343.0					
R 407	634	13.2	6.89	0.923	764	9.99	3.90
RA 407	762	428.0					
R 405	634	12.7	6.95	0.934	776	10.25	3.93
RA 405	762	482.0					
R 408	634	11.9	7.12	0.942	786	10.47	3.96
RA 408	762	329.0					
R 410	634	13.0	6.19	0.989	836	11.53	4.11
RA 410	762	445.0					
R 412	634	12.1	7.24	1.013	863	12.11	4.18
RA 412	762	360.0					
R 411	634	12.5	7.16	1.032	884	12.58	4.24
RA 411	762	424.0					
R 417	634	13.0	7.04	1.082	943	13.85	4.38
RA 417	762	411.0					
R 415	634	13.0	6.83	1.086	946	13.94	4.39
RA 415	762	387.0					
R 413	634	13.9	6.99	1.119	988	14.86	4.48
RA 413	762	423.0					
R 419	634	12.0	7.33	1.124	898	14.88	4.49
RA 419	762	374.0					
R 416	634	13.0	7.28	1.179	1063	16.51	4.62
RA 416	762	414.0					

Appendix 4 continued

(a) 10% SO_2, 90% O_2

Run No.	λ /nm	psg /mV	P_1 /torr	V_s /Kms^{-1}	T_2 /K	P_{21}	ρ_{21}
R 421	634	12.0	6.79	1.210	1102	17.37	4.69
RA 421	762	401.0					
R 423	634	11.0	6.87	1.183	1070	16.67	4.64
RA 423	762	374.0					
RI 418	634	13.0	7.82	1.225	1122	17.81	4.73
RA 418	762	395.0					
R 422	634	13.0	6.95	1.231	1130	18.00	4.74
RA 422	762	424.0					

(b) 15% SO_2, 85% O_2

R 431	634	14.0	6.62	0.784	663	7.39	3.32
RA 431	762	432.0					
R 432	634	12.0	6.70	0.826	706	8.23	3.47
RA 432	762	380.0					
R 429	634	14.0	6.46	0.879	764	9.38	3.66
RA 429	762	484.0					
R 424	634	13.0	6.45	0.906	792	9.94	3.74
RA 424	762	349.0					
R 425	634	12.0	6.87	0.922	809	10.29	3.79
RA 425	762	309.0					
R 430	634	13.0	6.54	0.924	812	10.34	3.79
RA 430	762	457.0					
R 426	634	12.0	6.75	0.969	865	11.42	3.93
RA 426	762	313.0					
R 433	634	14.0	6.54	1.026	934	12.81	4.09
RA 433	762	419.0					
R 434	634	12.0	6.79	1.063	976	13.67	4.17
RA 434	762	358.0					
R 427	634	13.0	6.71	1.081	1004	14.24	4.23
RA 427	634	344.0					
R 436	634	12.0	6.54	1.140	1052	15.25	4.32
RA 436	762	361.0					
R 435	634	12.0	6.70	1.777	1081	15.85	4.36
RA 435	762	351.0					

Appendix 4 continued

(c) 20% SO_2, 80% O_2

Run No.	λ /nm	psg /mV	P_1 /torr	V_s /Kml^{-1}	T_2 /K	P_{21}	ρ_{21}
R 439	634	12.0	6.37	0.814	731	8.18	3.33
RA 439	762	327.0					
R 437	634	12.0	6.45	0.884	814	9.71	3.55
RA 437	762	324.0					
R 442	634	12.0	6.54	0.909	846	10.31	3.63
RA 442	762	348.0					
R 438	634	11.0	6.45	0.916	853	10.43	3.64
RA 438	762	304.0					
R 443	634	12.5	6.62	0.967	919	11.68	3.79
RA 443	762	373.0					
R 444	634	14.0	6.45	1.074	1063	14.45	4.05
RA 444	762	399.0					
R 445	634	15.0	6.46	1.076	1067	14.51	4.06
RA 445	762	413.0					
R 446	634	12.5	6.70	1.123	1136	15.85	4.16
RA 446	762	337.0					

Appendix 5

Analysis of Shock Traces for the Dimol Emissions

5% CO_2, 95% O_2; T_1 = 293 K; F_T = 28 mls^{-1}

Run No.	Fitter λ/nm	psg /mV	α_t /m^{-1}	t_s /μs	λ_K	T_2 /K	P_{21}	P_1 /torr	V_s /Kms^{-1}
R 1	703B	4.0	0.583	10	2.287	1422	29.95	6.04	1.606
R 2	703B	4.3	0.877	12	2.207	1389	38.90	5.72	1.579
RA 2	703C	8.2	0.905	15	2.858				
R 3	703B	2.8	0.807	24	3.840	1363	28.11	7.03	1.558
RA 3	703C	5.9	1.002	27	4.537				
R 4	703B	3.1	0.696	20	2.469	1387	28.84	6.54	1.578
RA 4	703C	6.0	0.761	22	3.119				
R 5	703B	3.2	-	-	1.345	1090	20.30	6.37	1.330
RA 5	703C	6.1	0.978	25	1.701				
R 6	703B	2.5	1.003	22	1.242	606	7.76	5.42	0.830
RA 6	703C	5.4	1.053	12	1.050				
RA 7	703C	6.1	0.990	30	0.949	687	9.77	6.21	0.986
R 8	703B	4.0	0.994	17	0.892	684	9.70	6.54	0.926
RA 8	703C	8.2	0.916	25	0.896				
R 9	703B	2.9	1.227	32	1.035	677	9.52	6.12	0.917
RA 9	703C	6.5	1.208	39	0.886				
P 36	703B	3.1	0.983	20	1.252	1052	19.26	6.58	1.295
PA 36	703C	5.9	1.016	22	1.523				
P 37	703B	3.1	1.294	28	1.356	1063	19.35	6.87	1.304
PA 37	703C	5.5	1.185	14	1.746				

Appendix 5 continued

Run No.	Filter λ/nm	.psg /mV	α_t /m^{-1}	t_s /μs	$\lambda\lambda_K$	T_2 /K	P_{21}	P_1 /torr	V_s /Kms^{-1}
P 40	703C	3.0	1.002	18	2.948	1352	27.76	6.70	1.548
PA 40	634C	9.4	1.139	17	1.639				
P 41	634C	4.9	1.324	18	1.215	1352	27.76	6.70	1.548
PA 41	703C	5.2	1.032	16	2.940				
P 42	703C	4.9	0.794	16	3.578	1456	31.08	6.29	1.635
PA 42	703B	8.2	0.869	15	3.241				
R 14	703C	4.6	0.922	19	1.767	1163	22.31	6.46	1.393
RA 14	703B	7.3	0.880	12	1.469				
R 15	703C	4.8	0.944	17	1.682	1165	22.37	5.96	1.387
RA 15	703B	7.8	0.830	13	1.448				
R 16	703C	4.0	1.139	27	1.444	1014	18.25	6.79	1.261
RA 16	703B	6.5	0.859	11	1.058				
R 20	703C	5.5	0.856	22	1.279	1043	19.02	6.04	1.287
RA 20	703B	9.4	0.816	22	1.154				
R 19	703C	4.4	0.840	27	1.229	936	16.17	5.96	1.189
RA 19	703B	7.6	0.958	28	1.127				
R 25	634A	11.1	1.087	15	1.68	1414	29.70	6.54	1.600
RA 25	703B	7.5	0.816	13	2.76				
R 26	634A	10.5	0.796	10	1.50	1393	29.02	6.54	1.582
RA 26	634C	12.3	0.705	10	1.37				
R 27	632A	10.2	1.108	9	1.60	1361	28.05	6.62	1.557
RA 27	579	0.3	1.050	17	31.90				

Appendix 5 continued

Run No.	Filter λ/nm	psg /mV	α_t /m^{-1}	t_s /μs	λ_K	T_2 /K	P_{21}	P_1 /torr	V_s /Kms^{-1}
R 28	634C	5.8	1.043	15	1.65	1373	28.42	6.62	15.66
RA 28	579	0.1	1.072	6	93.00				
R 32	579A	0.3	0.670	7	18.20	1391	28.96	6.62	1.587
RA 32	579B	0.1	0.790	2	85.20				
R 35	703B	3.2	0.680	15	2.48	1375	28.48	6.62	1.569
RA 35	579B	0.1	0.873	8	87.00				
P 48	634A	11.3	0.984	13	1.61	1415	29.70	6.62	1.575
PA 48	579	0.6	1.018	8	20.60				
P 49	634A	11.7	0.938	12	1.43	1393	29.02	6.70	1.582
PA 49	634C	12.7	0.968	12	1.52				
P 50	634C	11.1	0.932	10	1.46	1393	29.02	6.66	1.582
PA 50	703B	7.5	0.748	12	2.52				
R 42	634C	5.9	0.986	11	1.42	1336	27.28	6.70	1.535
RA 42	579B	0.2	0.952	15	5.37				
R 43	634C	6.0	1.148	14	1.37	1068	19.70	6.70	1.315
RA 43	579B	0.4	1.031	3	3.16				
R 44	634C	6.3	1.222	16	1.77	1391	28.96	6.70	1.581
RA 44	579B	0.5	1.237		7.10				
R 45	634C	5.8	1.158	17	1.53	1338	27.34	6.70	1.537
RA 45	579B	0.2	1.113	16	5.32				
R 46	634C	6.1	1.285	23	1.52	1028	18.63	6.70	1.273
RA 46	579B	0.4	1.086	23	3.08				

Appendix 5 continued

Run No.	Filter λ/nm	psg /mV	α_t /m^{-1}	t_s /μs^{-1}	λ_K	T_2 /K	P_{21}	P_1 /torr	V_s /Kms^{-1}
R 47	634C	5.9	1.777	19	1.33	1010	18.15	6.70	1.258
RA 47	579B	0.4	1.065	16	2.34				
R 48	634C	5.8	1.106	15	1.27	1064	19.60	6.62	1.307
RA 48	579B	0.3	1.013	17	2.76				
R 49	634C	5.8	1.138	18	1.26	1050	19.21	6.70	1.300
RA 49	579B	0.3	1.127	26	2.90				
R 50	634C	7.6	0.827		0.94	694	9.94	6.62	0.936
RA 50	579B	0.7	0.827	21	0.40				
R 51	634C	7.6	0.876	14	1.14	871	14.47	6.62	1.125
RA 51	579B	0.6	0.798	30	1.54				
R 52	634C	7.4	0.983	13	1.18	939	16.26	6.62	1.192
RA 52	579B	0.5	1.014	23	2.27				
R 53	634C	7.4	0.853	21	1.10	826	13.31	6.62	1.081
RA 53	579B	0.5	0.808	41	1.27				
R 54	634C	7.6	0.965	11	1.62	1435	30.38	6.62	1.618
RA 54	579B	0.5	0.980	14	6.52				
R 55	634C	7.0	1.178	15	1.82	1402	29.33	6.62	1.600
RA 55	579B	0.3	1.004	20	6.41				
R 56	634C	7.1	0.965	13	1.58	1430	30.20	6.62	1.614
RA 56	579B	0.4	1.034	13	6.55				

Appendix 5 continued

Run No.	Filter λ/nm	psg /mV	α_t /m^{-1}	t_s /μs^{-1}	λ_K	T_2 /K	P_{21}	P_1 /torr	V_s /Kms^{-1}
R 57	634C	7.2	0.899	14	1.18	986	17.50	6.70	1.236
RA 57	579B	0.5	0.809	24	2.20				
R 58	634C	7.2	0.938	17	1.12	996	17.77	6.62	1.245
RA 58	634C	69.6	1.009	19	1.37				
R 59	634C	7.0	0.909	13	1.21	1094	20.40	6.70	1.332
RA 59	634A	70.7	1.007	19	1.30				
R 60	634C	7.0	0.868	16	1.06	1072	19.80	6.70	1.313
RA 60	634A	70.8	1.032	13	1.27				
R 61	634C	7.2	0.964	29	1.13	823	13.23	6.70	1.078
RA 61	634A	71.0	0.988	17	1.15				

Appendix 6

The Integration Time

It was shown in Chapter 4 that the rise in emission at the shock front is not instantaneous, i.e. vertical. This arises because of the finite slit width used. The voltage recorded by the transient recorder is an average rather than an instantaneous record at any point. The situation can be illustrated by imagining that:

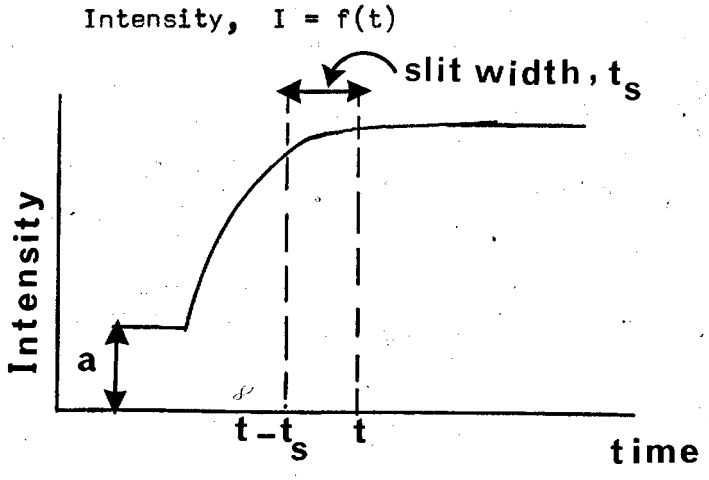

$$\text{so } I_{obs} = \int_{t-t_s}^{t} f(t)dt/t_s .$$

However, what happens near the beginning i.e. $t<t_s$

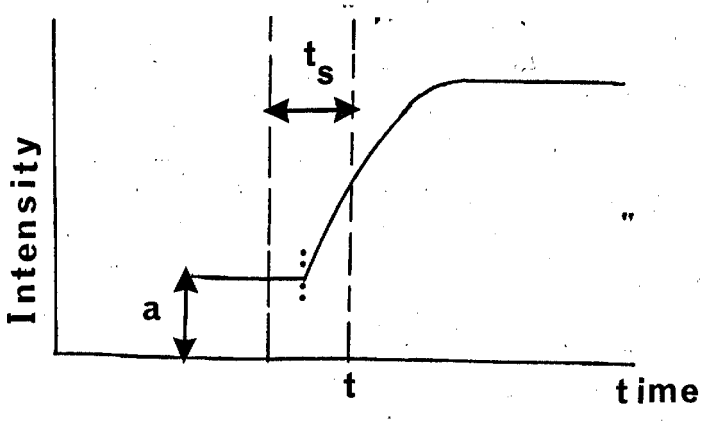

$$\text{Now } I_{obs} = \left\{a(t_s-t) + \int_{o}^{t} f(t)dt\right\}/t_s .$$

So two different integrated forms are required. This is also true in the numerical integration.